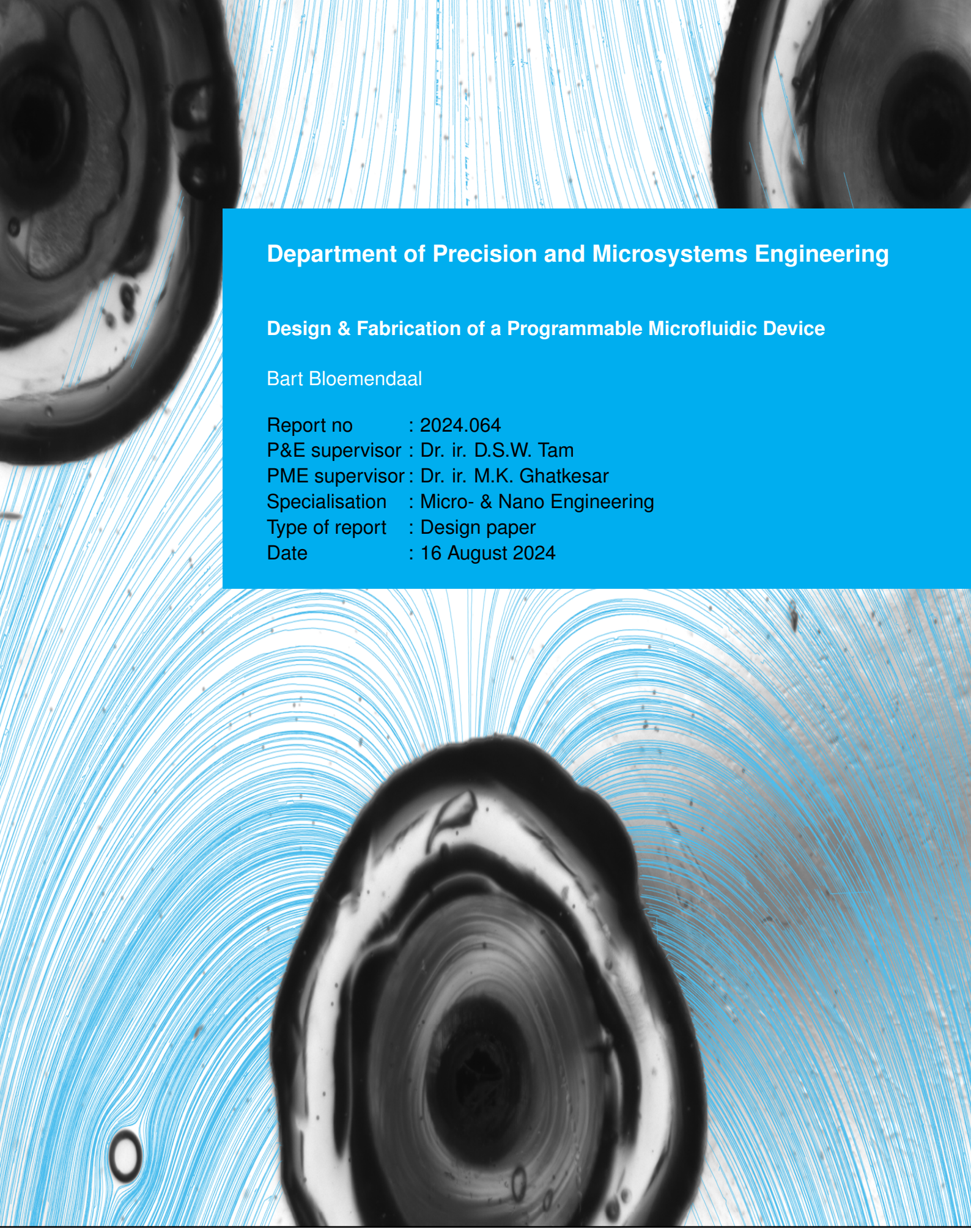

Department of Precision and Microsystems Engineering

Design & Fabrication of a Programmable Microfluidic Device

Bart Bloemendaal

Report no : 2024.064
P&E supervisor : Dr. ir. D.S.W. Tam
PME supervisor : Dr. ir. M.K. Ghatkesar
Specialisation : Micro- & Nano Engineering
Type of report : Design paper
Date : 16 August 2024

Summary

This article presents the design, fabrication, and testing of a programmable microfluidic device aimed at achieving precise hydrodynamic manipulation of particles and fluids. The device is fabricated using advanced techniques such as femtosecond laser ablation and cold oxygen plasma bonding, resulting in highly accurate microfluidic channels with minimal surface roughness. These precise channels are essential for ensuring consistent flow dynamics, which are critical for the device's functionality.

A significant innovation in the device's design is the use of a three-layer structure (glass-PDMS-glass) created through precise laser machining. This design approach provides high structural stiffness, which is necessary to maintain a constant channel volume and ensure reliable performance under pressure. The inlets and outlets are designed with careful consideration to minimise flow disturbance, ensuring that the flow remains consistent and predictable. The fabrication process has been optimised to achieve clean edge definitions and uniform outflow, which are critical for maintaining the integrity of the flow field.

The study explored the impact of laser ablation parameters on the fabrication quality. Through detailed characterisation, it was found that lower power settings minimise thermal shock, reducing surface roughness and improving edge quality. However, these settings also increase fabrication time, presenting a trade-off between precision and efficiency. The results indicate that a focal point velocity of 50mm/s and 3% of the laser's full power provide the best edge definition, for the microfluidic application.

The thesis highlights the theoretical aspects of flow modeling, employing the panel method and half Rankine body theory to predict and analyse flow fields within the device. The experimental results closely align with these theoretical models, confirming the accuracy and effectiveness of the fabrication techniques. Notably, the creation of uniform flow fields and the successful formation of half Rankine bodies validate the device's capability to perform as designed. These results are critical because they establish the device's potential to manipulate particles with high precision.

Furthermore, the research identified the challenge of maintaining flow rate accuracy when using external reservoirs. The findings revealed discrepancies between the digital readouts and actual flow rates, highlighting the need for further refinement in the device's flow control systems. Despite these challenges, the experimental validation of flow fields, particularly the formation of half Rankine bodies, confirmed the device's ability to approximate theoretical models, which is crucial for its intended applications.

Overall, this research contributes significantly to the field of microfluidics by introducing a versatile and precise platform that can be tailored for various experimental applications. The insights gained into particle distribution within the flow and the formation of stagnation points offer valuable information for optimising the device's performance in future applications. The ability to manipulate particles and fluids with high precision in real time opens up possibilities for significant advancements in areas such as single-cell analysis.

Future research should focus on optimising the fabrication techniques to further reduce production time while maintaining or improving edge quality. Exploring more complex laser parameters and alternative materials could enhance the device's performance. Additionally, integrating a real-time control system will be a crucial step in advancing particle manipulation on this microfluidic chip. Developing robust and reliable interfaces between the microfluidic chip and external systems will also be essential for long-term usability and integration into various applications.

Contents

Design & Fabrication of a Programmable Microfluidics Device

Based on Hydrodynamic trapping

by

Bart Bloemendaal

Supervisor:	Daniel S.W. Tam
PME Supervisor:	Murali K. Ghatkesar
Project Duration:	June, 2023 - September, 2023
Faculty:	Faculty of Mechanical Engineering, Delft

Cover:	A literature review on the principles of hydrodynamically driven microfluidics
Style:	TU Delft Report Style

TU Delft

Contents

1

Abstract

Microfluidics has emerged as a dynamic field with applications spanning various industries. By exploring the intricacies of fluid behaviour at the microscale, ranging from 1 milliliter down to 1 nanoliter, microfluidics has led to groundbreaking advancements in fields such as medical diagnostics, pharmaceuticals, biotechnology, environmental monitoring, energy, nanotechnology, and the oil and gas sector. Yet, what we see is that these device designs are directly linked to a single purpose and do not offer multi-functionality. To break this paradigm, this thesis aims to create a microfluidic device that utilizes hydrodynamic principles to manipulate droplets and particles in real-time with the use of reconfigurable virtual channels. This creation aims to be a non-intrusive multi-functional tool that could be used to trap, transport, sort, separate, and mix particles within the size range of 10 to 500 microns.

2

Introduction

Microfluidics is a rapidly evolving field at the intersection of physics, engineering, and biology. This emerging discipline explores the behavior of fluids at the microscale (from 1 milliliter down to 1 nanoliter) [1]. Leading to groundbreaking advancements in various industries, for example, in medical diagnostics, by the ability to isolate cells and viruses such as HIV, malaria, and Covid-19. In the pharmaceutical industry, microfluidic devices lead to increased efficiency of drug discovery and drug delivery. In biotechnology, they enable single-cell analysis and the ability to create "organs-on-chips", whereby the effects of drugs and toxins can be tested on human tissue. Microfluidics also act as a great tool in environmental monitoring to detect pollutants and contaminants in water and measure air quality. And, in the energy and nanotechnology sector, they can be used as microreactors for nanoparticle synthesis or function as a microscale fuel cell. Finally in the oil and gas industry, they give insight into droplet coalescence of crude oil/water mixtures, which could result in more knowledge on separating the mixture.

These developments are mainly made possible by advancements in microfabrication technologies, whereby 3D printing and laser cutting have seen extensive innovation. As a researcher, being able to rapidly prototype and fabricate your microfluidic cell allows for quick iteration and a well-functioning product.

Generally, these devices are fabricated with a specific operation in mind, thereby only having a single purpose. This could either be to transport, trap, sort, separate, or mix particles/droplets in suspension. These manipulations can be achieved using different methods. In this thesis, we distinguish between non-hydrodynamic manipulation and hydrodynamic manipulation methods. The non-hydrodynamic methods are categorized into four principles: the first one being acoustophoresis, where the principle relies on particles being translated to a node of a standing acoustic wave, which is introduced between the channel walls. The second method is electrokinetics, which allows for manipulation mechanisms in the form of electrophoresis, electroosmosis, and dielectrophoresis. Each of these methods uses an electric field to exert a force on either the particle or the solution. The third method is manipulation by optical rays, such as focused laser beams, are used to manipulate, often by trapping microscopic particles at the focal point. The final method is to apply a magnetic field to a magnetically susceptible particle to transport or trap it at a desired location.

The hydrodynamic category distinguishes manipulation by passive flow control and active flow control. Passive flow control relies on the geometry and topology of the flow field of the device, while active control techniques operate based on introducing a predefined flow, which in turn is then utilized to influence the flow dynamics by creating areas of stagnation and streamline patterns.

This technique was initially pioneered by G.I. Taylor in 1934 when he hydrodynamically trapped a droplet using an analog four-roll mill. These rollers generated an extensional flow along the vertical axis, causing the droplet to translate over this axis. In the 1980s, G. Leal digitalized

this process by automating the control of four mills. More recently, a research group supervised by C.M. Schroeder developed a Stokes cell based on a similar cross-slot configuration principle. This design accommodated two inlets and two outlets, enabling the manipulation of droplets and particles across a broader area within the cell. Consequently, it allowed for the tracking of path lines resembling the alphabet within the flow. Over the years, they refined their design and accumulated knowledge, ultimately enabling the research of lipid cell behaviour and ring polymer properties.

Other hydrodynamic studies introduce the notion of creating virtual channels in a two-dimensional uniform flow field. These virtual channels are created by inserting or removing flow through perpendicularly placed apertures. Particles or droplets can be transported or trapped within these virtual channels, allowing for the study of their dynamic behavior and properties.

This thesis will focus on applying the principle of reprogrammable virtual channels in a microfluidic cell to manipulate particles, cells, cell clusters, and fluids. This method of manipulation is non-intrusive and operates independently of many particle properties that constrain other manipulation techniques. It will distinguish itself by introducing a significantly more novel design, whereby real-time control happens at a significantly faster pace compared to existing devices. This will allow for more accurate control and better capabilities to utilize it for studies, removing the need to develop dedicated microfluidic devices for single studies.

In future research, this device will find applications in interfacial studies of droplets to uncover breakup and coalescence behavior. The capabilities to control the kinematics and dynamics of the flow on the small scale makes it a good platform for rheology experiments. Additionally, it will allow for long-time visualization of motile particles, such as algae and bacteria. These particles move around within the medium and require active correction to stay within the camera's field of view.

3

Particle Manipulation Methods

As discussed in the introduction there are various methods of particle manipulation, in this section the most prominent methods are taken under the loupe. Consequent to an assessment of the performances, a rationale is established for discontinuing the discussed particle manipulation methodologies.

3.1. Acoustic Method

The fundamental principles of acoustophoresis are rooted in the interactions between acoustic waves and particles within the microfluidic environment. The acoustic trapping devices consists, on one side, of a transducer that produces the acoustic wave, and a matching layer, also referred to as a coupling layer, which is required to achieve proper acoustic transmission into the system [3]. Depending on the type of manipulator at the other side of the microfluidic channel, a reflective layer is present (Figure 3.1) that reflects the transmitted wave, leading to a standing wave. Two different orientations of these standing waves can be utilized for particle manipulation. The first one is the orientation depicted in Figure 3.1, referred to as a layered resonator. The second orientation is the transversal resonator, which has its standing wave perpendicular to the incident direction of actuation. Acoustic manipulation often finds itself with a stream of particles that require redirecting or separation. Depending on the magnitude of the primary acoustic radiation force, particles will be redirected to nodes on the standing wave.

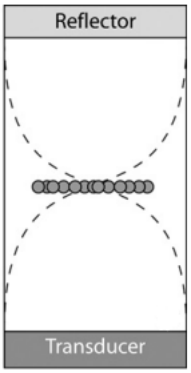

Figure 3.1: Schematic depiction of an acoustic manipulator, whereby particles are accumulated at the node of a standing wave [2].

Limitations of acoustic tweezers are that the fabrication and design of these systems are tedious, rendering these systems costly. The effects of particle size and flow rates are quite specific in these kinds of manipulators. In practical terms, a particular design would demonstrate optimal performance solely within restricted ranges of particle sizes and flow rates [4]. This method is also dependent on the properties of the particles and the surrounding fluid. Particles with significantly different acoustic properties may not respond well to the acoustic forces, limiting applicable materials.

3.2. Electrical Method

Electrical Particle Manipulation relies on the interaction between an electric field, that can interact with either particles or the solution. When voltage is applied to the microfluidic device, electric fields are generated, enabling precise particle manipulation. Generally, there are three different methods for electrokinetic particle manipulation: electrophoresis, electro-osmosis, and

dielectrophoresis.

Electrophoresis (EP) involves applying an electric field across the channel, driving charged particles in stationary liquid towards a specific direction, resulting in efficient particle transport and precise positioning [4]. Electro-osmosis occurs when an electric field is applied to the microchannel's surface. Charged ions at the liquid–solid interface create a net flow, known as plug flow, which can be used for pumping, mixing, or splitting fluids within the device [5]. Dielectrophoresis (DEP) imposes a non-uniform (often Alternating Current) electric field that manipulates the surrounding medium and particles with different dielectric properties [6]. This causes the particles to experience varying forces, creating specific regions of particle concentrations or separations within the microchannel.

Limitations of this technology include its high dependence on particle or cell polarizability and its general requirement for low-conductivity media. These factors limit its use in cell-related applications.

3.3. Optical Tweezers

The principle of optical tweezers is to utilize the momentum transfer of focused laser beams, to trap and manipulate microscopic particles with very high precision [7]. When a laser beam passes through a particle with a high refractive index, such as a polystyrene bead or a cell, the beam's photons experience a change in momentum due to scattering and reflection (see Figure 3.2). This results in radiant pressure that directs the particle into the center of the beam, thereby trapping the particle within the laser's focal point.

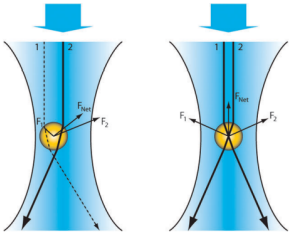

Figure 3.2: Principle of optical tweezers whereby a particle experiences the net force to the center of the beam due to the difference of transferred momentum [7]

A passive method for optical sorting uses an array of laser beams arranged in a three-dimensional lattice structure [8]. This structure is traversed by two different adjacent flows with low Reynolds numbers (laminar flows). One of these flows contains two different groups of particles, which flow through the lattice structure. Then selectively a species of particles is pushed into the upper flow field.

Limitations of optical tweezers include the limited manipulation range, as the particle can only be trapped in the focal point of the laser. Expanding the focal point would decrease trap stiffness and result in insufficient force to trap particles. Complex optics and a high-power laser are required, increasing costs. The high laser intensity can cause damage to organic tissue [4], and the effectiveness of optical tweezers is highly dependent on particle size and refractive index.

3.4. Magnetic Method

For the magnetic method, a permanent magnet or electromagnet produces a non-uniform magnetic field in the flow cell, attracting magnetic or magnetically labeled particles or cells toward the higher magnetic field [9]. With this principle of applying a magnetic field gradient, particles can be transported and sorted within the flow domain. Magnetic manipulation can also induce mixing and stirring within the flow cell. This is accomplished by introducing rotating or oscillating magnetic fields, generating fluid flows to mix reagents, samples, and other fluids.

Limitations of magnetic particle manipulation include relatively low spatial resolution due to the rapid weakening of a magnetic field, especially through glass or plastics. Precise particle control is difficult to achieve due to the influence of particle size, shape, and magnetic properties. Creating a uniform magnetic field tends to be challenging, affecting the accuracy of the manipulation. Finally, the types of particles that can be manipulated are limited; particles are required to have paramagnetic or supermagnetic properties. If these properties are not present, the particle has to be coated or labeled.

3.5. Performance Assessment

In the introduction a general description is given on the goal of this project. Fitting this goal, certain properties are required for the manipulation method, the discussed methods all suffer from limitations that cause their discontinuation for this project.

For the acoustic method, although it offers gentle non-contact manipulation without the need for any external maskers or labels, it does not fit the project. Because in reality such devices are optimized for specific particle sizes, for they are dependent on the wavelengths of the wave harmonics.

The electrical methods of manipulation offer efficient transport and positioning yet they are highly dependent on the particle or cell polarizability and are limited to low-conductive media. This limits the use of a range of particles and media, that would potentially be of interest.

The optical method allows for high accuracy of non-contact manipulation even for microscopic particles, hereby also limiting the domain of manipulation to trapping at the focal point. The use of a laser brings several other limitation such as the potential harm to biological samples and its sensitivity to the refraction index of the intended particles.

Magnetic methods are versatile for transport and mixing because of the present understanding and capability of producing precise non-uniform magnetic fields. Yet there are limitations in spatial resolution, precise control, and the types of particles that can be manipulated.

The decision to refute the applications of these methods, in this project, is mainly based on the dependencies on particle properties. The project aims to allow for the non-intrusive manipulation of particles whereby particle properties are not altered, which results in the discontinuation of electrical, magnetic and optical manipulation. Also the scope is to be versatile and multi-functional which does not align with acoustic manipulation method.

4

Hydrodynamic Particle Manipulation

In the previous section, we covered nearly all particle manipulation methods except for hydrodynamic manipulation, which happens to be the most prominent method for our interest. The reasons for favouring this method of manipulation is, that it does not require any particle specific properties, it is not bound by the need for complex control mechanisms as in electrical, magnetic and acoustic manipulation. It also allows for the molecule, droplet or particle to be manipulated in a less invasive manner [10].

This chapter will delve further into the topic of hydrodynamic particle manipulation, on its principles, the applicable theory and existing research utilizing this concept.

4.1. Fundamental Principles

To be able to apply complex potential theory, certain constraints to geometry are required, in lubrication theory this is referred to as the Hele-Shaw condition. This condition is satisfied if the flow is inviscid, incompressible and in steady state. The geometry consists of two parallel flat plates with a narrow gap, specifically this is referred to with dimension h (see figure 4.1), which compared to both the length (l) and width (w) is significantly smaller. Solving the momentum equations for the boundary conditions of the system leads to a rather unusual and unexpected result. Because it requires viscous flow between closely spaced parallel plates to produce the same potential-line and streamline patterns as a two-dimensional ideal flow [12]. This allows for accurate flow prediction in the two dimensional x-,y plane.

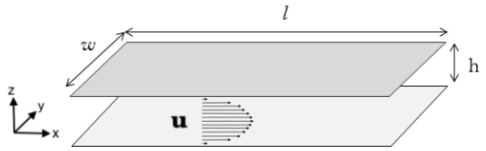

Figure 4.1: Shematic view of a Hele-Shaw cell With length l, Width w and height h, seen with a pressure driven fully developed uniform flow in the x direction [11].

Within this flow cell a pressure gradient propels the flow with a parabolic profile (Poiseuille flow) seen in figure 4.2, in this flow a particle can be transported. Though due to instabilities the particle won't travel on the centerline of the parabolic profile but will find an equilibrium point between a shear gradient lift force and a repulsive force from the wall, which originates from the asymmetry of the corresponding wake vorticity distribution of the particle [13].

Yet this uniform flow only allows for transportation of a particle, for trapping additional flow(s) are to be added, these flows introduce a zero velocity region within fluid interfaces, also known as stagnation points. The particle would then be trapped on this fluid interface which by itself could be further manipulated by active control of the inflowing fluid. This can be achieved by, for

example a crossed flow system (figure 4.4), referred to as a stokes cell. Whereby two opposing inlets introduce the fluid and the two slots perpendicular to these function as outlet. In the middle of the crossed cell a stagnation point occurs that can be manipulated by controlling the flow in one of the four channels. Another configuration that allows for zero velocity regions in a uniform flow is to introduce inlets or/and outlets perpendicular to the uniform flow also referred to as sources and sinks. These stagnation points can in turn also be manipulated via the strength of these sources and sinks, keep in mind that for this to work the mass balance is to be maintained, what flows in has to flow out for the fluid is incompressible.

There are other methods of hydrodynamic particle manipulation, these methods rely on the presence of micro-structures or micro-patterns in the channel, for example by the use of posts, ridges and grooves. Particles can be guided by these micro-structure such as in the case of Deterministic Lateral Displacement (DLD) [14], whereby particles of different sizes deterministically choose paths between obstacles of differing sizes. Another manipulation method by channel geometry is the introduction of a spiraling channel. Wherein particles are separated and concentrated depending on their size due to the centrifugal forces acting on the fluid, these forces cause secondary flows which are perpendicular to the primary flow direction and which are also referred to as vortices [15]. In fluid dynamics this is also known as a Dean flow.

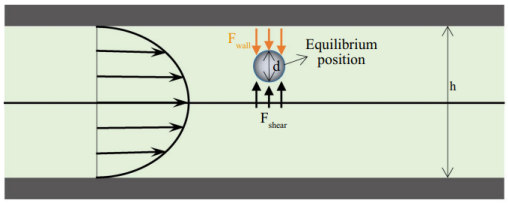

Figure 4.2: Shematic view of a fully developed Poiseuille flow with a suspended particle and the force equilibrium it experiences [4].

4.2. Key Concepts in Theory

The two dimensional ideal flow can be predicted by applying complex potential theory, complex potential theory is a mathematical framework used to analyze the behavior of inviscid and incompressible fluids, such as air or water [12]. The theory is a powerful tool for simulating flow around a two dimensional cross-section such as aerofoils, ship hulls buildings and more general flows around objects. To be able to analyse it in two dimensions, the depth-averaged velocity field is used for the velocity field.

Complex potentials combine the streamfunction and the velocity potential into a combined complex potential function $\Phi(z)$, whereby z represents a vector of the planar spatial coordinate. The planar flow domain in complex potentials has a real and a complex direction comparable to the x-y directions in a Cartesian coordinate system. The complex potential function can be regarded as an analytic function which satisfies the Cauchy-Riemann equations, making sure that the flow field is smooth and well-behaved.

The complex potential function allows for the representation of various types of flow such as a uniform flow, the representation of a flow source or sink, a vortex and a combination of these. Superposing these flow elements, complex flow patterns can be constructed to represent the flow around objects. To allow for the application of complex potential theory certain boundary conditions have to be imposed, at a solid liquid interface a no-slip boundary condition is imposed and at infinity free stream conditions are applied. These conditions form the base of the complex potential function and subsequently the velocity field and pressure distribution.

Limitations of using potential flow theory is that it is based on several simplifying assumptions, for it assumes an absence of viscosity and compressibility in the fluid. It would not perfectly correspond with real world flow behaviour, yet it is still a powerful tool to produce an analysis of many representations of fluid flow.

4.3. Particle Parameters and Behaviour

Particle behaviour is a important parameter to be able to predict the particle's trajectory. The following properties have to be considered in microfluidic studies.

Size dependency - For significantly small scale microfluidics, Brownian motion has to be taken into consideration. Brownian motion is the random movement of particles due to collision with neighbouring particles, the smaller the particle the more intensely it experiences the collision with the surrounding molecules. The mean displacement a Brownian particle experiences is proportional to the square root of time [16], meaning for larger particles Brownian effects of displacement can be neglected.

The particle size also dominates the inertial effects inside the flow, traditionally this is neglected within microfluidics since Reynolds numbers are much smaller than one. Though it plays a significant role in lateral behaviour. The lift created by the particle due to the parabolic Poisseuille flow introduces a lateral migration, this lift force scales from "particle diameter to the sixth divided by the channel height to the power four" to "particle diameter to the third divided by the channel height" [13], depending on whether the particle is present close to the wall or rather at the center-line. Concluding the particle's diameter plays a significant role into the height of the equilibrium position within the cell.

Shape dependency - Particle shape determines the wake vorticity produced by the particle traveling through the stream, due to the particle's position being closer to the wall on one side, the wake becomes asymmetric. This asymmetry results in the repulsion force of the wall exerted onto the particle [13]. Anisotropy in particles also results in alternative behaviour within the flow. A particle of arbitrary shape when transported in a fluid experience forces and momenta on all three coordinate axes [17], the difference in geometry could result into rotation or tumbling.

Material density - The density of a particle relative to the density of the suspending fluid plays a crucial role in determining whether a particle will sediment or float in the microfluidic channel. In literature most experiments are done with polystyrene beads that are naturally buoyant, thus trying to minimize any additional forces that would guide the particle away from the centerline. Particle density adds in the balance of the equilibrium position between shear force and the wall repulsion force, thereby migrating the particle over the parabolic flow structure to another position. Density also strongly influences the particle's inertia within the flow thereby influencing its ability to marginate [18].

4.4. State of the Art of Hydrodynamic Manipulation Techniques

Pioneering Work - The pioneer of hydrodynamic trapping is G.I Taylor, he designed a four-roll mill (see figure 4.3a) that could be used to trap a droplet at the center [19], with this apparatus he investigated the deformation of a drop of fluid submerged into another fluid with the same density. Finding that the droplet was unstable along the extensional flow axis in the horizontal direction, resulting in translation along this axis. The system would control the position of the droplet by manually controlling the rotation of either the left or right set of rollers. In 1986 Bentley and Leal [20] (figure 4.3b) improved the system by having the rollers digitally controlled using a computer. This method was significantly more successful in keeping the droplet at the stagnation point at the center of the rollers.

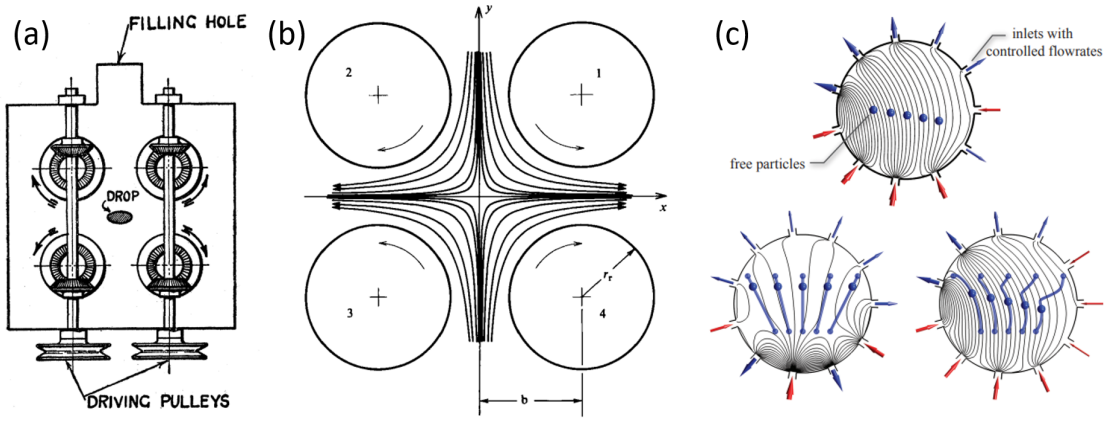

Figure 4.3: **a** Schematic view of G.I. Taylor's four-roll mill apparatus [19]. **b** Schematic view of the four-roll mill including its streamlines by Bently & Leal [20]. **c** Schematic of the theoretical circular cell with visualization on the configurations of the inlets and outlets, and their influence on the streamlines and particles [21].

Theoretical Manipulation - More advanced digital control gave rise to the possibilities of complex manipulation such as particle assembly. A theoretical study has been made to analyze the possibility to assemble arbitrary structures, from identical constituents in a sequential manner [21]. M.P. Brenner and colleagues theorized a modified circular Hele-Shaw cell with seven controlled flow rates seen in figure 4.3. Whereby individual particles are introduced into the cell and assembled into an aggregate. The goal of the assembly is to represent any arbitrary shape such as, a letter from the English alphabet. The reason for the seven inlets, is to control the position of the aggregate and the newly introduced particle. Four inlets for the positions of both the aggregate and the particle, two more inlets are required for the stagnation point flow superimposed on the local mean flow, and finally the last inlet is required for volumetric conservation.

Practical Hydrodynamic Trap - Based on the theoretical study of particle manipulation in a Hele-Shaw cell, new studies have been done with more practical applications. Setting up an automated micro scale particle trap, based on a stagnation-point-flow generated in a microfluidic device. The device consists of four channels, with two inlets and two outlets arranged in a cross-like configuration, as shown in figure 4.4. The design is chosen to be on a small scale to allow for analysis on micron and sub-micron scale particles, the dimensions are given in table 4.1. In the cell polystyrene particles get trapped in the stagnation point that occurs in the center [22]. The hydrodynamic trap was designed and fabricated by a group of researchers led by C.M. Schroeder, this group expanded on the topic with a series of follow-up studies. Starting with a more comprehensive overview on the system's design [23], and giving insight on hydrodynamic trap responses as a function of design parameters. Earlier versions of the device are characterized by the configurations of the outlets: the top outlet narrows down thereby constricting flow, the bottom outlet also narrows but less strongly, leaving a wider gap for the flow. But in contrast to the top outlet the bottom outlet is equipped with a membrane valve to control the flow.

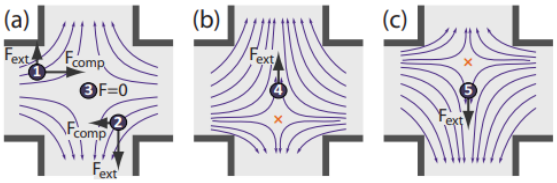

Figure 4.4: **a** All forces perceived by the particle in the flow domain. **b** & **c** are the result of translating the stagnation point over the extensional axis[22].

Successive to this, a new device was introduced, whereby also the left and right channels were equipped with narrower parts far down the channels. And the right part also got equipped with a membrane valve. This allowed for translation over a two dimensional region within the cell, compared to the one-dimensional translation over the extensional axis. This would allow the control of particles among certain contours within the domain, demonstrated in the study by producing the contour of the letter I [24]. In the same study the capability to single out a particle

from a crowded particle solution is demonstrated.

After improving the performance of the cell by better understanding the dependency on geometry and flow parameters, a new study was done to analyze the flow dynamics. By investigating the performance of a hydrodynamic trap, actuated by varying combinations of proportional-integral-derivative controllers [25]. Also describing the performance of traps across a broad spectrum of Peclet numbers and response times.

Obtaining this better understanding on particle and trap dynamics, led to the creation of more complex cell configurations, resulting in the introduction of a six slotted stokes cell. This configuration allowed for the fundamental studies on particle–particle interactions and introduced a method for directed assembly of colloidal polystyrene particles [26]. This was done with the introduction of model predictive control, which greatly simplified the microfluidic device by eliminating the need for integrated electrodes, there to measure flow velocity, and eliminating the on-chip membrane valves. The predictive modeling also allows for the control of several particles independently. Following this study a new study was carried out, whereby the goal was to systematically analyze flow topologies during multiplexed particle manipulation [27]. This study analyzed a six channeled stokes cell that is capable of three distinct flow topologies, by having either zero, one or two stagnation points. It examines on how tuning the controller parameters, can result in the desired trapping of multiple particles, which can be used to experiment with deformable soft materials with good accuracy.

With the experience gathered from manipulating spherical particles in differently configured stoke cells, the group expanded on the topics of, manipulation and control over anisotropic polystyrene particles [28]. Followed by the manipulation of Lipid vesicles, which are fluid filled softcontainers enclosed by a lipid bilayer membrane [29]. Hereby experimentally determining the flow-phase diagrams for these vesicles in extensional flow. Another application of their developed Stoke cell is the analysis of the dynamics of ring polymers and their nonequilibrium behavior [30]. Understanding these dynamics is essential for various applications in materials science and biophysics.

Reconfigurable microfluidics - On a larger "millimeter to centimeter" scale (see table 4.1), a study on reconfigurable microfluidics was done by a different research group, this study focused on manipulating droplets by the use of liquid-walled virtual channels, in a two dimensional flow domain [31]. The device shaped virtual channels by the means of hydrodynamic forcing, these virtual channels could transport, split, merge and mix minute volumes of liquid. The device is a rectangular flow cell with inlets (injections) and outlets (aspirations) perpendicular to the flow direction. These behave as if they were sources and sinks within the flow. The idea was to deliver a generic multipurpose microfluidic device, that would break the paradigm that states that the function of the design is directly linked to its functionality [31]. In the study David P. Taylor and Govind V. Kaigala prove their capability to produce the virtual channels and showcasing their capacity to manipulate flow, which can be seen in figure 4.5. The figure displays all the achieved stages of the earlier mentioned manipulation methods. The study highlights the potential of virtual channels in microfluidics by its capability to analyze liquids with different viscosities, to study non-Newtonian liquids by analyzing its rheology, or to manipulate flow in

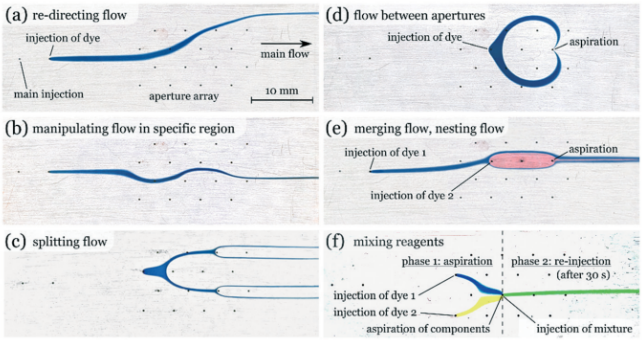

Figure 4.5: a The directing of a virtual channel to a certain position at the open boundary. **b** Manipulating flow with multiple injections and aspirations redirecting the virtual channel through specific regions of the cell. **c** Production of multiple stagnation point that split the flow. **d** Circular flow created between two apertures. **e** Nesting of a specific fluid within the flow of a different fluid. **f** Two-step mixing of liquids first aspire the two different die's into an capillary through an aperture where they will mix by diffusion and then reinject the mixture from the same aperture of aspiration [31].

microfluidc cells with changing gap heights. It is worth noting that this device lacked any feedback control integration, instead, all trajectories and shapes were pre-programmed.

Programmable hydrodynamic forcing in a closed loop - To conclude the most recent study of hydrodynamic particle manipulation was a doctoral thesis on designing a reconfigurable microfluidic device by making use of hydrodynamically produced virtual channels. These channels allowed for flexibility in its function resulting in a multi-purpose device that is able to perform multiple operations in a single run [1]. The design benefits from a priori particle path prediction, which refers to the ability to predict the path that the particle or cell will follow within the virtual channels, having these predictions allows for trapping, separation or sorting operations. The a priori estimation technique for particle trajectory is used to optimize these trajectories over the stable streamlines. In addition to that real time feedback control is implemented using Proportional Integral Derivative (PID) control, which is used to correct for deviations in the particle's path, compared to the predestined particle trajectory. The PID manipulated the flow rates that were introduced into the cell by inlets and outlets, configured perpendicular to the main flow direction. Kislaya's study utilized the same driving principles as the previously mentioned study, but introduced more novelty and practicality.

Achieved performances and parameters

All the quantitative parameters of interest from the mentioned practical studies have been gathered and depicted in table 4.1. Thereby documenting and organizing the devices performances and relate each device's strong features and weaknesses. Providing a quick and concise overview of the critical parameters to achieve various performances.

For the parameters: the height refers to the dimension that is much smaller than the other two dimensions, adhering to the set Hele-shaw condition, length is the dimension that is aligned to the main flow direction, and the width is the in plane dimension that is perpendicular to the length. The path length refers to the length of the trajectory the particle travelled within the cell, and the time refers to the amount of seconds the particle took to traverse this path. From these values an average velocity is computed which is displayed in the column next to it.

The viscosity is given for a better comparison in performance, a larger viscosity would lead to more internal drag on the particle. The particle size is shown and the accuracy of performed trapping in respect to the desired location. The performance statistics of the trap stiffness of the devices are given, and the pressure within the cell at the main inlet.

Remarkable is the difference in scale between the set of stoke cell studies and the reconfigurable virtual channel studies. These large differences makes comparing them complex.

Another important aspect to consider is that all studies are conducted in fluids with viscosities similar to that of water, typically referred to as aqueous emulsions.

Article	Height (µm)	Length (µm)	Width (µm)	Path length (µm)	Time (s)	Avg. Velo-city (µm/s)	Viscosity (Pa*s)	Particle size (µm)	Accuracy (µm)	Trap stiffness (pN/nm)	Inlet pressure (kPA)
Hydrodynamic trap for single particles and cells, C.M. Shroeder 2010 [22]	NA	NA	NA	NA	575	NA	0.001	0.1	1	~10e-5 - 10e-4	NA
A microfluidic-based hydrodynamic trap: design and implementation, C.M. Shroeder 2011 [23]	30	300	300	NA	Minutes	NA	0.001	*0.1-15	NA	NA	NA
Manipulation and Confinement of Single Particles using Fluid Flow C.M. Shroeder 2013 [24]	30	300	300	230	320	0,72	0.001	0.5 & 2.2	$\sigma_x = 0.19$ $\sigma_y = 0.22$	NA	NA
Characterizing the performance of the hydrodynamic trap using a control-based approach, C.M. Chroeder 2014 [25]	NA	400	400	NA	NA	NA	0.00126	0.1 & 2.2	NA	NA	NA
Stokes trap for multiplexed particle manipulation and assembly using fluidics, C.M. Shroeder 2016 [26]	100	400	400	820	328	2,5	0.00126	2.2	NA	1.1e-3 & 1.3e-3	NA
Flow topology during multiplexed particle manipulation using a Stokes Trap, C.M. Shroeder 2019 [27]	100	400	400	NA	95	NA	0.00140	2.2	NA	Na	0 - 34.5
Orientation control and nonlinear trajectory tracking of colloidal particles using microfluidics, C.M. Shroeder 2019 [28]	100	400	400	262	12	22	0.00113	1.3 & 2.2	$\sigma_x = 0.55$ $\sigma_y = 0.20$	$\kappa_x = 8.3e-4$ $\kappa_y = 2,7e-3$ $\kappa_\phi = 9.1e3/rad$	17,2
Reconfigurable microfluidics: real-time shaping of virtual channels through hydrodynamic forces, David P. Taylor 2020 [31]	NA	40000	10000	65500	87	750	0.001	NA	5% relative to virtual channel width	NA	NA
Particle Manipulation-on -chip using programmable hydrodynamic forcing in a closed loop, A. Kislaya 2020 [1]	500	300000	100000	15000	45 - 160	80 - 333	0.001	180-200	NA	NA	2.5

Table 4.1: Table containing all quantified parameters of interested from the discussed papers.

5

Project goal

The goal of this thesis is to design a microfluidic device capable of locally manipulating the flow topology and the flow field at a small scale, all without introducing any physical barriers but through hydrodynamic forcing. This will allow us to generate various flow patterns, including extensional flows, controlled shear flows, and unsteady shear flows. Such manipulation will enable the creation of virtual structures within the flow. These virtual structures offer dynamic and flexible control over emulated particles, facilitating biophysical studies of motile particles ranging in size from 10 microns to 500 microns, with velocities ranging from 100 microns per second to 1 millimeter per second. Additionally, the device will be useful for interfacial studies of droplet breakup or droplet coalescence and will facilitate control of the kinematics and dynamics of small-scale flows, making it an ideal platform for rheology experiments.

The flow manipulator will consist of a Hele-Shaw flow cell, with the top plate modified to accommodate multiple tube connections for use as additional inlets and outlets. These inlets and outlets can be represented as sources and sinks in a uniform flow, which can, in turn, be utilized to manipulate streamline patterns and generate the virtual flow structures.

This project is based on a previous project by A. Kislaya, which demonstrated the feasibility of virtual channels and produced a 3D printed prototype for particle manipulation. However, the device's setup, in terms of geometry and inlet configurations, only offered design-specific flow control over a significant time scale (45 to 160 seconds, see table 4.1). Figure 5.1 represents the device, which has an inlet and outlet for the uniform flow on either side in the x-direction. In the middle of the device, the connections of the inlets can be seen. This configuration has a limited number of inlets, thereby limiting its functionality in producing virtual structures over the cell's area.

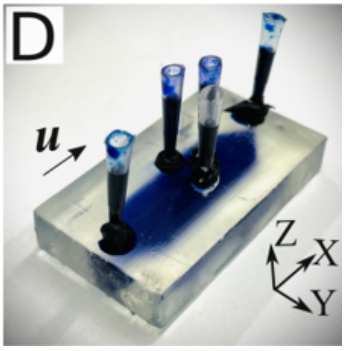

Figure 5.1: Microfluidic device produced by A. Kislaya's Phd-thesis [1]

This project will explore new fabrication methods to manufacture a device robust for various particle manipulations. The focus will be on creating a multifunctional device, where end-users might program the locations of virtual structures instead of needing to fabricate a new microfluidic device with the desired manipulation locations. The design will include real-time control over particle positions via imaging of the channels and a PID controller to determine the flow inputs in the sources and the sinks.

5.1. Project Distinctions and Ambitions

This project will distinguish itself by improving the specifications and performance of existing projects, primarily in comparison to the two projects that utilized virtual channels([1] & [31]).

In Table 4.1, average velocities over specific paths are displayed alongside their corresponding timescales. We can observe that for A. Kislaya, the maximum average velocity is 333 micrometers per second. When comparing this velocity to the dimensions of the channel, it becomes evident that it takes a considerable amount of time to migrate over significant portions of the chip. This project aims to address this issue by introducing a more sophisticated PID controller that allows for a higher frequency control, consequently resulting in better performance at high velocities.

By examining the figures in D. Taylor's article, it is possible to calculate the average velocity of a droplet, transported over a specific predetermined path which is visible in table 4.1. This velocity is notably greater than Kislaya's average velocity. However, a direct comparison of these velocities does not yield a relevant performance analysis, as the channels vary in size by an order of magnitude. To provide a more meaningful comparison, these velocities are normalized to the channel's length and inverted to depict a normalized timescale that indicates the time it takes for the particle to be transported over the channel's length. These values can be found in Table 5.1.

	C.M. Schroeder 2013	**C.M. Schroeder 2016**	**C.M. Schroeder 2019**	**David P. Taylor 2020**	**A. Kislaya 2022**
Normalized time scale (s)	41.7362	160.0000	18.3217	53.1350	900.9009

Table 5.1: Normalized velocities with respect to the channel length

Velocity-wise, a significant performance difference between Taylor and Kislaya is observed. Taylor's device takes significantly less time to transport particles over its domain, yet in Taylor's article there is no indication of active control, the trajectories of the droplet is pre-programmed. Introducing feedback control to yield more accurate positioning often comes with a sacrifice in velocity, especially if the feedback control is not robust.

So even though Kislaya's device operates at a slower velocity it allows for real time adjustments and more accurate position control. Yet this control has an acquisition frequency of 2 Hertz, to capture the average in-plane displacement. Only monitoring changes in the flow field twice per second is not considered fast feedback control. This project aims to significantly improve on that, trying to obtain an acquisition frequency of at least 30 Hertz.

For the works of Schroeder's group, the scope of the projects deviate too much to meaningfully compare performances. Their projects aim for micro scale manipulation in the sub-micron range (see column 9 of Table 4.1). This thesis does not share the goal of manipulating on such small scales, another difference is that the thesis will focus on delivering a device that allows for a more diverse set of functions, and to be able to manipulate multiple particles independently. Yet their obtained trap-stifnesses indicate achieved values, which could be used for comparisons to the final result.

6

Microfluidic Cell Design requirements

For the fabrication of a properly functioning microfluidic Cell certain requirements have to be met. Understanding all elements that have to be included in such a device is crucial in delivering a robust and modular device. For this an extensive list of requirements is set up and discussed in this section.

Channel Geometry - Precise dimensions are essential for proper control within a microfluidic system. The microchannel's length, height, and width must be exactly designed to accommodate the intended flows and adhere to the Hele-Shaw conditions. Accurate channel geometry allows for consistent and reproducible results. For the first iteration, the Hele-Shaw cell will have a length of about 300 millimeters, a width of 100 millimeters and a height of 0.5 millimeter. Though in the subsequent iterations these dimensions will vary, to accommodate droplets and particles with significantly different sizes.

Material Selection - The choice of materials is critical in microfluidic system design. Biocompatible materials are necessary when working with biological samples to prevent adverse reactions. Additionally, low autofluorescence materials are essential for optical analysis, ensuring that the system does not interfere with sensitive detection methods [32].

Flow Control - Accurate flow control mechanisms are pivotal for the success of microfluidic systems. Real-time monitoring and control of fluid flow rates enable precise manipulation of samples and reagents. This control is crucial for achieving consistent and reproducible results in various applications.

Sample Handling - Sample injection and retrieval ports must be integrated into the system to facilitate the introduction and collection of samples.

Environmental Requirements - Microfluidic systems often operate under challenging environmental conditions. Considerations such as shear forces and temperature control are vital to ensure the system's stability and reliability.

Optical Compatibility - For applications requiring microscopy or optical analysis, the materials used in the microfluidic system must be transparent and compatible with optical systems. Integration into optical setups should be seamless to enable precise observations and measurements [32].

Cleaning and Sterilization - Microfluidic systems must be designed for easy disassembly and cleaning. Resistance against biofouling is essential to prevent contamination and maintain system performance over time.

System Integration - The integration of sensors, electrical components, and pump connections into the microfluidic system is essential for automation and precise control. Compatibility with other instrumentation and components is vital for the system's functionality.

Safety Requirements - Built-in safety measures and shutdown protocols should be incorporated to prevent accidents and protect both the system and users. Safety is of paramount importance, especially in applications involving hazardous substances.

Data Handling - Microfluidic systems often generate large amounts of data. Compatibility with data analysis software and the implementation of machine learning algorithms can enhance the system's capabilities, allowing for real-time data processing and decision-making.

6.1. Inlet and Outlet Configurations

The inlets and outlets are required to have a right angle in comparison to the channel ceiling, also not containing chips or shaving residues from machining or laser drilling. This to be able to deliver a uniform source of flow, that spreads out equally in all directions.

Another important factor of uniform flow delivery is the orthogonality of the inlet to the channel ceiling. Machining or punching a slightly unaligned hole could cause the in-going flow to not spread uniformly, thereby not depicting the 2-dimensionality of the representative model. To prevent this nanoports are to be glued onto the locations of the apertures. These nanoports are pieces of hardware often seen in microfluidics and allow for "clean" flow insertion, by properly fixing tubing to the device. Applying standard issue hardware improves repeatability for follow-up or repeating projects.

In the sense of fluidic connectivity, diameters of these nanoports are crucial to determine the volumetric flow rate and thereby the magnitudes of manipulation. Sizing should also be carefully chosen to minimize leakage around the connecting locations and to ensure mass conservation during fluid transfer.

6.2. Material Considerations

In many microfluidic applications, such as cell culture, organ-on-a-chip systems, or single-cell analysis, living biological entities like cells or tissues are involved. These cells are highly sensitive to their micro environment, including the materials they come into contact with. Non-biocompatible materials can lead to cell damage, altered cell behavior, or cell death.

Proper sterilization of the devices is essential for not contaminating the experiments. This means the material is to be able to tolerate at least one of the sterilization methods. These methods include; wet heat (autoclaving), dry heat (flaming, baking), solvents (ethanol), and radiation (ultraviolet light) less common options are X- rays, gamma rays or ethylene oxide [32].

Optical and fluorescent microscopes are typically used for analyzing flow, thereby transparency is key to function. Yet this is not only determined by the material properties, it also depends on what machining method is used to finish the material surfaces. Surface roughness such as created with micro milling interferes with observations under a microscope.

Lastly mechanical properties such as stiffness and cyclic loading fatigues are crucial considerations in designing chips. The channel ceiling requires minimal deformation to adhere to its intended geometry. Also, cyclic loading occurs by pressurizing during experiments and relieving the cell in alternating cycles, even though the pressure gradients are low, a high number of cycles could lead to fatigue.

6.3. Fabrication Techniques

In table 6.1 the more prominent methods of microfluidic chips are discussed. Alternative methods are discussed by Simon M. Scott and Zulfiqur Ali in their article on Microfluidic Devices fabrication [33]. Mentioning all these methods would exceed the scope on fabrication of this review. Proper knowledge by reviewing available fabrication methods lead to a functioning part, if the incorrect fabrication techniques are used, material properties could be altered and the surface finish compromised, thereby affecting transparency.

Method	Description	Advantages	Limitations
Wet etching	Chemical removal of layers of material by the use of masks in liquid phase.	- Cost-efficient - Short production time	- Not suitable for high-aspect ratios - Low precision
Dry etching	Physical removal of layers of material by the use of masks in gas or plasma phase.	- High Precision - High resolution	- Requires clean-room
Photolithography	Transferring patterns from a mask to a light-sensitive material by exposing it to ultraviolet light.	- High precision - Cost effective	- Requires clean-room - Limited materials - Long processing time
Soft lithography	Transferring a pattern from an elastomeric stamp, mold, or master onto a substrate.	- Short production time - low cost	- Requires clean-room - Long processing time - High costs - Low precision
Micro-injection molding	Injection of molten plastic into a master mold.	- Large-scale process - Low residual stress - Suitable for high aspect-ratio features	- Residual stresses - Not suitable for high-aspect ratios
Hot embossing	Reproducing micro-structures on an heated plastic substrate through replication.	-Large-scale process - Suitable for high aspect-ratio features	- Long processing time - Requires sealing steps
Micro milling	Removing material on a micrometer scale through mechanical ablation.	- Large-scale process - Suitable for high aspect-ratio features	- Long processing time - Limited resolution - Requires sealing steps
3D printing	Layer-by-layer deposition of material.	- Compatible to bio-materials - Short run time - Cost efficient - Versatile	- Limited materials - Limited resolution

Table 6.1: Table containing the most prominent manufacturing techniques described in the book; Organ-on-a-chip Engineered Micro environments for Safety and Efficacy Testing [34]

7

Conclusion

Hydrodynamic manipulation techniques have evolved significantly, from manual control to sophisticated closed-loop systems. From trapping particles over the extensional flow direction to more complex in plane transportation.

For the Stokes cell studies offer a great insight on characteristics of hydrodynamic manipulation of particles, but due to the configuration this is within a limited flow domain. The Stokes cell studies differ significantly in their goal with respect to this project. The interests of analysis in the Stokes cell is focused on the manipulation of sub-micron and micron range particles. Whereby this study is interested in larger particles.

The manipulators that utilize virtual structures for their manipulation, show versatility in operation and leave promising results. Yet the feedback control is missing or very slow, this leads to the inability to be utilized for research that requires more accurate control.

This thesis project aspires to improve on the previously developed devices, by introducing more advanced control, more functionality and a straight forward multi purpose user interface. Allowing for the device to be used in further research. The project aims to do so while answering the following research question;

- How can we design a user-friendly and reconfigurable microfluidic cell, and what is the influence of key feature parameters on its performance?

To answer this, a set of sub research questions have been formulated to be able to characterize the influential parameters that make for a well functioning microfluidic device.

- What is the relationship between channel geometry and the development of fluid flow within the microfluidic cell?
- How do the configuration and geometrical aspects of the inlets impact the flow field within the microfluidic cell?
- Which feedback control model would be effective in optimizing the microfluidic cell's performance?
- What impact do the characteristics of integrated systems (e.g. the pump) have on the overall performance of the microfluidic cell?
- What is the effect of tube stiffness on the behavior of incoming fluid within the system?

These questions form the structure of the thesis whereby each question symbolises a new phase in the project, building up to a functioning device.

For the manufacturing process, the most suitable approach involves 3D printing a master mold, which is subsequently used to create a PDMS pattern through photolithography. The

rationale for preferring this process is because it allows for rapid prototyping and has a convenient learning curve. These processes also minimally alter material properties, maintaining the required transparency to track flow patterns.

Alternatively, this project will also explore in fabricating a sandwich structure device, whereby the assembly consists of two parallel glass plates separated by a PDMS gasket. With the function to improve on transparency allowing for better tracking.

One of the glass plates will contain a laser drilled hole pattern where the tubes will be connected to, the other glass plate will remain plain. The gasket will be manufactured using a 3D-printed mold, with the PDMS pattern being created from it.

8

Research Plan

Figure 8.1 displays the current planning of this thesis, by spreading the major tasks over a span of 36 weeks. There has been a legend included that displays a predicted level of risk each task brings.

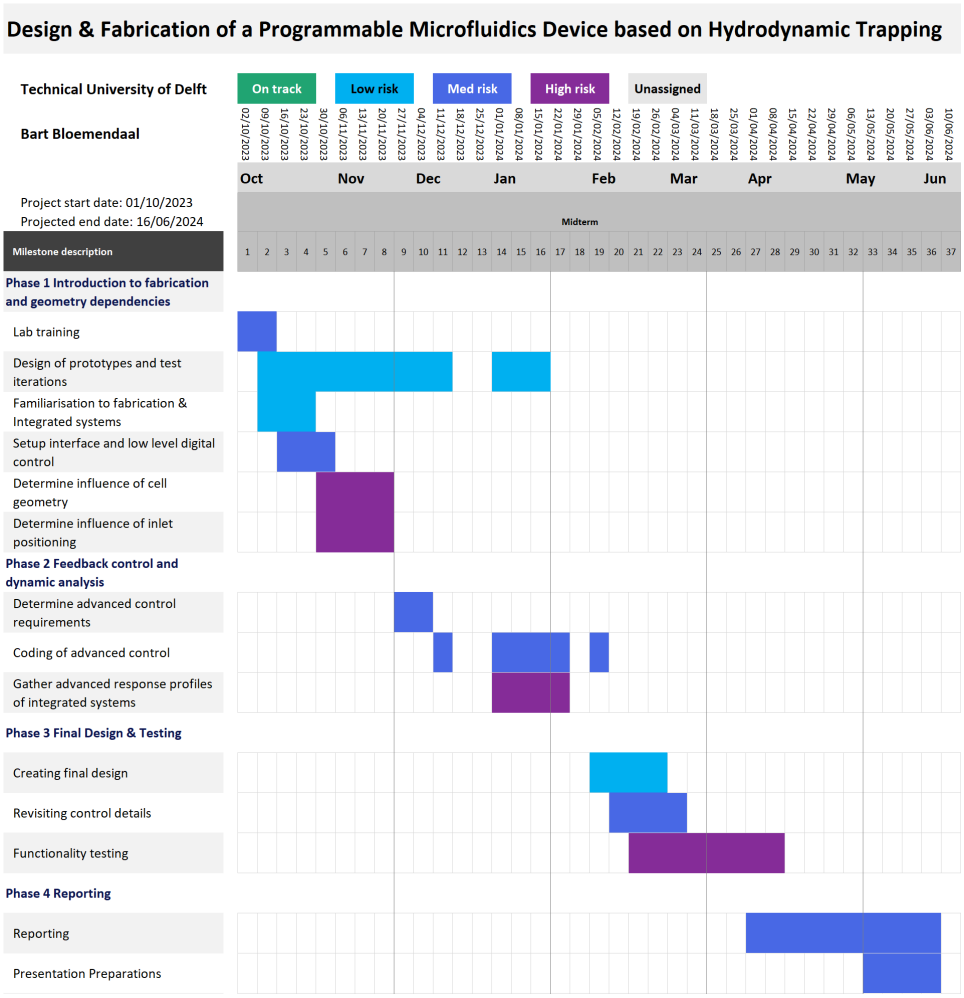

Figure 8.1: Gentt chart of the required activities in the project

8.1. Risks and Mitigations

In this section, highlights are given on potential problems that might occur during the project. Yet these are only speculations for it is impossible to predict accurately what will happen. However, table 8.1 provides a summary of potential risks and corresponding risk mitigation strategies.

Stage	Risk	Mitigation
Material	Sourcing and availability	- In-time indication of consumption
	Bubble forming	- Prepare resign in vacuum chamber - Apply vibrations after pour
	Ansisentrpoic curing	- Right exposure - Proper alignment
	Surface roughness	- Smooth master mold - Surface coating - Surface machining
Fabrication	Improper tolerances	- Exact master mould - Post processing
	Too much leakage at glued interface	- Post treatment - Removal, reprocessing and realignment
	Too much leakage at inlets	- Post treatment - Removal, reprocessing and realignment
	Inlet misalignment	- Post treatment - Removal, reprocessing and realignment
Structural	Collapsing	- Design analysis - Structural safety factors
	Stretching/tearing	- Structural safety factors - Pressures limits
Control	Slow response rates	- Higher end controller - Proper integration of systems
	Malfunctioning	- Redundancy - Higher end controller
Testing	Critical failure	- Incremental work ethic - Safety systems
	Safety hazard	- Physical emergency stop - Digital safety functions, Safety equipment
External devices	Hardware availability	- Early orders - Multiple suppliers
	Pump malfunctioning	- Accumulate technical knowledge - Familiarise with the experts

Table 8.1: Overview of potential risks and mitigations

If major setbacks are encountered during the project, resulting in significant delays the research plan of section 9 should be revised. At the halfway point a midterm assessment will be done, whereby either the current planning is to be affirmed or altered. To end up with a more realistic planning for the second half of the project.

To mitigate the risk of design incompatibility with the project goal, two different device configurations will be investigated. Primarily the device that consists completely out of PDMS, is favoured. Yet this brings the risk of not functioning very well with the observation techniques. Therefore this risk is mitigated, by also producing a glass sandwich structure design.

Bibliography

[1] A. Kislaya, "Particle Manipulation-on-chip Using programmable hydrodynamic forcing in a closed loop Publication date 2022 Document Version Final published version Citation (APA) Kislaya, A. (2022). Particle Manipulation-on-chip: Using programmable hydrodynamic forcing in a closed loop," *Delft Institutional Repository*, 2022.

[2] J. Nilsson, M. Evander, B. Hammarström, and T. Laurell, "Review of cell and particle trapping in microfluidic systems," 9 2009.

[3] A. Lenshof, M. Evander, T. Laurell, and J. Nilsson, "Acoustofluidics 5: Building microfluidic acoustic resonators," *Lab on a Chip*, vol. 12, pp. 684–695, 2 2012.

[4] S. Zhang, Y. Wang, P. Onck, and J. den Toonder, "A concise review of microfluidic particle manipulation methods," 4 2020.

[5] D. Kumar, A. Shenoy, J. Deutsch, and C. M. Schroeder, "Automation and flow control for particle manipulation," 9 2020.

[6] B. Cardenas-Benitez, B. Jind, R. C. Gallo-Villanueva, S. O. Martinez-Chapa, B. H. Lapizco-Encinas, and V. H. Perez-Gonzalez, "Direct Current Electrokinetic Particle Trapping in Insulator-Based Microfluidics: Theory and Experiments," *Analytical Chemistry*, vol. 92, pp. 12871–12879, 10 2020.

[7] A. Lenshof and T. Laurell, "Continuous separation of cells and particles in microfluidic systems," *Chemical Society Reviews*, vol. 39, pp. 1203–1217, 2 2010.

[8] M. P. MacDonald, G. C. Spalding, and K. Dholakia, "Microfluidic sorting in an optical lattice," *Nature*, vol. 426, pp. 421–424, 11 2003.

[9] A. Van Reenen, A. M. De Jong, J. M. Den Toonder, and M. W. Prins, "Integrated lab-on-chip biosensing systems based on magnetic particle actuation-a comprehensive review," 6 2014.

[10] A. T. Brimmo and M. A. Qasaimeh, "Stagnation point flows in analytical chemistry and life sciences," 2017.

[11] A. Kislaya, A. Deka, P. Veenstra, D. S. Tam, and J. Westerweel, "Ψ -PIV: a novel framework to study unsteady microfluidic flows," *Experiments in Fluids*, vol. 61, 2 2020.

[12] P. K. Kundu, I. M. Cohen, and D. R. Dowling, *Fluid mechanics.* Elsevlier, 2016.

[13] A. Karimi, S. Yazdi, and A. M. Ardekani, "Hydrodynamic mechanisms of cell and particle trapping in microfluidics," *Biomicrofluidics*, vol. 7, 4 2013.

[14] L. R. Huang, E. C. Cox, R. H. Austin, and J. C. Sturm, "Continuous Particle Separation Through Deterministic Lateral Displacement," *Science*, vol. 304, pp. 987–990, 5 2004.

[15] A. A. S. Bhagat, S. S. Kuntaegowdanahalli, and I. Papautsky, "Continuous particle separation in spiral microchannels using dean flows and differential migration," *Lab on a Chip*, vol. 8, no. 11, pp. 1906–1914, 2008.

[16] A. Einstein and A. D. Cowper, "Investigations on the theory of the brownian movement," tech. rep., -, 1925.

[17] G. Bagheri and C. Bonadonna, "On the drag of freely falling non-spherical particles," *Powder Technology*, vol. 301, pp. 526–544, 11 2016.

[18] R. Toy, E. Hayden, C. Shoup, H. Baskaran, and E. Karathanasis, "The effects of particle size, density and shape on margination of nanoparticles in microcirculation," *Nanotechnology*, vol. 22, 3 2011.

[19] G. Taylor, "Stability of a viscous liquid contained between two rotating cylinders," *Philosophical Transactions of the Royal Society of London. Series A, Containing Papers of a Mathematical or Physical Character*, vol. 223, pp. 289–343, 1 1923.

[20] R. R. Lagnado, N. Phan-Thien, and L. G. Leal, "The stability of two-dimensional linear flows," *Physics of Fluids*, vol. 27, no. 5, pp. 1094–1101, 1984.

[21] T. M. Schneider, S. Mandre, and M. P. Brenner, "Algorithm for a microfluidic assembly line," *Physical Review Letters*, vol. 106, 2 2011.

[22] M. Tanyeri, E. M. Johnson-Chavarria, and C. M. Schroeder, "Hydrodynamic trap for single particles and cells," *Applied Physics Letters*, vol. 96, 5 2010.

[23] M. Tanyeri, M. Ranka, N. Sittipolkul, and C. M. Schroeder, "A microfluidic-based hydrodynamic trap: Design and implementation," *Lab on a Chip*, vol. 11, pp. 1786–1794, 5 2011.

[24] M. Tanyeri and C. M. Schroeder, "Manipulation and confinement of single particles using fluid flow," *Nano Letters*, vol. 13, pp. 2357–2364, 6 2013.

[25] A. Shenoy, M. Tanyeri, and C. M. Schroeder, "Characterizing the performance of the hydrodynamic trap using a control-based approach," *Microfluidics and Nanofluidics*, vol. 18, pp. 1055–1066, 5 2015.

[26] A. Shenoy, C. V. Rao, and C. M. Schroeder, "Stokes trap for multiplexed particle manipulation and assembly using fluidics," *Proceedings of the National Academy of Sciences of the United States of America*, vol. 113, pp. 3976–3981, 4 2016.

[27] A. Shenoy, D. Kumar, S. Hilgenfeldt, and C. M. Schroeder, "Flow topology during multiplexed particle manipulation using a Stokes Trap," *PHYSICAL REVIEW APPLIED*, 8 2019.

[28] D. Kumar, A. Shenoy, S. Li, and C. M. Schroeder, "Orientation control and nonlinear trajectory tracking of colloidal particles using microfluidics," *Physical Review Fluids*, vol. 4, 11 2019.

[29] D. Kumar, C. M. Richter, and C. M. Schroeder, "Conformational dynamics and phase behavior of lipid vesicles in a precisely controlled extensional flow," *Soft Matter*, vol. 16, no. 2, pp. 337–347, 2020.

[30] Y. Zhou, K. W. Hsiao, K. E. Regan, D. Kong, G. B. McKenna, R. M. Robertson-Anderson, and C. M. Schroeder, "Effect of molecular architecture on ring polymer dynamics in semidilute linear polymer solutions," *Nature Communications*, vol. 10, 12 2019.

[31] D. P. Taylor and G. V. Kaigala, "Reconfigurable microfluidics: real-time shaping of virtual channels through hydrodynamic forces," *Lab on a Chip*, vol. 20, no. 10, pp. 1720–1728, 2020.

[32] T. Ching, X. Nie, S. Y. Chang, Y. C. Toh, and M. Hashimoto, "Techniques and materials for the fabrication of microfluidic devices," in *Principles of Human Organs-on-Chips*, pp. 1–36, Elsevier, 1 2023.

[33] S. M. Scott and Z. Ali, "Fabrication methods for microfluidic devices: An overview," 3 2021.

[34] J. M. Wilkinson, "Need for alternative testing methods and opportunities for organ-on-a-chip systems," in *Organ-on-a-chip*, pp. 1–11, Elsevier, 2020.

Design & Fabrication of a Programmable Microfluidic Device

Bart Bloemendaal
Departments of Precision and Microsystem Engineering & Process and Energy
Faculty of Mechanical Engineering (ME)
Delft University of Technology
Delft, The Netherlands

***Abstract*—This study presents the development of a programmable microfluidic device designed for precise hydrodynamic manipulation of particles and fluids. Utilising femtosecond laser ablation and cold oxygen plasma bonding, the device features highly accurate microfluidic inlets with minimal surface roughness, ensuring consistent flow dynamics. Experimental validation confirmed the device's ability to generate uniform flow fields and half Rankine bodies, demonstrating its potential for real-time reconfigurability in various applications, including particle manipulation and flow field analysis. The research lays the groundwork for future advancements in microfluidic technology, emphasising high precision and structural integrity.**

***Index Terms*—Microfluidics, Laser ablation, Plasma Bonding**

I. Introduction

Microfluidics is a rapidly evolving field at the intersection of physics, engineering, and biology. This emerging discipline explores the behavior of fluids at the microscale (from several millimeters to micrometer scale) [1], leading to groundbreaking advancements in various industries. For example, in medical diagnostics, devices have been designed to isolate cells and viruses such as HIV, malaria, and COVID-19, demonstrating the potential applications of microfluidics [2]. In the pharmaceutical industry, microfluidics contribute to increasing efficiency of drug discovery and drug delivery [3]. In biotechnology, microfluidic technologies facilitate single-cell analysis and allow for the creation of "organs-on-chips", whereby the effects of drugs and toxins can be tested on human tissue [4]. Microfluidics is also utilised in environmental monitoring, to detect pollutants and contaminants in water and measure air quality [5]. In the energy and nanotechnology sector, these devices can be used as microreactors for nanoparticle synthesis or function as a microscale fuel cell [6]. Finally in the oil and gas industry, they give insight into droplet coalescence of crude oil/water mixtures [7], which result in more knowledge on separating the mixture. These developments are supported by the advancement of microfabrication technologies, including extensive innovation in soft lithography, 3D printing and laser ablation. As a researcher, being able to rapidly prototype and fabricate a microfluidic cell allows for a quick iteration process.

Microfluidic devices are designed with a specific function in mind. This could either be to transport, trap, sort, separate, or mix particles in suspension. These manipulations can be achieved using different methods, and can be broadly labelled as either passive or active techniques. Passive flow manipulation finds its principles of function in the topology of the channel. By introducing obstructions, turns, or implementing a spiraling channel on a larger scale [8], the goal is to utilise secondary flow structures for sorting or mixing different particles. Passive flow control primarily targets the mixing or separation of particles based on differing particle properties.

Active methods of flow manipulation include acoustophoresis, where particles are translated to a node of a standing acoustic wave introduced between the channel walls [9]; electrokinetics, which manipulates the flow using charge, either through electrophoresis [10], electroosmosis [11], or dielectrophoresis [12], with each method utilising an electric field to exert a force on either the particle or the solution; optical trapping, where focused laser beams trap microscopic particles at the focal point [13]; and magnetic manipulation, which applies a magnetic field to transport or trap magnetically susceptible particles at a desired location [14].

Another approach to using such external fields is to control particles by actively manipulating the flow field. Such hydrodynamic flow manipulation is an active control technique requiring active flow control. Used to influence flow dynamics by creating areas of stagnation and modifying streamline patterns. In contrast to previously mentioned techniques, hydrodynamic flow manipulation can be done on a large surface and is non intrusive, meaning that it does not require specific particle properties and does not apply significant intrusive external forces.

This technique was initially pioneered by G.I. Taylor in 1934 when he hydrodynamically trapped a droplet using an analog four-roll mill [15]. These rollers generated an extensional flow, causing a droplet to translate over the extensional flow axis. In 1980, G. Leal improved the manual four-roll mill by incorporating digital control [16].

More recently, a research group supervised by C.M. Schroeder developed a Stokes cell based on a cross-slot configuration cell, with a cell area of 200 by 200 microns.This design was created using PDMS soft lithography and featured two inlets and two outlets, enabling the manipulation of droplets and particles by an extensional flow. Consequently, it created particle trajectories resembling letters of the alphabet within the flow [17]. This device was used for research on lipid cell behaviour and ring polymer properties [18].

Recent studies on hydrodynamic flow manipulation have introduced the concept of creating virtual channels within a two-dimensional uniform flow field. These virtual channels are created by inserting or removing flow through perpendicularly placed apertures and rely on liquid-liquid interfaces from two

different flow origins to form a physical barrier. Particles can be transported or trapped at these interfaces.

The working principle has been evaluated in a study aimed at demonstrating real-time reconfigurability of the flow field [19]. A more comprehensive thesis was done by A. Kislaya focused on the design and fabrication of a microfluidic device. This device benefits from a priori particle path prediction, offering the user the ability to integrate multiple functionalities such as trapping, separation, or sorting onto a single device [1]. This doctoral work served as the inspiration for the current project.

To be able to approximate two dimensional flow, the Hele-shaw condition has to be adhered too. Hele-Shaw flow refers to the laminar flow occurring between two parallel plates. These plates, each having a length l and a width w, are separated by a distance h along the z-direction [20]. The Hele-Shaw condition is applicable when the in-plane dimension l is significantly larger than the channel height h (i.e., $l \gg h$). This condition is typically met at an in-plane distance of approximately h from the boundary of the flow domain. The velocity profile in the z-direction exhibits a parabolic shape, driven by the pressure gradient in the (x,y) plane [CITE]. To simplify the analysis and reduce the complexity of the flow description, the concept of depth-averaged velocity is often introduced. This velocity represents the average of the parabolic velocity profile across the gap h. It provides a two-dimensional approximation of the flow field, which is particularly useful in modelling and simulations, allowing the complex three-dimensional flow to be treated as a simpler two-dimensional problem while still capturing the essential dynamics of the flow [21].

For active flow control, it is paramount that the channel volume in the chip stays constant. Therefore, high stiffness is required. This rules out the fabrication technique of soft lithography of PDMS, and requires the exploration of other fabrication methods. Despite the resin-printed chip developed by Kislaya demonstrating good performance, successfully manipulating particles with precise trajectory control down to the accuracy of a single particle diameter, several areas for further performance enhancement have been identified. These enhancements pertain to fabrication and active control. This project will focus on developing a fabrication strategy for a chip that applies the principle of reprogrammable virtual structures in a fluidic cell to manipulate particles, cells, cell clusters, and fluids. This method of manipulation is non-intrusive and operates independently of many particle properties that constrain other manipulation techniques.

This project aims to distinguish itself through a more novel design, emphasising manufacturing accuracy, structural stiffness, and edge detailing. This is done by making use of femtosecond laser ablation to create a three layer structure of glass-PDMS-glass, with high machining precision. This method facilitates the machining of surfaces that, once assembled, will constitute the faces of the channel, allowing for clean edges that result in a more uniform outflow of fluid from the inlet, enabling more precise control over the flow. The end goal is to create a multi functional platform that will fulfill the needs of various kinds of experimental studies.

In future research, this device will find applications in interfacial studies of droplets, to uncover breakup and coalescence behaviour. The ability to control the kinematics and dynamics of the flow on the small scale makes it a good platform for rheology experiments. Additionally, it will allow for long-time visualisation of motile particles, such as algae and bacteria. These particles move around within the medium and require active correction to stay within the field of view of a microscope or camera.

II. Design and Modelling

As proposed in the introduction, this project aims to develop an alternative method of microfluidic chip fabrication. This method is intended to accommodate the chip characteristics required for programmable hydrodynamic forcing at relatively large dimensions. This preference for larger surfaces introduces complexities regarding flexibility. A larger surface is generally more prone to bending compared to smaller structures. Given that the channel is pressurised, stiffness is crucial to maintaining a constant volume. If the channel is fabricated using conventional soft lithography, material deformation would introduce significant structural changes. A quick back-of-the-envelope calculation on linear beam theory shows, that for a $15mm$ wide and $45mm$ long PDMS chip, a maximum deflection of $0.162mm$ can occur at $100mbar$ of pressure difference. This would be a significant increase in volume altering the flow field, in a device where the predictability of fluid interaction is key. Stiffer channels can be made using 3D resin printing, but a drawback from this technique is that the internal structure is difficult to inspect. 3D printing often suffers from defects and it is difficult to print a void without using support. This support material is difficult to remove, potentially resulting in leftover material in the channel. The printing of holes for the inlets can also bring complications, where either the edge is not circular or is not completely flat.

This leads to another goal of the design, to produce a theoretically near perfect fluid source. Striving to achieve a uniform outflow of fluid from the inlets into the channel. Therefore, edge definition and manufacturing precision are paramount, as small cracks, burrs or other asymmetries might change the uniformity of the flow into the channel, thereby diverging from the ideal potential flow theory that is used to predict the flow. To be able to achieve this definition at the edge of the inlet, the use of 3D resin printing is not suitable.

Here, we explore a new fabrication method using a bonded glass-PDMS-glass sandwich structure (Figure 1). The inlets of

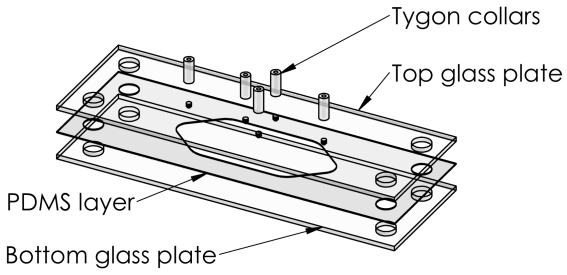

Fig. 1: Exploded view of the layers of the chip including the Tygon™ collars.

fluid flow are machined into glass microscopy slides, and the channel is machined into the PDMS gasket layer. This raises two questions: How does one precisely machine and achieve smooth edge definition in glass? And how does one fabricate channels in thin layers of PDMS? The solution for both questions is found in the technique of femtosecond laser abrasion. This necessitates extensive expertise and characterisation in femtosecond laser ablation, which constitutes a substantial portion of this project. In addition, a design for a connection between the glass layer and the tubing of the pump is required. This connection is achieved by bonding Tygon™ collars to the glass surface with a gel based adhesive. A more extensive elaboration of the fabrication process is found in the subsequent section of this paper.

A. *Material and Dimensioning*

The materials used for the device are glass microscopy slides, Polydimethylsiloxaan (PDMS) sheets, and Tygon™ tubing. The microscopy slides are the Premium clear slides from Epredia™, these slides in comparison to other tested brands have relatively low tolerances and right angles at the corners. This is required for alignment in the machining process, it also results in a chip that has all layers aligned. The PDMS sheets that are used are $200\mu m$ thick spin coated sheets. This technique involves depositing a liquid PDMS solution onto a substrate, which is then spun at high speeds to create a uniform, thin film. The resulting PDMS layer can be precisely controlled in thickness and surface properties, making it ideal for creating microfluidic devices. Due to the flat surface the glass PDMS interface forms a liquid tight seal. The Tygon™ tubing collars are chosen for the flexible material and the large outer diameter $(2mm)$ ratio with respect to the inner diameter $(0.76mm)$. This thickness of the material allows for a larger surface of adhesion to the glass, allowing for more durable bonds.

Three different geometry configurations are proposed, the general structure of these geometries are displayed in Figure 2. All configurations use the same characteristic length (L_C) set at $15mm$. Configuration 1 does not include the red marked hole and has a channel length of $30mm$, the second configuration differs from the first by having a channel length of $45mm$, and the third configuration sees the introduction of a sixth inlet marked in red in Figure 2. The inlets are designed to include a blind and a through hole as depicted in Figure 3. This is an

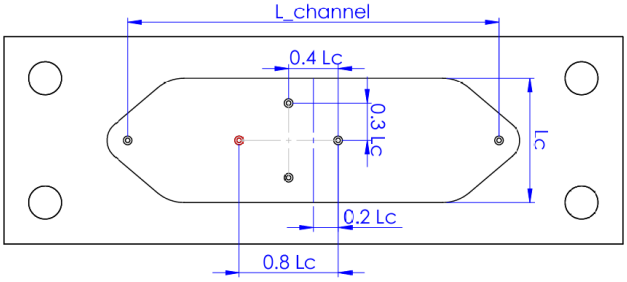

Fig. 2: Schematic top view of the inlet configurations that have been fabricated. With a characteristic length of $15mm$ determined from the width of the channel. The red inlet is present in only one of the three configurations.

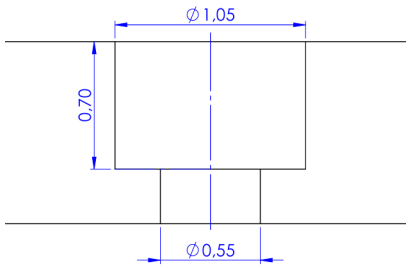

Fig. 3: Schematic side view of the hole morphology, build up from a blind hole with the $1.05mm$ blind hole and a $0.55mm$ through hole.

important step for assembly, the blind hole serves as a guide for aligning the Tygon™ collars and also acts as a clearance space for debris released during the machining of the through hole.

B. *Integrated Systems*

Next to the microfluidic flow cell, additional fluidic systems are required for the whole system to work. Figure 4 is a schematic representation of the integrated setup, where the supply of flow is generated by a pressure pump, and the flow rates are monitored using flow sensors.

1) Pressure Pump: The pressure pump used is Fluigent™ Microfluidic Flow Control System MFCSTM-EZ, which is a pressure based flow controller for microfluidics and nanofluidics applications. The benefits of this system is that it allows for stable and pulsation free flow with short response times down to $40ms$. The flow rate through the channel is controlled independently which is essential for precise particle manipulation.

2) Flow Sensor: The flow rate is measured by the flow sensor through locally heating the liquid. The flow rate is defined by two temperature sensors that measure the heat profile, and are symmetrically located on both sides of the heat source. The sensors measure the temperature variation, and from that determine a flow rate. Fluigent™'s FLOW UNIT is able to provide accurate data on the flow of water and isopropanol. The system is accompanied by user-friendly software that includes manual flow control and a machine learning algorithm designed to optimise pump response rates.

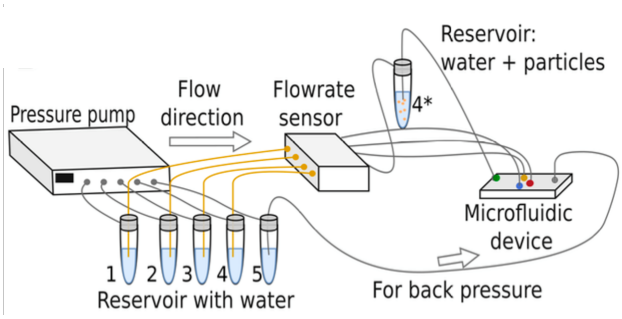

Fig. 4: Schematic representation of the integrated systems used in the setup [1].

3) Additional Components: To connect all parts of the system, four types of tubing were utilised. Two types were used for the flow sensor, and two others for connecting to the chip. The tubing for the sensor has an outer diameter of $1/32$" and an inner diameter of 0.25mm. The material of these sensor tubes are: PTFE, and PEEK, PTFE is chosen for its flexibitlity while peek is employed on the outflow side of the sensor because it provides a reliable fit with Luer adapters. These adapters connect to a third type of tubing, a PTFE tube with an outer diameter of $1/16$" and an inner diameter of 0.75mm. Since this PTFE tubing is relatively rigid, a fourth type of tubing, Tygon™, with an inner diameter of 0.75mm and an outer diameter of 2mm, is added for flexibility. This flexible tubing connects to the chip, preventing a rigid link between the sensor and the chip. The Tygon™ tubing is connected to both the PTFE tubing and the chip using 20-gauge stainless steel couplers.

C. Hydraulic Resistance

All the mentioned parts exert a hydraulic resistance onto the flow, this is to be computed to set up the pressure pump. Due to the inherent design of the pump it is required to determine the pressure requirements in advance of experiments. The δP minimally required to push liquid at certain pressures can be calculated using the equations for hydraulic resistance. Computing these values for every component and adding them up in an electrical circuit analogy results in the total resistance of the system. In Figure 5 the individual and the total pressure drops are displayed for each component for different flow rate values. From the data, it can be concluded that the tubing used around the flow sensor is the dominant factor in forming hydraulic resistance. Additionally, it can be inferred that the pressure pump must provide a minimum pressure difference of $14mbar$.

D. Flow Modelling Theory

Predicting and modeling flow in fluid dynamics is a challenging task. It often necessitates simplifications and approximations; otherwise, highly complex computational fluid simulations would be required. These simulations are time-consuming and unsuitable for real-time feedback control over a flow field. Therefore, the channel's height is designed to favor simplification of the flow field, adhering to the Hele-Shaw condition, which allows for accurate predictions of a two-dimensional flow field using potential flow theory. The primary concepts employed are the panel method from potential theory to model the flow fields, and the half Rankine bodies theory is utilized to validate performance.

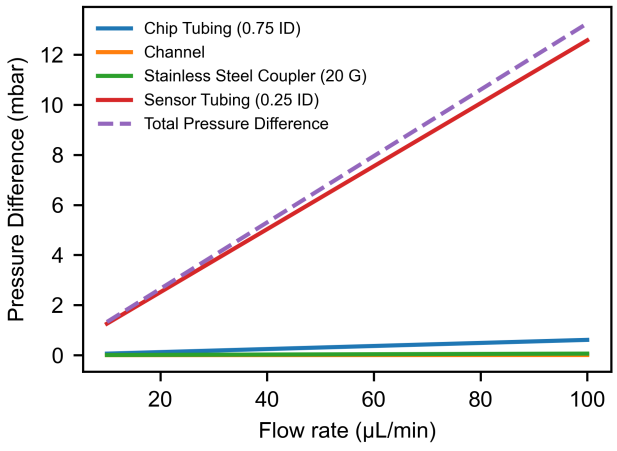

Fig. 5: Pressure loss over various components of the integrated system, in relation to applicable flow rates.

1) Panel method: The panel method is a numerical technique in fluid mechanics used to solve potential flow problems involving solid boundaries, like aerofoils and ship hulls. It simplifies the flow field by assuming potential flow, which is inviscid, incompressible, and irrotational, leading to the governing Laplace equation. The body's surface is discretised into small flat segments, or panels, each associated with a source/sink strength to model the normal component of flow velocity. The method ensures a no-penetration boundary condition, which makes the flow follow the body's contour without intersecting it.

2) Half Rankine Body: A half Rankine body is a theoretical model in fluid dynamics and potential flow theory, used to study flow around streamlined bodies, an example is shown in Figure 6b. It is derived by superimposing a uniform flow with a source-sink pair, resulting in a streamlined, semi-infinite object. The potential function (ϕ) and stream function (ψ), obtained by solving the Laplace equation under appropriate boundary conditions, describe the flow around this body. The symmetric flow analysis along the plane dividing the source and uniform flow offers insights into minimising flow separation and resistance, aiding in the design of efficient aerodynamic and hydrodynamic shapes.

E. Modelled Flow Fields

Applying panel method theory to solve several flow configurations, leads to the modelled flow profiles seen in Figure 6, these profiles are aimed to be replicated with experiments. The Uniform flow field (Fig. 6a) will give an insight into the velocity profile in the chip, whereby the model is representing the mid plane velocity field also referred to as Depth-Averaged Velocity. This is the velocity profile in a two-dimensional plane, yet in practice the channel does have a height. Considering flow is transported due to a pressure gradient, the assumption can be made that there is a parabolic Poisseuille profile, meaning that the measured velocity in the chip is dependant on the position of particles on this profile. Therefore, the uniform flow field experiment will give an insight on the distribution of particles on the parabolic velocity profile.

Figure 6b is a representation of a half Rankine body. For experiments, the half Rankine body will give valuable insight on the inflow through the inlets. If the machined holes are non-circular or have roughness around the edge this will disturb the flow at that location resulting in a non-uniform flow distribution. The stagnation point that is present in a half Rankine body also provides valuable insight on the ratio of flow rates between the uniform flow and the source.

The flow profiles seen in Figures 6c & 6d will be replicated for the sake of proving reprogrammability, demonstrating the novelty of the device.

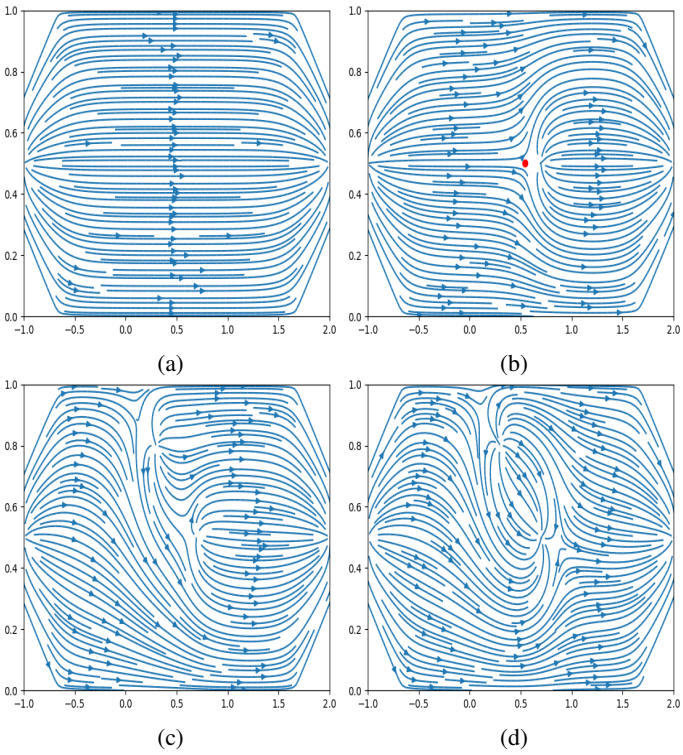

Fig. 6: A collage of images displaying four distinct flow field configurations obtained using the panel method. The scale bars in each image are measured in units of the characteristic length. (a) Is an example of an elementary flow also being the uniform flow. (b) Is a source and a uniform flow creating a half Rankine body with the red dot representing a stagnation point. (c) Is an example of two active sources in a uniform flow field. (d) Includes a source and a sing creating a flow profile within the uniform flow. All scales are representing the fraction of the characteristic length.

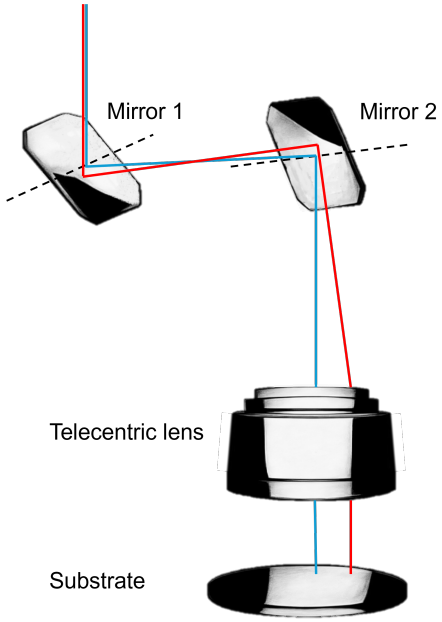

Fig. 7: Schematic representation of laser beam manipulations by rotating mirrors and a telecentric lens. The image illustrates two distinct rays of light, each striking the mirrors at a different angle of incidence. Also depicted is the function of the telecentric lens, which aligns the beams to be perpendicular to the substrate.

III. Fabrication Process

A. Laser Ablation

To perform precise micromachining of glass, the 515 nm, 15 Watt Lasea LS Lab femtosecond laser is utilised. This laser employs a highly focused beam to micromachine the surface of the glass, which includes cutting, marking, drilling, texturing, removing thin layers, or engraving microscopic details on a seemingly small surface. The femtosecond refers to the shutterspeed of the laser, this results in pulses of the duration of 10^{-15} seconds, also referred to as ultra short pulsed laser. Ultrashort pulse durations allow for precise material ablation through a nonlinear process called multiphoton absorption. The intense energy quickly causes the material to be directly vaporised without significant thermal diffusion [3], delivering high fabrication quality due to a quasi-non-thermal interaction with the material. In comparison, longer pulse lasers have the inherent heat related drawbacks of micro cracking, melt zones, molten material ejection and surface distortions. These distortions, if present, will greatly affect fluid flow from the inlets in the microfluidic chip.

Inherently, the micro machining of glass is complicated, as conventional subtractive manufacturing techniques do not yield the desired smoothness of the glass. Machining with light is an alternative, but it also presents its own challenges. Due to the transparency of glass, its absorption of energy through light is limited. Additionally, if too much power is used, the thermal shock is likely to crack the glass. The available theoretical framework is limited, and in-house expertise on manipulating glass and PDMS using a femtosecond laser system is minimal. This has led to a direction of this project, to take a deep dive into the characterisation of the different parameters that influence the quality of the cut. The parameters of interest are the speed of the focal point of the laser, and the percentage of the transmitted laser power. The impact of these parameters on edge quality and glass machining time is examined in the characterisation section.

Another factor to consider is the laser's focal point, which is translated using a set of rotating mirrors that direct the light beam onto a telecentric scan lens (see Figure 7). This lens bends the light beam, aiming it to be perpendicular to the substrate. This minimises the telecentricity error, which means that the light rays are not perfectly parallel to the optical axis. The drawback is that the lens also limits the area of machining, the area of focus is to be determined.

B. Piezoelectric Direct Discharge

To bond the lattice structure of glass and PDMS, cold oxygen plasma, also known as Piezoelectric Direct Discharge (PDD®)

is utilised. Piezoelectric Direct Discharge (PDD®) technology is a sophisticated method used to generate cold active plasma at low temperatures, it is particularly effective for bonding the materials: PDMS and glass. The process makes use of a piezoelectric element that, when subjected to an electrical field, produces a mechanical strain. This strain induces a discharge that generates cold plasma at atmospheric pressure. The generated cold plasma contains a mix of ions, electrons, and neutral particles, including reactive oxygen groups. When this plasma is directed onto the surfaces of PDMS and glass, it effectively modifies their surface properties. For PDMS, the plasma treatment breaks the silicon-oxygen bonds on the surface and introduces hydroxyl (–OH) groups, rendering the surface hydrophilic and increasing its surface energy [22].

On the glass slide, the plasma treatment also generates hydroxyl groups on the surface, making it similarly hydrophilic. The presence of these reactive groups on both surfaces facilitates the formation of strong covalent bonds when the PDMS and glass are brought into contact. The hydroxyl groups from the PDMS and glass undergo a condensation reaction, resulting in the formation of siloxane (Si–O–Si) bonds, which are robust and durable. To get rid of the reactions resultant H_2O, the assembly is added into a heat treatment cycle of $65°C$ to evaporate the water.

PDD® technology is advantageous because it operates at low temperatures, preventing thermal deformation and thermal damage to the materials being bonded. Additionally, the process is rapid and does not require the use of harsh chemicals. This method ensures a strong, uniform, and reliable bond between PDMS and glass, which is essential to prevent leakage in microfluidic devices.

C. Integration of Inlets/Outlets and Connection Interfaces

The inlets/outlets of the chip are vital components for the function of the device. Minimal flow disturbance is desired; therefore, alignment and accuracy are key. Standard Luer connection pieces, which are commonly used to connect the tubing with the inlets/outlets, are either bulky or difficult to position. A solution for this involves creating an assembly that can be used as an alignment jig. Figure 8 depicts the alignment of the syringes to the chip. For a better overview, the computer aided design can be viewed in Appendix I. This filament printed stand uses a modular insert geometry allowing different syringe configurations to be inserted. These syringes are precisely aligned with the blind holes that were machined into the glass. These blind holes facilitate the insertion of the tip of the syringe. Before inserting the syringe, Tygon collars are put on the body of the syringe and the designated surfaces are coated with adhesive. These Tygon collars are fabricated using a lathe, Tygon™ is a PVC like material that is used for tubing in microfluidics. Bonding anything that has to withstand a load to glass turned out to be a challenge. Yet after trial and error a gel-based chemical adhesive was found that is also resistant to weak organic solvents like isopropanol. In the final assembly step, the Tygon collars are slid down over the shafts of the syringes ensuring a perfect alignment. A secondary function of the syringes that are fit in the blind holes is to function as a plug, thereby preventing the flow of glue inside the chip.

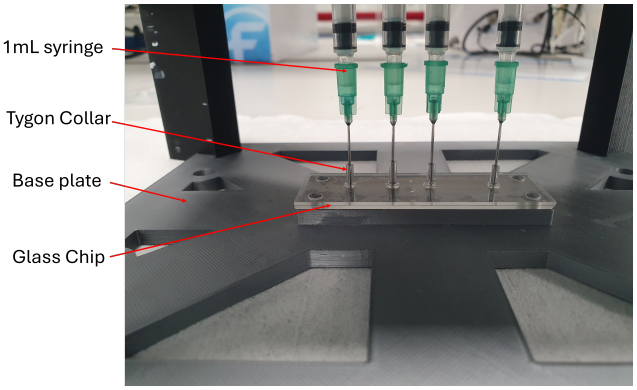

Fig. 8: Filament printed structure used for aligning syringes to the inlets on the chip.

D. Flow Visualisation

To visualise the flow field, particles are used as they depict a silhouette on the recording. The trajectory of the particles can be translated to streamlines in the flow. The particles that are used are polyethylene fluorescent particles with a diameter ranging between $20-25\mu m$. The material has a density equal to that of deionised (DI) water, this to keep the particle neutrally buoyant in solution. To prepare the solution, DI water is first boiled to degass it, then a tween solution is added. Tween, also known as polysorbate, is commonly used as a surfactant for dispersing hydrophobic particles in aqueous solutions. Trying to make the particle solution without tween will result in a non-uniform distribution of particles mainly at the water surface and clumps at the container wall. The drawback of using the tween surfactant is that it increases the surface tension. This increased surface tension magnifies the risk of small bubbles getting stuck in the channel. Therefore, extra care is to be taken during the experiments when the solution is introduced.

Another drawback of the solution is that the flow sensor is not compatible with measuring the flow. This is the reason for the need for additional reservoirs that are placed behind the flow sensor. The risk of this is that an extra element of uncertainty is added to the system, potentially changing the fluid behaviour.

IV. Characterisation

A. Laser Characterisation

To properly understand how laser parameters affect manufacturing quality, systematic characterisations are done to optimise surface quality and fabrication accuracy. The predominant parameters that are varied are the focal point velocity of the laser, the outlines of the perimeter, and the percentage of power that is being transmitted from the 15 Watt laser source. All measurements are performed on a Keyence VHX-700 digital microscope. This microscope has the advantage of offering extensive depth measurement capabilities.

Additionally, a key factor in all experiments is to set up proper fume and debris extraction. All experimental data was collected by introducing a stream of pressurised air that is close

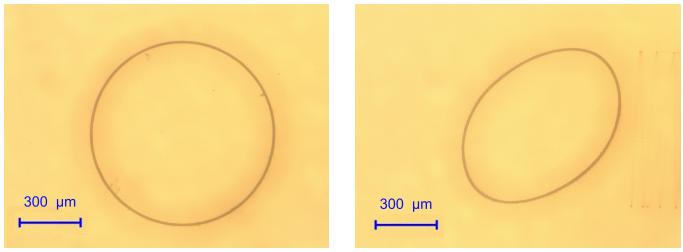

(a) (b)

Fig. 9: Two perimeters, intended to be circular, machined with varying laser focal point velocities. (a) at $100mm/s$, (b) at $1750mm/s$, the images are taken at 300 times magnification.

to vertically directed at the cutting surface, this to promote extra airflow during machining. The extraction nozzle, which sucks up debris and fumes, is to be aimed as closely as possible to the surface that is being machined in order to concentrate the suction force, so it can extract the more stubborn pieces of debris. Not extracting debris properly, results in the scattering of the light beam on small grains of glass, limiting the input of energy.

1) Velocity Characterisation: To determine the influence of the laser's focal point velocity in the xy-plane, three sample sets of ablation are analysed. Each set contains ten circular cuts with a diameter of $1mm$. The cuts start at a planar velocity of $50mm/s$ and incrementally increase with $50mm/s$, up to $500mm/s$. Additional measurements were performed, where the focal point velocity of the laser has been measured in steps up until $2250mm/s$. Two example measurements are depicted in Figure 9, which show that at very high laser focal point velocities, the designed perimeter is not accurately maintained. This is the result of the errors that originate from the angular acceleration rate of the actuators that drive the mirrors. The inherent sensitivity of the mirrors renders even the slightest misalignment capable of significantly affecting the precision of the cut, highlighting the importance of determining when the accuracy is maintained and when it deteriorates.

Using the OpenCV module in Python to process the images allows for the detection of the outer perimeter of the cut. From these measurements, the perimeter lengths and average diameters can be calculated. The roundness of the cut can then be assessed by analysing the perimeter and the measured pixel area within it. This roundness is quantified by multiplying the area by 4π and dividing by the square of the perimeter, which provides a metric for how closely the shape approximates a perfect circle. If the image contains a perfect circle, this value should equal one, as the measured area should match the area that can be derived. A non-circular shape scores poorly on this scale since a circle minimises perimeter length for maximum surface area. The obtained roundness value and average diameter are depicted in Figure 10a. These parameters are measured from the recognised perimeters on all images. The script measures 100 different diameters per image, at different angles, to determine a standard deviation and an average diameter.

The graph in Figure 10a implies that up until $500mm/s$ the designed geometry is achieved, at higher velocities, the laser

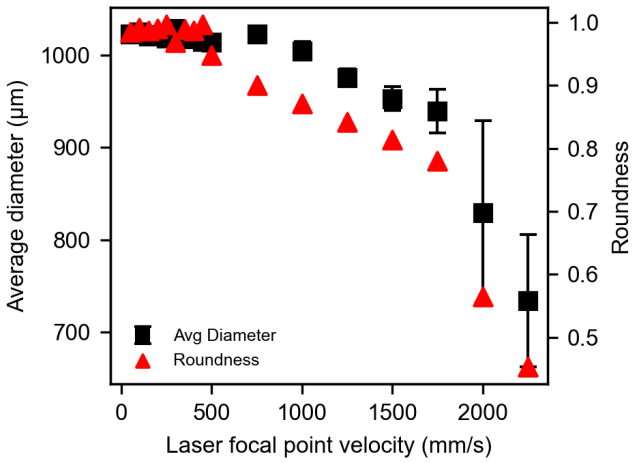

(a)

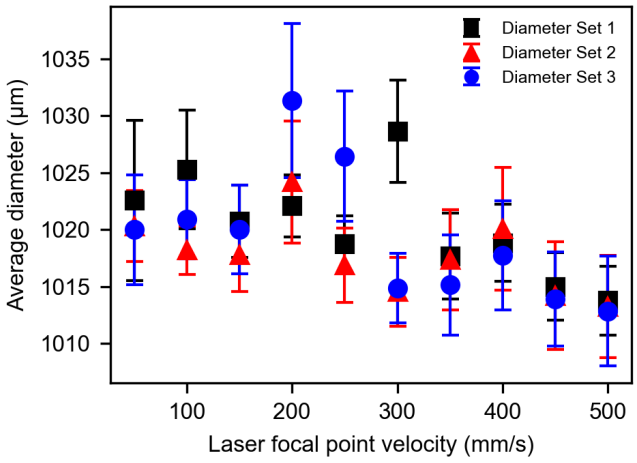

(b)

Fig. 10: Graphs showing the average diameter of a cut perimeter including standard deviations from the diameter. With on the x-axis the laser focal point velocity and on the y-axis the diameter of the cut, the intended diameters of the cuts are set to 1 mm. (a) Shows a single sample group of a larger range of velocities and includes the roundness of the perimeters. (b) Depicts three sample groups to display repeatability and tolerances.

becomes inaccurate, suggesting that the actuators responses are not following the idealised motions. To verify the reproducibility and tolerances of the laser machine, three sets of tests were performed, all yielding similar results. This is illustrated in Figure 10b. The diameters generally lay within a $< 5\mu m$ distance apart with some larger deviations occurring due to burs that are present around the perimeter of the cut.

2) Power Characterisation: The main contributor to the definition and roughness of the cut is the power. A higher power leads to more thermal input, thereby increasing the internal thermal dynamics of the material. To define the influence of laser power, three sets of measurements were performed, with two example measurements depicted in Figures 11a & 11b, the difference between the two depicted cuts is the laser power.

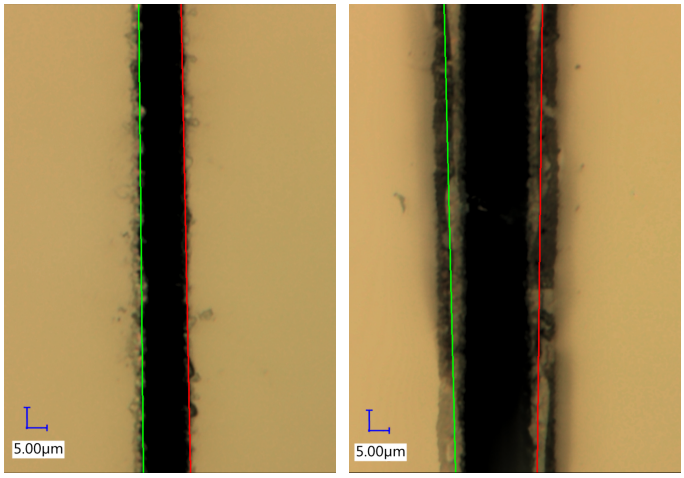

(a) (b)

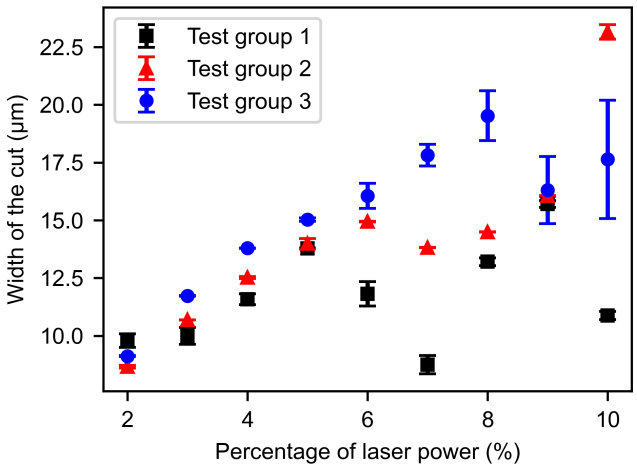

(c)

Fig. 11: Example of two straight cuts with different percentages of power and their associated widths, at 2000 times magnification, (a) 3 % cut, (b) 8 % cut. Also depicted are the fitted lines of the left (green) and right (red) edge, these represent the average position of the edge. (c) Is the width of the cuts graphed for three identical test samples.

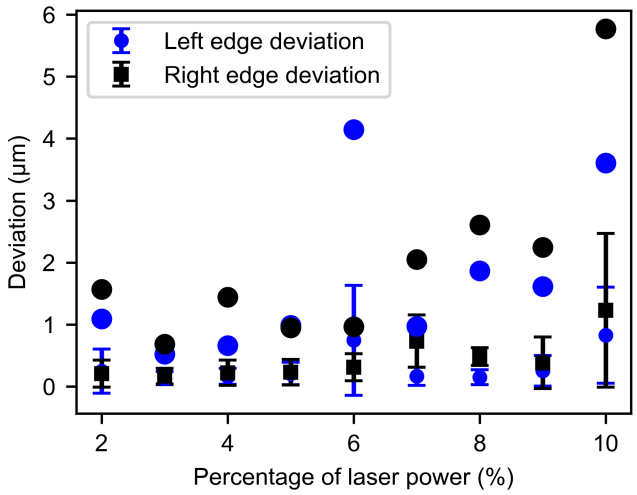

(a)

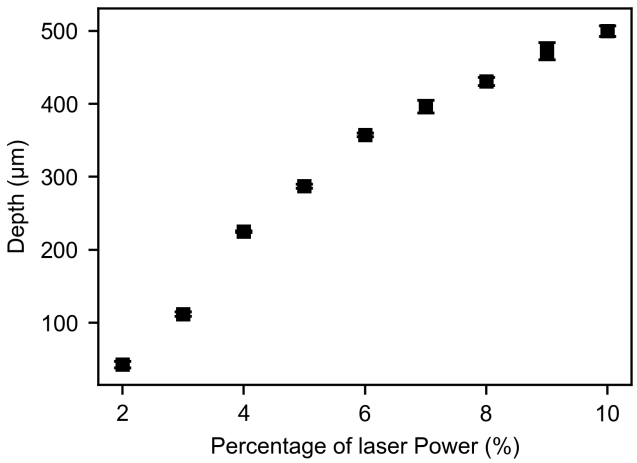

(b)

Fig. 12: Graphs on the influence of laser power. (a) A box plot showing the measured roughness of both the left and right edges for different percentages of power, including outliers representing extreme deviations. (b) The measured depth per cut in respective to power, using a focal point velocity of $50mm/s$ and 1000 repetitions.

The unit of power used during the analysis is the percentage of transmitted power from the 15 Watt source. Although the system can transmit the full 15 Watts, the requirement for precise edge detailing inclines to limit the maximum power transmitted to 10% of the source. Higher power levels are beyond the scope of this analysis.

In the Figures 11a & 11b, the left and right edges of the cut are fitted with a green and a red fit respectively, these fits represent the mean positions of the edges. The fits are compared by their distance apart, representing the width of the cut. In Figure 11c, the widths of cuts at different power levels are displayed. For each power level, three samples are analysed to assess the reproducibility of the cut width.

The fitted lines are also compared to the real edges of the cut material that the fitted lines approximate. From this, the roughness of the cuts can be determined. First, a binary image is made defining a clear edge of the material. Then, the fit of the edge can be compared to the real edge. From this, an horizontal distance can be measured in pixels. This is done for all pixels rows along the edge, resulting in information on the roughness of the cut. In Figure 12a the average deviation is plotted for all the different levels of power, along with extreme deviations observed. This data gives insight in the peaks an valleys in the roughness of the edge of the material, displaying a trend of increasing roughness with increasing power levels.

3) Depth Characterising: After characterising the two predominant parameters of interest, it is required to optimise for machining time. Due to the inherent transparency of glass, its absorption of energy from light is limited. This results in a time consuming procedure to get through a millimeter of glass. Therefore, the limited availability of the laser system has to be optimally used. Measurements are made to define the depth

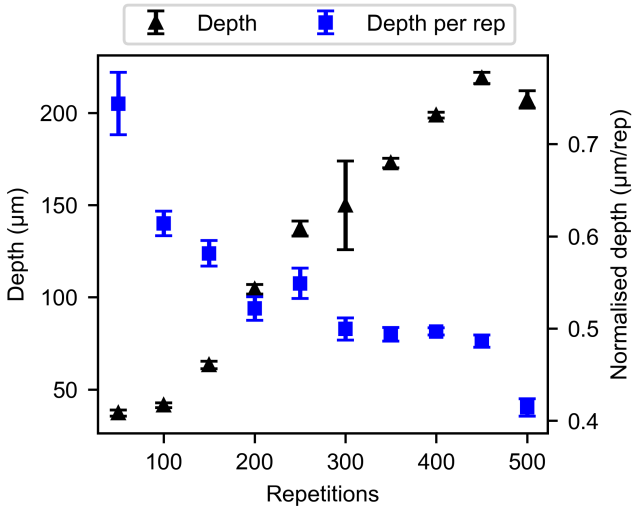

(a)

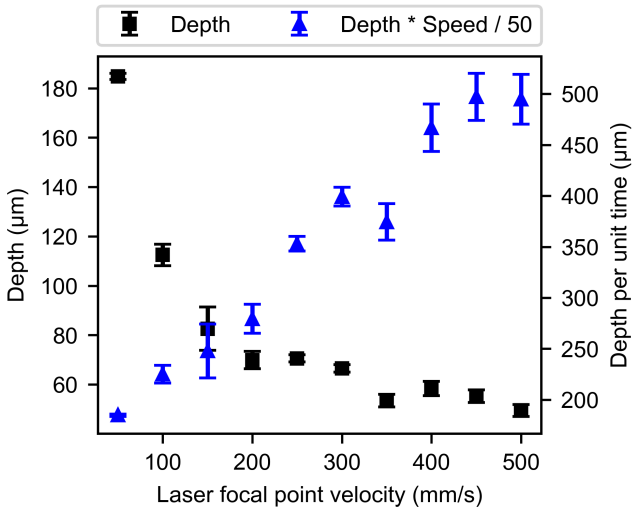

(b)

Fig. 13: The depth of cut acquired with varying focal point velocities and repetitions. (a) Normalised depth acquisition with respect to a single rep, at 5% power and a focal point velocity of $50mm/s$. (b) Depth acquired per unit time at 5% power and 1000 repetitions.

of the cut for different amounts of repetitions that the laser performs, the depth that is acquired by using different focal point velocities of the laser beam, and the depth that is acquired with varying power fractions. To measure the depth of a cut the Keyence VHX-700 digital microscope is used, the microscope makes a series of images at different z-coordinates. The images are then combined to generate a 3D image, which also provides detailed information on the geometry.

Increasing the number of repetitions correlates to a deeper cut. Yet, doubling the amount of repetitions does not result in a doubling of depth, as can be concluded from the normalised value of depth acquired per repetition, depicted in Figure 13a. The reason for this is that at increasing depths the laser gets out of focus with the glass surface making cutting less

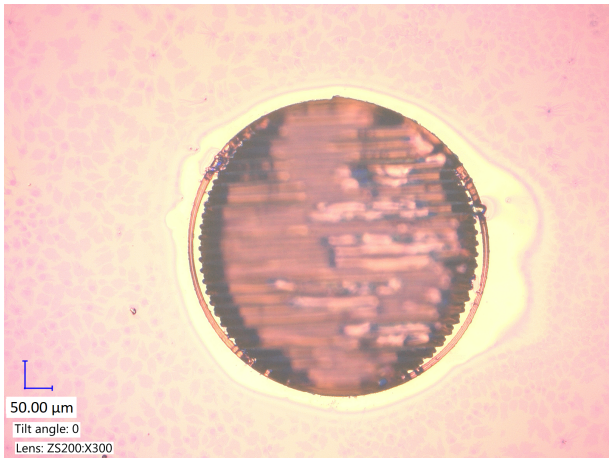

Fig. 14: An exemplary cut at a high focal point velocity $(400mm/s)$, which resulted in residual material, in yellow, being left behind within the perimeter.

efficient. Therefore, it is more beneficial to program a step-wise machining operation, lowering the z-stage periodically to accommodate the optimal distance for the laser to focus on the machined surface. In practice, the software accompanying the femtosecond laser makes this tasks tedious and time consuming.

For the focal point velocity of the laser a similar depth analysis is performed, whereby the number of repetitions is set and the speed is varied. This does result in different machining times, since the slower cutting speed will take up more time. To determine the depth of a cut within equal time frames, a coefficient is established to standardise machining time. The coefficient consists of the laser focal point velocity divided by 50, the coefficient standardises the time for the recipe to finish a $50mm/s$ cut. So for $100mm/s$ this coefficient is two. This because you can perform the recipe of the $50mm/s$ two times in the same time frame. The results are depicted in Figure 13b. From this data, it is evident that, in terms of time efficiency, faster focal point velocities are more favourable. Yet in practice with these speeds the hatching profile becomes inaccurate, as portrayed in Figure 14. The figure shows that some material remains within the cutting perimeter.

The final depth characterisation is made on the percentage of power that relates to certain depth of the cut. In Figure 12b, the obvious correlation between more energy and greater depth is shown. The main takeaway message from these results are that the increase of power does not linearly increase the depth.

B. Intermediate Conclusions

To conclude on fabrication characterisation, the focal point velocity that is to be utilised is limited within $500mm/s$ to maintain a circular profile. But for hatching smaller details, this limit is further decreased to $100mm/s$ or below. For power transmission on the lower side of the tested data points, reproducibility is most accurate, and edge roughness is minimised. Therefore, the power used to manufacture is 3%, this choice is made over the 2% power usage. Since the loss in accuracy and the increased roughness are minimal, the decreased time required allows for a glass slide to be fabricated

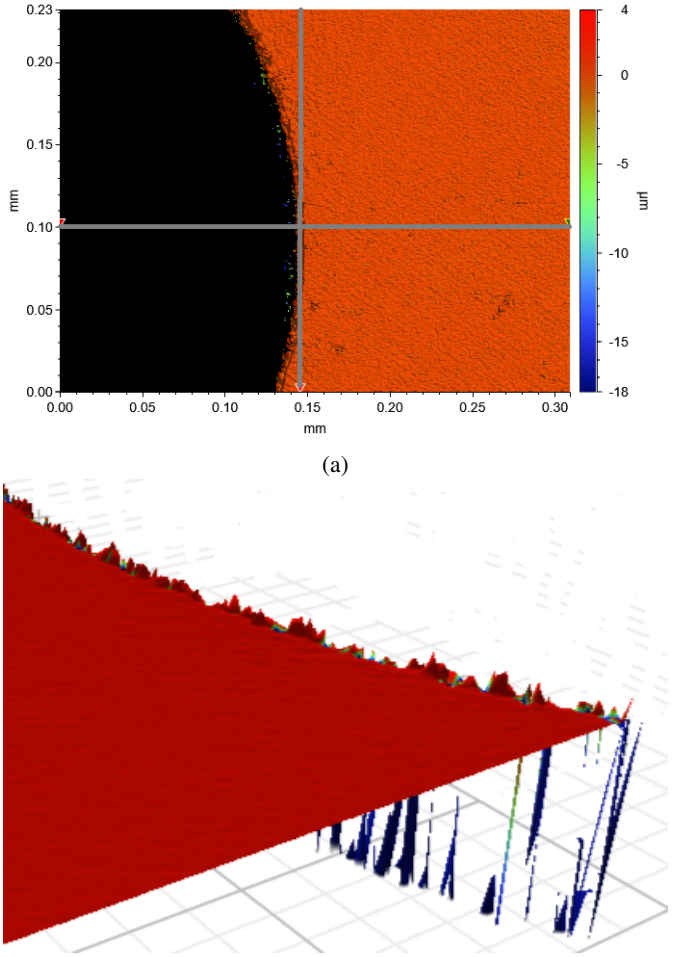

(a)

(b)

Fig. 15: White light interferometry results, (a) a top view of an arbitrary hole with a surface profile heat map. (b) Isometric view zoomed in at the edge of the cut surface.

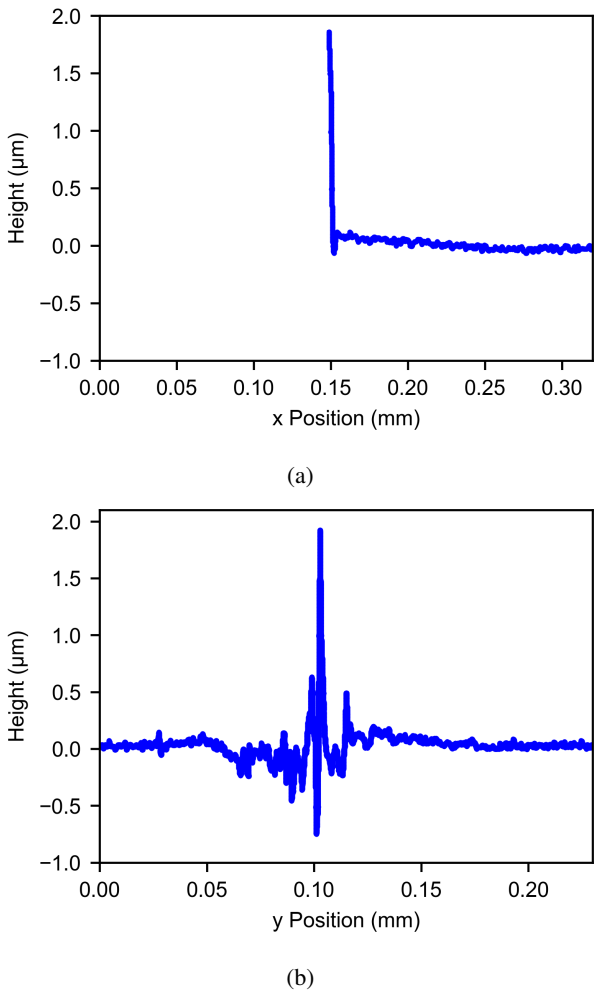

(a)

(b)

Fig. 16: Out of plane surface profile deducted from the grey axis depicted in Figure 15a. (a) Height profile over the x-axis. (b) Height profile over the y-axis.

within 10 hours, fitting within a day of available laser time. The programming used to set up the laser machining job is also optimised, by setting multi-step cuts with each step containing 50 repetitions, again to optimise time usage during fabrication.

At the start of the optimisation steps, an additional observation was made regarding the area where accurate cuts were still being achieved. During the optimisation process, a row of 10 different circles were created, each spaced 5 mm apart. It was observed that the last two objects did not accurately reflect their intended geometries. This led to the conclusion that the telecentric lens limits the effective cutting area to a radius of 40 mm from the center. To address this, the Aerotech stage, which moves the substrate, can be translated to reposition the laser's focal point to a different location on the substrate.

V. Results

A. *Surface Profilometry and Roughness Measurements*

Using white light interferometry, a detailed surface profile can be mapped around the edge of an inlet. These images have been obtained by scanning for an interference pattern of a narrow green band of light with a depth of focus of $25\mu m$. Various bands of light were empirically tested; but, due to the transparency of the glass, most wavelengths failed to produce an interference pattern, with the only exception being a narrow green band of light that successfully produced an interference pattern.Figure 15a depicts a representative sample from a series of measurements, from the surface profile around an edge on the glass. The figure presents a top view heat map of the surface of the material. Although the surface appears to be of a nearly uniform orange color, variations in the height profile are present. These variations are examined on two-dimensional planes aligned with the x- and y-axes, as illustrated in Figure 15a. These planes serve as the x-axis for two graphs that depict the height profiles. Figure 16a presents the surface profile for the horizontal grey axis in Figure 15a. Imagine slicing the image along the grey axis and then displaying the resulting side view. Figure 16b illustrates the surface profile of the vertical grey line. At the intersection of the x and y axis an extreme is found in the surface profile, indicating a peak in the material. Plotting the profiles into a 3D perspective results in Figure 15b.

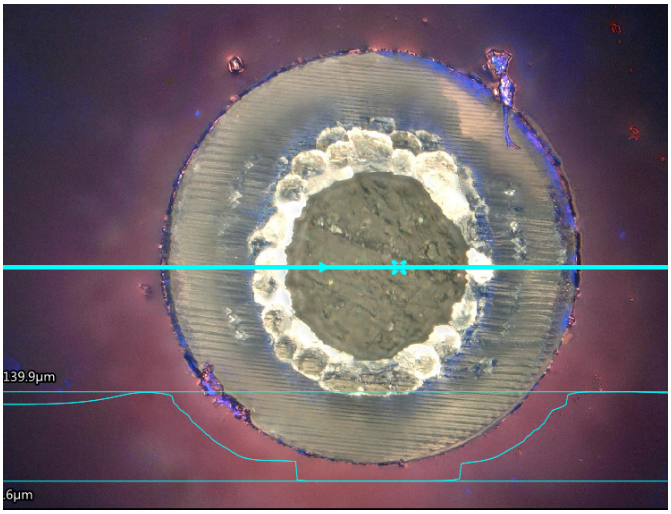

(a)

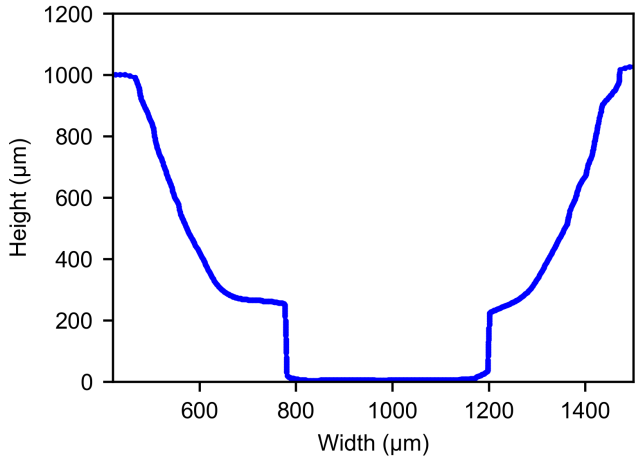

(b)

Fig. 17: (a) Top view of final inlet morphology, captured with a purple ink layer for better definition for the depth profile of the glass. The debris seen around the perimeter of the cut are fibers from the stylus used to coat the surface. (b) Section side view of the final inlet graphed in respect of width to height, deducted from the blue axis on Figure 17a.

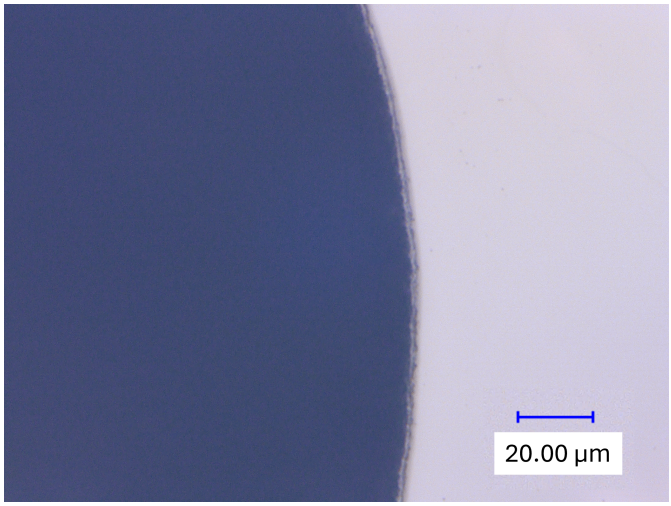

(a)

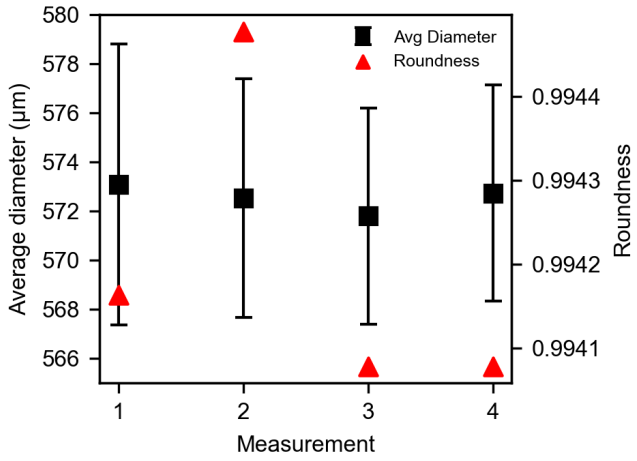

(b)

Fig. 18: (a) Small depth of focus black and white image of the edge of the inlet on the side of the channel. (b) A graph of the exact dimensions of the inlet that is facing the channel, the designed hole diameter is $550\mu m$.

B. Morphological Characterisation of Fabricated Device

The final inlet morphology can be viewed in Figure 17a. This image represents the profile of the full inlet including a blind hole and a through hole. The intended depth of the blind hole is designed to be $300\mu m$, the section side view depicted in figure 17b represents the true dimensions of the fabricated holes. The designed blind hole depth is quite well fabricated to specification, yet not exact since the femtosecond laser that is used does not have any measurement components to measure what has been machined. Additionally, the blind hole features tapered side walls, which were intended to be straight in the initial design.

Another significant characteristic, seen in Figure 17a, is the presence of bubble-like spots surrounding the perimeter of the through hole, resulting from melted droplets of material that flattened and solidified. These spots originate from the fabrication procedure, where a blind hole is first created, then the glass slide is flipped, and the through hole is machined. The final edge at the end of the machining direction inherently suffers from this phenomenon. While the material can be cleaned with post-processing steps, these require significant precision and time and pose an additional risk of breaking the material. The melt bubbles also interfere with the results of Figure 17b, making the through hole dimension appear significantly smaller than its intended $550\mu m$. Therefore, measurements are done on the side of the inlet facing the channel, which exhibits a clean edge definition, as seen in Figure 18a. Figure 18b plots the exact values of the hole characteristics, showing a sharp edge definition with a roundness of 0.9942 and an average diameter of $572.538\mu m$, with a standard deviation of $4.852\mu m$. Compared to the CAD and machining scripts, the average diameters of the inlets are about $25\mu m$ oversize.

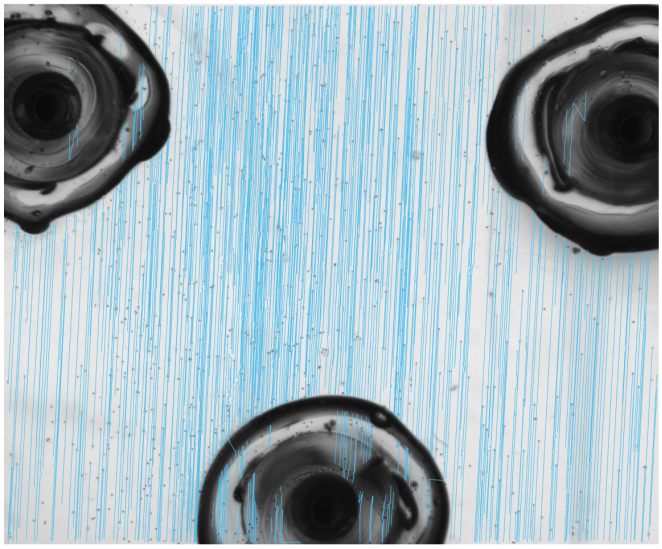

(a)

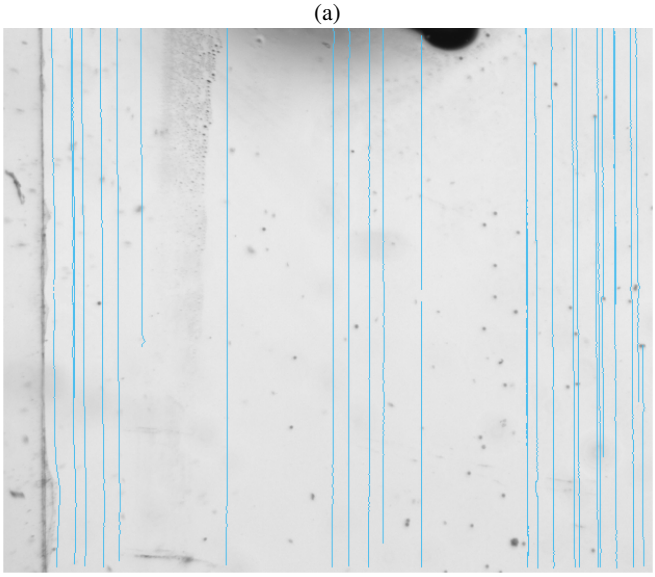

(b)

Fig. 19: (a) Streamlines of particles representing the direction of the uniform flow field, aimed at the three inlets in the center of the chip. (b) Streamlines of particles representing the direction of the uniform flow field, focusing on the boundary of the channel.

C. Flow Visualisation Results

For the analysis of the flow field the recordings of the particle solution are processed to display their trajectory within the flow. These trajectories are then either compared to each other or a theoretical equivalent. This provides insight into the characteristics and performance of the flow field in the microfluidic chip. However, due to the limitations of image processing, some of the trajectories are not very smooth. Additionally, particles within the black inlet regions are difficult to identify, which accounts for some of the random trajectories observed in those areas.

1) Uniform Flow Field: The uniform flow field is an elementary flow that is characterised by parallel streamlines

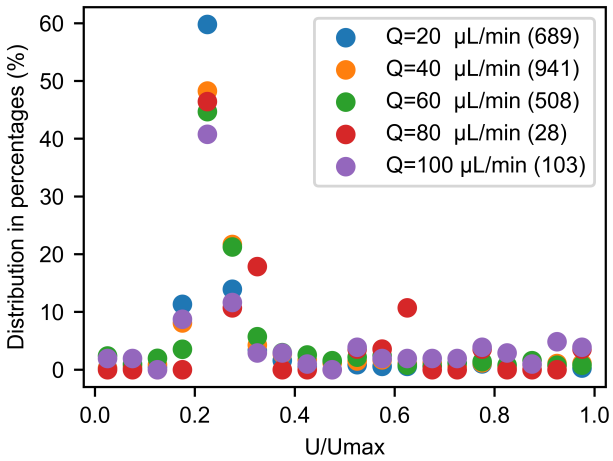

Fig. 20: Distribution of particles with specific flow velocities measured at different flowrates. On the x axis the velocity of the particle is compared to the theoretical maximum. The y-axis represents the percentage of particles that are present in each velocity fraction. The legend displays the total amount of data points and the flowrate at which they were obtained.

when the flow is fully developed. The experiment performed to validate the uniform flow field, makes use of only activating inlet 1, also referred to as the uniform inlet. The camera is focused on the center of the chip, with the full height of the chip in focus. A result of such an experiment is displayed in figure 19a. Additional experiments were conducted focusing on the uniform flow field near a physical boundary. Such a case is shown in figure 19b, In theory the Hele-Shaw condition is not valid within approximately one height from the boundary. This experiment aims to see whether the streamline is straight and parallel even close the wall. It is noteworthy that in the background image some particles are visible yet they do not have a streamline associated to them. This is due to the particle not moving over the recording. These particles are stuck to the surface of the glass yet they remain in the background image. A notable observation here is that a contamination in the form of a fiber is deviating the streamline of the particle closest to the wall. This can be viewed in the lower part of the image.

The second set of results obtained from the uniform flow field experiments compares the velocity distribution of the measured particles, over the height of the channel. The measured velocities are compared to the theoretical maximum velocity in the Poiseuille flow profile. The results of these measurements can be used to find a height preference of the particles on the Poissuelle velocity profile. Five different experiments have been performed each with a different flow rate for the uniform flow field. Resulting in Figure 20, that displays, on the x-axis the particle velocity (u) compared to the computed maximum flow velocity (u_{max}), each dot represents a range of particles that are contained in a $0.05U/U_{max}$ region. For example, particles in the range of 0.0 - 0.05 U/U_{max} are represented by the dot that falls in that region. The y-axis represents the percentage of the total observed particles corresponding to specific velocities. It can be observed that particles tend to

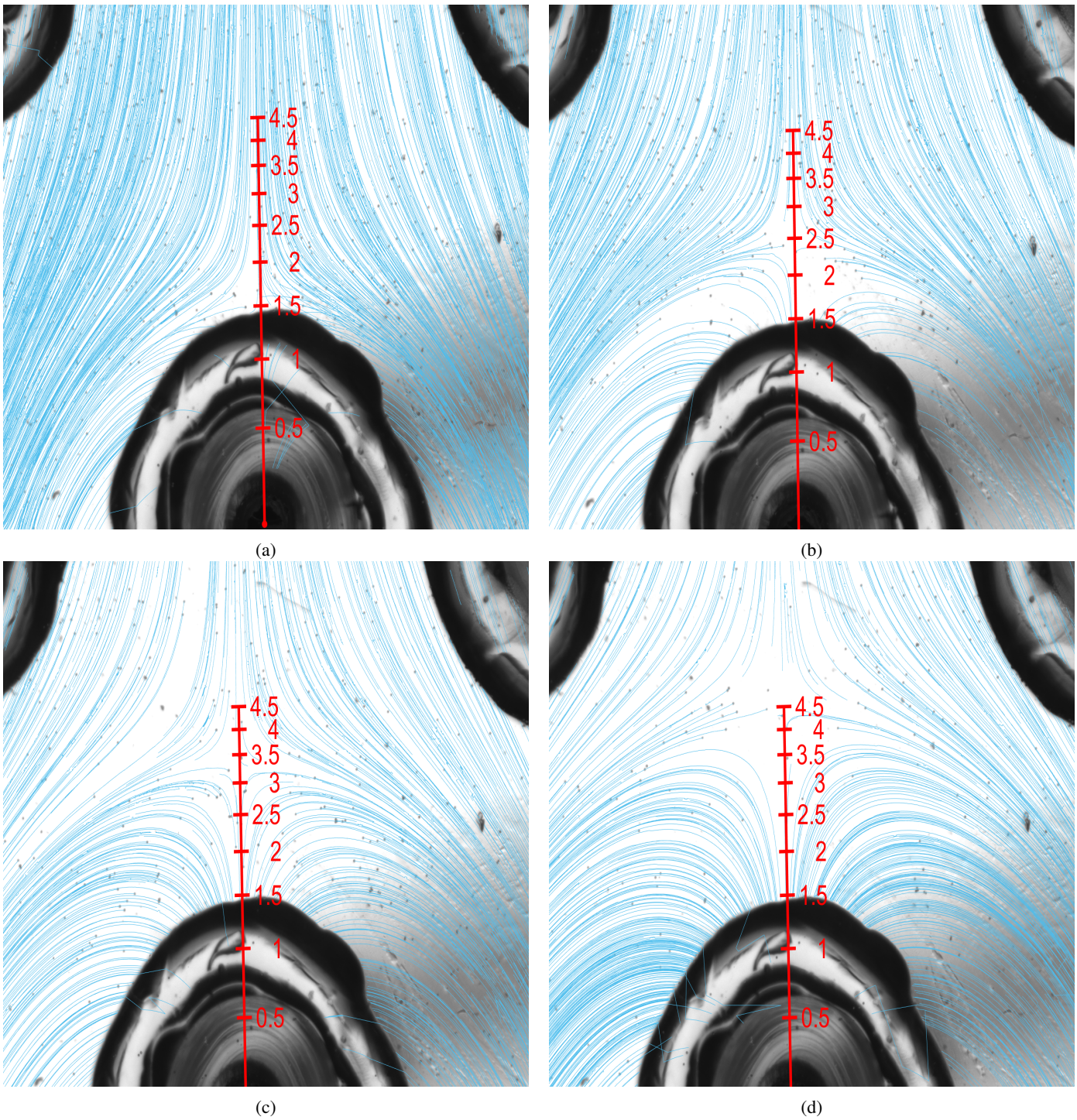

Fig. 21: Four representations of different half Rankine bodies consisting of different ratios of uniform flow and source. Each image includes a ruler that depicts the position of the stagnation point on theoretical basis, determined by the strengths of the uniform flow field and the source. (a) Half Rankine body with the uniform flow rate set to $20\mu L/min$ and the source $30\mu L/min$, resulting in a ratio of 2:3. (b) The flow profile of a uniform flow rate of $20\mu L/min$ and a source of $40\mu L/min$, with a ratio of 1:2. (c) Flow field with the uniform flow rate $20\mu L/min$ and a source flow rate of $60\mu L/min$, with a ratios of 1:3. (d) Half Rankine body with a uniform flow rate of $20\mu L/min$ and a source strength of $80\mu L/min$, resulting in a ratio of 1:4.

occupy a preferred position on the Poiseuille velocity profile, where the velocity is 20-25 % of the maximum, with the highest concentration of particles found at this location.

2) Half Rankine Body: To determine the characteristics of the outflow near the edges of the inlet, experiments focused on forming half Rankine bodies are performed. Uniform and symmetric outflow of fluid suggests a clean source while large asymmetries and deviations from a blunt body indicate a lack of roundness. Four half Rankine body experiments are presented in figure 21. Integrated into these images are visual rulers used to identify the position of the stagnation point relative to the theoretical stagnation point. The rulers are arranged to indicate the positions of the stagnation points, referenced to the ratios of flow rate between the uniform flow and the flow from the source. If the flow rate of the uniform flow and the source are equal, the stagnation point should be positioned at the marking for one. Additionally, the number of particles that have been recorded are depicted in the label of the graph. Using the panel method, the dimensions for the indicators are determined and implemented into the figures. Unfortunately, no clear method of determining symmetry has been derived before publication, therefore the only quantitative value of verification for the half Rankine body is the distance to the stagnation point.

The four measurements shown in Figure 21 were conducted at the following flow rates: for the uniform flow, all experiments maintained a consistent flow rate of $Q_{uni} = 20\mu L/min$. The source strengths were, for 21a, $Q_{source} = 30\mu L/min$; for 21b, $Q_{source} = 40\mu L/min$; for 21c, $Q_{source} = 60\mu L/min$; and for 21d, $Q_{source} = 80\mu L/min$. Respectively the ratios between these flow rates are 1:1.5, 1:2, 1:3, and 1:4. Subsequently, the theoretical markings of ratios seen on the red scale bars are compared to the stagnation points in the flow. What can be observed is that the theoretical points of stagnation and the real point do not overlap.

D. Pump Response

To verify the real flow rates that get transmitted to the chip additional experiments were formulated. Seen in Figure 4 is a reservoir that is located behind the flow sensor. Even though mass is conserved, this reservoir could alter the behaviour of the flow rate trough the system. The experiments were performed as following; first, a specific flow rate is set without using the subsequent reservoirs. Then, measurements were taken to compare the flow sensor data to the true mass that was ejected over a 10 minute period. Afterwards, the experiments were repeated but this time including the reservoirs. The data is depicted in Figures 22a & 22b, and gives insight into the real flow rates that are present in the system, and their relation to the desired flow rate. Determining the actual flow rate ratios yielded the following results: 1:2.42 for Figure 21b, 1:3.51 for Figure 21c, and 1:4.51 for Figure 21d. Accounting for measurement errors, these ratios align closely with the experimental data, indicating that the stagnation points observed correspond well with the theoretical predictions.

E. Alternative Flow Profiles

To demonstrate the reprogrammability of the flow field, two experiments were conducted, each showcasing different

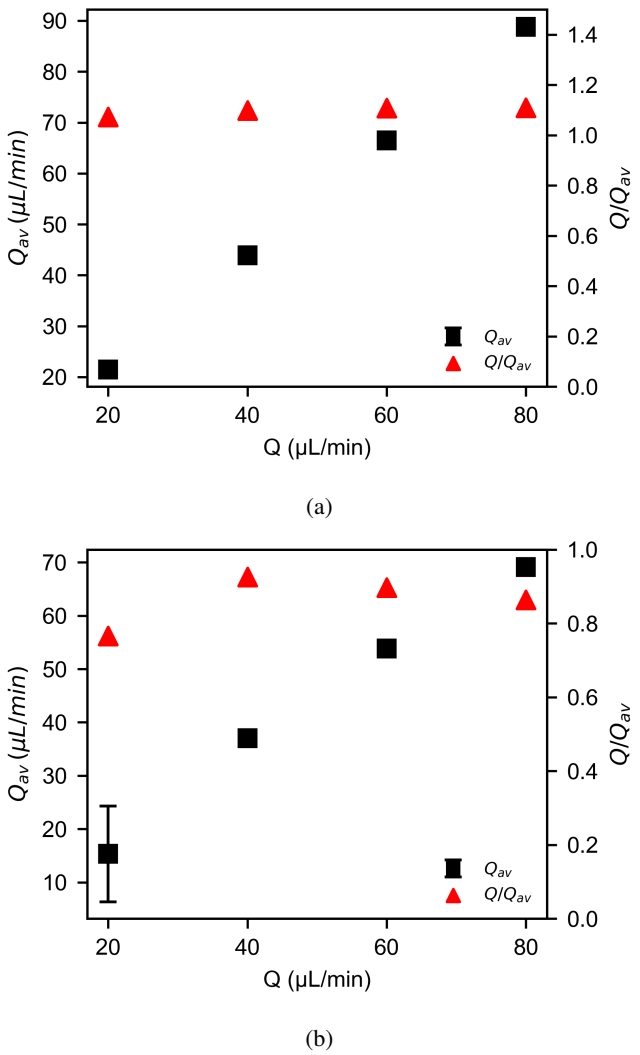

Fig. 22: Real measured flow rates deducted from mass measurements. (a) Flow rates without additional reservoirs, (b) Flow rates including the subsequent particle reservoirs.

flow configurations. These experiments involved introducing a second source or sink alongside the uniform flow field. The flow field shown in Figure 23a represents a physical approximation of the theoretical model illustrated in Figure 6c, though only a portion of it was captured within the camera's field of view. A similar comparison is made between Figures 23b and 6d, with the key difference being the presence of a sink rather than a source.

VI. Discussion

The primary goal of this study was to design and fabricate a programmable microfluidic device capable of hydrodynamically manipulating particles, cells, and fluids within a reconfigurable flow field. Though time limitations and complexities resulted in the readjustment of goals of the project to deliver a well characterised template that is likely to be able to perform said functions in the future. The experimental findings for characterisation indicate several key insights.

For fabrication, it is important to emphasise a stepwise approach for cutting into depth. Not lowering the focal point

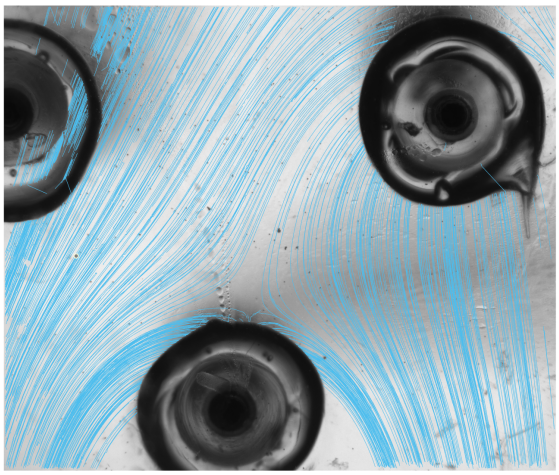

(a)

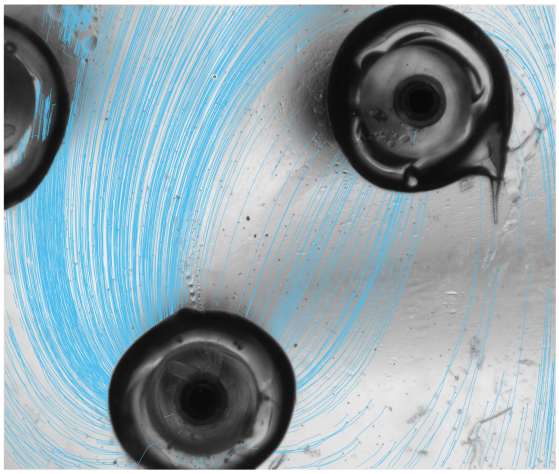

(b)

Fig. 23: Flow profiles representing the panel method models, (a) Partial image of a physical representation of Figure 6c, where two sources are active in a uniform flow. (b) Partial image of a physical representation of Figure 6d, depicting the interaction of an active source and sink within an uniform flow.

of the laser to the correct surface height results in significant limitations on the ability to machine down any material.

For optimal surface finish, the lowest energy settings are most favorable, as they introduce minimal thermal shock, thereby reducing the formation and size of burrs around the cut perimeter. However, the drawback of using low power is that it removes less material per pass, which consequently extends the duration of the machining process. Considering these factors, the most favorable setting for this project is 3% of the full 15 Watts of power from the source. This also determines the dimension used for the hatching profile, which is ideal when there is a 50% overlap with the subsiding cuts. Therefore the hatching distance is set to half the width of the cut resulting in a $5\mu m$ distance.

The focal point velocity of the laser also plays a significant role in acquiring a well defined geometry. A high velocity means that the machining operation will take less time, but it will result in inaccuracies with respect to the perimeter. At the small scale ($< 1mm$), the use of laser focal point velocities that reach over $100mm/s$ leads to material being left inside the designed perimeter. Thus, to achieve well defined inlets at this scale, the velocity is to be set to $50mm/s$.

However, white light interferometry reveals that the fabrication process produces an edge profile with a $2\mu m$ ridge along its perimeter. Even though this is small compared to the other dimensions, this could pose as a nesting location for bubbles. The second insight that was acquired by the white light interferometry, is that the surrounding glass surface did not suffer from any deformation or splashing surface debris.

The morphological imaging of the final inlets reveals a straight, parallel profile relative to the through hole, with excellent edge detailing an essential feature for this project. In contrast, the blind hole exhibits a tapered profile due to debris accumulation. During machining, debris tends to collect in the bottom corners, obstructing the light for subsequent laser passes. This results in a stacking issue, where each pass encounters increasing material buildup, leading to tapered sides. Despite this, maintaining an appropriate tolerance for a 20-gauge syringe ensures that the alignment operation remains unaffected.

Regarding the flow field results, the uniform flow field when fully developed is very unidirectional, except for some processing errors that occur around the inlets where the Tygon collars block the light. This is a characteristic of laminar flow, which is something to be expected in microfluidics. The distribution of particles within the flow tends to follow a specific bias, occurring at the height where the parabolic flow profile reaches 20-25 % of the maximum velocity. The exact height position of the particles is currently unknown. To determine a more accurate position, an experiment could be conducted using a high-magnification objective to capture recordings. By adjusting the height of the objective to achieve precise focus, the velocity profile of the particles can be measured, leading to a clearer and more definitive understanding of their positions within the flow. Different studies have explored the position of particles within a flow field, revealing that particle distributions are determined by the particles reaching an equilibrium position due to the influence of two opposing forces, that are exerted on a neutrally buoyant particle moving along a straight channel [23]. An asymmetry in the wake vorticity generates a force that pushes the particles away from the wall, while an opposing force, known as the shear gradient lift force, arises from the curvature of the parabolic velocity profile. According to literature, under conditions of small Reynolds numbers, the equilibrium position to which particles migrate is typically located around $r = 0.62R$ [24]. This value can vary slightly depending on the Reynolds number. The designed channel, with the targeted flow velocities, exhibits a Reynolds number in the range of 10^{-1}, therefore the theory might be applicable. Yet, this requires more research with a method of visualising true particle depth.

The formation of the half Rankine bodies confirms the ability of the device to form stagnation points that can be

used to trap particles. The flow fields appear to be quite symmetric, however, this will require future image processing to verify the interface of where the source and the uniform flow field interact. At first glance, the dimensions of the Rankine half-body do not correspond to the flow rate ratios used to capture the images. This discrepancy raises concerns about the accuracy of the flow rates generated by the pressure pump setup. Therefore, additional experiments were performed to verify the digital readouts. The experimental data demonstrated that the digital readout from the flow sensor does not accurately represent the true flow rates when a reservoir is positioned downstream. A potential reason could be the layer of air present in the reservoir. During flow experiments, we found that this layer has an equilibrium position that is reached after some time.

When the new ratios are calculated from the experimental data on flow rates, we can conclude that the ratios from the half Rankine bodies are within a margin, correct, confirming the ability of the chip to approximate theoretical models, on the basis of stagnation point position. Additionally, the results from the alternative flow profiles, show the potential of reconfiguring the flow field in real time. These findings support the claim made in the title about the chip's programmable capabilities.

This study builds upon previous research in microfluidic device fabrication and flow manipulation, particularly the work by A. Kislaya. The advancements made in this study are in general all fabrication based, where the fabrication and assembly technique led to better defined inlets and at higher precision in respect to positioning. Also, the use of glass significantly improved transparency in comparison to the resin printed flow cells.

Potential future improvements include further refinement of laser ablation parameters. This could reduce fabrication time while maintaining or improving edge quality. This could be done by further improving on programmed laser operations, such as taking smaller steps, but also explore and vary more complex laser parameters such as burst time, or a change to a different wavelength of light. Another improvement can be made on the interface between the external system and the glass. The initial performance of the Tygon™collars following bonding was generally satisfactory. However, their long-term reliability proved to be suboptimal. This would require time consuming repair with the additional hazard of contaminating the channel with glue residuals. These turned out to be extremely difficult to remove. Due to the unbreakable nature of the glass-PDMS-glass bond without causing glass fracture and the glue's significant resistance to strong organic solvents like acetone, the only feasible solution was to utilise a laser to evaporate the material behind the glass. This process frequently resulted in a scorch mark within the channel. The collars could also harbour air bubbles within the adhesive, these would occasionally release during experiments thereby failing the experiments.

An additional alteration could be made to be able to alter the design in such a way that only one side is bonded. During experiments occasionally debris in the form of fibers or particles would enter the chip. Having only one side bonded would allow for the disassembly to open up the channel. This approach allows the channel to be effectively cleaned of contaminants. However, it necessitates a form of clamping that complicates the chip's airtightness. Nonetheless, achieving a reliable seal can significantly enhance the chip's durability.

The future goal for the device is to serve as a platform for active particle manipulation by dynamically altering the flow field in real time. Specifically, it is intended to study motile algae in suspension, with the aim of controlling their position or constraining them to a specific frame of reference, such as the field of view of a camera. The chip can also be used for experiments on the behaviour of visco-elastic fluids. Viscoelastic fluids display complex flow behaviors, such as shear thinning, shear thickening, and normal stress differences. And more research is required to better define the behaviours. The chip can provide a good platform for fluid control for such studies.

VII. Conclusion

The principles of hydrodynamically driven microfluidics have been effectively demonstrated through the design and fabrication of a programmable microfluidic device. This study utilised advanced microfabrication techniques, including femtosecond laser ablation and cold oxygen plasma bonding, to achieve high-precision microfluidic channels with smooth edges and minimal roughness. The experimental findings provide several key insights into the fabrication and functionality of the device.

The successful creation of a uniform flow field and half Rankine bodies validates the device's capability to create elementary flow structures. Additionally, the device proved its ability to change the flow field in real time to create more complex flow structures, showcasing the potential for controlling particle trajectories within the flow field and opening up possibilities for a wide range of applications.

Furthermore, the detailed characterisation of laser ablation parameters provide a solid foundation for future glass structure- and microfluidic device fabrication. The advancements made in this study pave the way for the development of new sorts of custom made microfluidic devices with high precision. These devices hold the potential to improve various designs in different fields by providing more precise, and structurally stiffer platforms for microfluidic applications.

The insights gained into particle distribution within the flow and the formation of stagnation points offer valuable information for optimising the device's performance in future applications. The ability to manipulate particles and fluids with high precision in real time can lead to significant advancements in areas such as single-cell analysis, organs-on-chips, pollutant detection, and nanoparticle synthesis.

Future research should focus on optimising the fabrication techniques to further reduce production time while maintaining or improving edge quality. Exploring more complex laser parameters and alternative materials could enhance the device's performance. Additionally, integrating a real-time control system will be a crucial step in advancing particle manipulation on this microfluidic chip.

Developing robust and reliable interfaces between the microfluidic chip and external systems will also be essential for

long-term usability and integration into various applications. Finally, further studies on particle behavior within the flow fields, including detailed visualisation of particle depth and interactions, will provide deeper insights into the mechanisms driving particle manipulation in microfluidic devices. These efforts will contribute to the creation of multifunctional platforms that can be tailored to specific research needs without the necessity of developing dedicated microfluidic devices for each study.

REFERENCES

[1] A. Kislaya, "Particle Manipulation-on-chip Using programmable hydrodynamic forcing in a closed loop Publication date 2022 Document Version Final published version Citation (APA) Kislaya, A. (2022). Particle Manipulation-on-chip: Using programmable hydrodynamic forcing in a closed loop," *Delft Institutional Repository*, 2022.

[2] A. Escobar, A. Diab-Liu, K. Bosland, and C. Q. Xu, "Microfluidic Device-Based Virus Detection and Quantification in Future Diagnostic Research: Lessons from the COVID-19 Pandemic," 10 2023.

[3] A. H. Hamad, "Effects of Different Laser Pulse Regimes (Nanosecond, Picosecond and Femtosecond) on the Ablation of Materials for Production of Nanoparticles in Liquid Solution," in *High Energy and Short Pulse Lasers*, InTech, 9 2016.

[4] S. N. Bhatia and D. E. Ingber, "Microfluidic organs-on-chips," 2014.

[5] P. Aryal, C. Hefner, B. Martinez, and C. S. Henry, "Microfluidics in environmental analysis: advancements, challenges, and future prospects for rapid and efficient monitoring," 1 2024.

[6] S. A. Khan, A. Günther, M. A. Schmidt, and K. F. Jensen, "Microfluidic synthesis of colloidal silica," *Langmuir*, vol. 20, pp. 8604–8611, 9 2004.

[7] T. Krebs, C. P. G. H. Schroen, and . R. M. Boom, "A microfluidic study of oil-water separation kinetics," *WIT Transactions on Engineering Sciences*, 2012.

[8] A. A. S. Bhagat, S. S. Kuntaegowdanahalli, and I. Papautsky, "Continuous particle separation in spiral microchannels using dean flows and differential migration," *Lab on a Chip*, vol. 8, no. 11, pp. 1906–1914, 2008.

[9] J. Nilsson, M. Evander, B. Hammarström, and T. Laurell, "Review of cell and particle trapping in microfluidic systems," 9 2009.

[10] S. Zhang, Y. Wang, P. Onck, and J. den Toonder, "A concise review of microfluidic particle manipulation methods," 4 2020.

[11] D. Kumar, A. Shenoy, J. Deutsch, and C. M. Schroeder, "Automation and flow control for particle manipulation," 9 2020.

[12] B. Cardenas-Benitez, B. Jind, R. C. Gallo-Villanueva, S. O. Martinez-Chapa, B. H. Lapizco-Encinas, and V. H. Perez-Gonzalez, "Direct Current Electrokinetic Particle Trapping in Insulator-Based Microfluidics: Theory and Experiments," *Analytical Chemistry*, vol. 92, pp. 12871–12879, 10 2020.

[13] A. Lenshof and T. Laurell, "Continuous separation of cells and particles in microfluidic systems," *Chemical Society Reviews*, vol. 39, pp. 1203–1217, 2 2010.

[14] A. Van Reenen, A. M. De Jong, J. M. Den Toonder, and M. W. Prins, "Integrated lab-on-chip biosensing systems based on magnetic particle actuation-a comprehensive review," 6 2014.

[15] G. Taylor, "Stability of a viscous liquid contained between two rotating cylinders," *Philosophical Transactions of the Royal Society of London. Series A, Containing Papers of a Mathematical or Physical Character*, vol. 223, pp. 289–343, 1 1923.

[16] R. R. Lagnado, N. Phan-Thien, and L. G. Leal, "The stability of two-dimensional linear flows," *Physics of Fluids*, vol. 27, no. 5, pp. 1094–1101, 1984.

[17] M. Tanyeri and C. M. Schroeder, "Manipulation and confinement of single particles using fluid flow," *Nano Letters*, vol. 13, pp. 2357–2364, 6 2013.

[18] Y. Zhou, K. W. Hsiao, K. E. Regan, D. Kong, G. B. McKenna, R. M. Robertson-Anderson, and C. M. Schroeder, "Effect of molecular architecture on ring polymer dynamics in semidilute linear polymer solutions," *Nature Communications*, vol. 10, 12 2019.

[19] D. P. Taylor and G. V. Kaigala, "Reconfigurable microfluidics: real-time shaping of virtual channels through hydrodynamic forces," *Lab on a Chip*, vol. 20, no. 10, pp. 1720–1728, 2020.

[20] P. K. Kundu, I. M. Cohen, and D. R. Dowling, *Fluid mechanics.* Elsevlier, 2016.

[21] D. Li, L. Song, C. Zhang, L. Yu, and X. Xuan, "A depth-averaged model for Newtonian fluid flows in shallow microchannels," *Physics of Fluids*, vol. 33, 1 2021.

[22] A. Tony, I. Badea, C. Yang, Y. Liu, K. Wang, S. M. Yang, and W. Zhang, "A Preliminary Experimental Study of Polydimethylsiloxane (PDMS)-To-PDMS Bonding Using Oxygen Plasma Treatment Incorporating Isopropyl Alcohol," *Polymers*, vol. 15, 2 2023.

[23] A. Karimi, S. Yazdi, and A. M. Ardekani, "Hydrodynamic mechanisms of cell and particle trapping in microfluidics," *Biomicrofluidics*, vol. 7, 4 2013.

[24] J. P. Matas, J. F. Morris, and E. Guazzelli, "Lateral Forces on a Sphere Solid/Liquid Dispersions in Drilling and Production Fluides chargés en forage et production pétrolière," *Revue d'IFP Energies nouvelles*, vol. 59, no. 1, pp. 59–70, 2004.

Appendix

A Self Reflection

During the course of my master's thesis, I developed valuable research skills, as it was the first time I had to thoroughly explore a substantial body of literature. I discovered a growing interest in the dynamics at smaller scales, and when combined with my fascination with fluid mechanics, it deepened my intellectual curiosity in this field. I also gained valuable skills and knowledge in using a laser ablation system through the extensive time I dedicated to operating the machine. This significant time commitment led the lab technician to impose a weekly time limit on my use of the machine. Additionally, I became familiar with the Python environment; before my thesis, I had used every opportunity to avoid learning any coding language. Image processing required me to familiarize myself with Python, and now I feel a sense of accomplishment in adding this to my repertoire of skills. The project also taught me an invaluable lesson in problem-solving in experimental science. Rigorous failed experiments and experimental hardships proved to me that patience is key to obtaining good results.

The project has been a collaboration between Ning Ji and me. Ning has been an excellent partner throughout this endeavor; his skills in coding and fluid dynamics, along with his overall hard work, were instrumental in achieving the project's successful results. In general, he also made the days we spent on experiments significantly more enjoyable.

Another skill I have developed is the ability to adapt to the circumstances that a project presents. From the outset, we knew this would be an ambitious undertaking with many challenges. The project required developing expertise in micro-manufacturing, experimentation, fluid mechanics, and coding. However, combining all these tasks proved to be too time-consuming, necessitating a shift in the project's approach. Consequently, it evolved into a collaborative effort, with my focus shifting primarily to fabrication. At the start of the practical part of the project, I overestimated the ease of manufacturing glass using a laser system. I initially assumed that operating a laser ablation machine would be similar to using an abrasion machine like a mill. However, the reality was more complex. An analogy I could make is that it was like machining with an unfamiliar material for which no comprehensive literature was available. Additionally, the operator who provided instructions on the machine did not fully understand all of its features. This led to a significant amount of time being spent on fabricating glass slides to achieve the desired accuracy, making it even more rewarding to achieve the desired finish on the microfluidic chip.

One area I believe needs improvement is the challenge of faulty bonds between the Tygon collars and the glass surface during experiments. Despite trying multiple glues and several epoxies, issues with leakages and breakages persisted. The final glue used has shown good performance in strength, but over time, some bonds tend to trap air bubbles in the glue. These air bubbles can sometimes release during experiments, leading to obstructions in the flow and, thereby, causing the experiment to fail. This proved to be frustrating, and I believe there is much room for improvement in the bonding process. An argument could be made to use standardized Luer connections, yet in my experience, these connections are bulky and hard to align. If I had more time on the project, I would focus on finding a solution to create a more reliable interface between the chip and the tubing.

An additional improvement could be made by addressing the issue of chip contamination by pollutants such as dust, fibers, or glue residues. To mitigate this, I would recommend conducting experiments in a cleaner environment, such as a clean room. If this is not feasible, another option could be to clamp one of the glass slides instead of bonding it. While this might introduce challenges in maintaining the chip's airtightness, it would significantly enhance the chip's durability. Regarding cleaning strategies, I initially used strong organic solvents like acetone. However, this often proved insufficient, leading me to resort to using the femtosecond laser to evaporate contaminants within the chip. Unfortunately, this approach resulted in dark scorch marks on the glass, which compromised its transparency.

Time management during my project was an area where I faced significant challenges. It has never been my strong suit, as during the pandemic, I developed a habit of procrastinating when there is no immediate incentive. However, compared to my theoretical years, I have improved my work ethic by starting tasks a bit earlier, yet this still does not fully suffice for projects of this scope.

Overall, I am satisfied with the results of this project. I would have liked to further prove the concept and use the chip for active particle manipulation. However, I have come to realize that this is a complex task that would likely require a significant amount of time to achieve. Nevertheless, I feel accomplished in having created something new and contributing to this field of research. This experience has sparked my curiosity and motivated me to consider continuing in academia.

As my final remarks, I would like to thank Ning for his hard work, his help and his priceless companionship during some frustrating experiments. Secondly, I Would like thank Daniel for his patience with me, his guidance and his valuable intellect in fluids and holding us to a high standard. Lastly, I would like to thank Murali for his guidance, his appreciation, and his endless knowledge in manufacturing.

A.1 Gentt Chart Review

At the end of my literature survey I constructed a Gentt chart to create a general time line for the project, see Figure 1. Yet quite early in the project we decided that i would shift my focus to specialise more in fabrication since the familiarisation to the fabrication process took significantly longer than expected. This due to the inherent properties of glass and the lack of information available on machining glass. Therefore phase 1 got stretched out over a longer time frame up until March/April. Over the entire period until June nine chips were made depicted in Appendic L. Additionally two monts of extra time was needed to yield good results regarding nicely processed images from experiments.

Phase two has been given to the project of Ning Ji, where system responses have been charachterized, and early implementations of particle manipulation still have to be performed.

Additional tasks that the Gennt chart is missing fabrication of subsystems and integrated parts. And obtaining experimental data for flow structures.

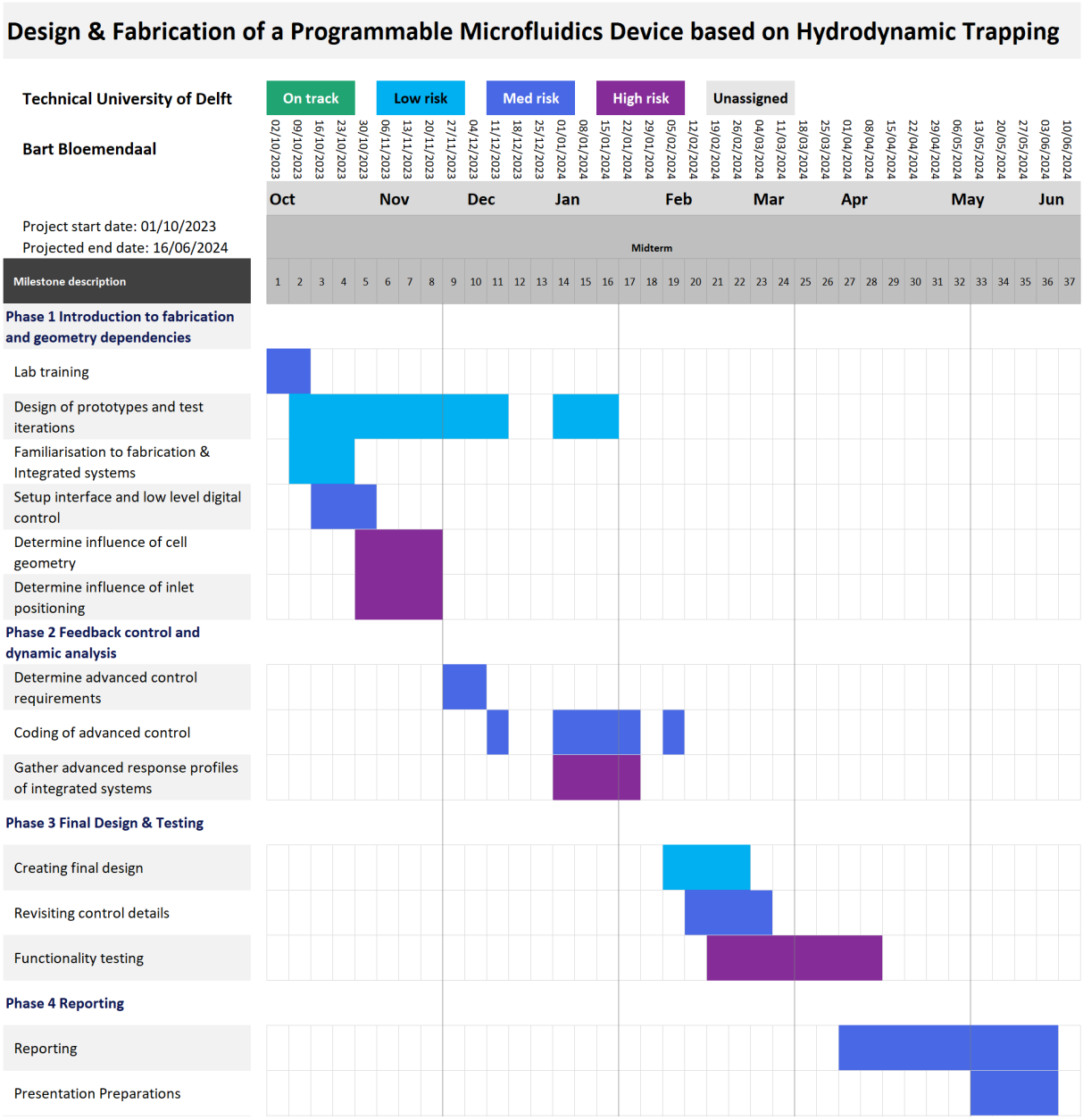

Figure 1: Gentt Chart

B Laser System Components

The Lasea Fs laser system is composed of several key components, each important for the precision and effectiveness of the laser ablation process. The list of vital components are:

- **Aerotech Stage:** Enables precise control of stage movement, providing accurate positioning for the laser area.
- **F-theta Lens:** Straightens the laser beam, ensuring it is perpendicular to the glass surface.
- **Mirrors:** Reflect the laser beam, aiming it at the desired location on the f-theta lens by rotation.
- **Pharos Laser Source:** Generates ultrashort laser pulses, greatly improving thermal dynamics on the substrate.
- **Camera:** Displays area of focus, that can be used to monitor the ablation process, and the cut perimeters.
- **Beam Expander:** An optical device used to increase the diameter of the laser beam.
- **Beam Splitter:** A beam splitter is an optical device used to divide a beam of light into two or more separate beams. A beam for both the camera and the laser.
- **Beam Shutter:** A beam shutter is an optical device used in laser systems and other optical setups to control the passage of a laser beam. It functions as a mechanical gate that can open or close to either allow or block the laser beam.
- **Beam Profiler:** Used to measure and analyze the spatial intensity distribution of a laser beam. It provides detailed information about the shape, size, and intensity profile of the beam.
- **Cooling System:** Maintains stable operating temperatures for the laser source, preventing overheating the system from overheating.
- **Bofa Fume Extractor:** A fume extraction unit connected to the laser cabinet. Through a movable nozzle within the cabinet, it extracts fumes and debris.

C Laser Parameters

The effectiveness of laser ablation depends highly on fine-tuning several critical parameters to the specific material and application. The significant parameters are:

- **Speed (mm/s):** The velocity of the laser focal point as it follows a designed perimeter.
- **Jump Speed (mm/s):** The velocity of the laser focal point when the source is blocked, used to skip discontinuous sections of the design perimeter.
- **Burst Rate:** The frequency at which pulses of laser energy are emitted in rapid succession.
- **Burst Time:** The duration over which a burst of pulses is emitted.
- **Repetitions:** The number of times the laser repeats the same pattern, impacting the depth and thoroughness of ablation.
- **Power:** The laser beam's power transmission, expressed as a percentage of a 15-watt source.
- **Hatching Pitch (mm):** The distance between adjacent hatching lines, crucial for surface removal using a patterned line approach.
- **Outlines and Outline Pitch (mm):** The number of additional outlines and the distance between them, which can achieve effects similar to hatching in certain shapes.
- **Layers:** The number of layers applied with a specified offset, also known as the layer pitch.

D Additional components

In addition to the systems associated with the femtosecond laser, several supplementary systems were employed: a general-purpose oven for heat treatment cycles, as shown in Figure 2; an ultrasonic bath for cleaning glass surfaces from debris, depicted in Figure 4; a piezo brush for activating PDMS and glass surfaces for plasma bonding, illustrated in Figure 5; and a lathe equipped with a 2 mm collet chuck for fabricating the Tygon collars, as seen in Figure 6. Another system includes a chemical fume booth, as shown in Figure 7, which is essential during the oxygen plasma bonding process due to the generation of ozone gas. The Keyence VHX digital microscope (Fig. 8), used to create the images of the fabricated results for image processing. The last two significant systems are the Nikon Eclipse Ti microscope (Fig. 9), which was used to obtain a view of the chip channels, and the sCMOS camera (PCO edge 5.5), shown in Figure 3, to which the microscope is connected.

Figure 2: General use oven

Figure 3: PCO edge 5.5

Figure 4: Ultrasonic bath

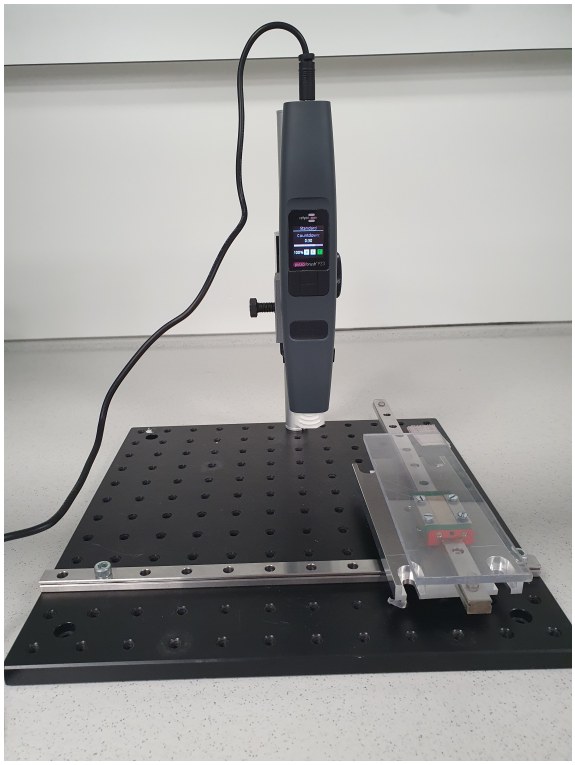

Figure 5: Piezobrush

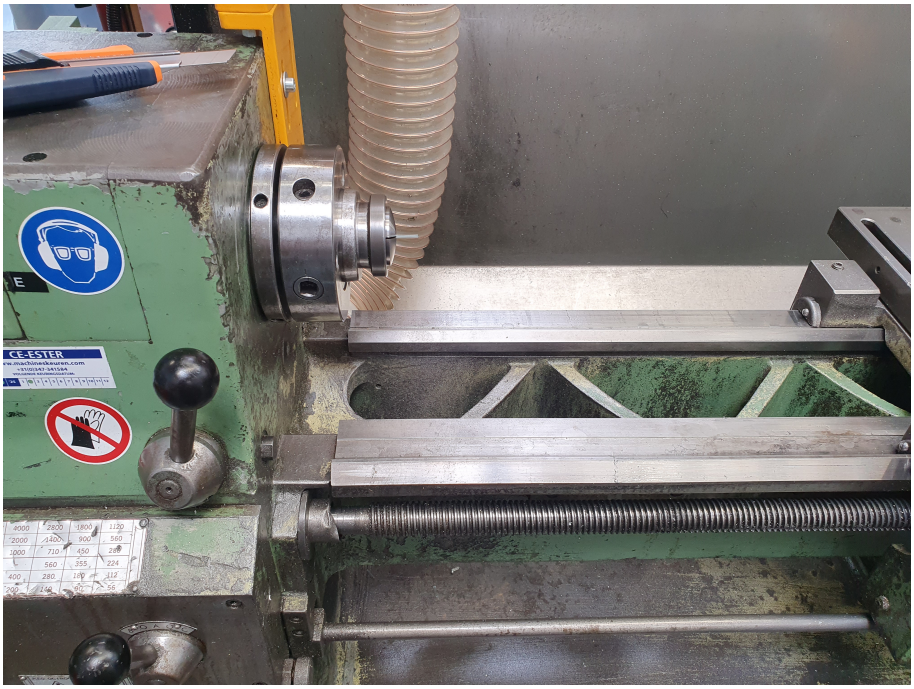

Figure 6: An image of a lathing machine including the Tygon tubing fixed into the collet chuck.

Figure 7: Fume booth

Figure 8: Keyence VHX700

Figure 9: Nikon microscope

E Fabrication Protocols

This appendix outlines the fabrication steps for the final chips using the 515 nm lens Lasea femtosecond laser setup. Additionally, it describes the fabrication process for the Tygon collar.

E.1 Laser Fabrication Protocol for Glass Slides

1. Begin the startup sequence for all software related to the laser system.
2. During the startup sequence, attach the custom-designed end stop/ceramic plate holder to the Aerotech stage. This end stop is designed to simplify the realignment of glass slides after the initial setup has been aligned. Lower the lens by 81.6 mm—this is the precise focus distance for the top surface of a glass slide using the end stop.
3. Ensure that you use clean microscopy slides with parallel sides and precise right angles at the corners. I recommend using Empredia Premium Plain Slides, as they have demonstrated good tolerances. Other glass slides I've tested were significantly less accurate and occasionally had sharp edges.
4. Place the glass slide against the end stop, and use the software's camera function to align the slide with the horizontal plane marker. To achieve precise alignment, gently twist the 3D-printed part. For easier adjustment, you can slide the part slightly backward along the guiding rails. Once the glass slide is parallel to the projected axis, mark the right bottom corner of the glass. Always use the right bottom corner since all scripts fabricate from right to left, and place your origin here.
5. Position the pressurized air nozzle and the fume nozzle close to the sample where the cut will be made. This ensures maximum debris removal during the process. Aim to place the pressurized air nozzle as perpendicular to the sample as possible for optimal debris clearance.
6. After alignment, place two markings as shown in Figure 10. The first marking has coordinates (-5, 12.5) mm relative to the right bottom corner. The second marking has coordinates (-70, 12.5) mm. These markings are essential for checking alignment during intermediate steps. Whenever the glass slide is removed and reinserted, always verify that both markings are properly aligned to avoid errors caused by rotation. From this point onward, always use these markings for reference.

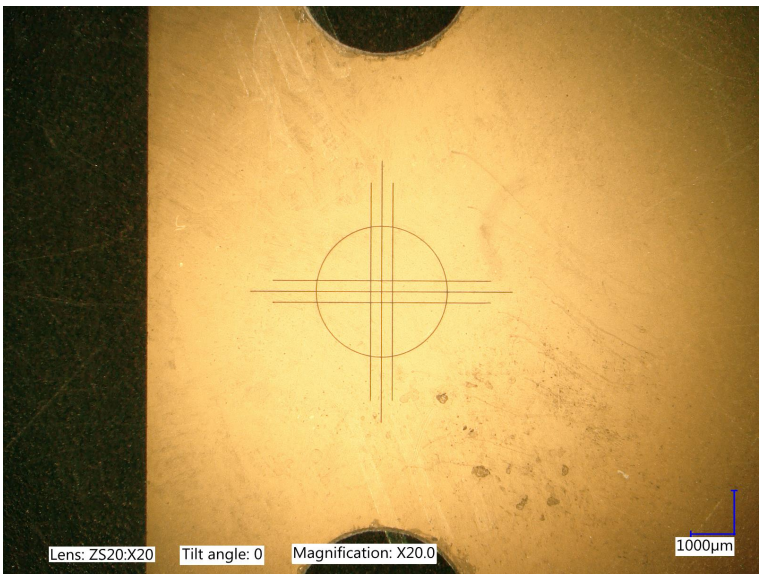

Figure 10: Alignment geometry

7. Now start one of the recipes for the blind holes. Additionally, begin fabricating the four holes that will be used for alignment during assembly. You can use one of the scripts designed for this, either to the halfway point or completely through. The halfway point script is faster per unit depth but requires an additional operation on the other side of the glass. The through-hole script takes 220 minutes but is completely passive.
8. Rotate the microscopy glass to the opposite side and use the alignment markings to realign the specimen.

9. Now proceed with fabricating the through holes. It is crucial to perform this step second, as it helps maintain the structural integrity of the glass, reducing the risk of cracking. Once this step is completed, the chip fabrication is finished.

10. An additional step can be performed to clean up any residual glass from the melt bath that may have formed on the surface in the blind hole. To do this, rotate and align the sample again and perform half the steps of the through-hole script. Use the script where the lower structs are turned off.

For the bottom plate, the same steps should be followed, minus the steps where the blind and through holes are cut.

E.2 Laser Fabrication Protocol for PDMS

1. Follow the startup sequence for the laser.

2. Ensure that both protective plastic covers are still attached to the PDMS sheet material.

3. Using tape, attach a sheet of PDMS to an alumina plate that will be used with the laser. The alumina plate protects the Aerotech stage from damage when the laser penetrates the sample. Make sure you tape the entire perimeter of the PDMS to prevent it from moving when the fume extractor is on.

4. Aim the nozzles of the pressurized air and the fume extractor toward each other, creating a flow stream above the sample. Ensure that the nozzles are not directly focused on the PDMS sheet, as this could cause the sheet to vibrate, potentially compromising the accuracy of the machine.

5. Find a section of the PDMS sheet that fits the geometry of your design. You can do this by moving the Aerotech stage over the perimeter of the designed sheet. Plan the location of the cut to use the sheet material efficiently.

E.3 Tips for Manufacturing of Glass Using FS Laser

1. Minimize the thermal input into the glass, as excessively high power levels can cause cracking. However, using lower power levels will significantly increase fabrication time. Aim to find a balance between achieving an acceptable surface finish and optimizing fabrication time.

2. Use lower focal point velocities (0-100 mm/s) if the interest lies with accurate machining at the small scale (¡1mm).

3. Layering your recipe in Lasea's Kyla software is a crucial step for achieving depth in your cuts. This process took me considerable time to master, but it is essential for obtaining significant depth. To layer effectively, you can add multiple instances of a struct by duplicating it and placing each copy at the same X and Y coordinates, while adjusting the Z position to create depth. In your script, it's important to include "actions" that move the stage incrementally before starting each new struct. Although Kyla software has a built-in layering function, it does not automatically adjust the stage's Z position with each subsequent layer. Since the laser spot size is 0.25 mm, the focus depth changes significantly over the 1 mm height of the glass, making this adjustment essential for precise cutting.

E.4 Fabrication of Tygon Collars

1. Prepare the lathe by fitting it with a 2.5 mm diameter collet chuck, and have a box cutter ready.

2. Insert the Tygon tubing so that the desired length of tubing extends out, then secure it by tightening the lever.

3. Start the lathe and fully extend the box cutter blade.

4. While the lathe is rotating, hold the side of the cutting blade against the side of the collet chuck and slowly push the box cutter through.

5. Turn off the lathe, and once it has stopped, release the tightening lever and remove the newly cut piece of Tygon material.

F Assembly Protocol

F.1 Chip Assembly

1. Place the glass slides and PDMS sheet in beakers filled with water. Place these in the ultrasonic bath and run a sinusoidal cycle for 5 minutes. Before this step, you can remove the thin plastic cover from the PDMS sheet, but it is essential to leave the stiff plastic cover on. If this cover is removed, a new PDMS sheet will need to be machined.

2. Prepare all the items needed for the assembly process: Preheat the oven to $65°C$, place the piezobrush assembly in a fume hood, prepare a liquinox or dish soap solution, and fill a medium petri dish with a layer of isopropanol. Also, prepare a razor, an X-Acto knife, and some tweezers.

3. When the ultrasonic treatment is complete, empty the beakers and proceed to clean all parts with the detergent solution, wiping them off using "piano paper." Repeat this process three times. Piano paper is a type of paper that does not leave fibers or other contaminants.

4. Rinse and wipe each individual part with isopropanol, and then use compressed air to remove any remaining isopropanol. Make a small peel between the stiff plastic cover and the PDMS sheet to make the later peeling process easier.

5. Place the bottom glass plate and the PDMS sheet in 3D-printed alignment tools. Ensure that the exposed PDMS side is facing upwards.

6. Place the assembly onto the piezobrush stage and adjust the height of the stage to achieve a maximum height difference of 1 cm, preferably 0.5 cm above the specimen. Begin activating the surface of the glass, followed by the surface of the PDMS, both for at least one minute per surface.

7. Once both surfaces are activated, lift the PDMS from the alignment tool by gripping the protective plastic cover on the bottom side or using tweezers. Align the holes on one end of the PDMS sheet with the round stubs (the other end should have partially squared stubs and notched alignment holes). Then, using a reversed peeling motion, press the two surfaces together. If an air pocket is trapped, peel back slightly and continue until both surfaces are fully adhered.

8. Begin peeling away the stiff plastic cover, taking care not to peel the PDMS from the glass. You can apply pressure with a razor at the interface of the peel to keep the PDMS in place.

9. Insert the top glass plate into the alignment mold, ensuring the blind holes are facing the alignment mold and the through holes are on the exposed surface. Activate both surfaces again.

10. Carefully attach the top and bottom surfaces using the reversed peeling technique, although this step may be more challenging due to the stiffness of the glass.

11. Place a plastic layer on the chip that is still secured in the alignment mold and transfer the assembly to the oven. Add additional weight, such as a smooth piece of scrap metal, to ensure the stack remains stable. Bake in the oven for seven hours.

G Safety Protocols

- In general, there were few safety hazards involved in fabricating the chip, with the primary risk being the potential for injury from cracking the glass or a ceramic alumina plate. If a cracking incident occurs, safety gloves should be worn, and the broken material should be disposed of in an appropriate waste container. In the event of an injury, the individual should seek assistance from the lab assistant in the office next door for further treatment.
- The assembly process was performed in a chemical lab, in this lab there are some applicable safety regulations that are listed below:

  1. **Chemical contamination:** Always wear protective equipment and long trousers to avoid skin contacting any of the surfaces, always assume thing are contaminated. When you have come in contact with hazardous chemicals, use the present safety equipment and alert the lab technician.
  2. **Sharp objects:** When using sharp objects such as an X-Acto knife or broken glass, always wear protective equipment. If an injury is sustained, use the available first aid kit and inform the lab technician immediately.
  3. **Gas leaks:** If any harmful chemical gases are released, you must leave the lab immediately. Sensors are in place to detect specific gases and provide warnings. When working with potentially harmful gases, always conduct the process in the fume hood. For example, during the surface activation process using oxygen plasma, harmful ozone gas is released, which can pose a health risk.

- The fabrication of the Tygon collars is done by using a lathe in the employee workshop, always wear protective clothing and follow the instruction by one of the technicians. Working with the lathe poses the following risks:

  1. **Entanglement**: Loose clothing, jewelry, or long hair can easily become entangled in the rotating parts of the lathe, leading to severe injuries. Always secure loose items and tie back long hair.
  2. **Flying Debris**: The lathe can produce flying chips, sparks, or fragments, which can cause eye injuries. Wearing safety goggles or a face shield is essential.
  3. **Tool Kickback**: Improper use of cutting tools or incorrect setup can cause the tool to catch and kick back, leading to potential injury. Always ensure tools are sharp, properly secured, and used at the correct speed and feed rate.
  4. **Pinch Points**: Hands or fingers can be caught between moving parts or in the gap between the workpiece and the tool, leading to crush injuries. Keep hands clear of the moving parts and use appropriate tools for adjustments.
  5. **Noise Hazards**: Lathes can produce high noise levels that may lead to hearing damage over time. Hearing protection should be worn when operating the lathe.
  6. **Material Ejection**: If the workpiece is not securely fastened, it can be ejected from the lathe at high speeds, posing a significant risk. Always double-check that the workpiece is securely clamped.

- During experiments in the Biofluids lab, the safety precautions of the chemical lab are also observed, though they are less restrictive due to the significantly lower amount of chemicals being used. A noteworthy hazard, however, is the use of sharp objects and glass; first aid kits are available in the lab for this reason.

H Expanded Theory

H.1 Half Rankine Body

A half Rankine body is a theoretical concept used in fluid dynamics and potential flow theory. It represents a simplified model to study the behavior of flows around streamlined bodies.

A Rankine body is formed by the superposition of a uniform flow and a source-sink pair. This results in a streamlined, closed body in an ideal fluid flow, exhibiting potential flow characteristics without viscosity and rotational effects. The half Rankine body is essentially half of this idealized shape, typically divided along a symmetry plane. It can represent flow around bodies such as a flat plate or a semi-infinite plane.

To form a half Rankine body the following flow elements are required: A source introduces fluid into the system, creating a radial outward flow. A uniform flow component represents the constant flow of fluid in a specific direction. By combining the source and uniform flow, the half Rankine body shape is derived. This shape typically appears as a semi-infinite streamlined object.

The half Rankine body is used to visualize flow patterns around semi-infinite objects and distribution of velocity and pressure around such bodies. Defined by the potential function (ϕ) representing the potential flow field, and the stream function (ψ) describing the streamlines and flow patterns, these functions are key to describing the flow for a half Rankine body. These functions are derived by solving the Laplace equation under the given boundary conditions (source and uniform flow).

Key features are, the flow around the half Rankine body is symmetric along the plane dividing the source and uniform flow. The analysis assumes inviscid, incompressible, and irrotational flow, making it an idealized model. The resulting body shape minimizes flow separation and resistance, providing insights into efficient aerodynamic and hydrodynamic designs.

H.2 Panel Method

The panel method is a widely used numerical technique in fluid mechanics, particularly for solving potential flow problems that include solid boundaries, such as aerofoils and ship hulls.

The panel method relies on the assumptions of potential flow, meaning the flow is considered invicid, incompressible and irrotational. These assumptions lead to the governing Laplace equation for the velocity potential and the stream function. The absence of rotational effects simplifies the mathematical treatment of the flow, making it possible to use superposition principles to build complex flow solutions from simpler ones.

To apply the panel method, the surface of the body under study is discretized into a series of small, flat segments known as panels. Each panel represents a portion of the body's surface, modelled from collocated points in the flow. The goal is to approximate the continuous surface by these discrete elements, allowing for a numerical solution with a no penetration boundary condition.

Each panel is associated with either a source/sink strength, depending on the specific formulation of the problem. Source/sink distributions are used to model the normal component of the flow velocity on the surface, ensuring that the flow does not penetrate the body.

The core of the panel method is the enforcement of boundary conditions. The primary boundary condition is the no-penetration condition, which requires that the normal component of the velocity at the surface of the body is zero. This condition ensures that the flow follows the contour of the body without intersecting it. Mathematically, this is expressed by setting the normal component of the flow velocity to zero at discrete collocation points, usually located at the midpoints of the panels.

I Designed Parts

This appendix contains technical drawings of the parts used in this project, with key dimensions highlighted. To facilitate future enhancements through the design of additional insert pieces, all base components have been designed with modularity in mind, allowing for easy modifications and design updates for the assemblies.

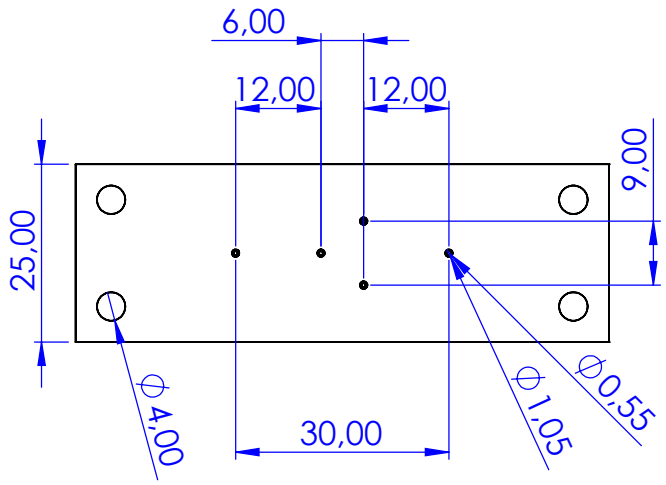

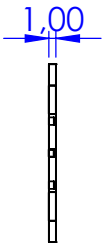

Config. 1

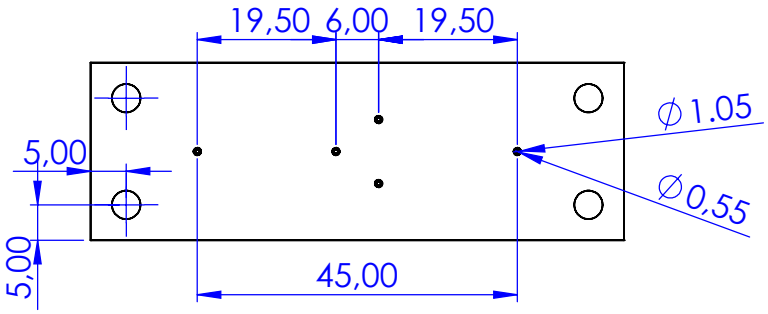

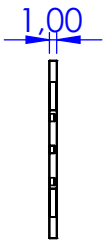

Config. 2

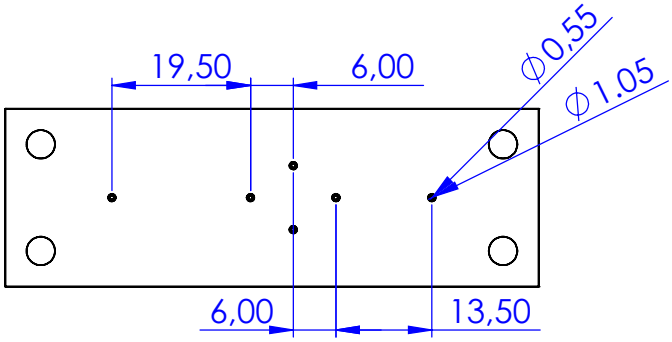

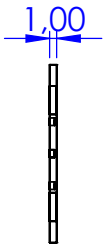

Config. 3

UNLESS OTHERWISE SPECIFIED: DIMENSIONS ARE IN MILLIMETERS SURFACE FINISH: TOLERANCES: LINEAR: ANGULAR:	FINISH:				3D printing	REVISION
					Chip Configurations	
	NAME	SIGNATURE	DATE			
DRAWN	Bart Bloemendaal					
CHK'D						
APPV'D						
MFG						
Q.A				MATERIAL:	DWG NO.	A4
				Glass	Chip configurations	
				WEIGHT:	SCALE: 1:2	SHEET 1 OF 2

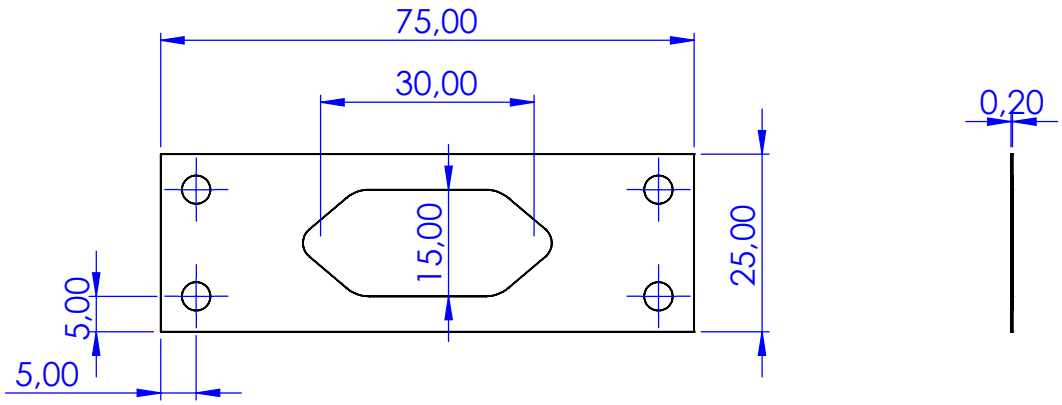

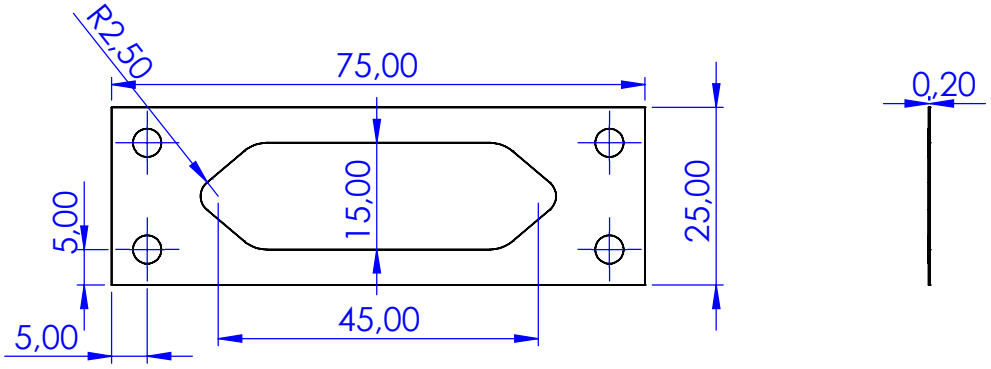

UNLESS OTHERWISE SPECIFIED: DIMENSIONS ARE IN MILLIMETERS SURFACE FINISH: TOLERANCES: LINEAR: ANGULAR:	FINISH:	DEBURR AND BREAK SHARP EDGES	DO NOT SCALE DRAWING / REVISION

	NAME	SIGNATURE	DATE
DRAWN			
CHK'D			
APPV'D			
MFG			
Q.A			

TITLE: PDMS layer configurations

MATERIAL:

DWG NO. Chip configurations

A4

WEIGHT:

SCALE:2:1

SHEET 2 OF 2

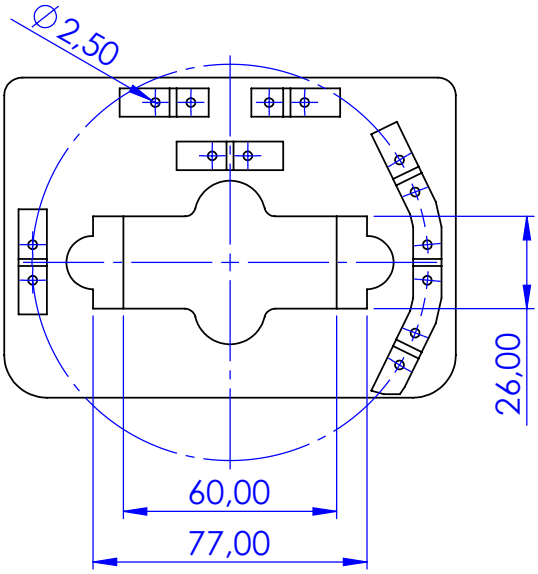

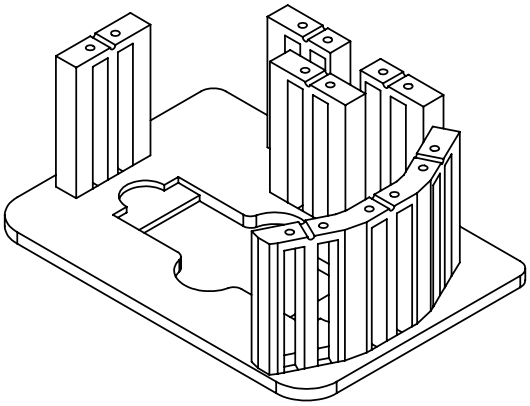

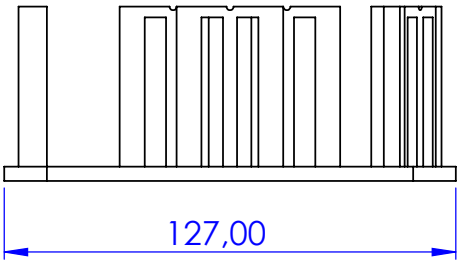

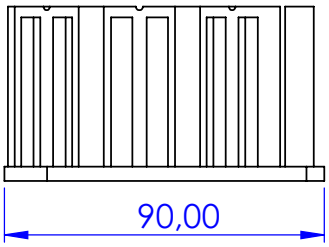

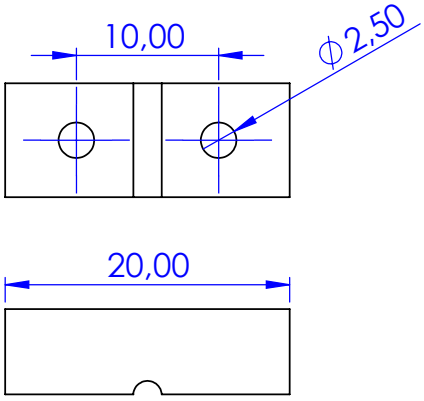

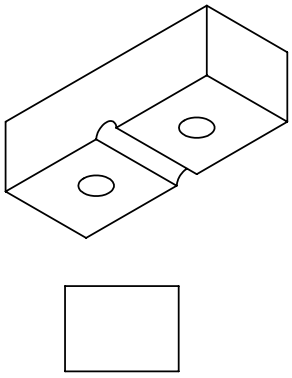

UNLESS OTHERWISE SPECIFIED: DIMENSIONS ARE IN MILLIMETERS SURFACE FINISH: TOLERANCES: LINEAR: ANGULAR:	FINISH:		3D printing	REVISION		
	NAME	SIGNATURE	DATE	Chip holder		
DRAWN	Bart Bloemendaal					
CHK'D						
APPV'D						
MFG						
Q.A				MATERIAL: PLA	DWG NO. Chip holder	A4
				WEIGHT:	SCALE: 1:2	SHEET 1 OF 1

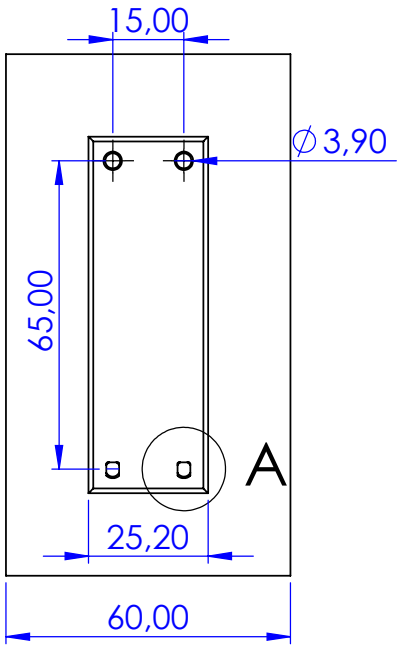

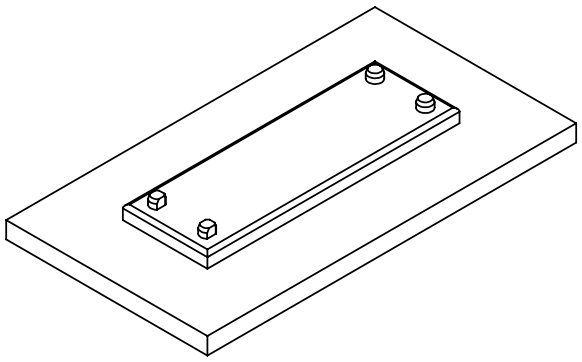

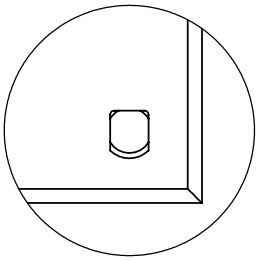

DETAIL A

SCALE 2 : 1

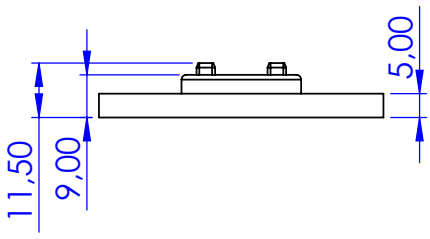

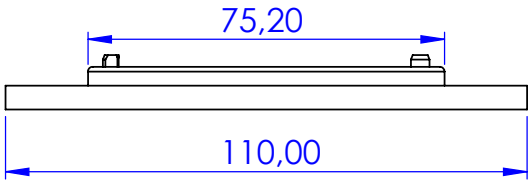

UNLESS OTHERWISE SPECIFIED: DIMENSIONS ARE IN MILLIMETERS SURFACE FINISH: TOLERANCES: LINEAR: ANGULAR:		FINISH:			3D printing	REVISION
					Alignment tool used for alligning the layered structure of Glass-PDMS-Glass	
	NAME	SIGNATURE	DATE			
DRAWN	Bart Bloemendaal					
CHK'D						
APPV'D						
MFG						
Q.A				MATERIAL: PETG	DWG NO. Dye v3	A4
				WEIGHT:	SCALE: 2:3	SHEET 1 OF 1

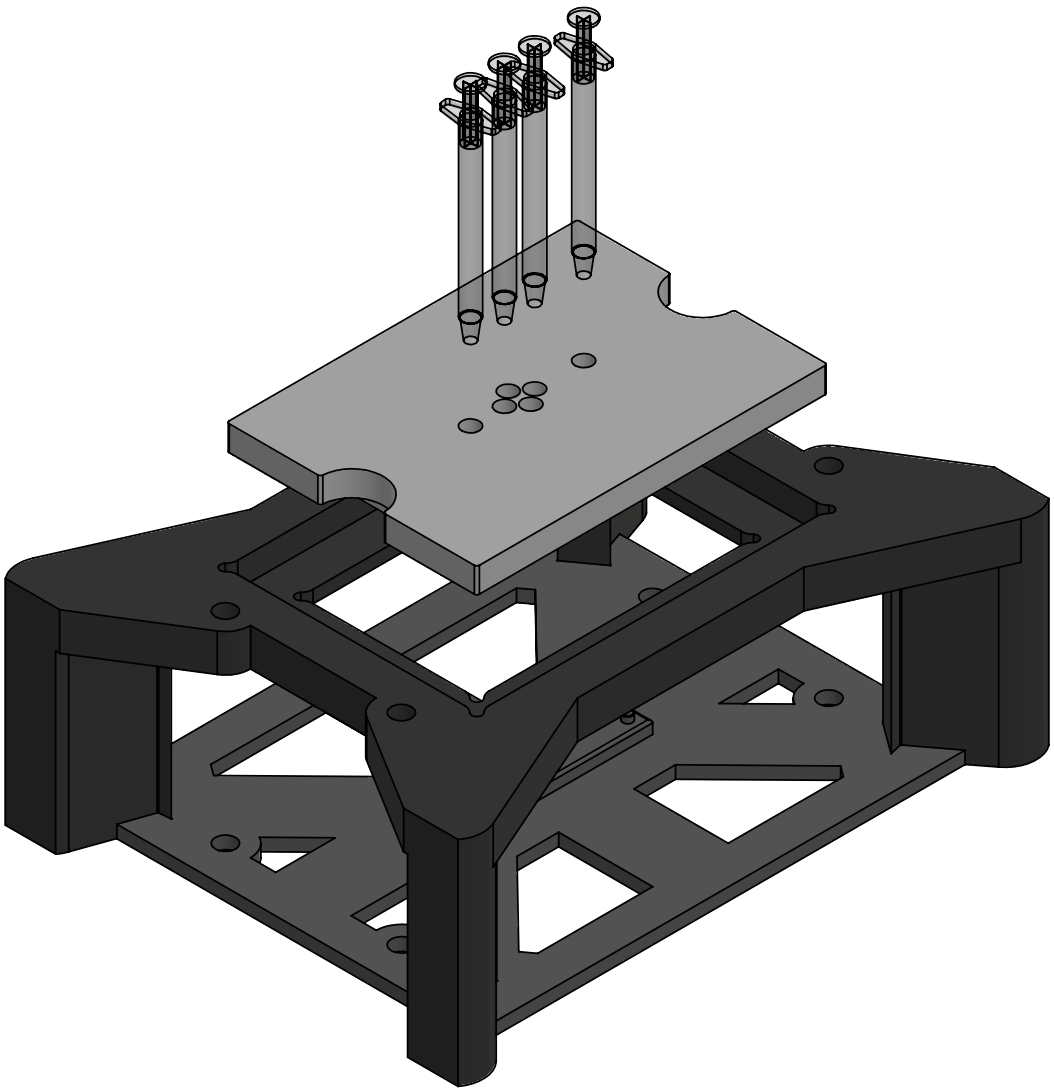

UNLESS OTHERWISE SPECIFIED: DIMENSIONS ARE IN MILLIMETERS SURFACE FINISH: TOLERANCES: LINEAR: ANGULAR:	FINISH:				3D printing	REVISION
	NAME	SIGNATURE	DATE		Glueing station that utilizes syringes to align needles with inlet positions on the chip.	
DRAWN	Bart Bloemendaal					
CHK'D						
APPV'D						
MFG						
Q.A				MATERIAL: PLA	DWG NO. Glue station	A4
				WEIGHT:	SCALE: 1:2	SHEET 1 OF 4

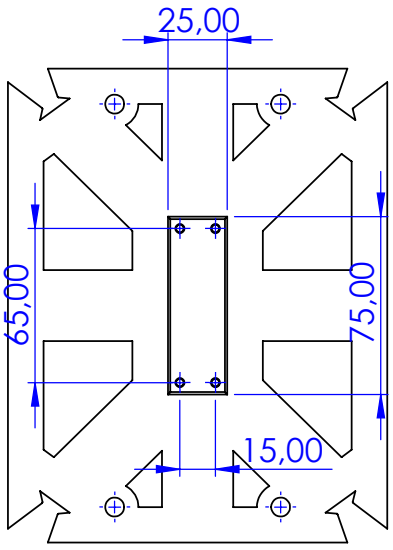

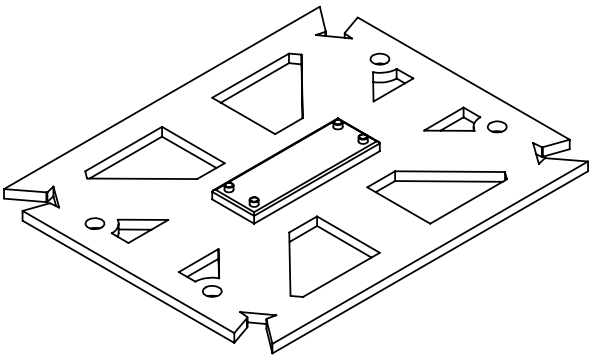

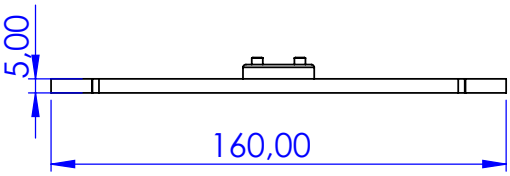

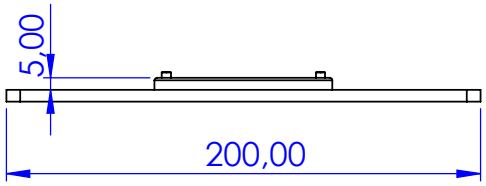

UNLESS OTHERWISE SPECIFIED: DIMENSIONS ARE IN MILLIMETERS SURFACE FINISH: TOLERANCES: LINEAR: ANGULAR:	FINISH:	DEBURR AND BREAK SHARP EDGES	DO NOT SCALE DRAWING / REVISION

	NAME	SIGNATURE	DATE
DRAWN			
CHK'D			
APPV'D			
MFG			
Q.A			

TITLE: Base plate, with dove tail inserts

MATERIAL:

DWG NO. Glue station

A4

WEIGHT:

SCALE:1:3

SHEET 2 OF 4

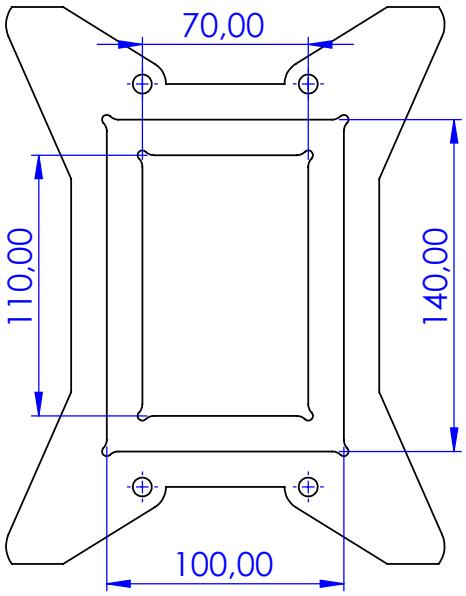

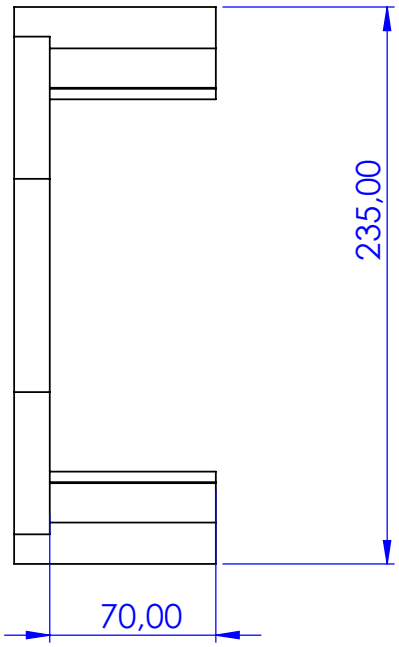

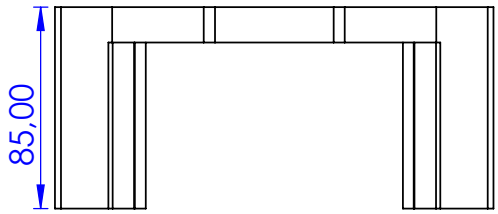

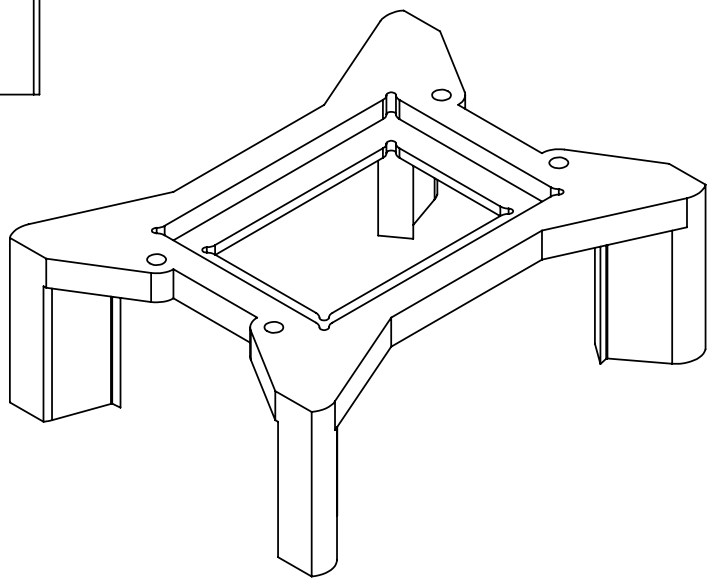

UNLESS OTHERWISE SPECIFIED: DIMENSIONS ARE IN MILLIMETERS SURFACE FINISH: TOLERANCES: LINEAR: ANGULAR:	FINISH:	DEBURR AND BREAK SHARP EDGES	DO NOT SCALE DRAWING / REVISION

	NAME	SIGNATURE	DATE
DRAWN			
CHK'D			
APPV'D			
MFG			
Q.A			

TITLE: Bridging structure

MATERIAL:

DWG NO. Glue station

A4

WEIGHT:

SCALE:1:3

SHEET 3 OF 4

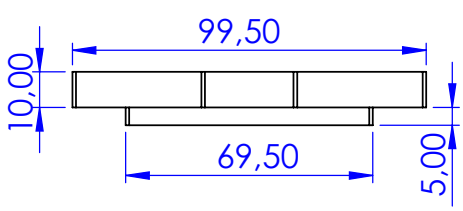

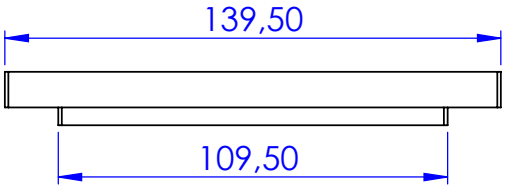

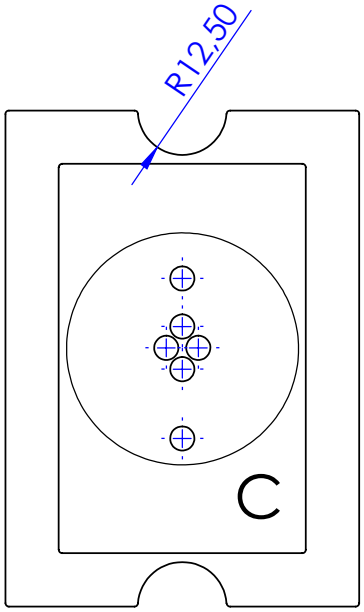

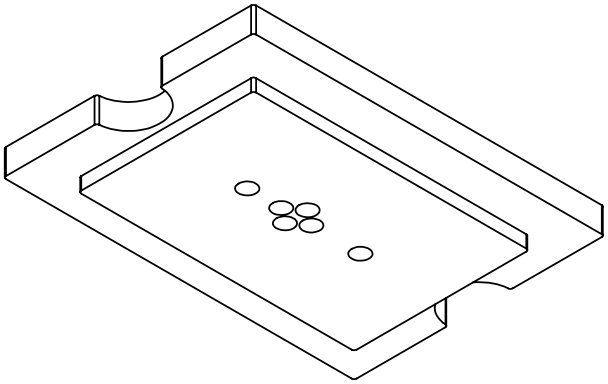

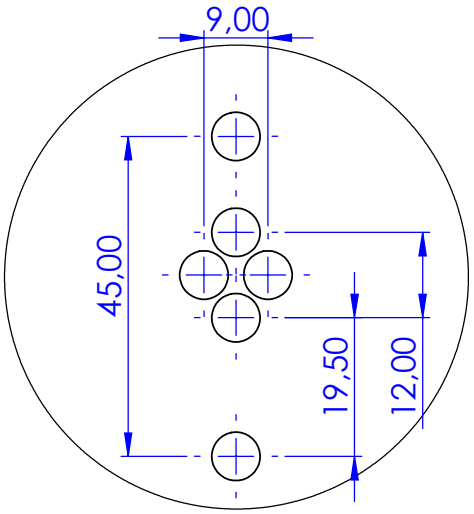

DETAIL C

SCALE 1 : 1

UNLESS OTHERWISE SPECIFIED: DIMENSIONS ARE IN MILLIMETERS SURFACE FINISH: TOLERANCES: LINEAR: ANGULAR:	FINISH:	DEBURR AND BREAK SHARP EDGES	DO NOT SCALE DRAWING / REVISION

	NAME	SIGNATURE	DATE
DRAWN			
CHK'D			
APPV'D			
MFG			
Q.A			

TITLE: Insert part for chips with Configuration 2 & 3

MATERIAL:

DWG NO. Glue station

A4

WEIGHT:

SCALE:1:2

SHEET 4 OF 4

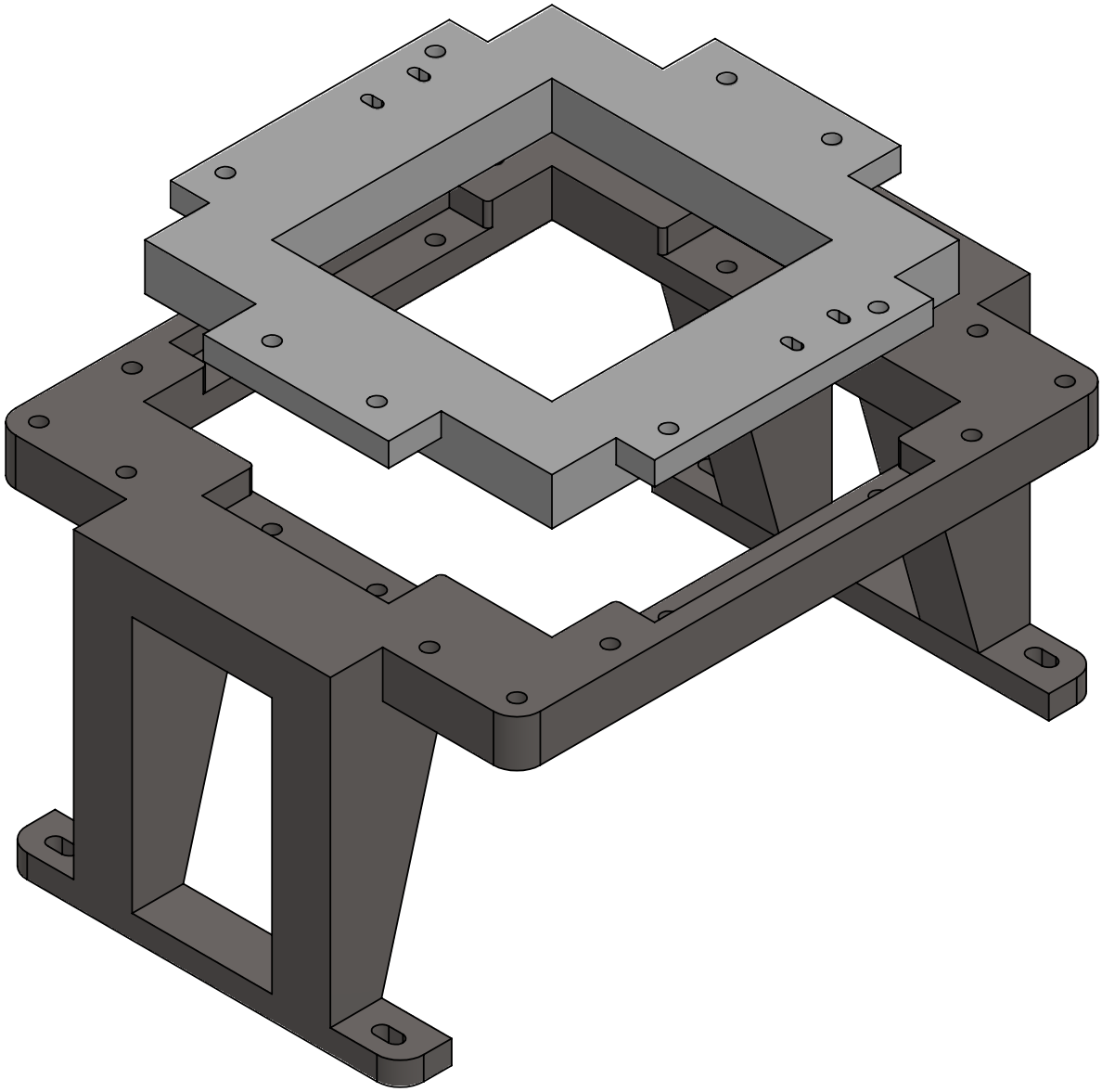

UNLESS OTHERWISE SPECIFIED: DIMENSIONS ARE IN MILLIMETERS SURFACE FINISH: TOLERANCES: LINEAR: ANGULAR:	FINISH:				3D printing	REVISION
	NAME	SIGNATURE	DATE		Microscope cover assembly To fix the lighting to the microscope	
DRAWN	Bart Bloemendaal					
CHK'D						
APPV'D						
MFG						
Q.A				MATERIAL: PLA	DWG NO. Microscope cover	A4
				WEIGHT:	SCALE: 1:2	SHEET 1 OF 3

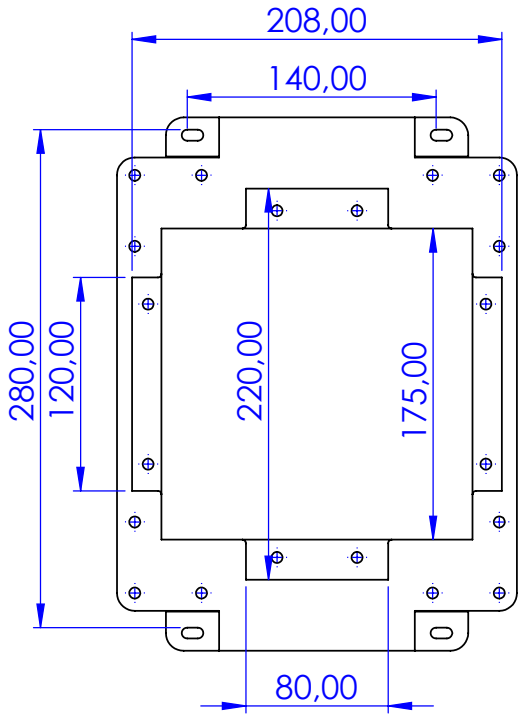

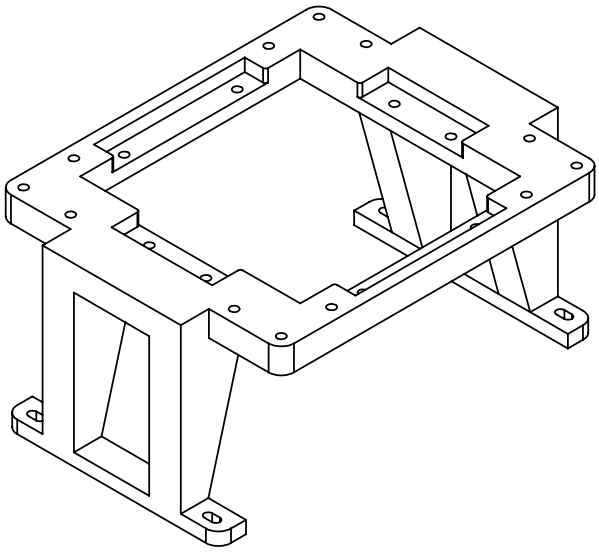

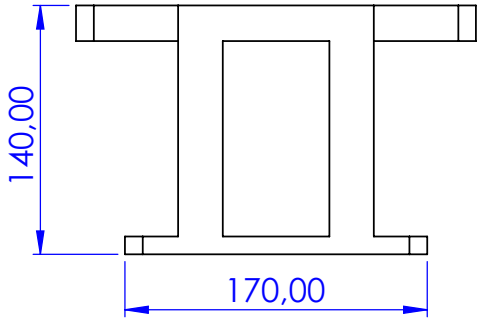

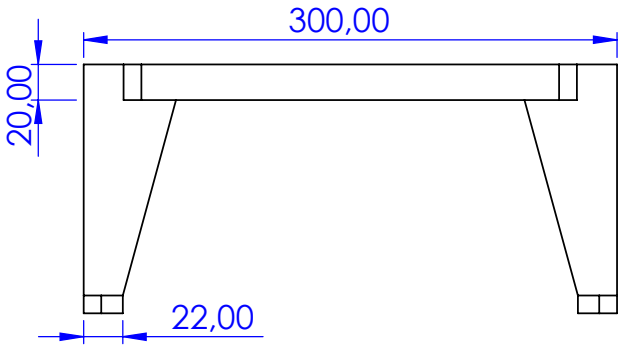

UNLESS OTHERWISE SPECIFIED: DIMENSIONS ARE IN MILLIMETERS SURFACE FINISH: TOLERANCES: LINEAR: ANGULAR:	FINISH:	DEBURR AND BREAK SHARP EDGES	DO NOT SCALE DRAWING / REVISION

	NAME	SIGNATURE	DATE
DRAWN			
CHK'D			
APPV'D			
MFG			
Q.A			

TITLE: Bridging structure

MATERIAL:

DWG NO. Microscope cover A4

WEIGHT:

SCALE:1:4

SHEET 2 OF 3

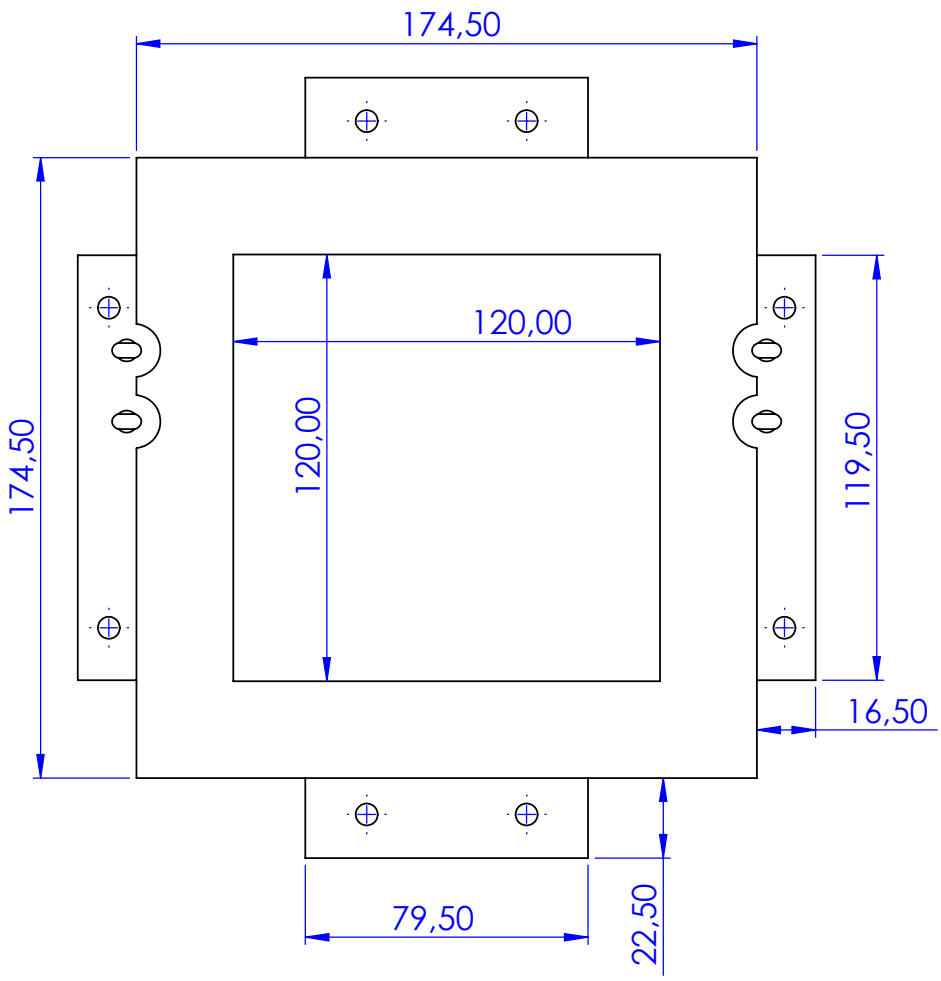

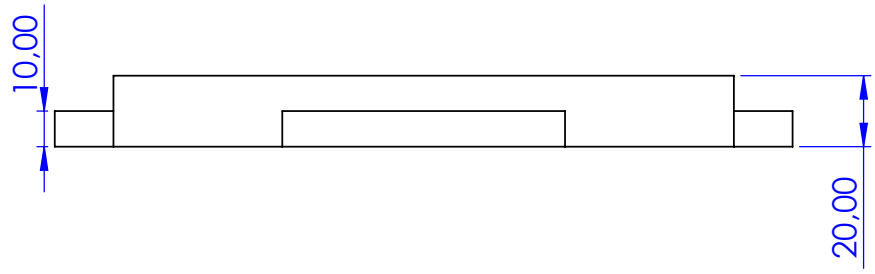

UNLESS OTHERWISE SPECIFIED: DIMENSIONS ARE IN MILLIMETERS SURFACE FINISH: TOLERANCES: LINEAR: ANGULAR:	FINISH:	DEBURR AND BREAK SHARP EDGES	DO NOT SCALE DRAWING / REVISION

	NAME	SIGNATURE	DATE
DRAWN			
CHK'D			
APPV'D			
MFG			
Q.A			

TITLE: Led frame insert

MATERIAL:

DWG NO. Microscope cover A4

WEIGHT:

SCALE:1:2

SHEET 3 OF 3

J Characterization Measurements

All the processed images from the different sets of manufacturing tests are depicted in this appendix.

J.1 Roundness and Diameters

This subsection presents all the measurements taken at various laser focal point velocities. The other critical parameters are the laser power, which is set at 5%, and the number of repetitions, which is fixed at 1000. These images are processed for roundness and diameters.

J.1.1 Set 1

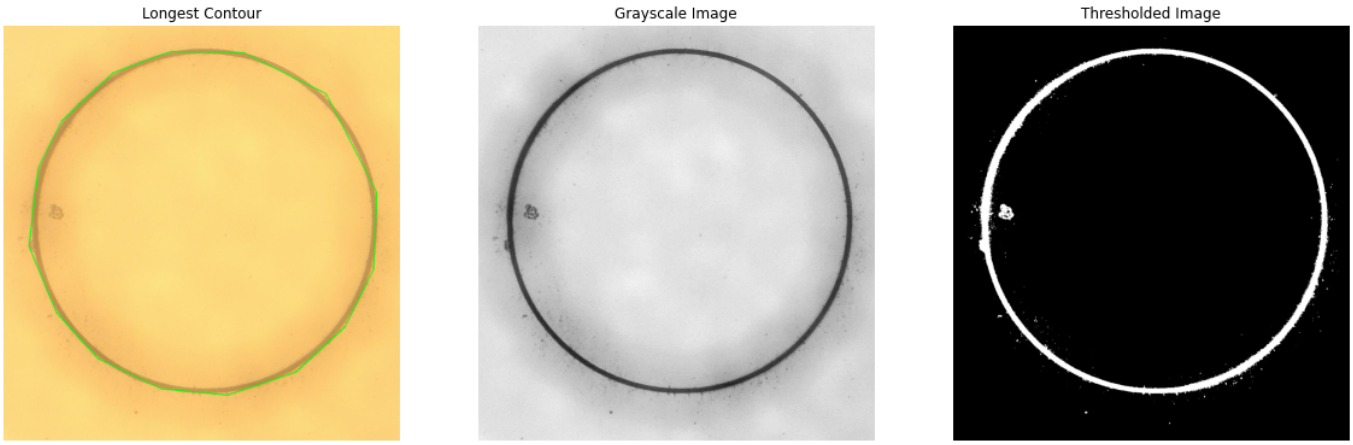

Figure 11: 50 mm/sec

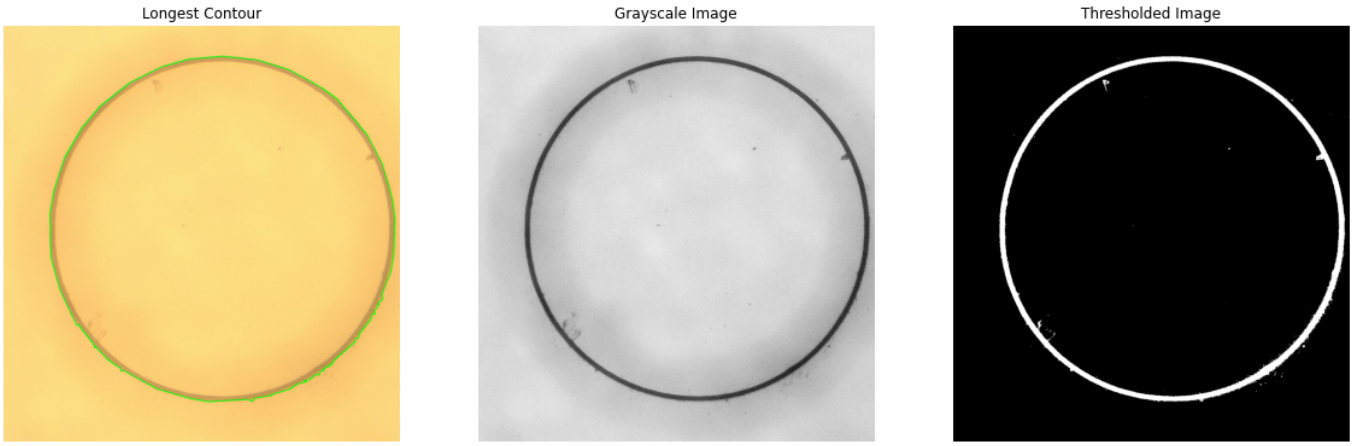

Figure 12: 100 mm/sec

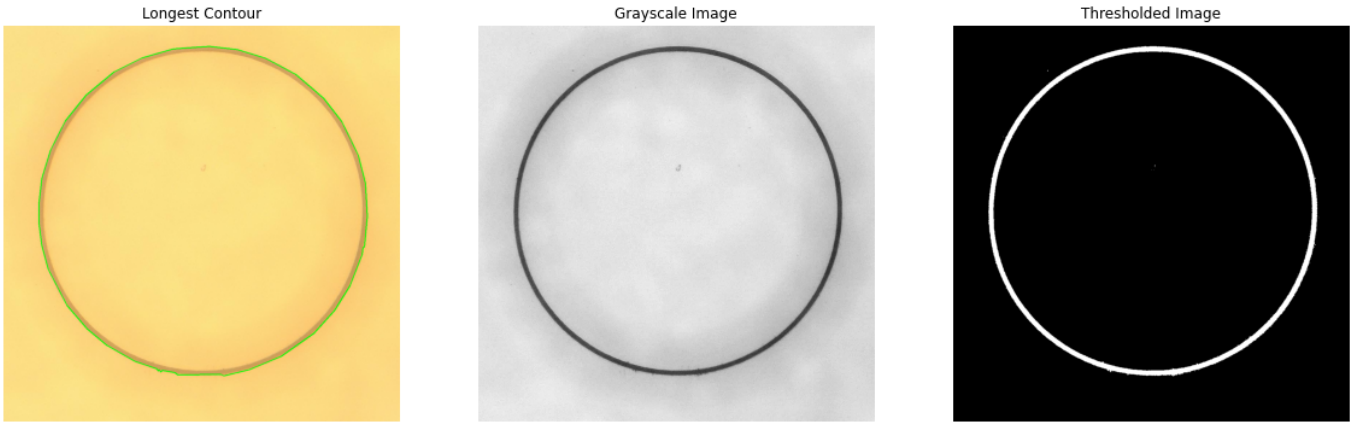

Figure 13: 150 mm/sec

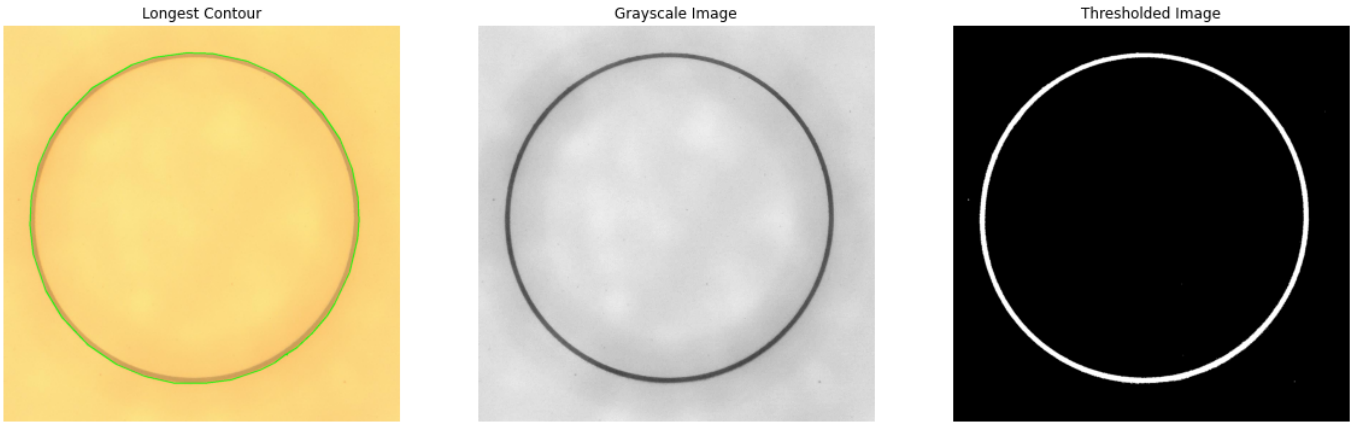

Figure 14: 200 mm/sec

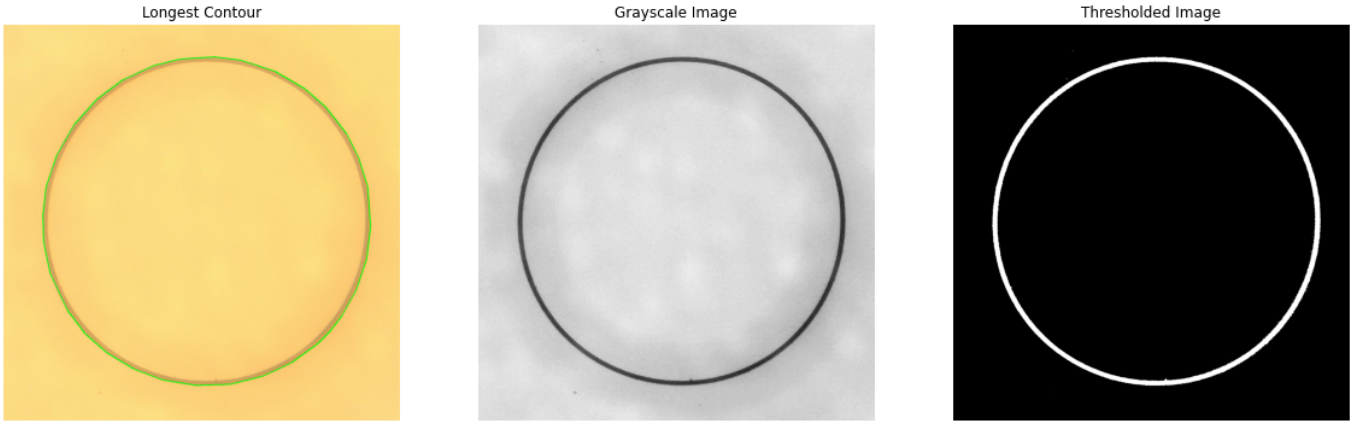

Figure 15: 250 mm/sec

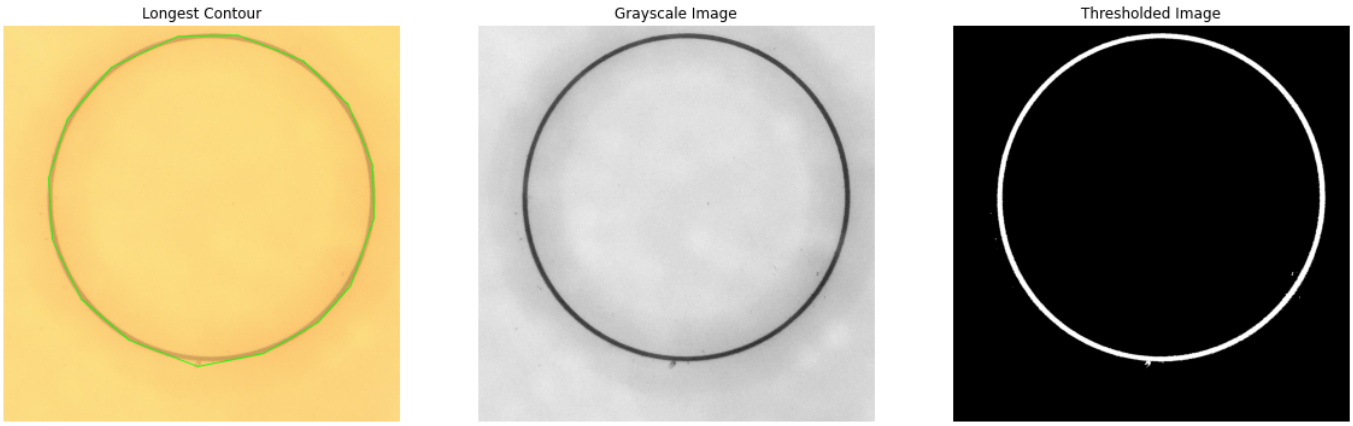

Figure 16: 300 mm/sec

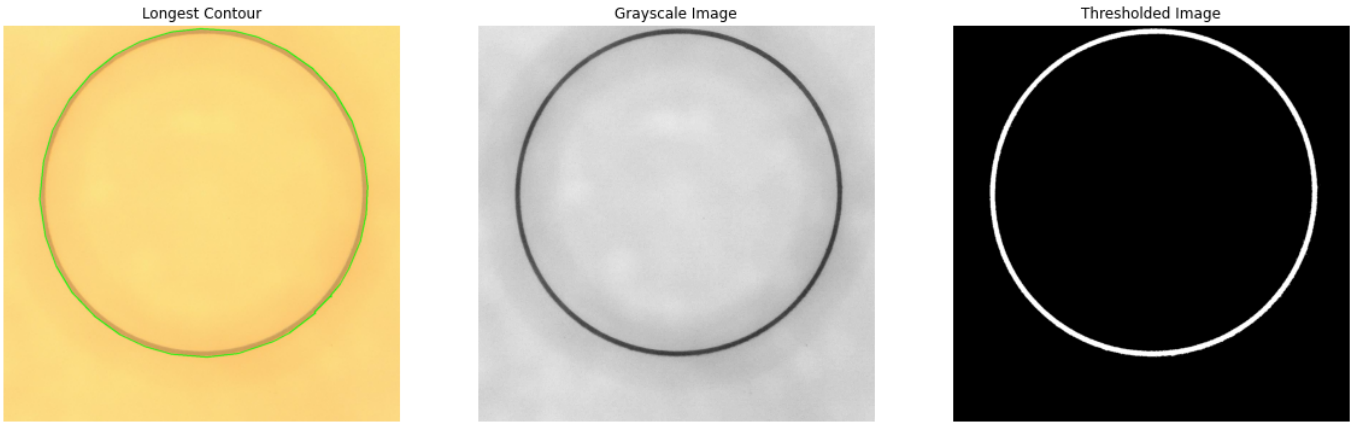

Figure 17: 350 mm/sec

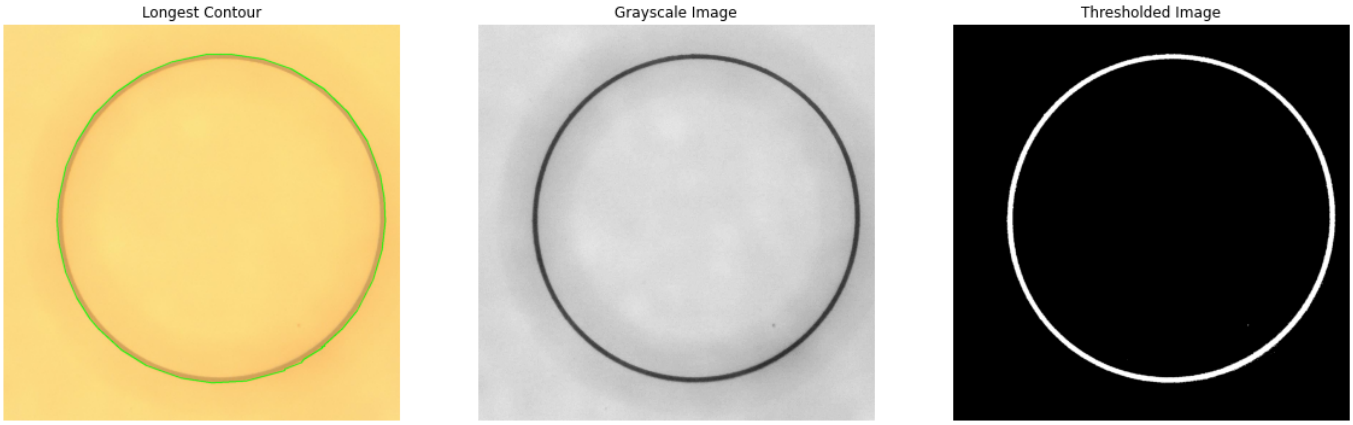

Figure 18: 400 mm/sec

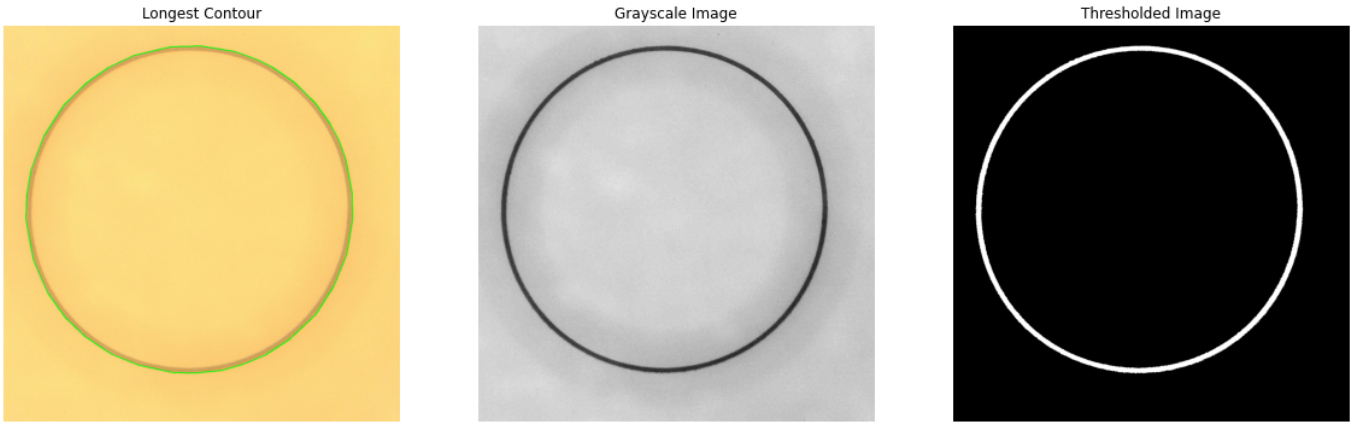

Figure 19: 450 mm/sec

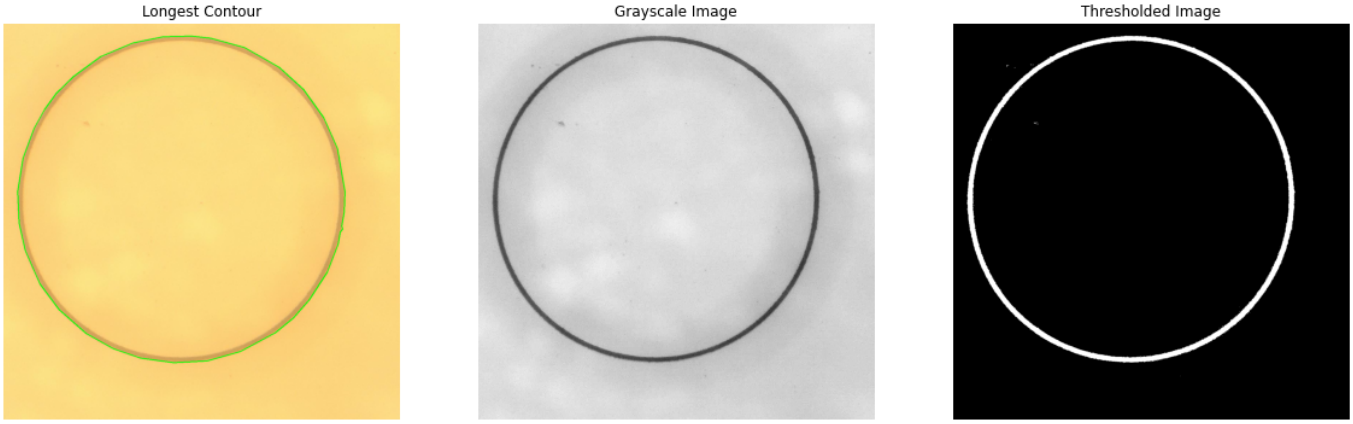

Figure 20: 500 mm/sec

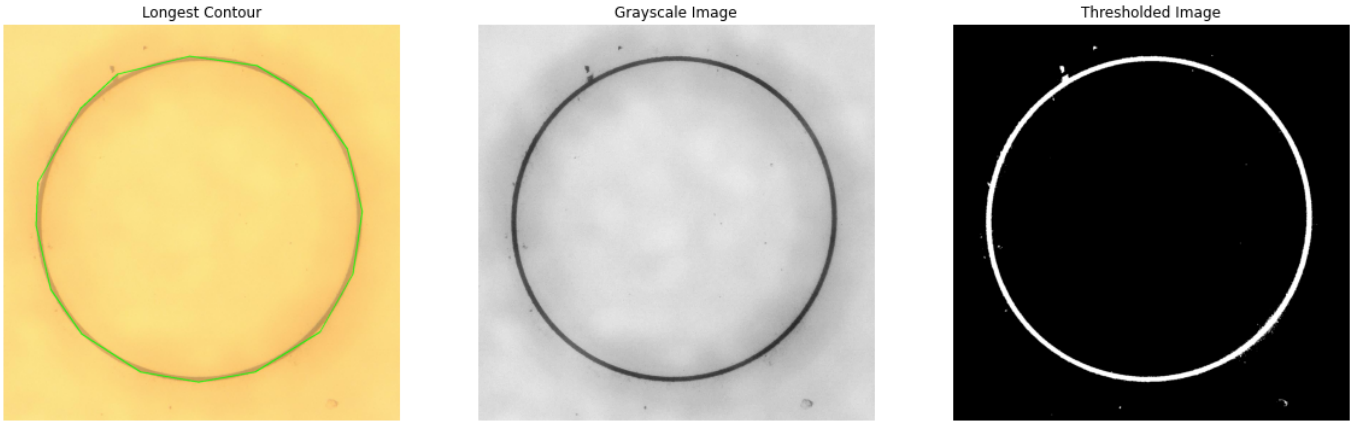

Figure 21: 750 mm/sec

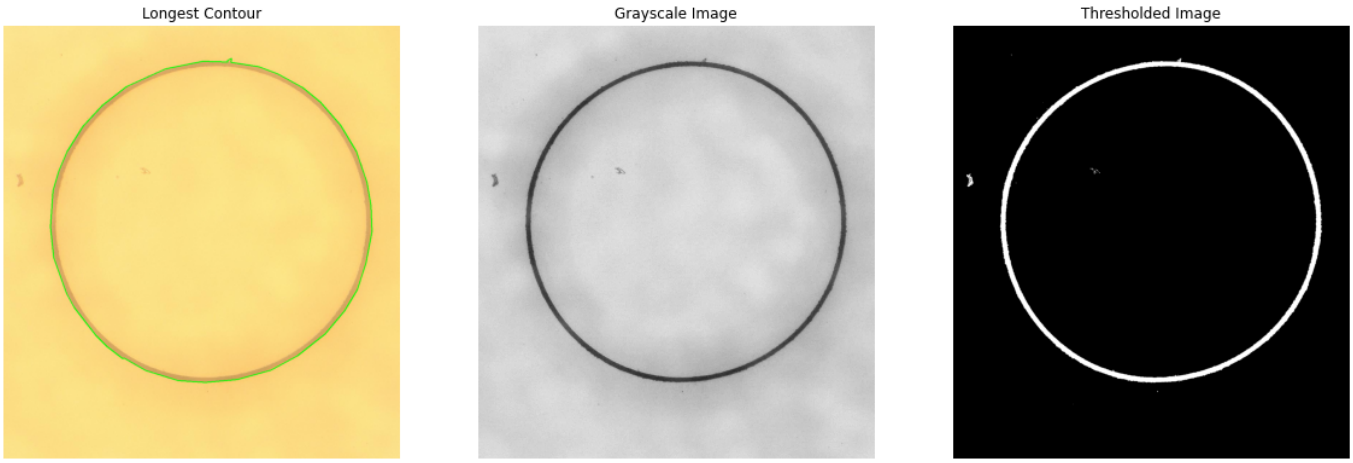

Figure 22: 1000 mm/sec

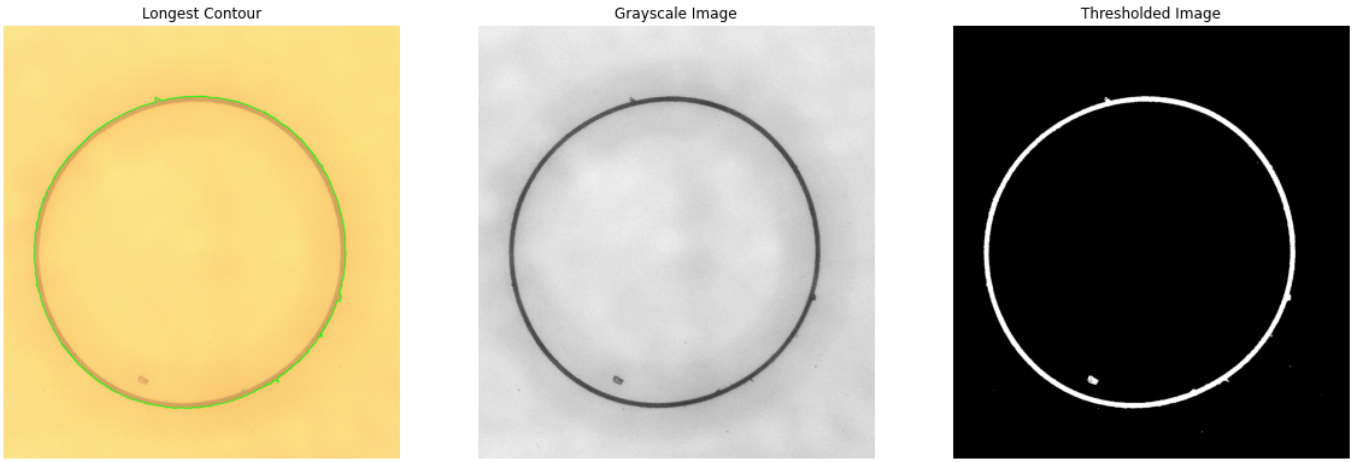

Figure 23: 1250 mm/sec

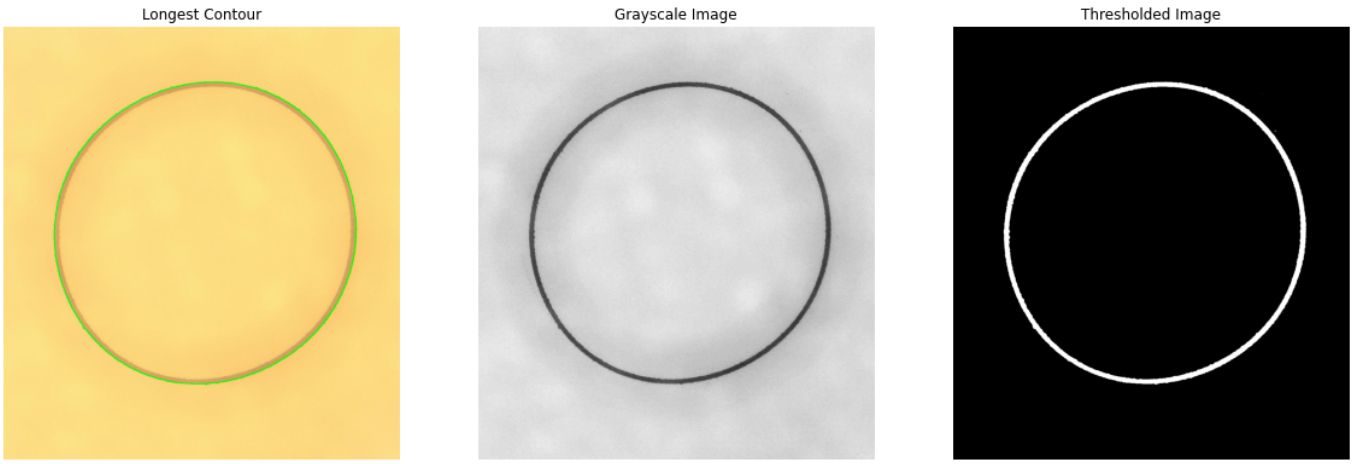

Figure 24: 1500 mm/sec

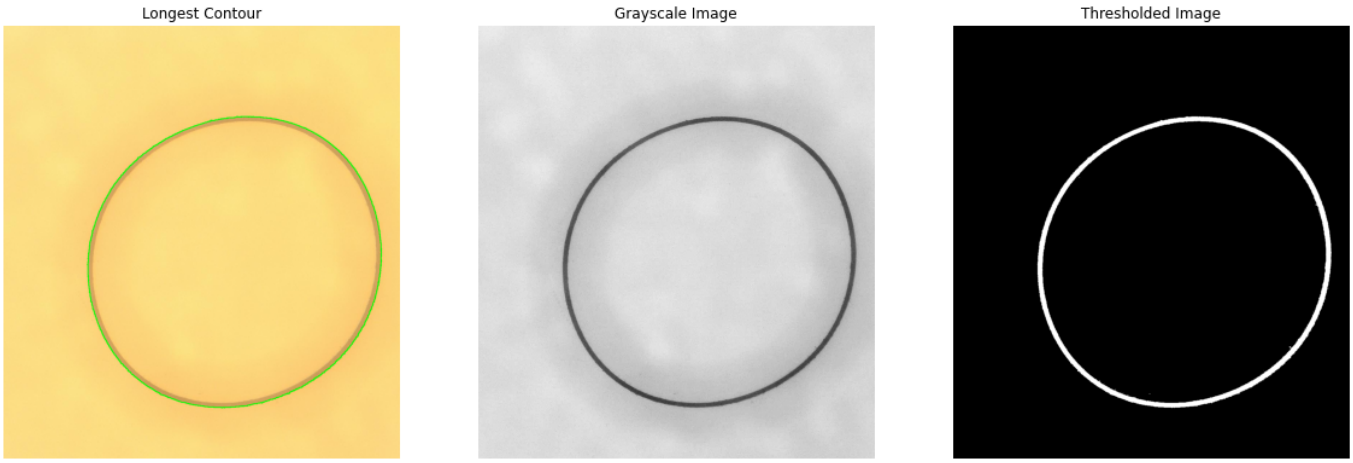

Figure 25: 1750 mm/sec

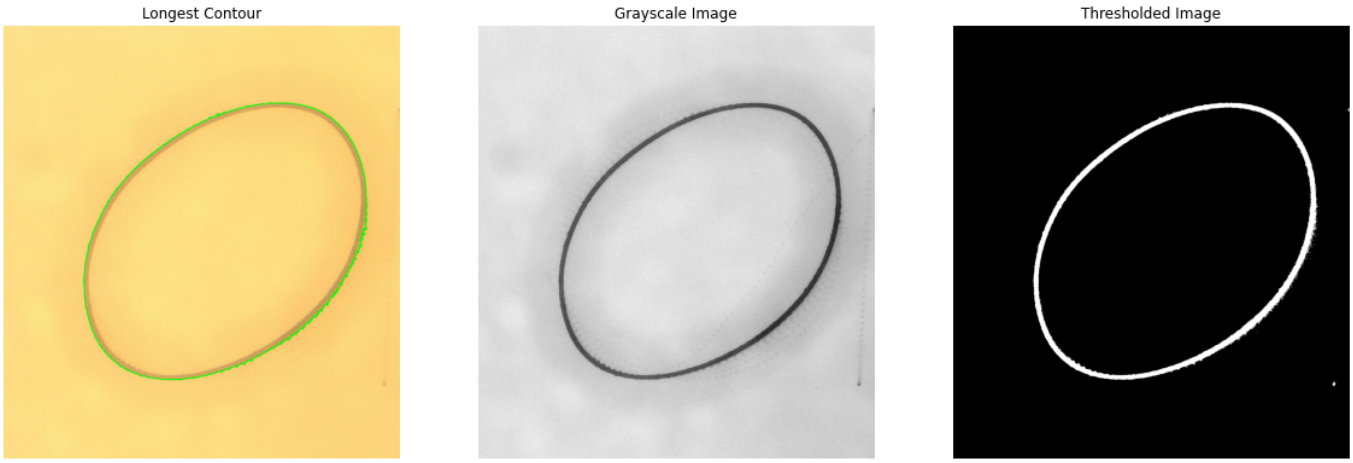

Figure 26: 2000 mm/sec

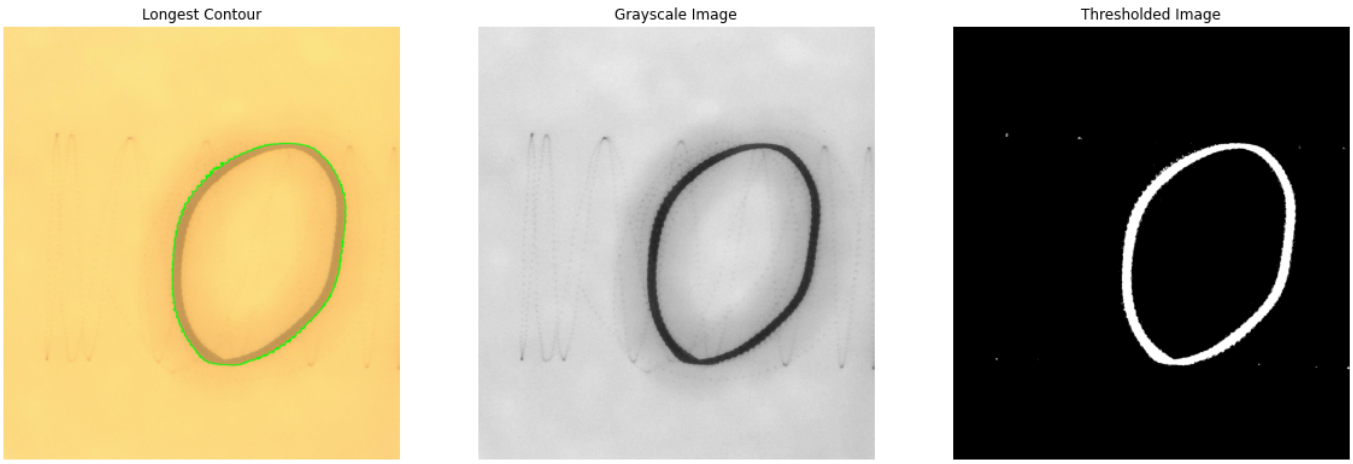

Figure 27: 2250 mm/sec

J.1.2 Set 2

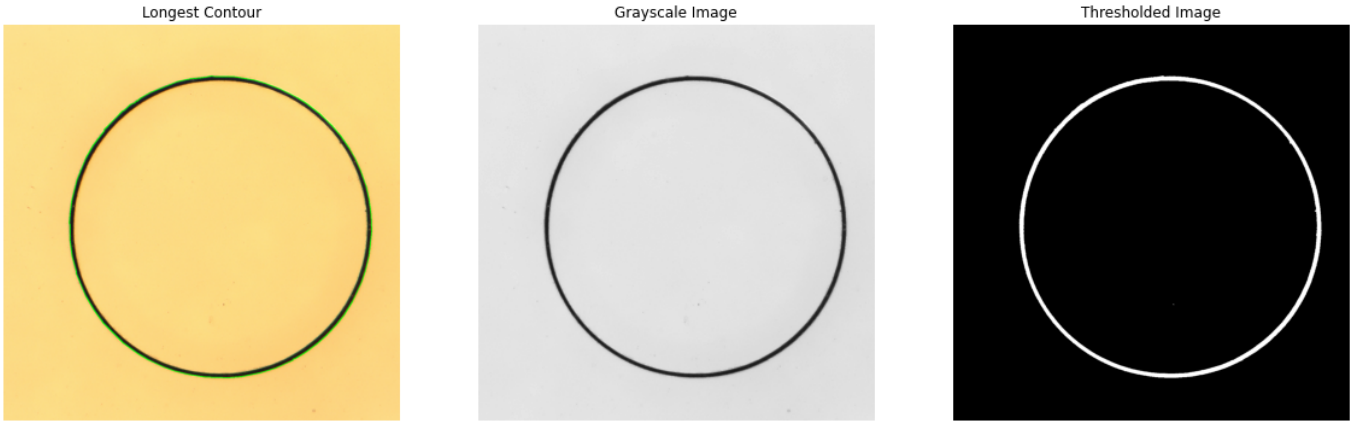

Figure 28: 50 mm/sec

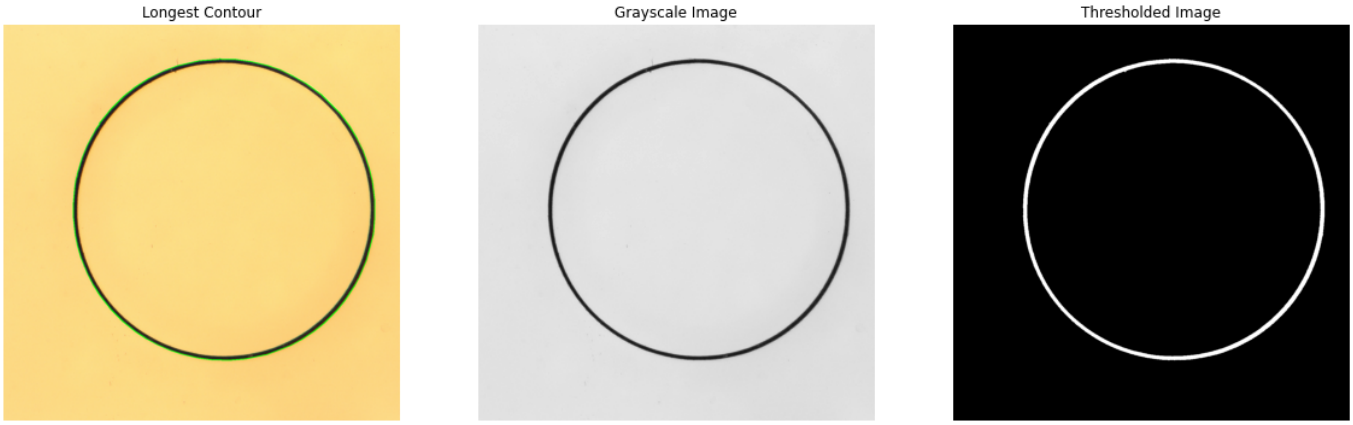

Figure 29: 100 mm/sec

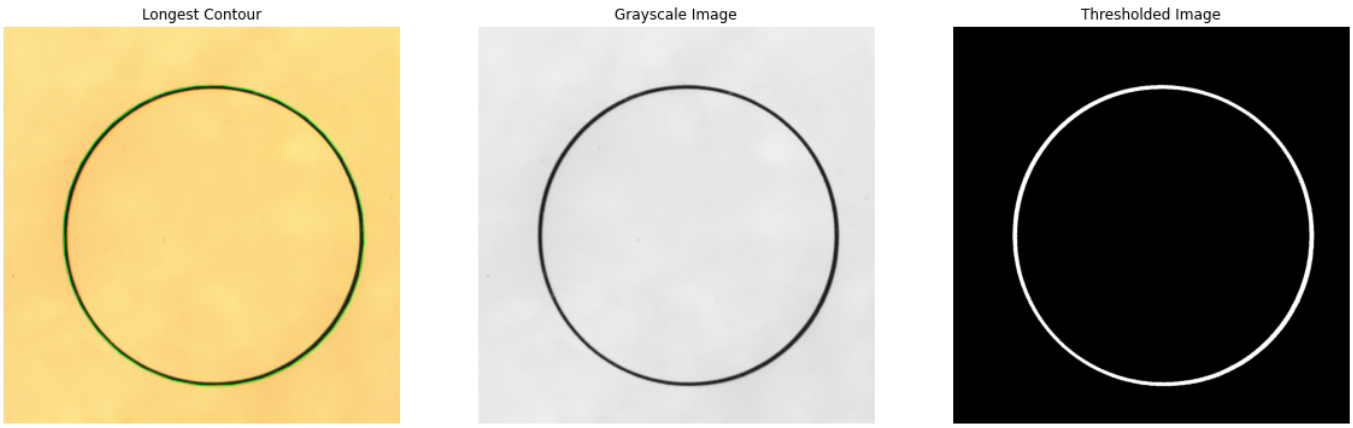

Figure 30: 150 mm/sec

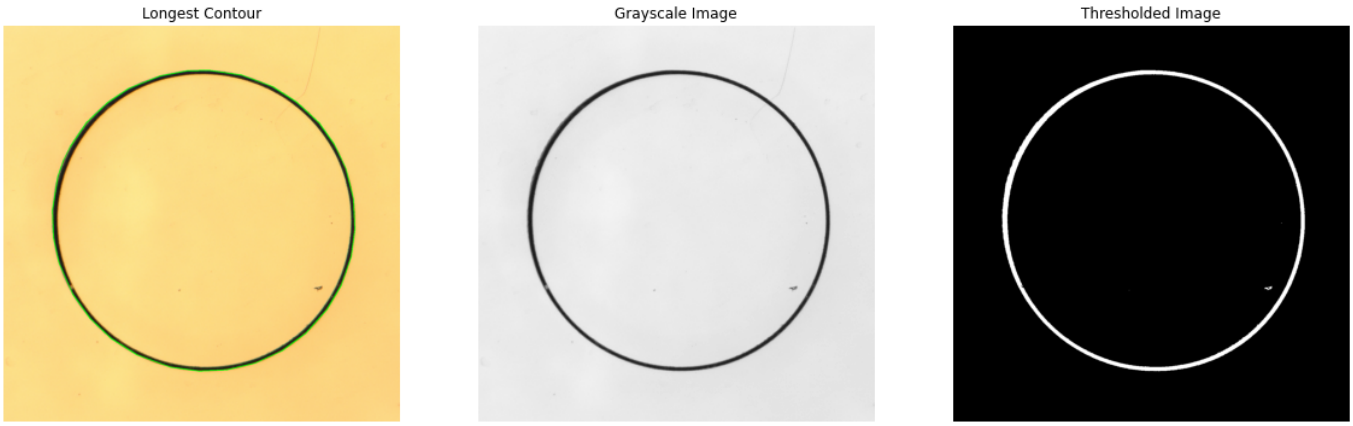

Figure 31: 200 mm/sec

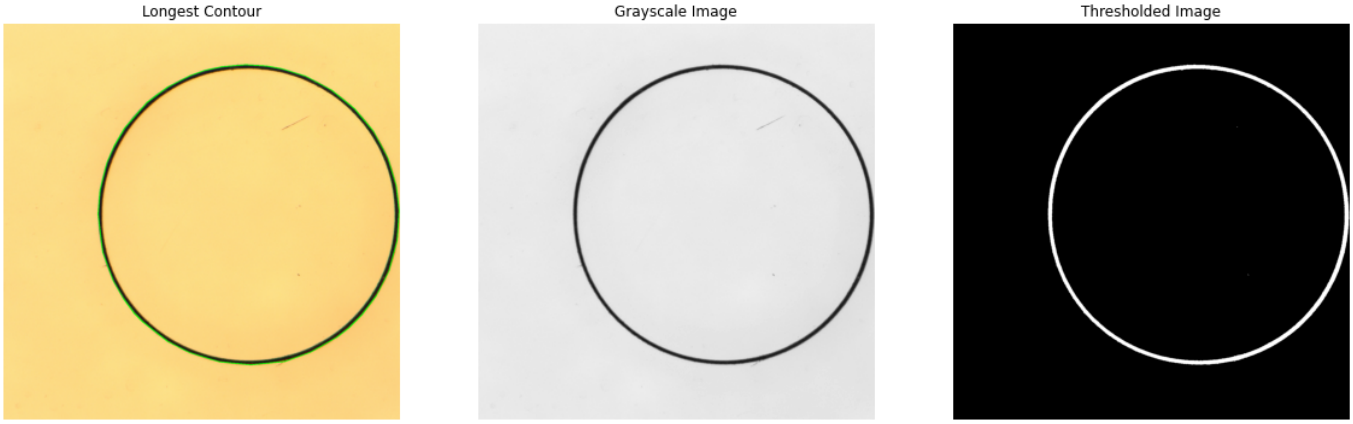

Figure 32: 250 mm/sec

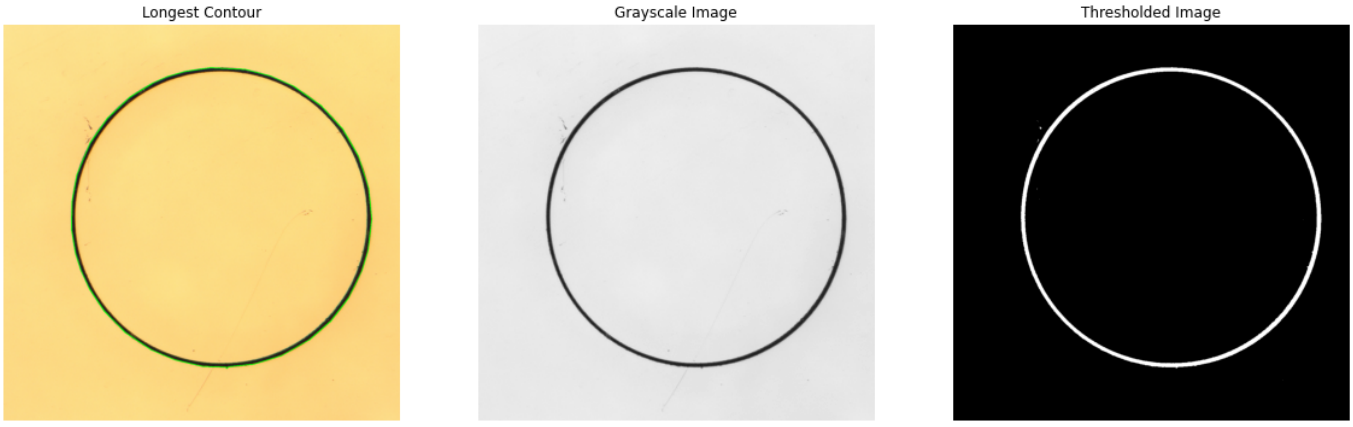

Figure 33: 300 mm/sec

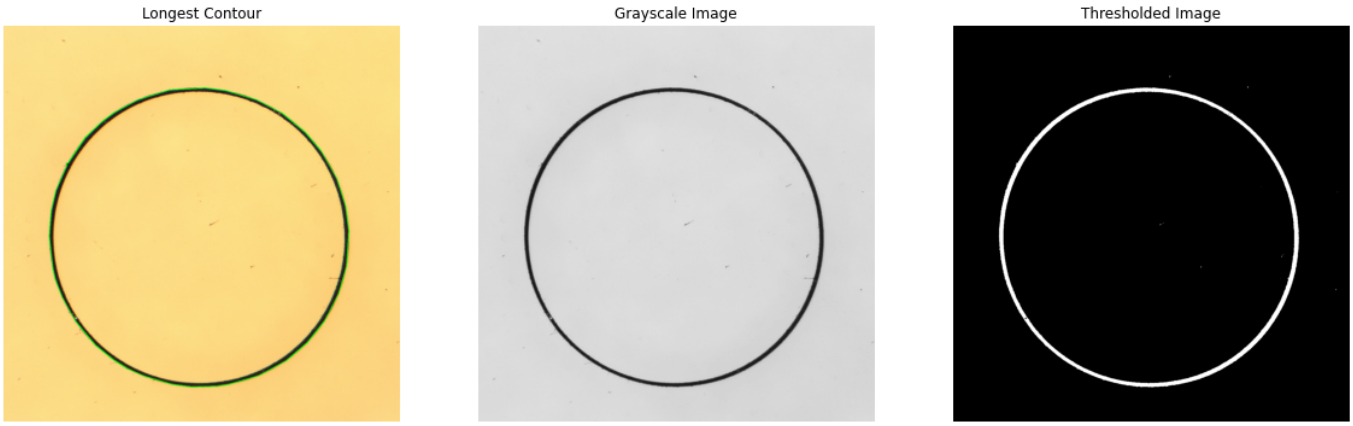

Figure 34: 350 mm/sec

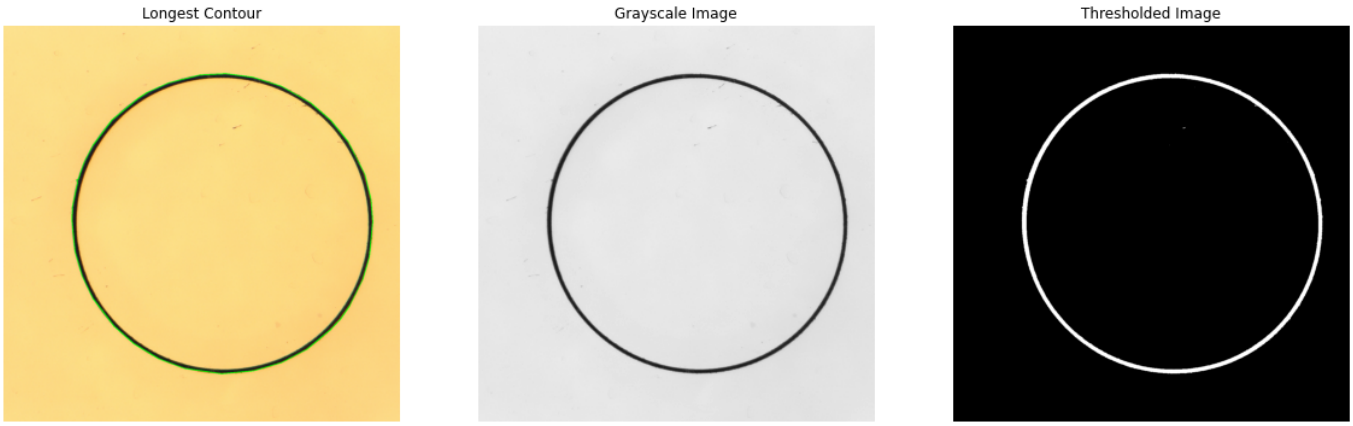

Figure 35: 400 mm/sec

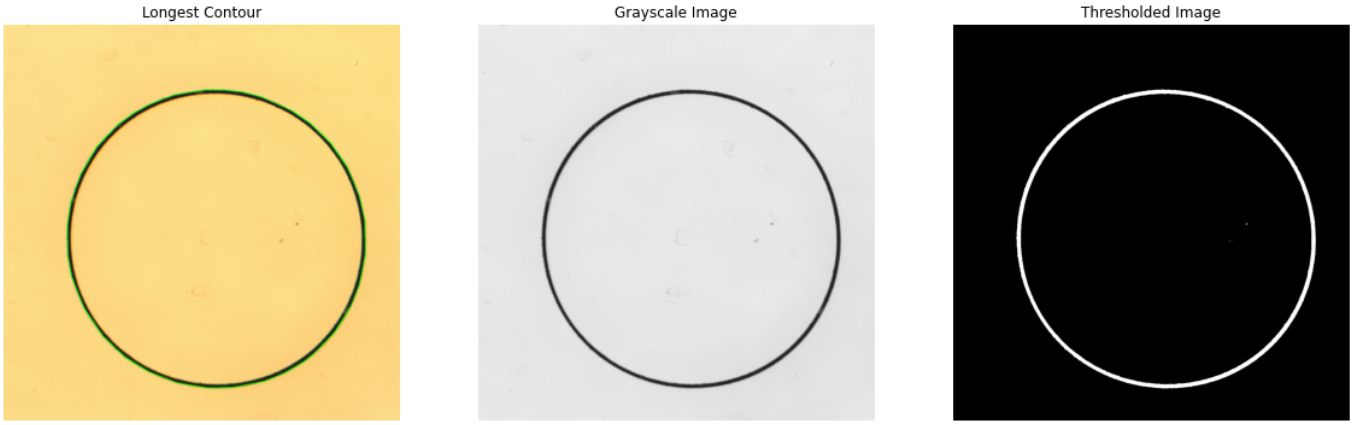

Figure 36: 450 mm/sec

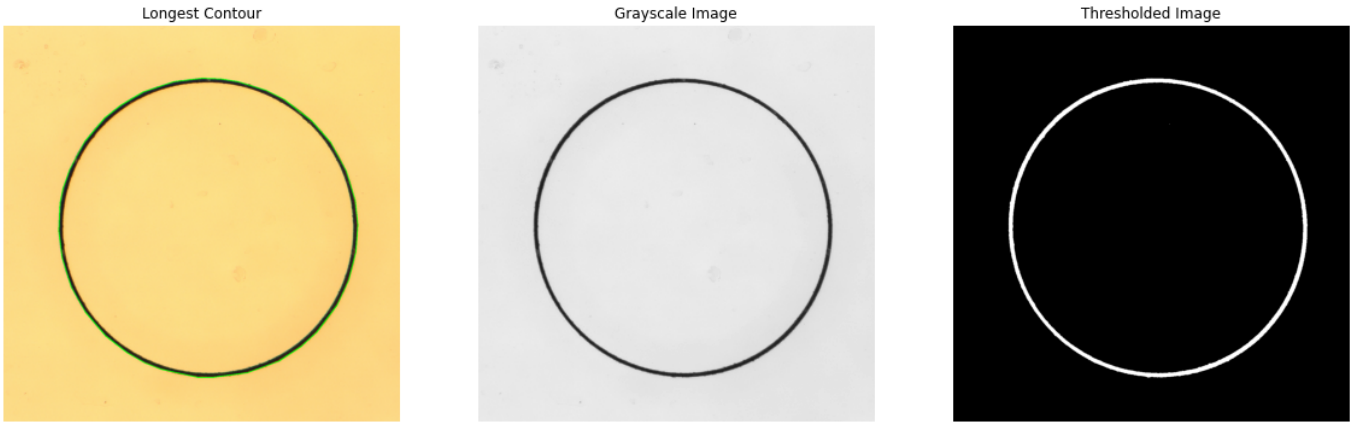

Figure 37: 500 mm/sec

J.1.3 Set 3

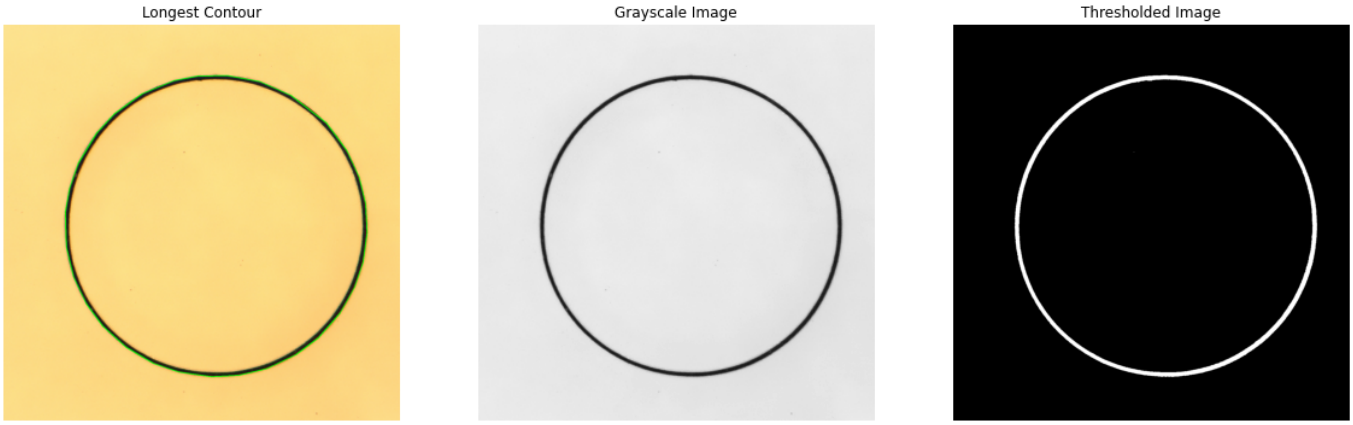

Figure 38: 50 mm/sec

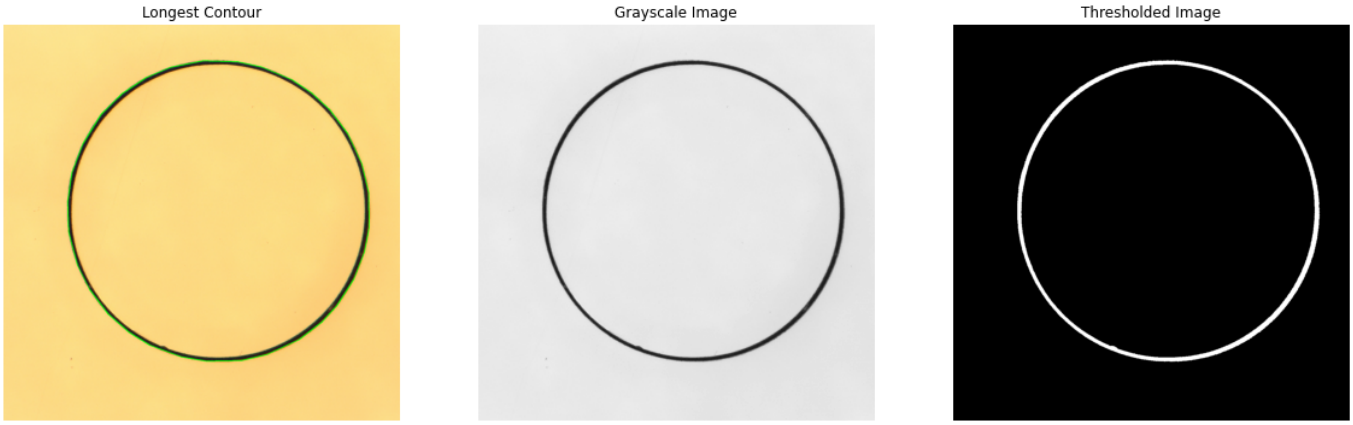

Figure 39: 100 mm/sec

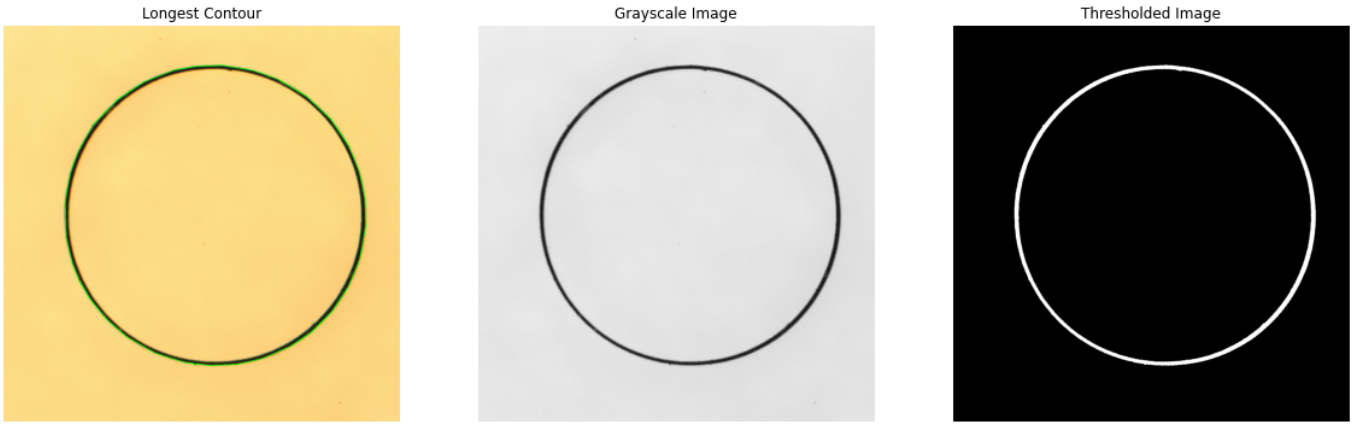

Figure 40: 150 mm/sec

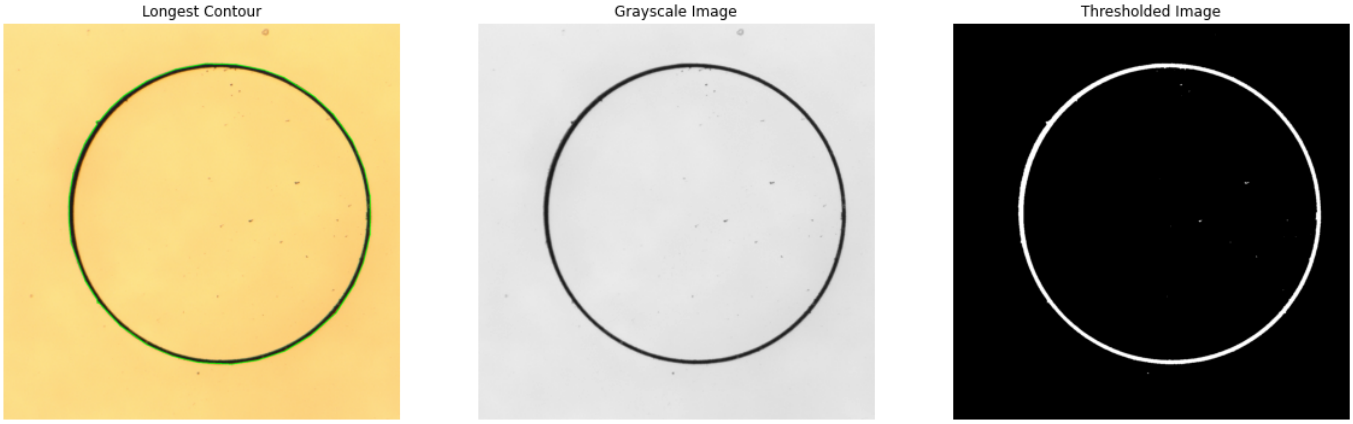

Figure 41: 200 mm/sec

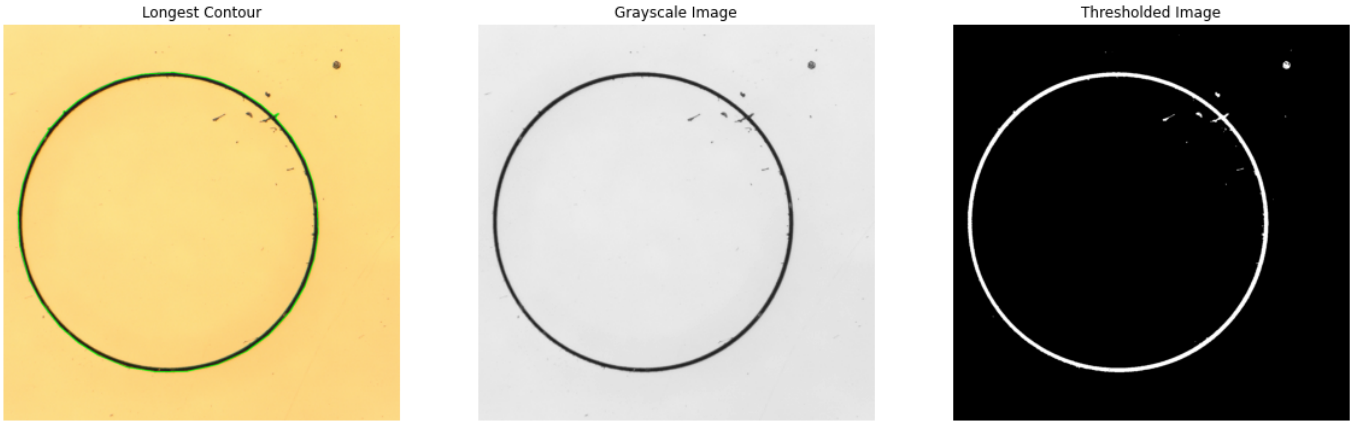

Figure 42: 250 mm/sec

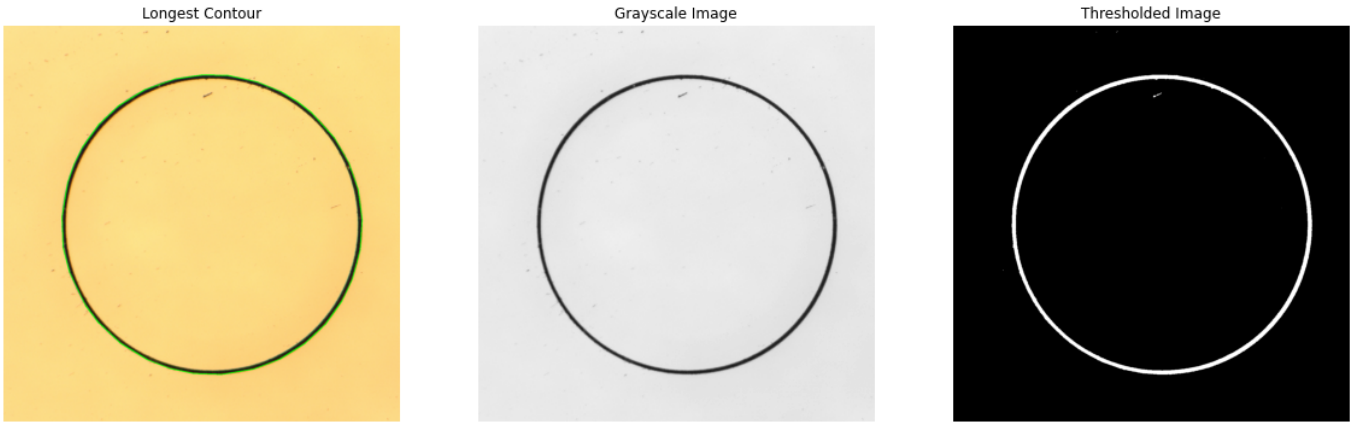

Figure 43: 300 mm/sec

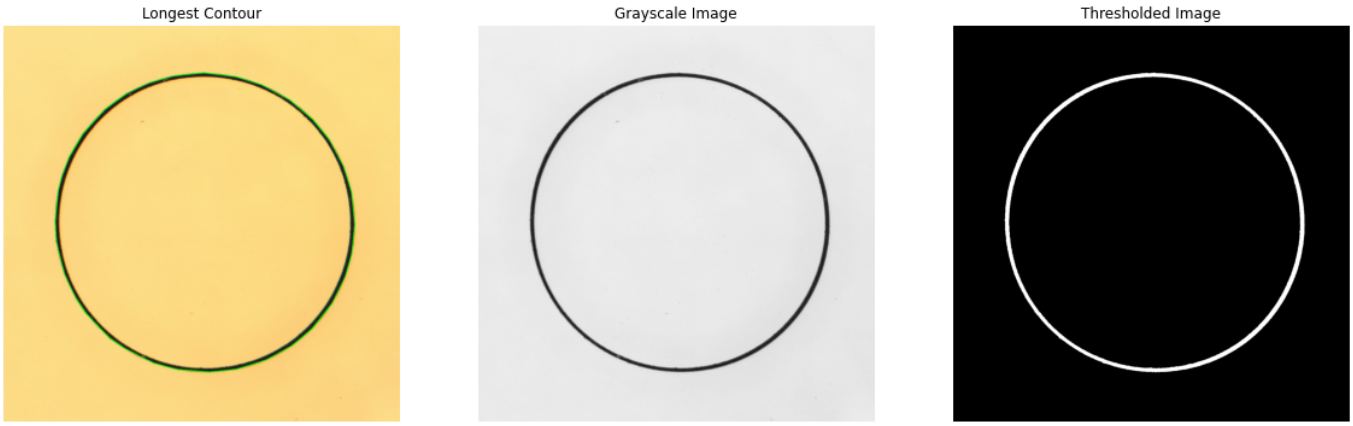

Figure 44: 350 mm/sec

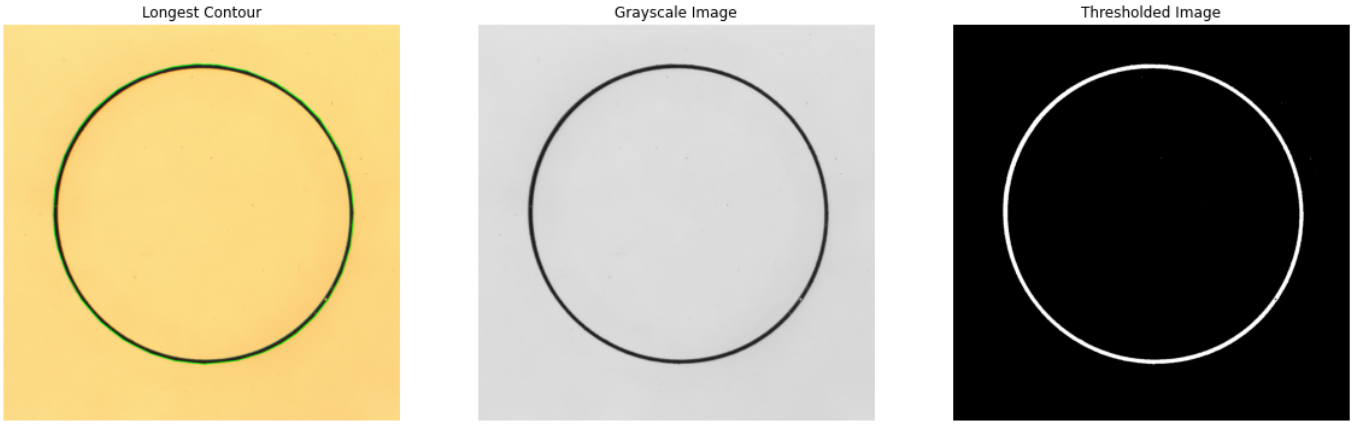

Figure 45: 400 mm/sec

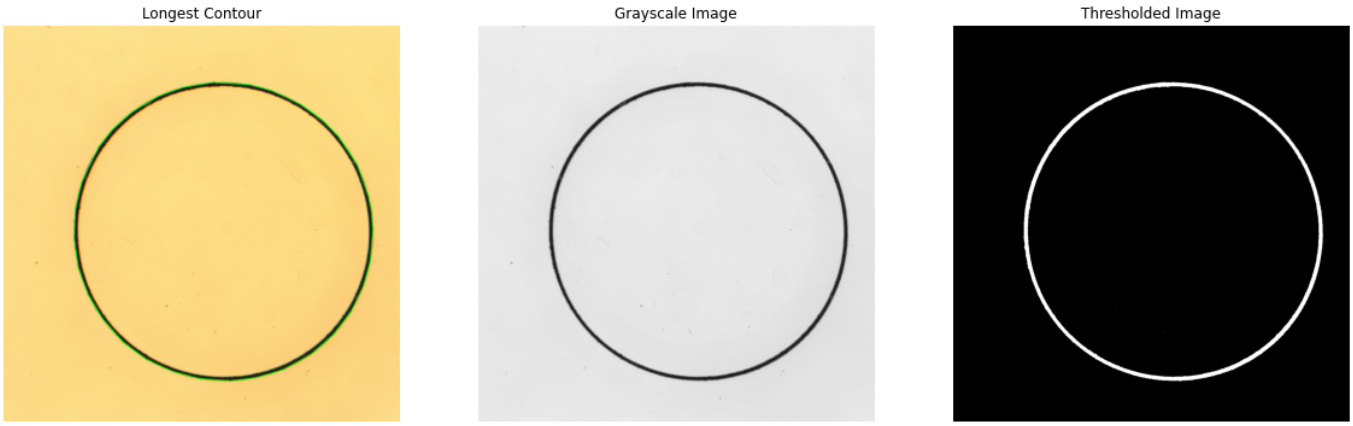

Figure 46: 450 mm/sec

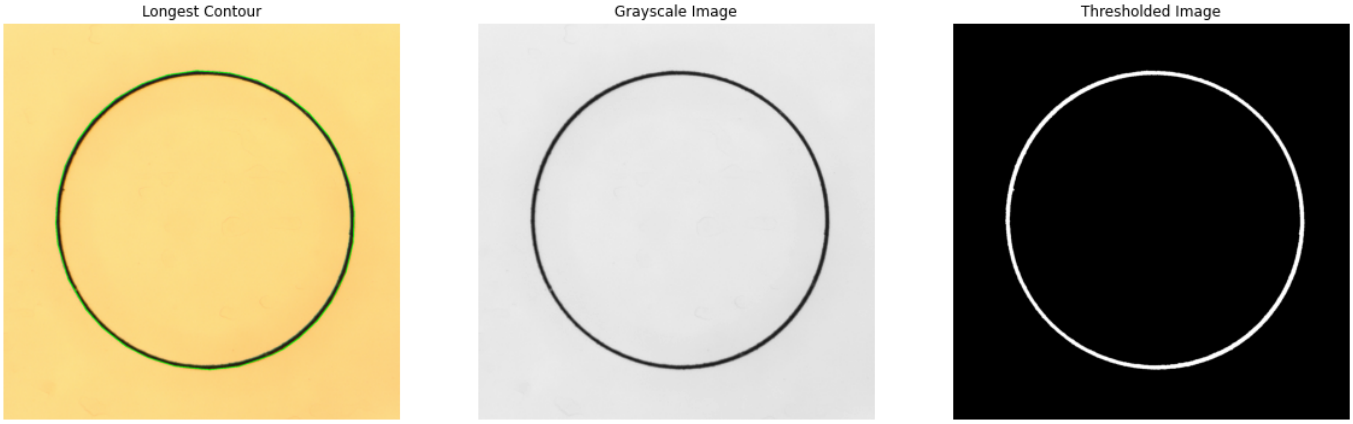

Figure 47: 500 mm/sec

Speed (mm/s)	**Avg Diameter** (μm)	**Standard Deviation** (μm)	**Roundness**
50	1040.57325575	7.027258595	0.98455550
100	1025.26590983	5.200238523	0.99172984
150	1020.71777344	3.176515607	0.98751000
200	1022.09147135	2.717326537	0.99092000
250	1018.73792860	2.461378844	0.99670000
300	1028.63749186	4.479040710	0.96884000
350	1017.66920302	3.765107617	0.98896000
400	1018.82988824	3.399998283	0.98728000
450	1015.00488281	2.952480230	0.99687000
500	1013.76139323	3.034171620	0.99486000
750	1022.57019043	5.911192820	0.90088000
1000	1004.55830892	9.866104770	0.87108000
1250	975.30097114	9.595887200	0.84191000
1500	952.89876302	12.693908750	0.81351000
1750	939.12346734	23.555044950	0.76005000
2000	829.57701325	99.747354060	0.56508000
2250	733.97047255	71.635884220	0.45307000

Table 1: Measurement Results for Set 1 at Various Speeds

Speed (mm/s)	**Avg. Diameter set 2** (μm)	**Standard Deviation** (μm)	**Roundness**
50	1020.301649	3.097520388	0.996553689
100	1018.182170	2.137344662	0.996243533
150	1017.811618	3.257210469	0.996643972
200	1024.176229	5.377769878	0.996660545
250	1016.867879	3.236092931	0.997061806
300	1014.536201	3.041706245	0.993918007
350	1017.351888	4.399214353	0.994698281
400	1020.067274	5.377736475	0.994468123
450	1014.172770	4.728723809	0.996865447
500	1013.257175	4.480508377	0.996766488

Table 2: Measurement Results for Set 2 at Various Speeds

Speed (mm/s)	**Avg. Diameter set 3** (μm)	**Standard Deviation** (μm)	**Roundness**
50	1019.996745	4.827779629	0.996118633
100	1020.913493	3.461531162	0.996550862
150	1019.996745	3.885110496	0.995106465
200	1031.306356	6.776719301	0.987915614
250	1026.421577	5.712529367	0.974855608
300	1014.841444	3.060428315	0.996853867
350	1015.147705	4.409479775	0.996757718
400	1017.741699	4.798683390	0.996757718
450	1013.906725	4.116117221	0.996779210
500	1012.846883	4.808591296	0.996612800

Table 3: Measurement Results for Set 3 at Various Speeds

J.2 Cut Width and Roughness

The next section focuses on varying the percentage of power that the laser uses to fabricate cuts. All experiments are performed with a focal point velocity of 50 mm/sec and 1000 repetitions. The scale bars in all images represent the amount of pixels in the image, converting the image to μm you have to multiply with the factor 5/44.

J.2.1 Set 1

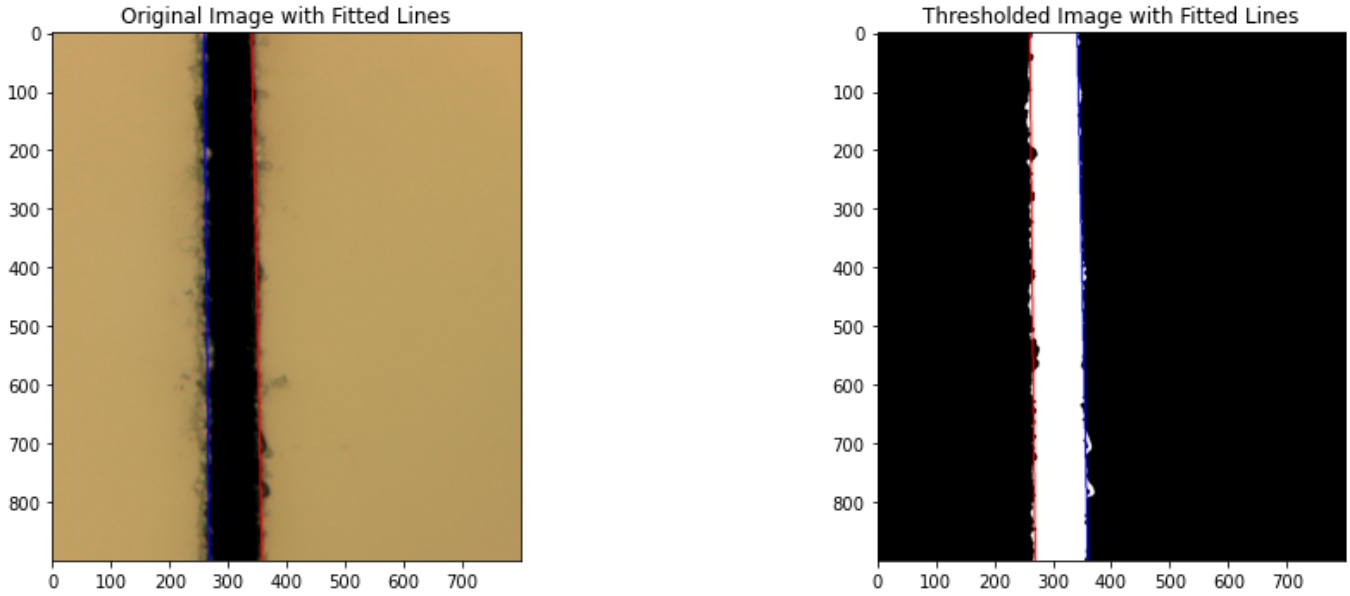

Figure 48: 2 %

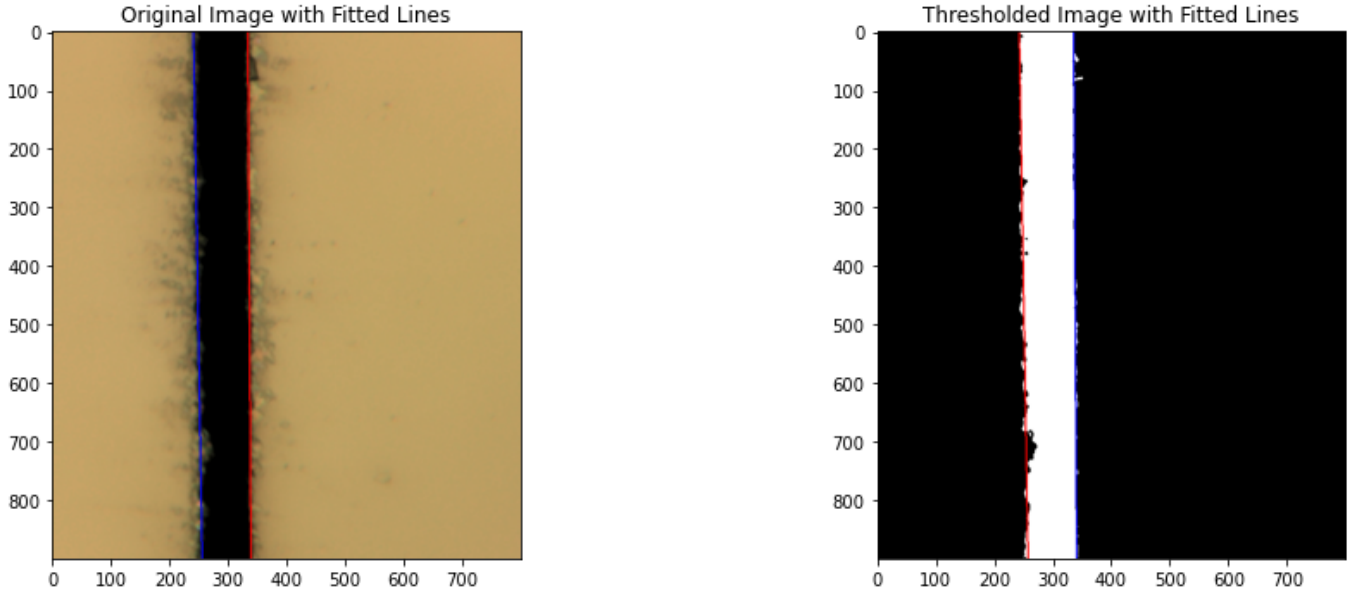

Figure 49: 3 %

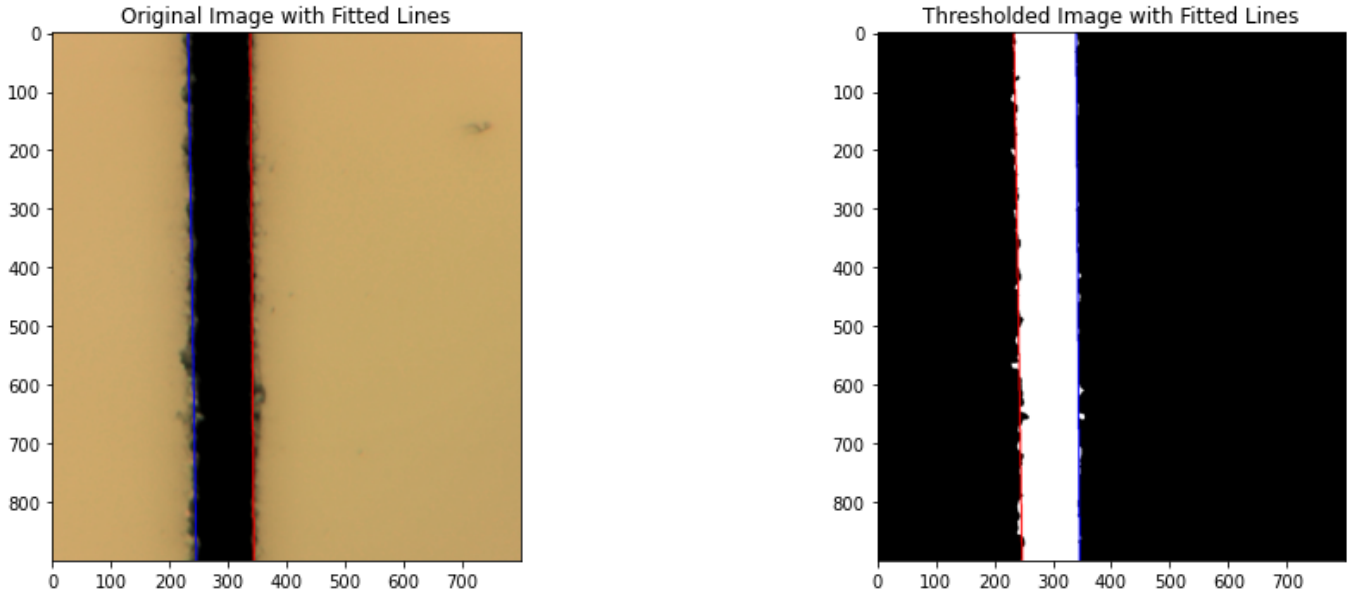

Figure 50: 4 %

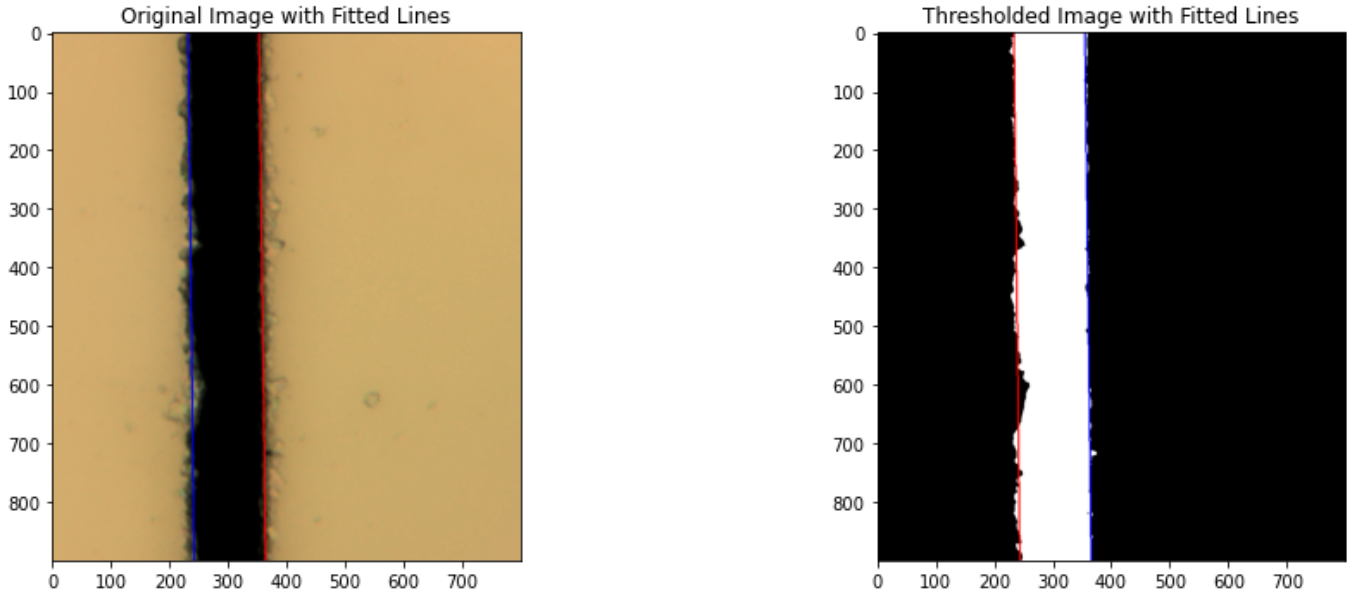

Figure 51: 5 %

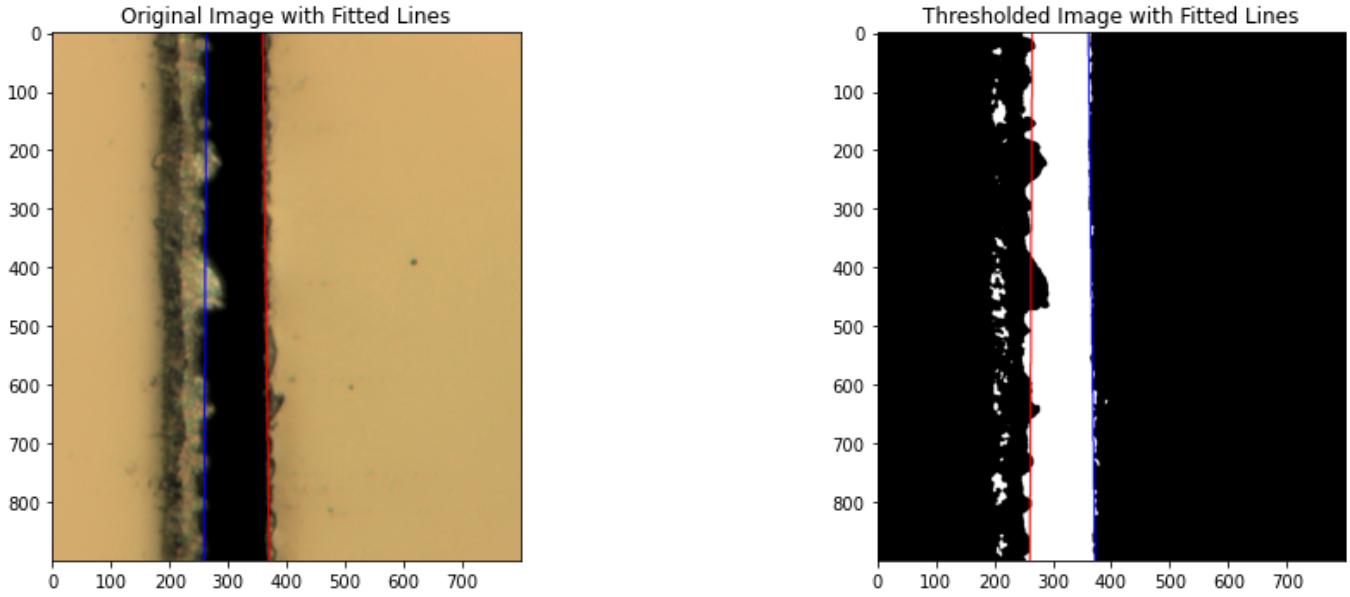

Figure 52: 6 %

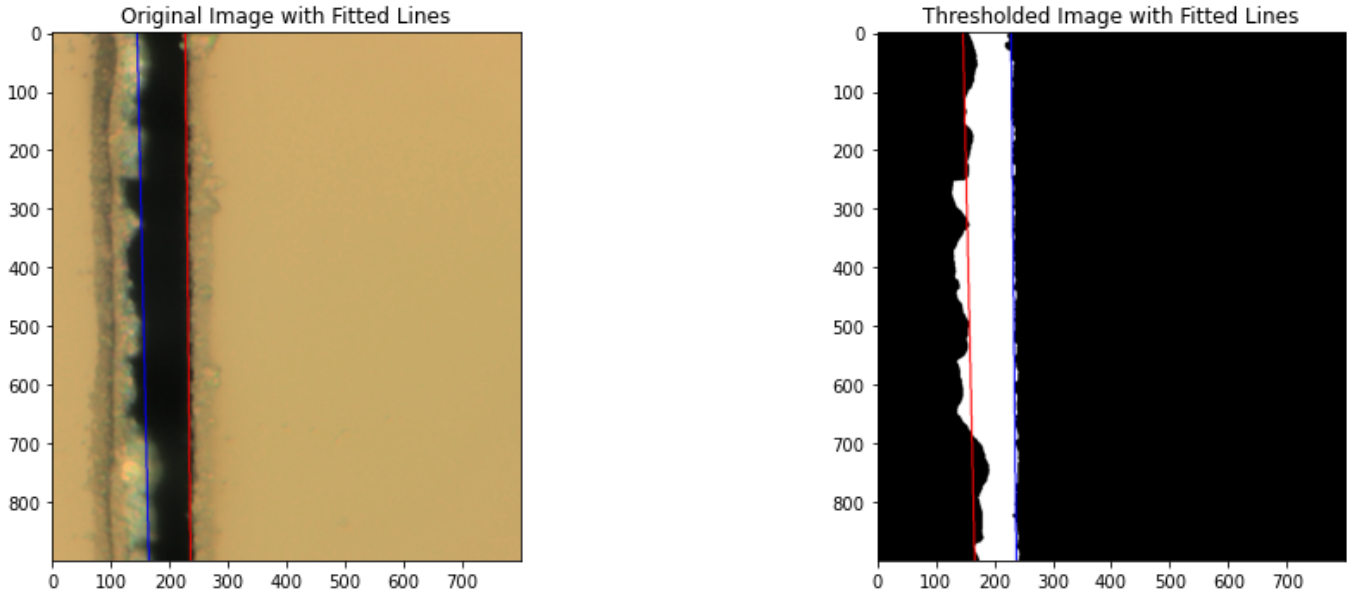

Figure 53: 7 %

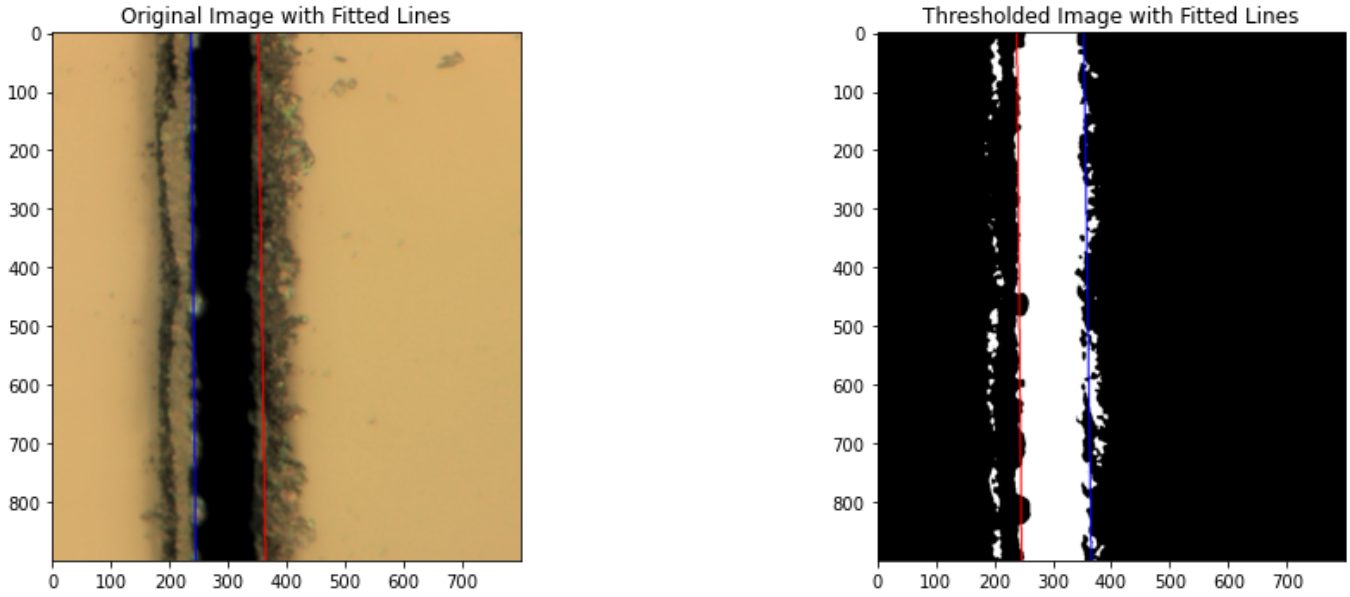

Figure 54: 8 %

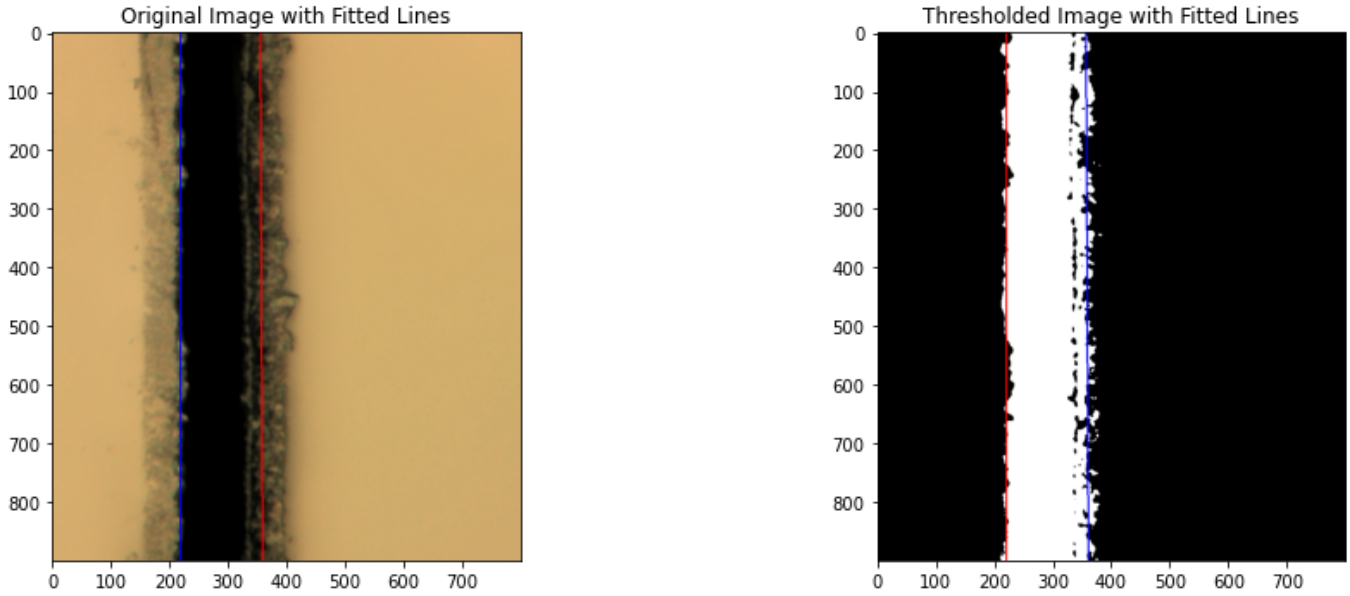

Figure 55: 9 %

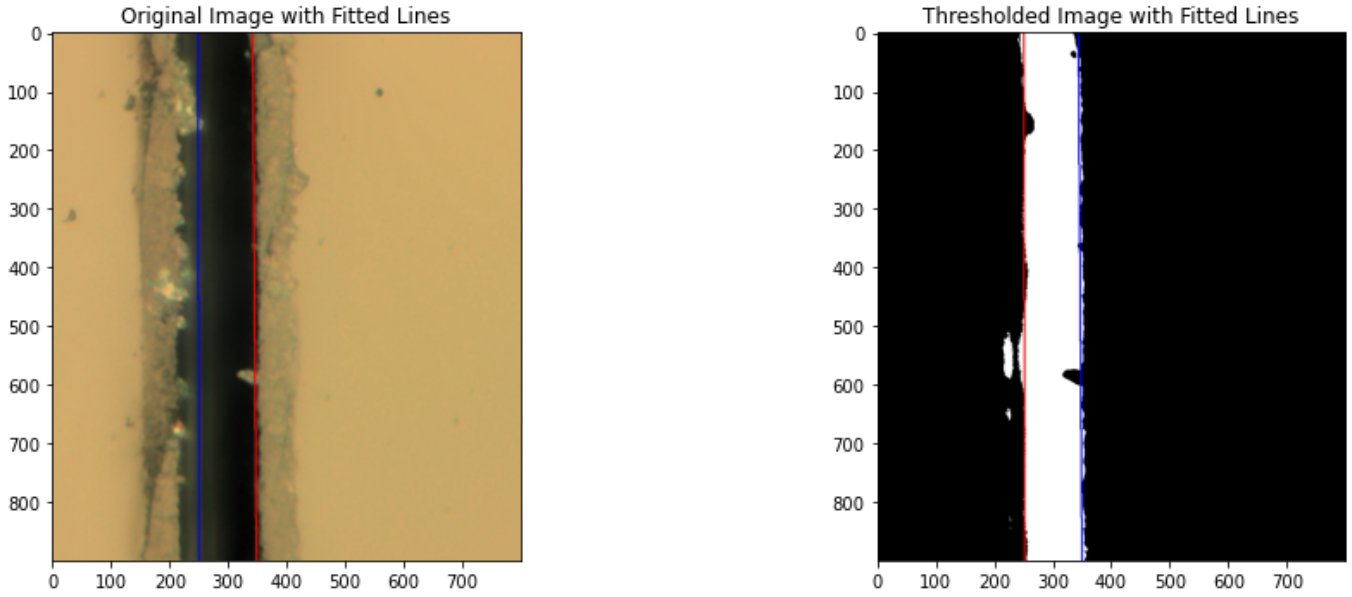

Figure 56: 10 %

J.2.2 Set 2

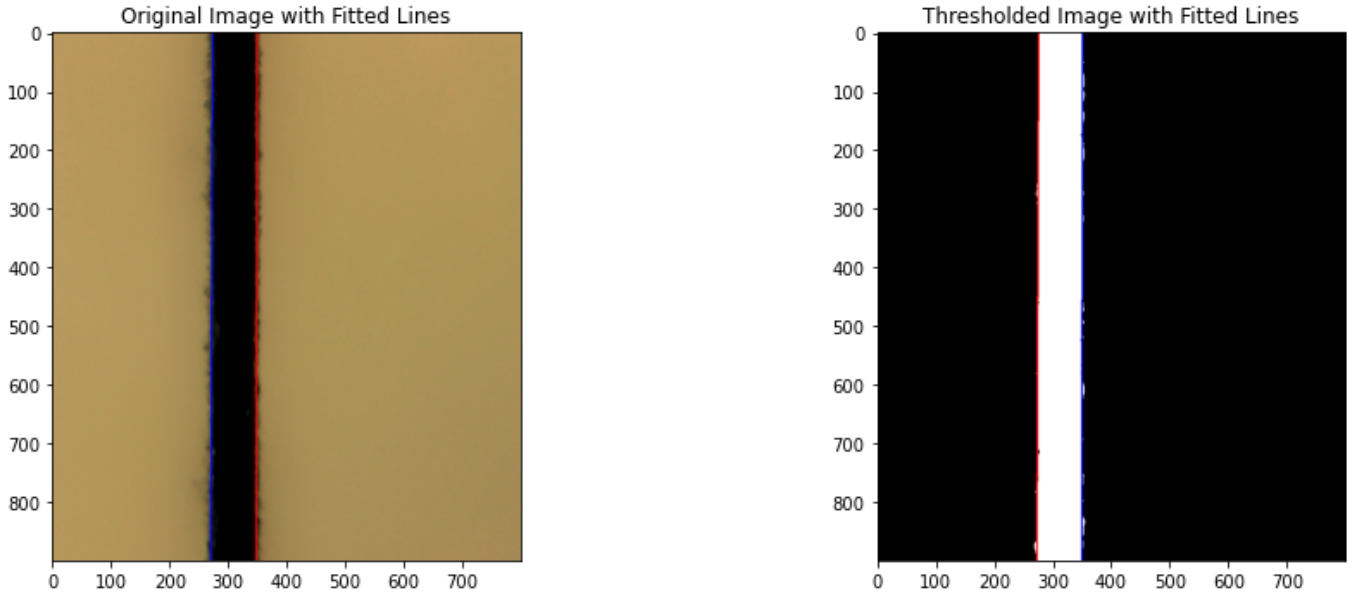

Figure 57: 2 %

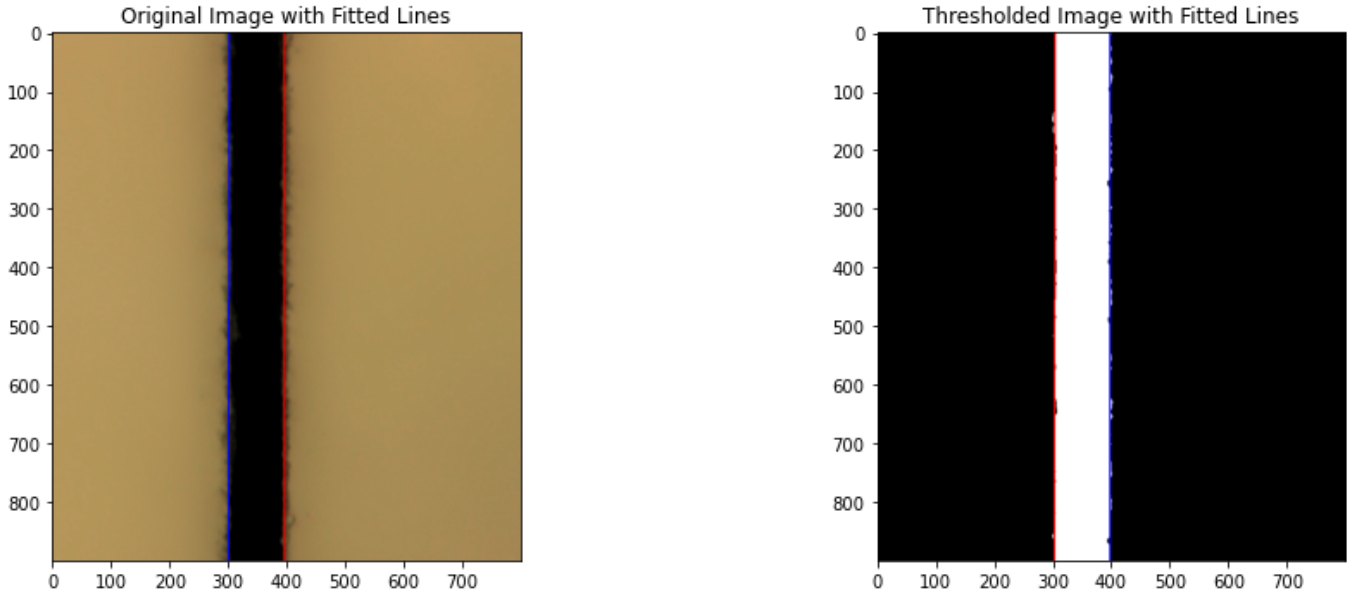

Figure 58: 3 %

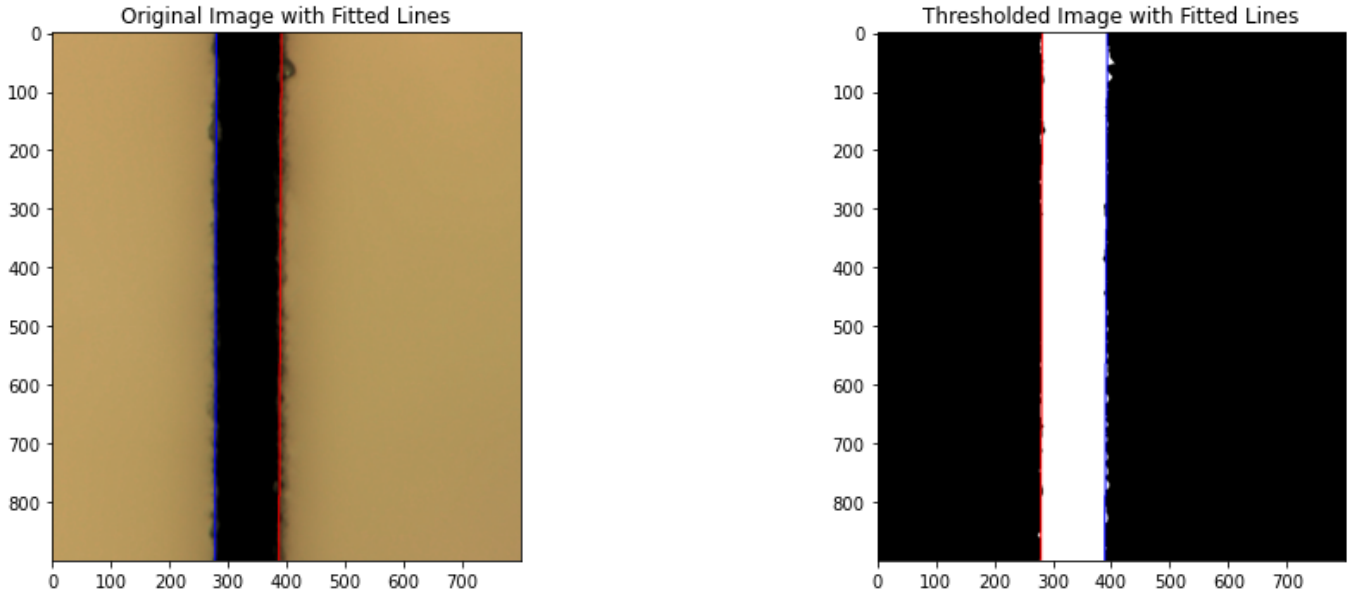

Figure 59: 4 %

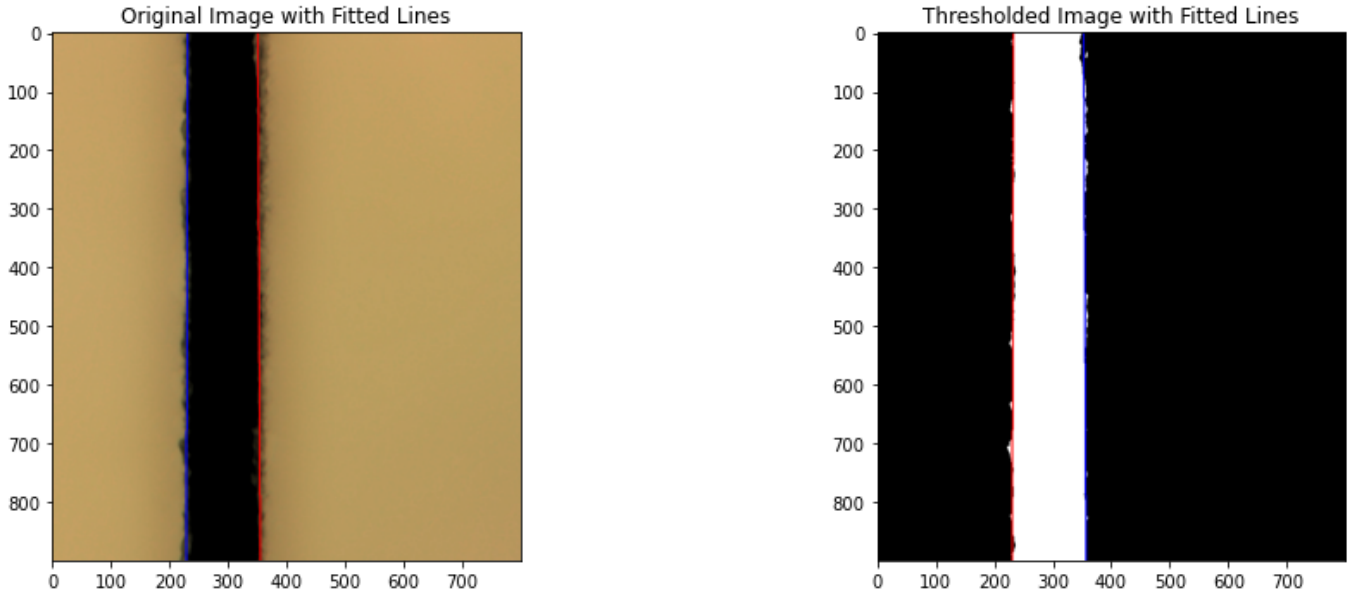

Figure 60: 5 %

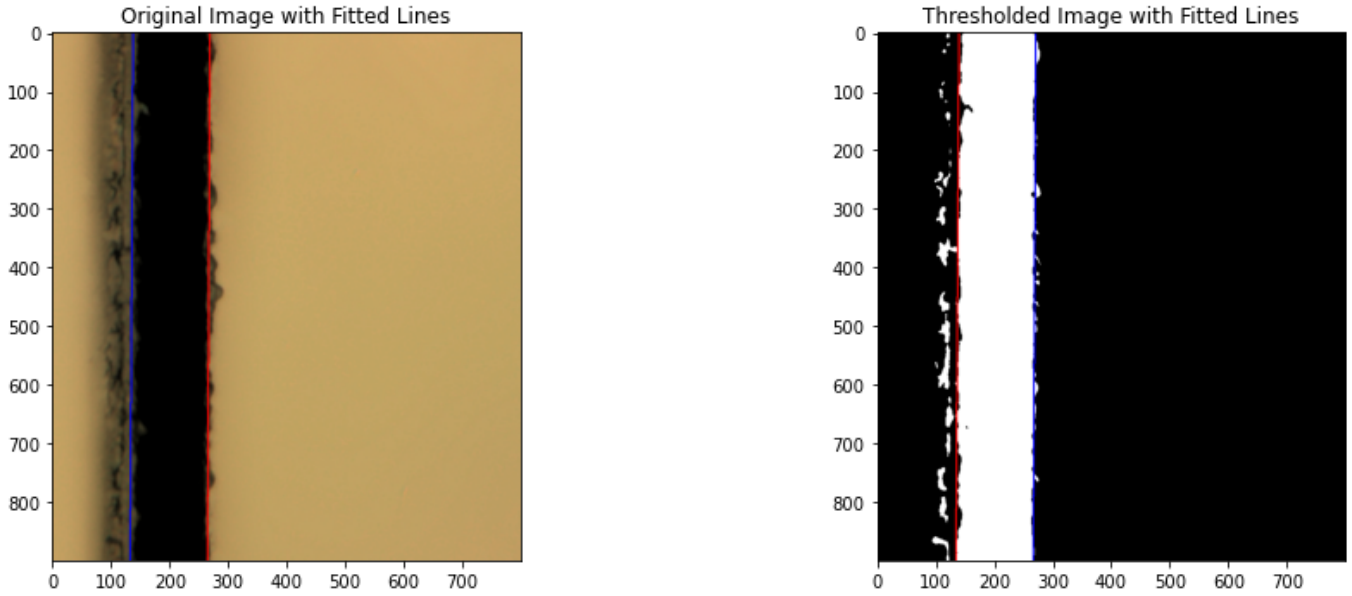

Figure 61: 6 %

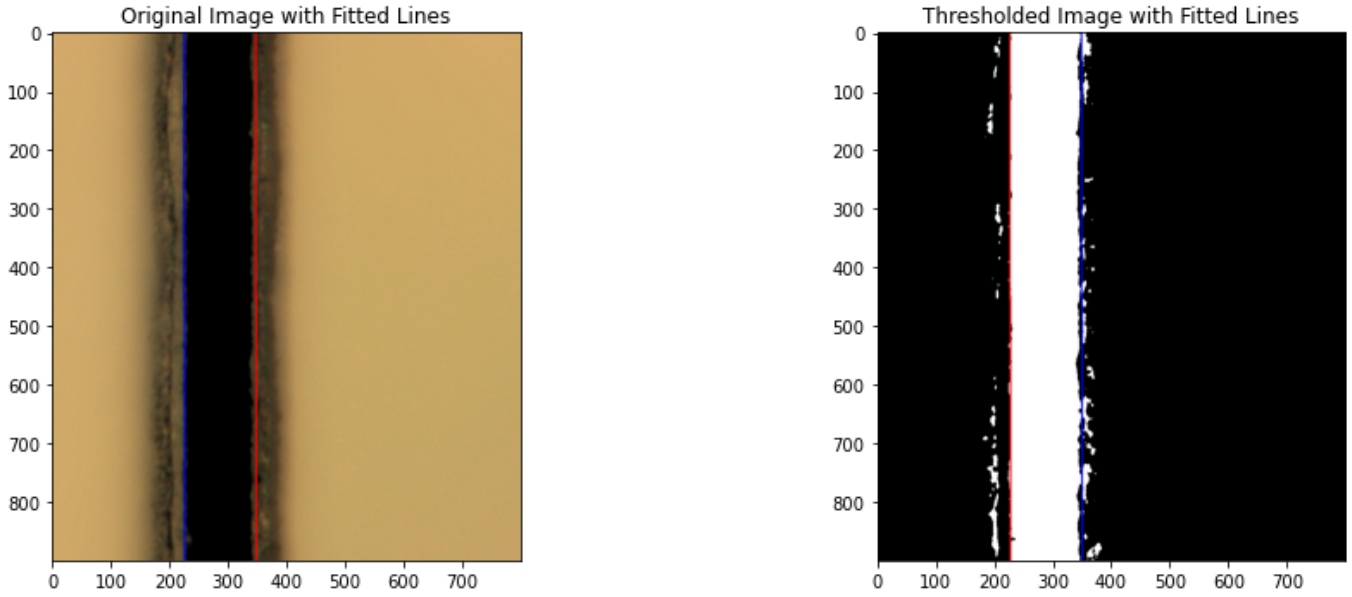

Figure 62: 7 %

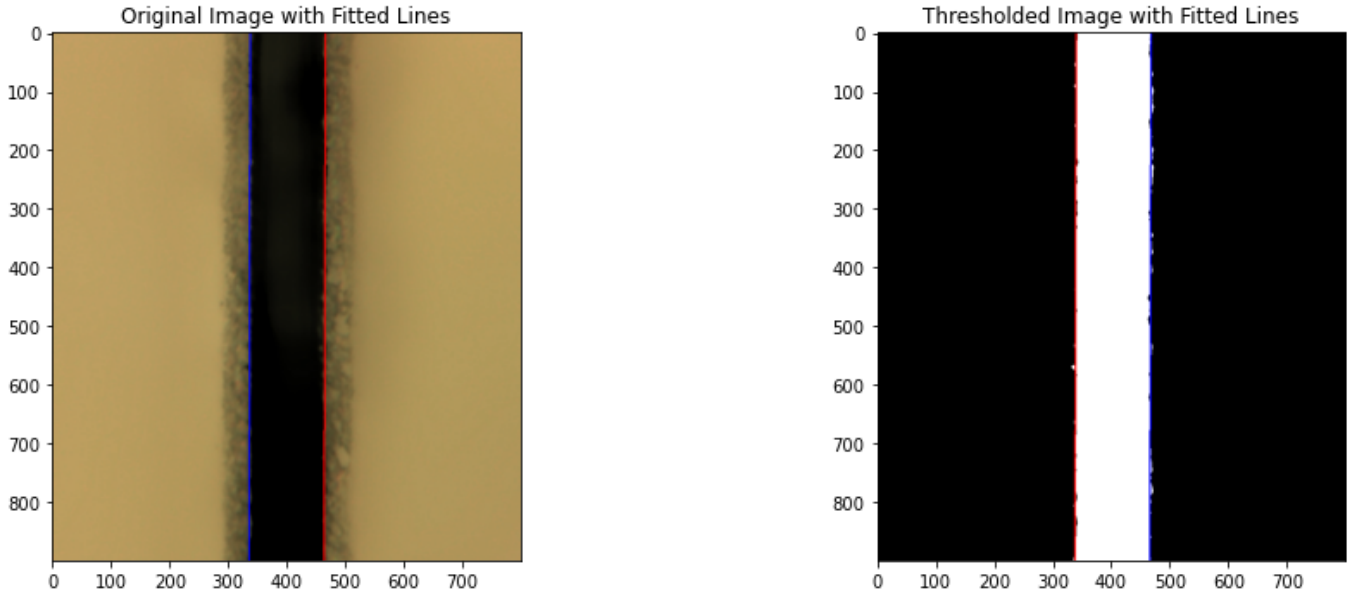

Figure 63: 8 %

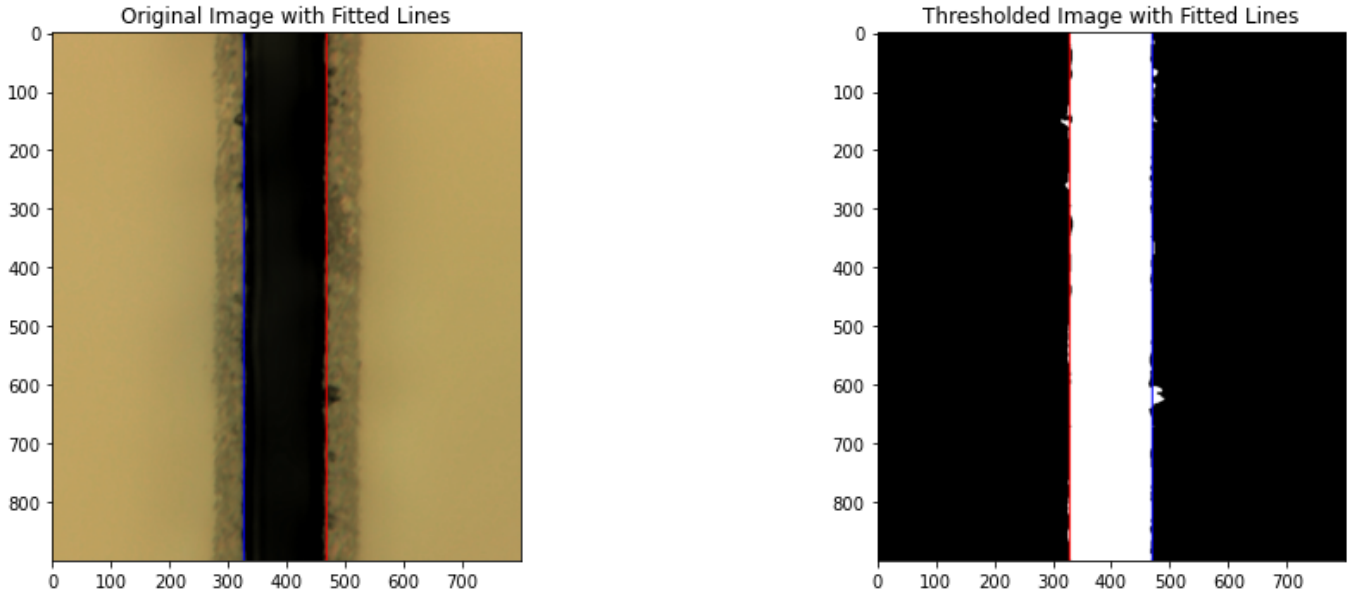

Figure 64: 9 %

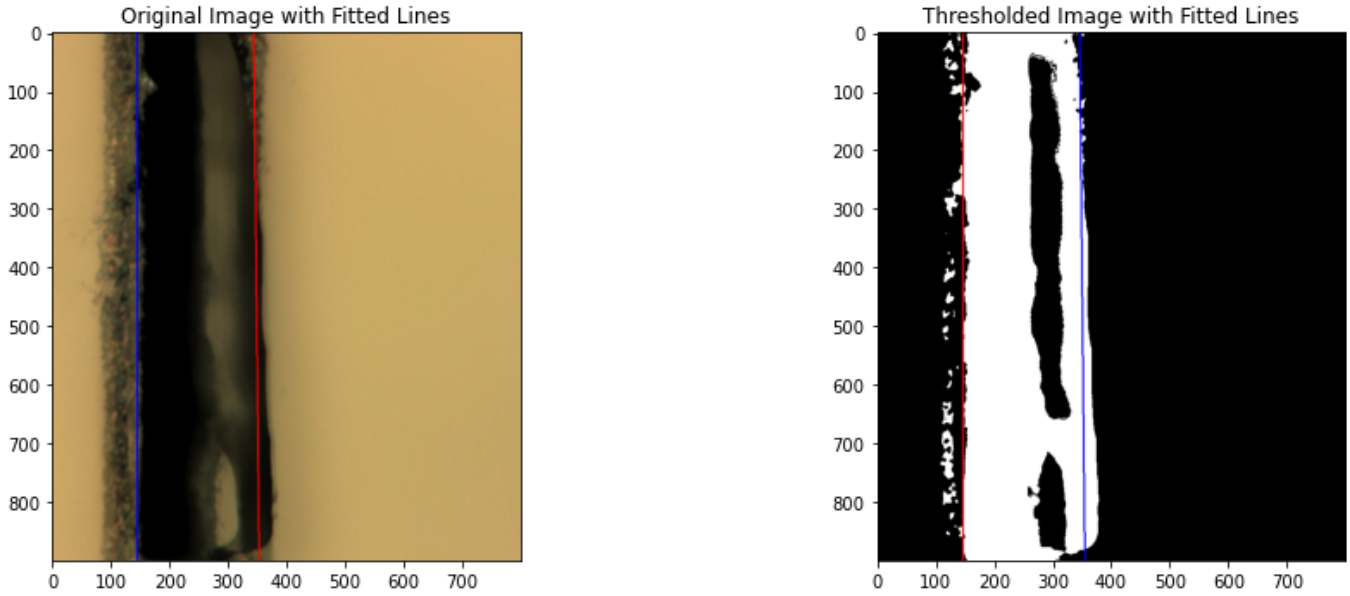

Figure 65: 10 %

J.2.3 Set 3

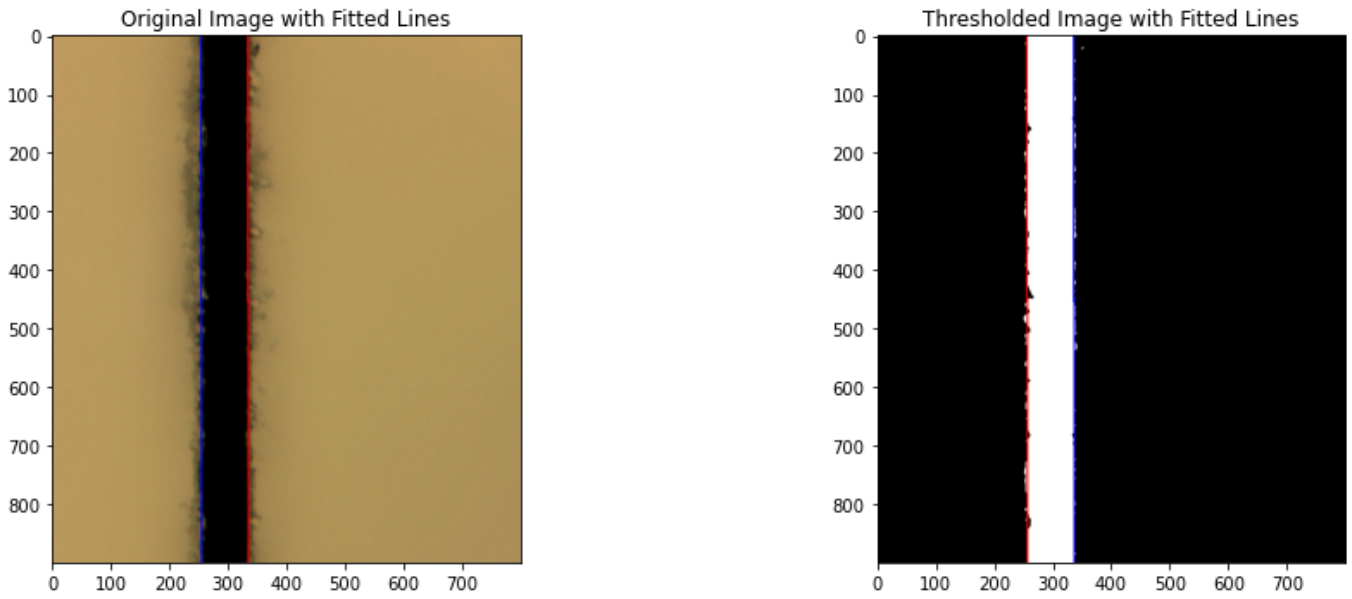

Figure 66: 2 %

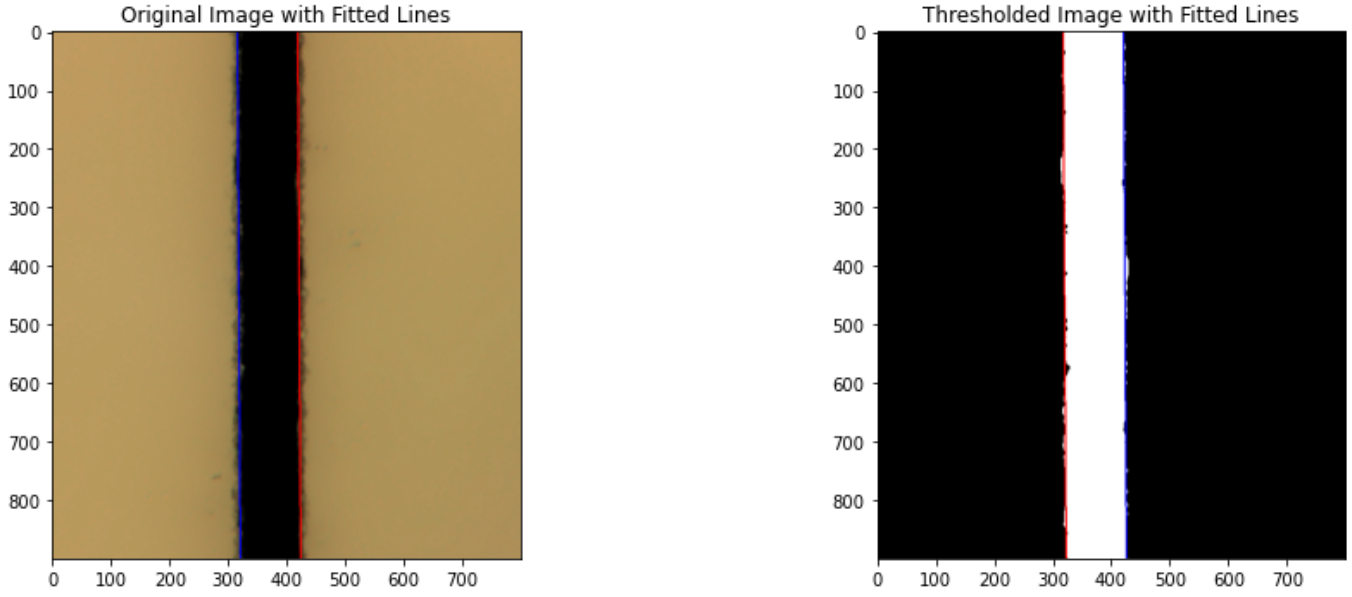

Figure 67: 3 %

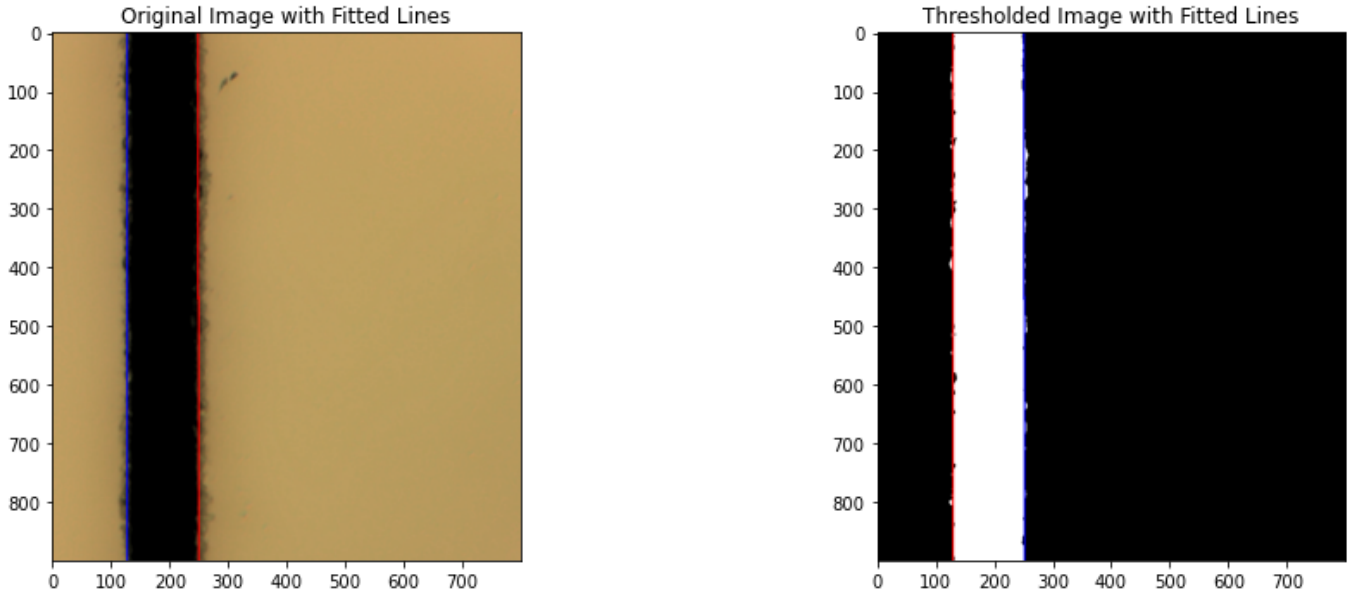

Figure 68: 4 %

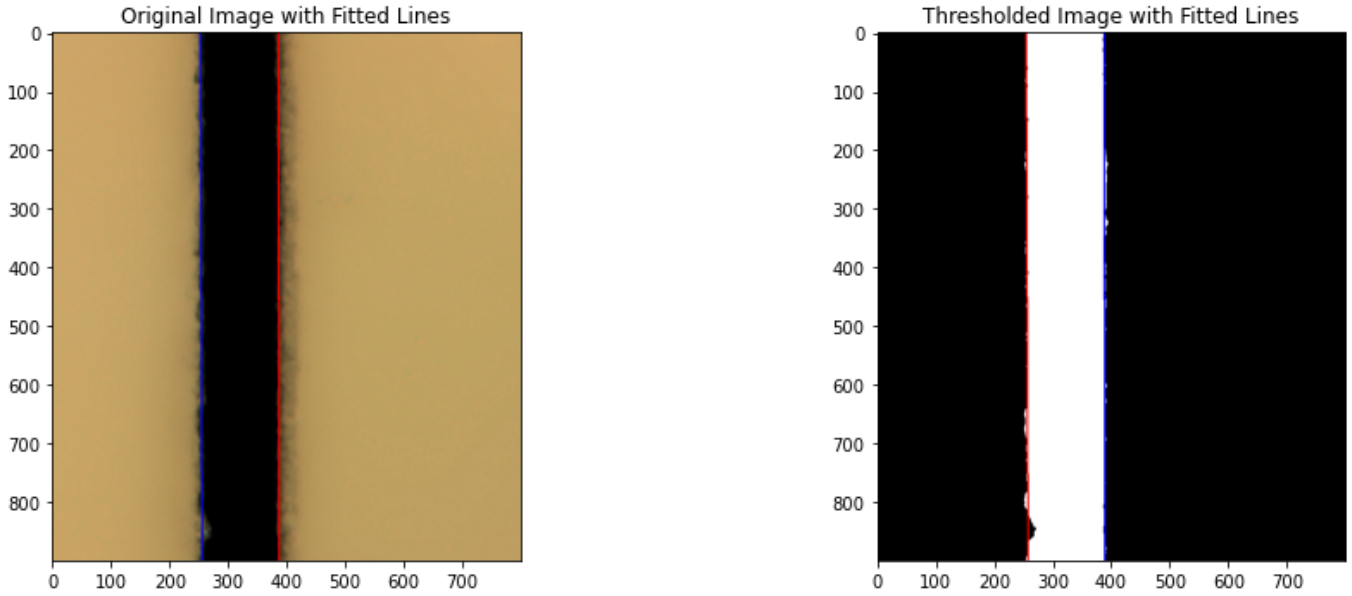

Figure 69: 5 %

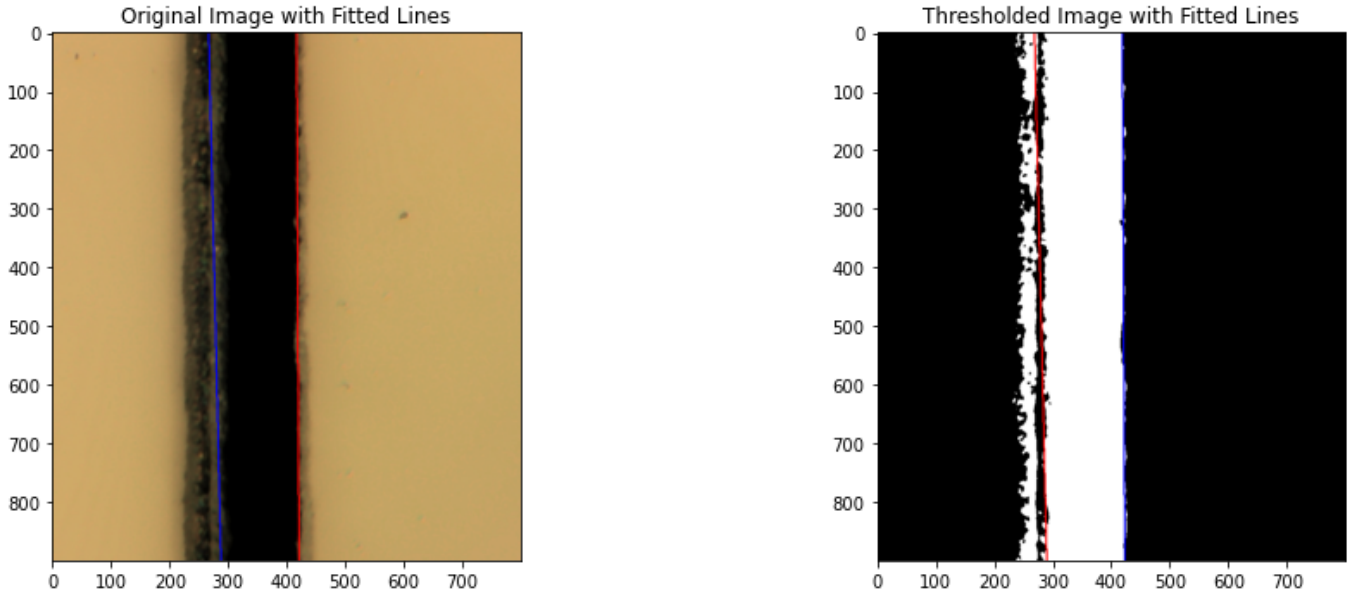

Figure 70: 6 %

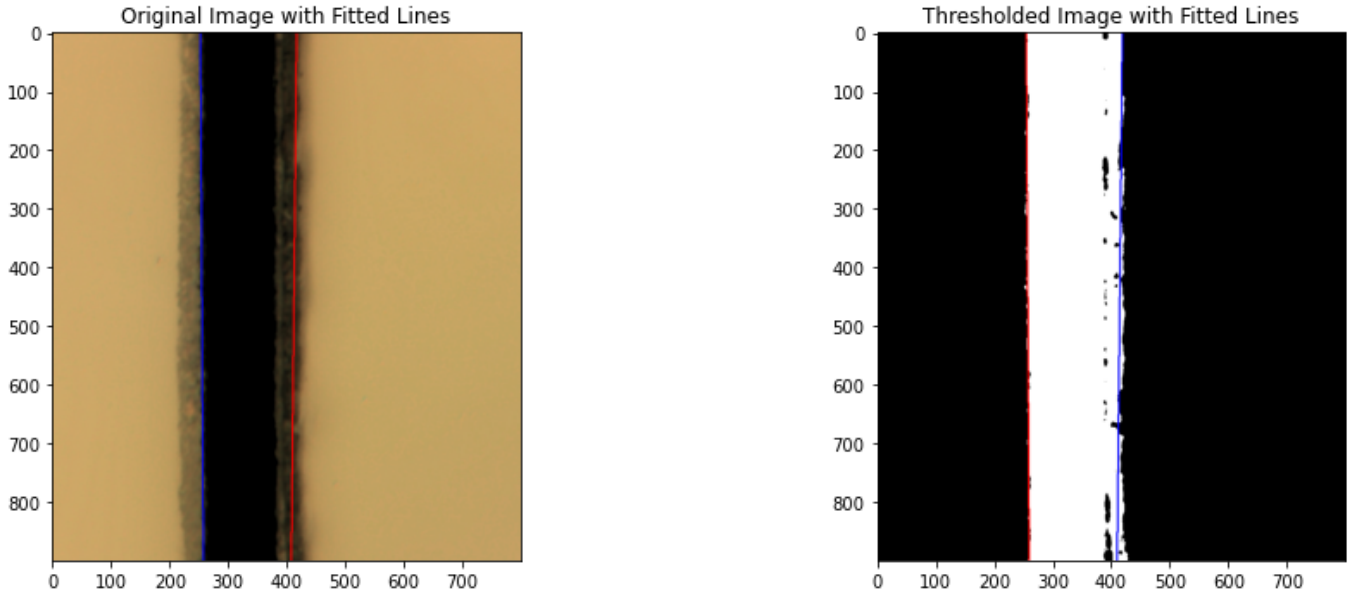

Figure 71: 7 %

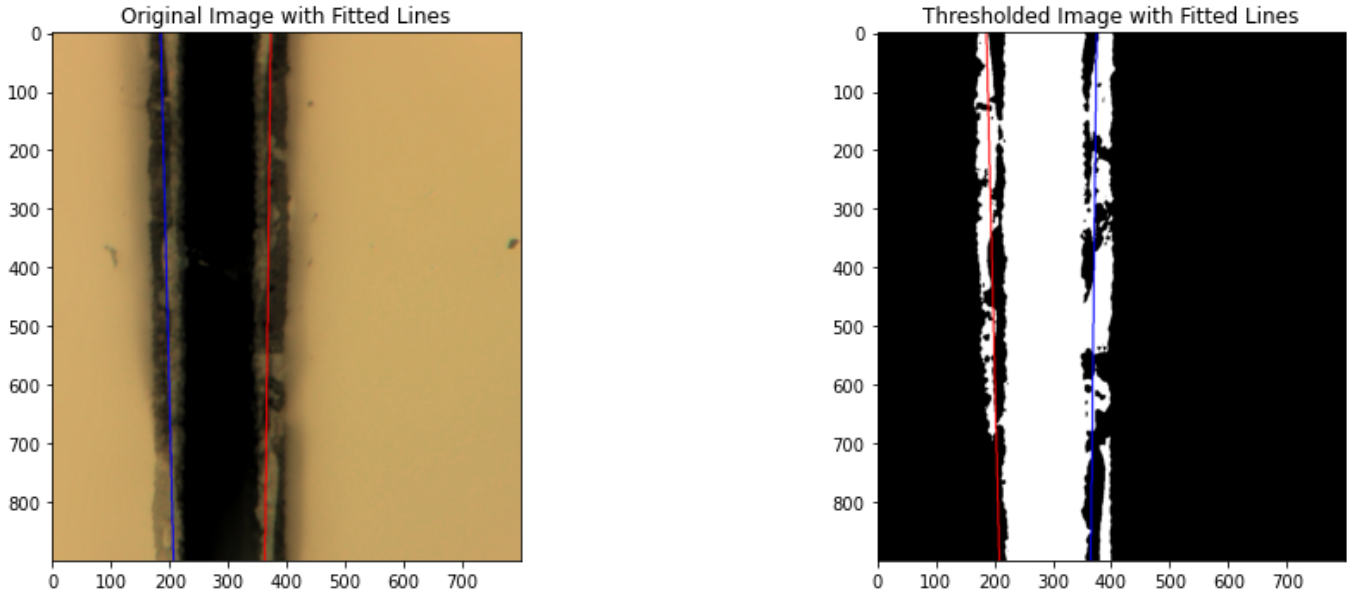

Figure 72: 8 %

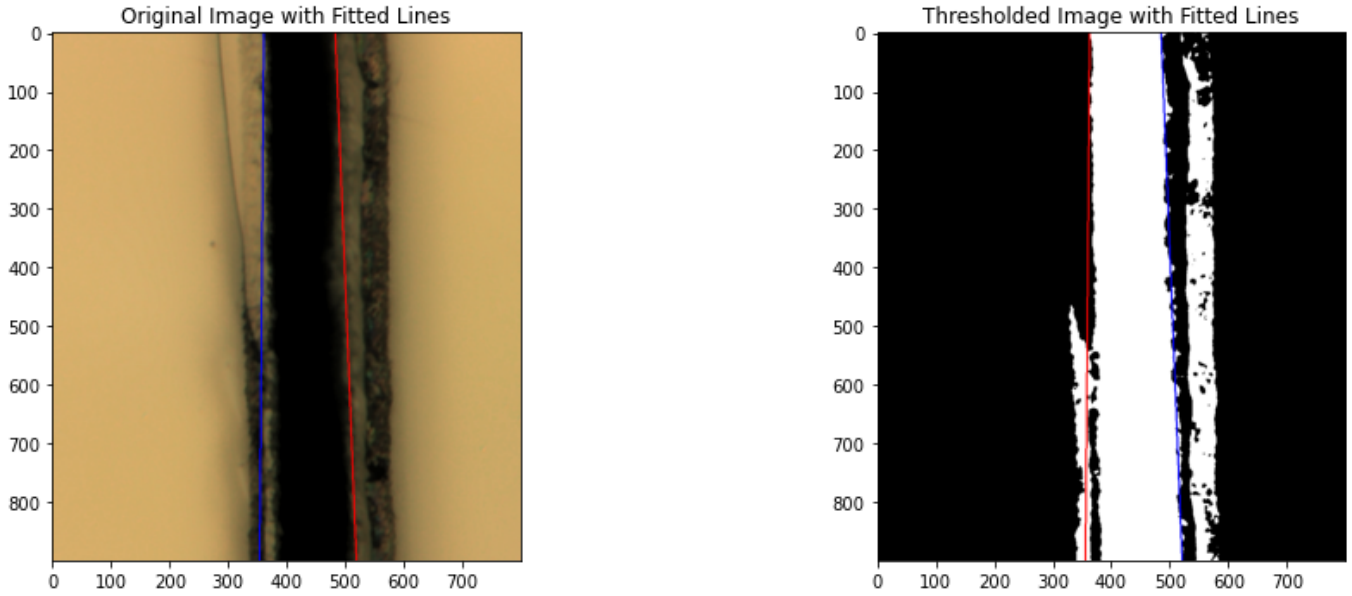

Figure 73: 9 %

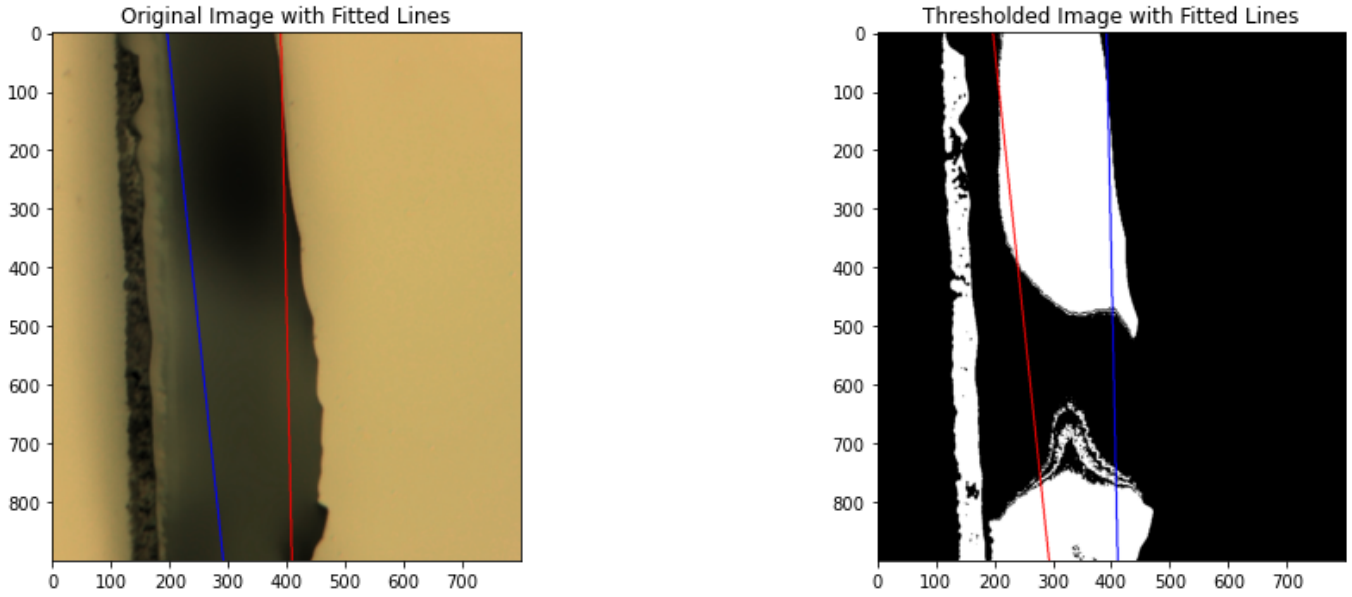

Figure 74: 10 %

The measured cut widths are presented in Table 4, along with the corresponding standard deviations for these measurements.

Power	**Width 1** (μm)	**SD 1** (μm)	**Width 2** (μm)	**SD 2** (μm)	**Width 3** (μm)	**SD 3** (μm)
	Set 1		**Set 2**		**Set 3**	
2	9.78923	0.29418	8.66214	0.06055	9.11696	0.01863
3	9.99245	0.36336	10.68068	0.00316	11.72465	0.01108
4	11.57339	0.23395	12.52222	0.04268	13.79252	0.00521
5	13.78720	0.01476	13.99163	0.21893	15.03092	0.07358
6	11.81367	0.52246	14.94020	0.00837	16.05895	0.54420
7	8.74537	0.39378	13.81576	0.00991	17.81789	0.47329
8	13.20549	0.16971	14.48821	0.00530	19.52113	1.07810
9	15.70355	0.14046	16.05056	0.01729	16.30844	1.45313
10	10.86973	0.17325	23.15098	0.31201	17.63685	2.55819

Table 4: Measurement Results for Widths and Standard Deviations in Set 1, Set 2, and Set 3

Tables 5, 6, and 7 represent the extreme distances with reference to the line that is fitted to each edge. With the column left side represent the dimensions in respect to the left edge of the cut. The column named right side refers to the edge that is on the right side of the image. The minimum value represents the distance in the -x direction, the max represents the maximum distance to the right side of the fit.

Power (%)	**Max (μm)**	**Min (μm)**	**SD (μm)**	**Max (μm)**	**Min (μm)**	**SD (μm)**
	Blue side set 1			**red side set 1**		
2	1.33674	-1.07668	0.49324	1.43918	-0.96233	0.38994
3	2.09431	-0.89361	0.53337	1.56891	-0.48342	0.30221
4	1.74350	-1.51507	0.44475	1.03605	-0.46497	0.24036
5	2.24883	-1.19704	0.67071	1.24956	-0.64456	0.25995
6	3.62232	-1.90026	1.32138	0.93881	-0.62635	0.30967
7	3.01059	-2.75878	1.63978	0.64629	-5.10511	0.70134
8	1.88634	-1.32501	0.70577	3.52567	-2.62799	1.24385
9	1.54279	-1.18902	0.60403	2.13278	-3.04269	1.03298
10	2.07537	-1.38209	0.59773	0.94420	-3.71013	0.85063

Table 5: Measurement Results for Set 1

Power (%)	**Max (μm)**	**Min (μm)**	**SD (μm)**	**Max (μm)**	**Min (μm)**	**SD (μm)**
	Blue side set 2			**red side set 2**		
2	0.47131	-0.49896	0.15464	0.51070	-0.47237	0.18168
3	0.43312	-0.52273	0.17369	0.43243	-0.68698	0.20983
4	0.65876	-0.60296	0.20856	1.44515	-0.78346	0.30095
5	0.64884	-0.98701	0.27680	0.65204	-0.95062	0.30935
6	2.87785	-4.14618	1.15952	0.96470	-0.70004	0.37933
7	0.97102	-0.49481	0.22146	2.05303	-1.22517	0.84679
8	0.44492	-0.86698	0.19441	0.55819	-0.61037	0.24745
9	0.66310	-1.61338	0.35582	2.24377	-0.82683	0.56464
10	3.42834	-3.60372	1.13295	2.75541	-5.76902	1.74717

Table 6: Measurement Results for Set 2

Power (%)	**Max (μm)**	**Min (μm)**	**SD (μm)**	**Max (μm)**	**Min (μm)**	**SD (μm)**
	Left side set 3			**red side set 3**		
2	1.26580	-0.67308	0.31969	0.43521	-0.49036	0.15827
3	0.96402	-0.66143	0.26134	0.59188	-0.59020	0.19673
4	0.73008	-0.75829	0.27727	0.70229	-0.56874	0.26449
5	1.59581	-0.66285	0.33745	0.59485	-0.48015	0.19451
6	2.35649	-3.78498	1.39991	0.53272	-0.80678	0.25074
7	0.55187	-0.66149	0.22289	2.03340	-3.89720	1.08912
8	3.64600	-2.96885	1.86091	3.71201	-3.06328	1.99845
9	3.13611	-3.62392	1.78812	1.50583	-1.44508	0.53144
10	5.42705	-2.33636	1.72394	4.81038	-11.82479	4.22821

Table 7: Measurement Results for Set 3

J.3 Depth to Repetitions

In this section the analysis is made on the effect of repetitions to the depth of the cut. Using a focal point velocity of 50 mm/sec and a power of 3%.

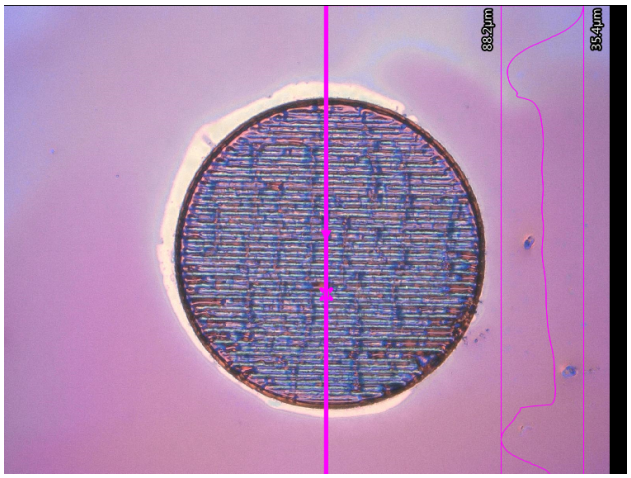

(a) 50 reps

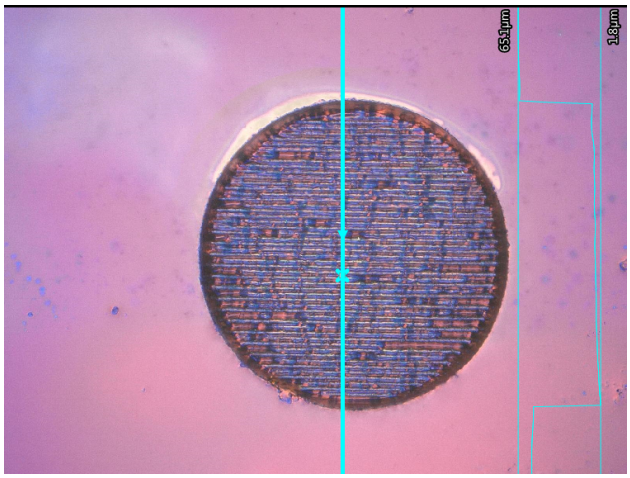

(b) 100 reps

Figure 75

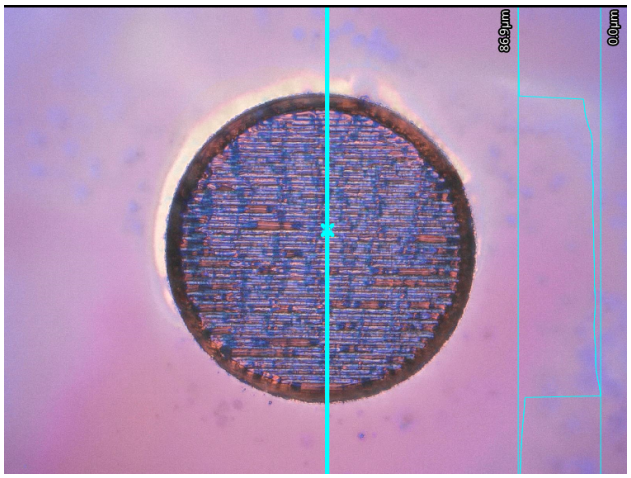

(a) 150 reps

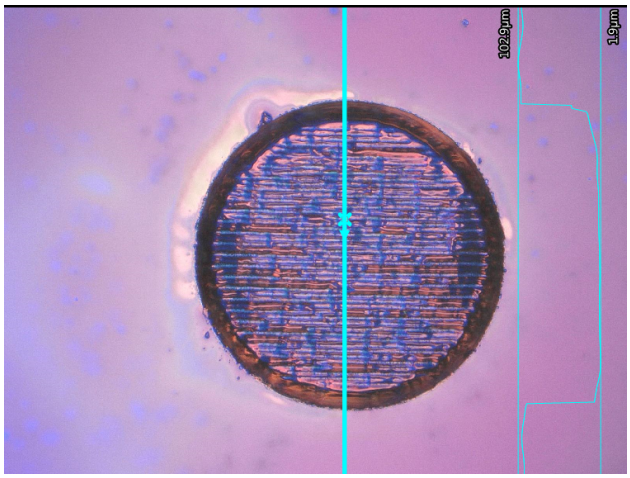

(b) 200 reps

Figure 76

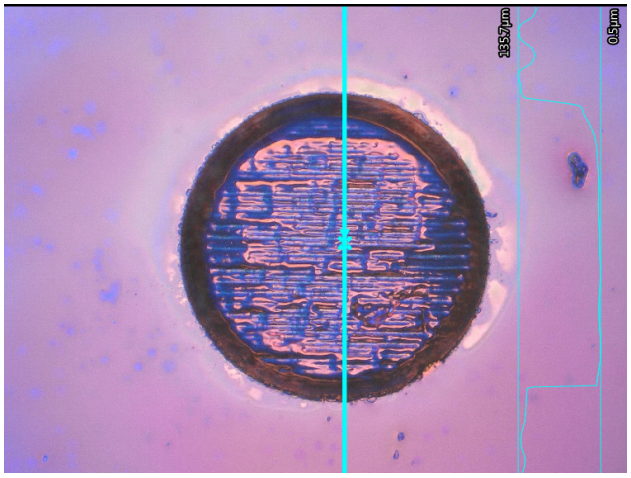

(a) 250 reps

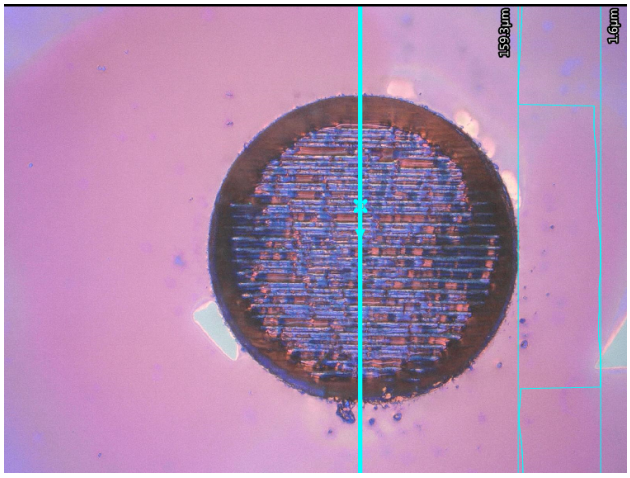

(b) 300 reps

Figure 77

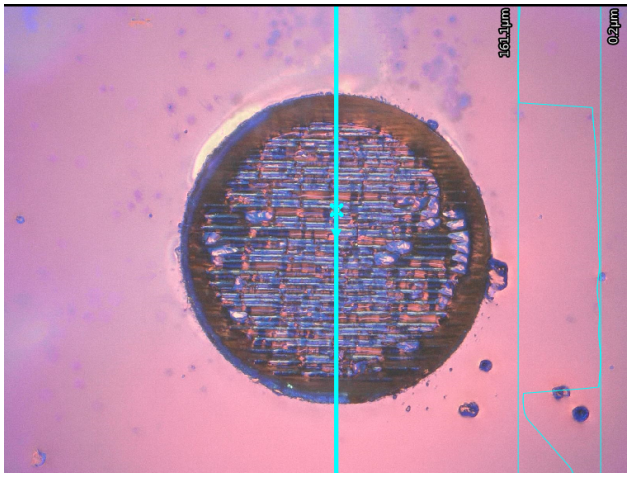

(a) 350 reps

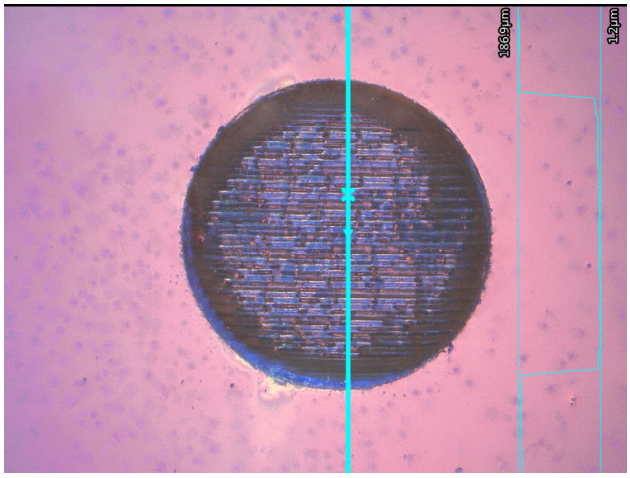

(b) 400 reps

Figure 78

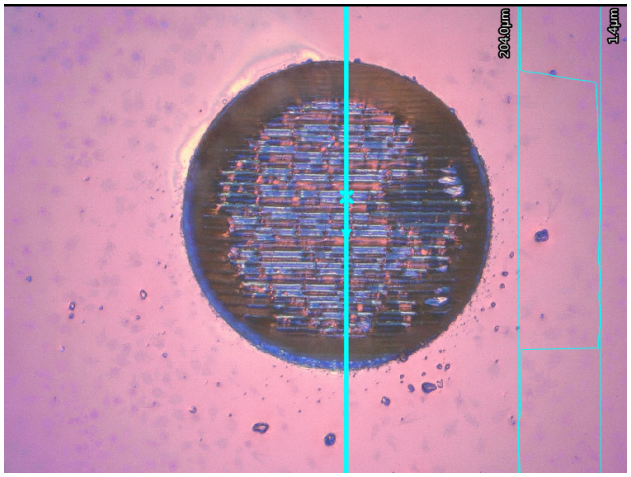

(a) 450 reps

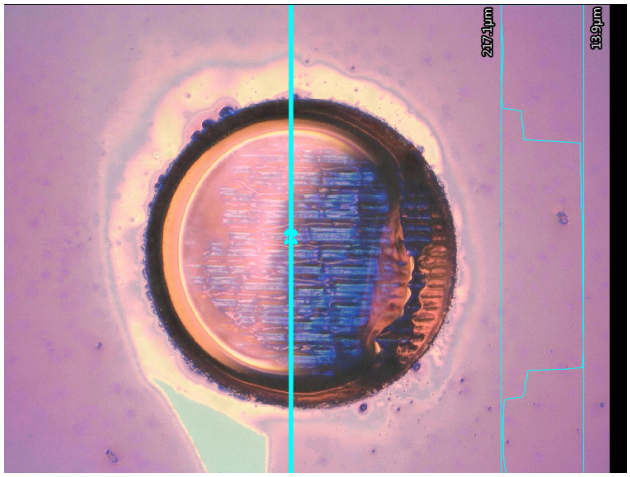

(b) 500 reps

Figure 79

Here are the depth profiles illustrated in the following series of graphs:

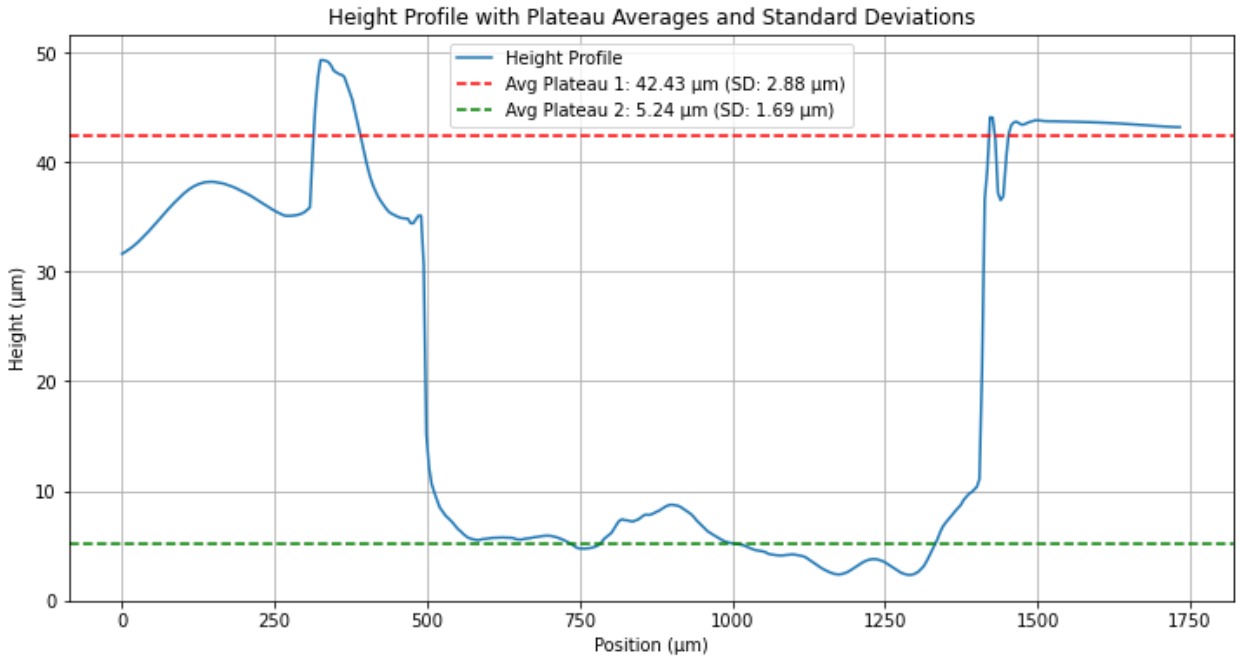

Figure 80: 50 reps

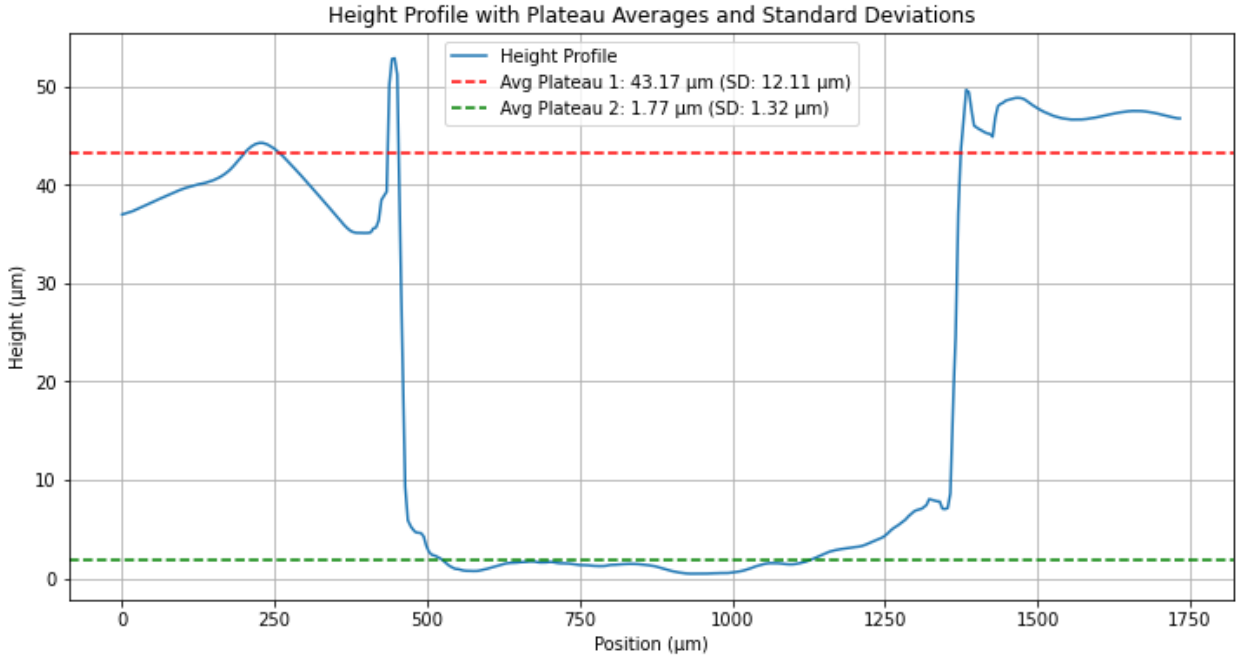

Figure 81: 100 reps

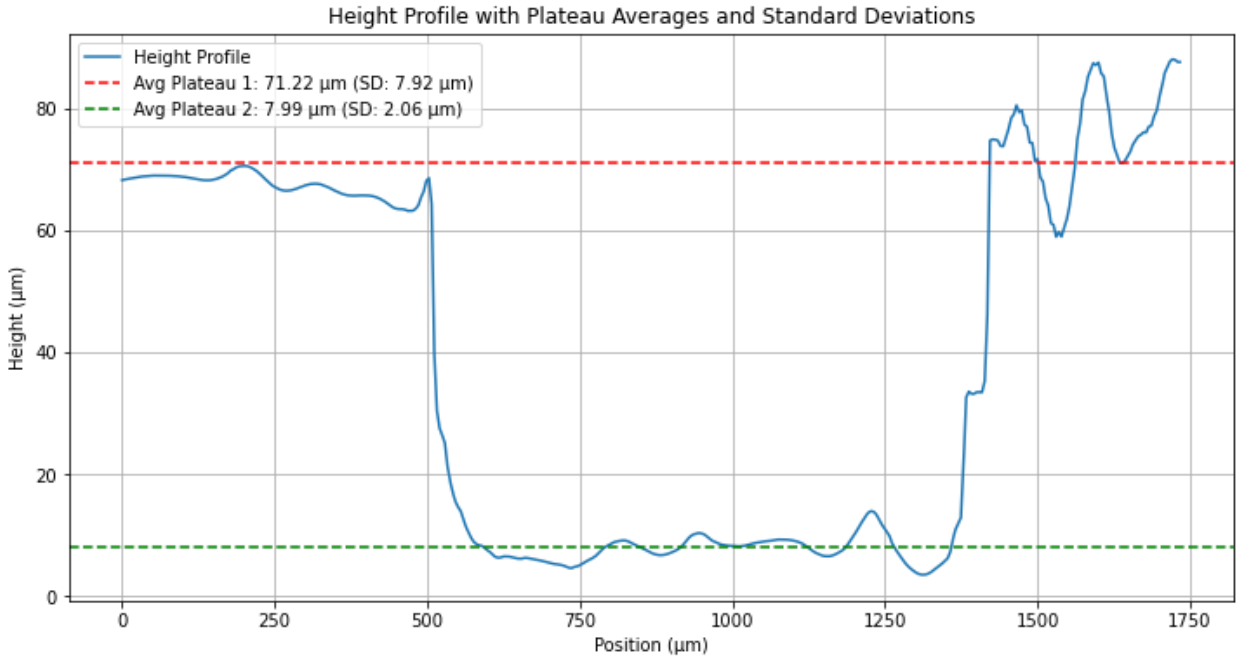

Figure 82: 150 reps

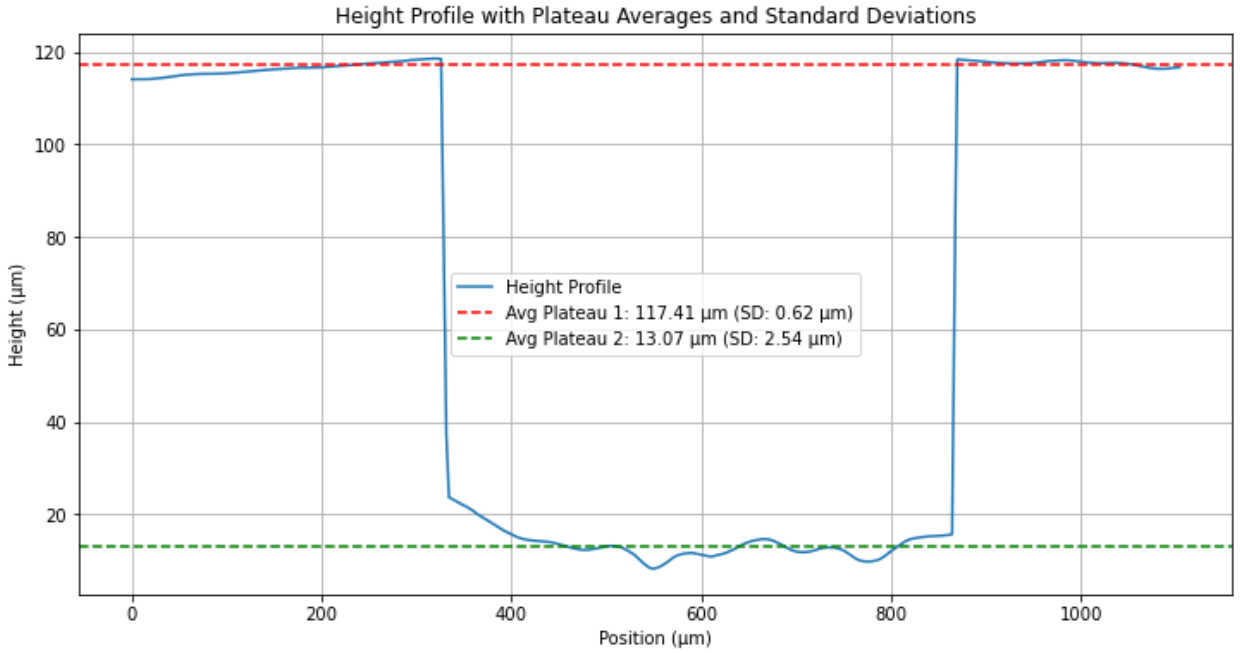

Figure 83: 200 reps

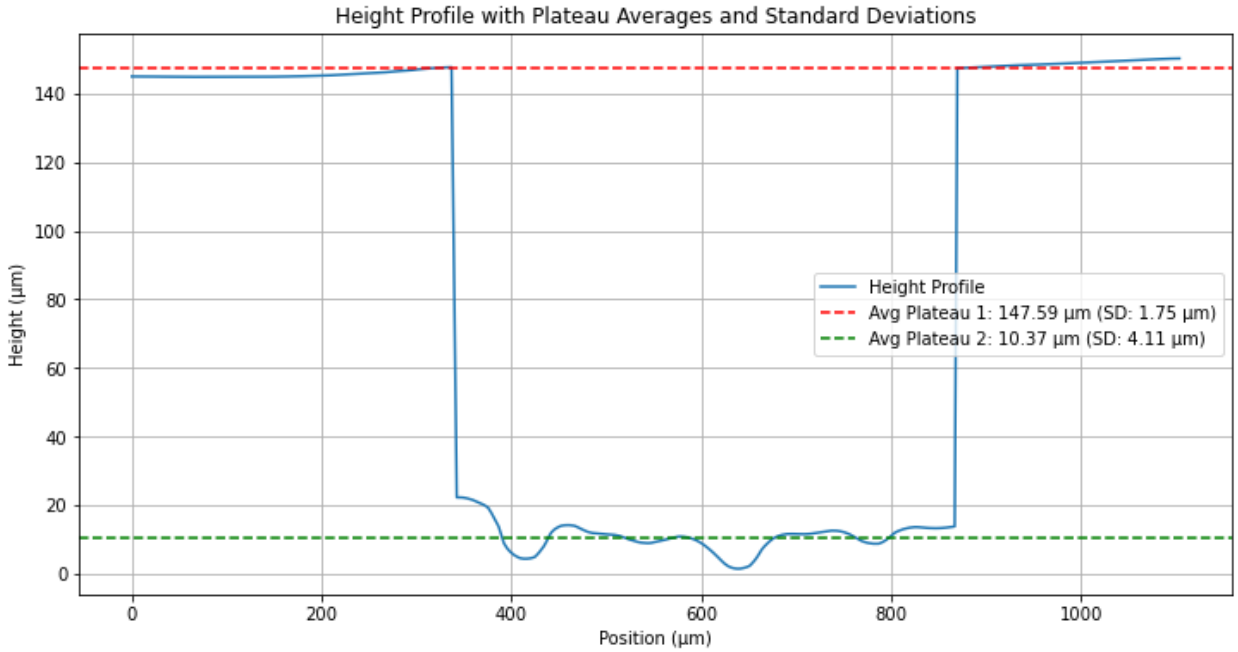

Figure 84: 250 reps

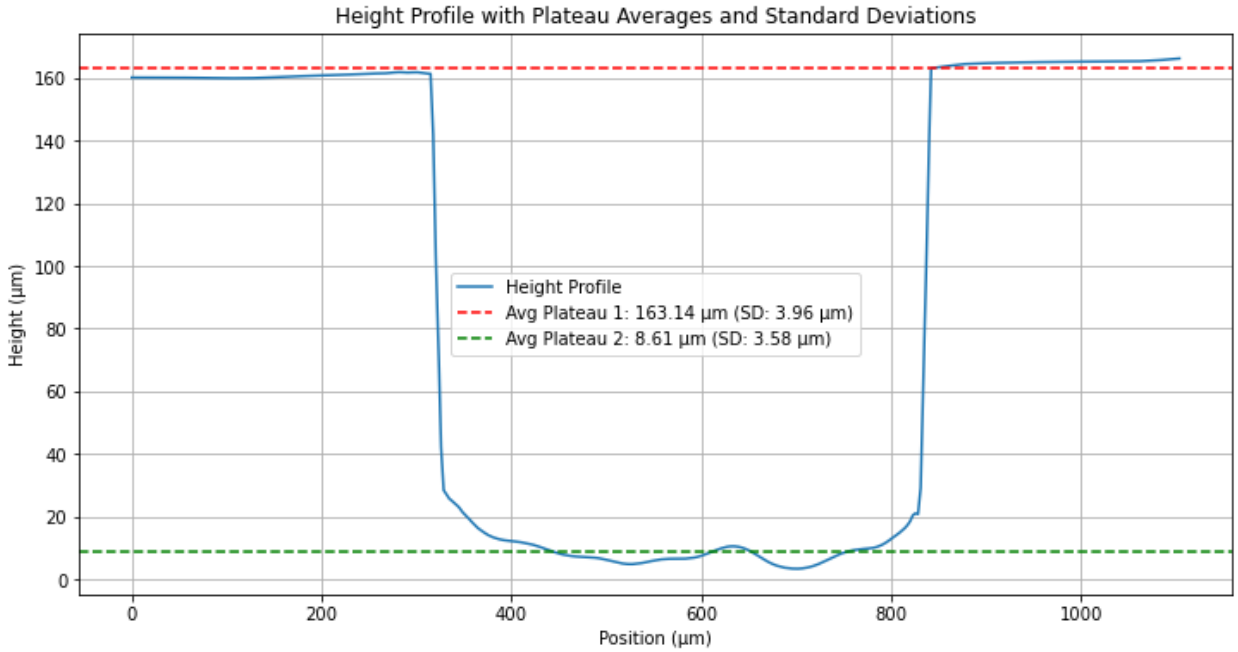

Figure 85: 300 reps

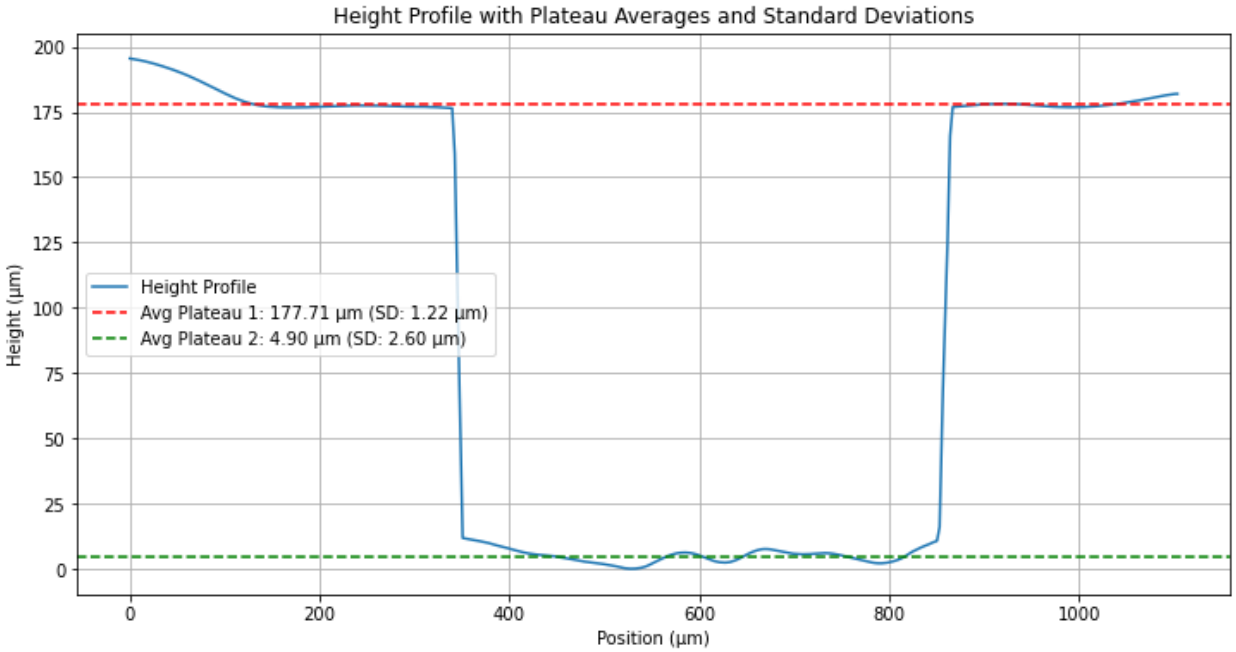

Figure 86: 350 reps

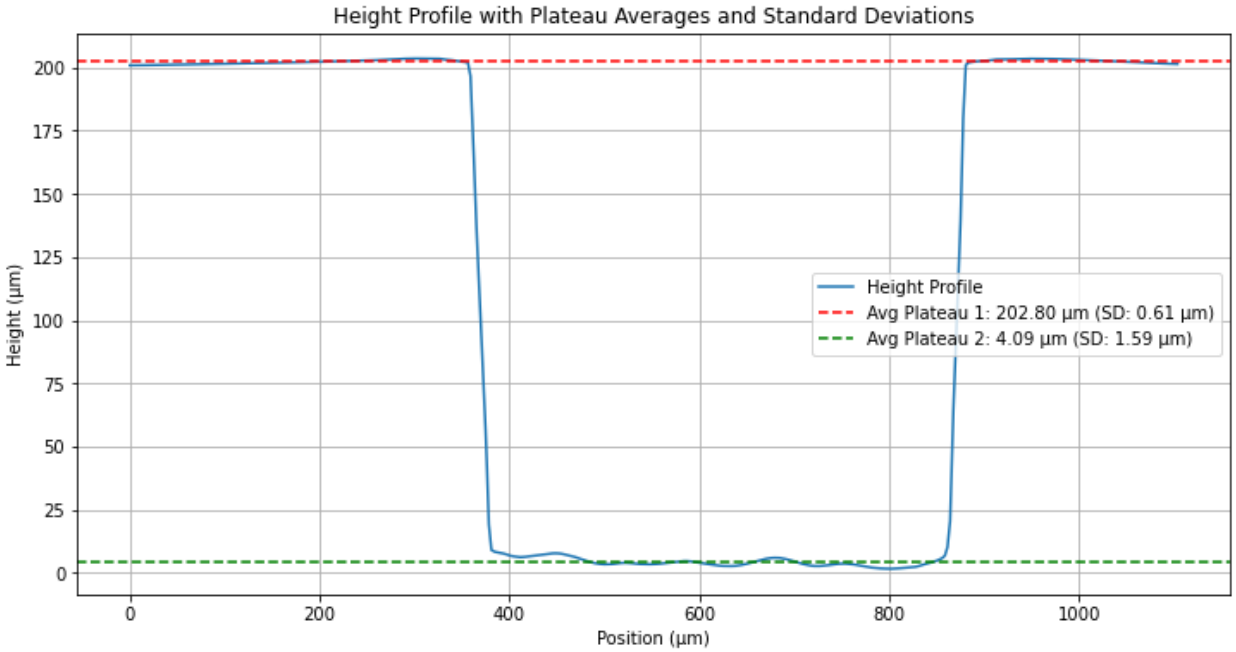

Figure 87: 400 reps

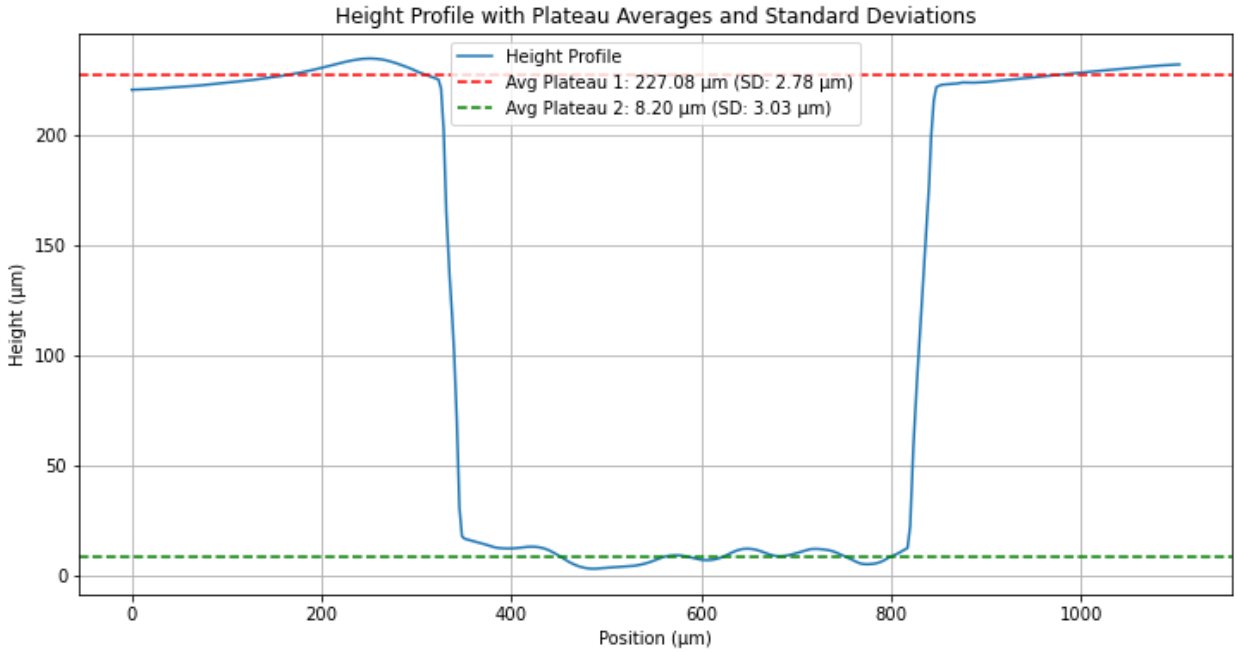

Figure 88: 450 reps

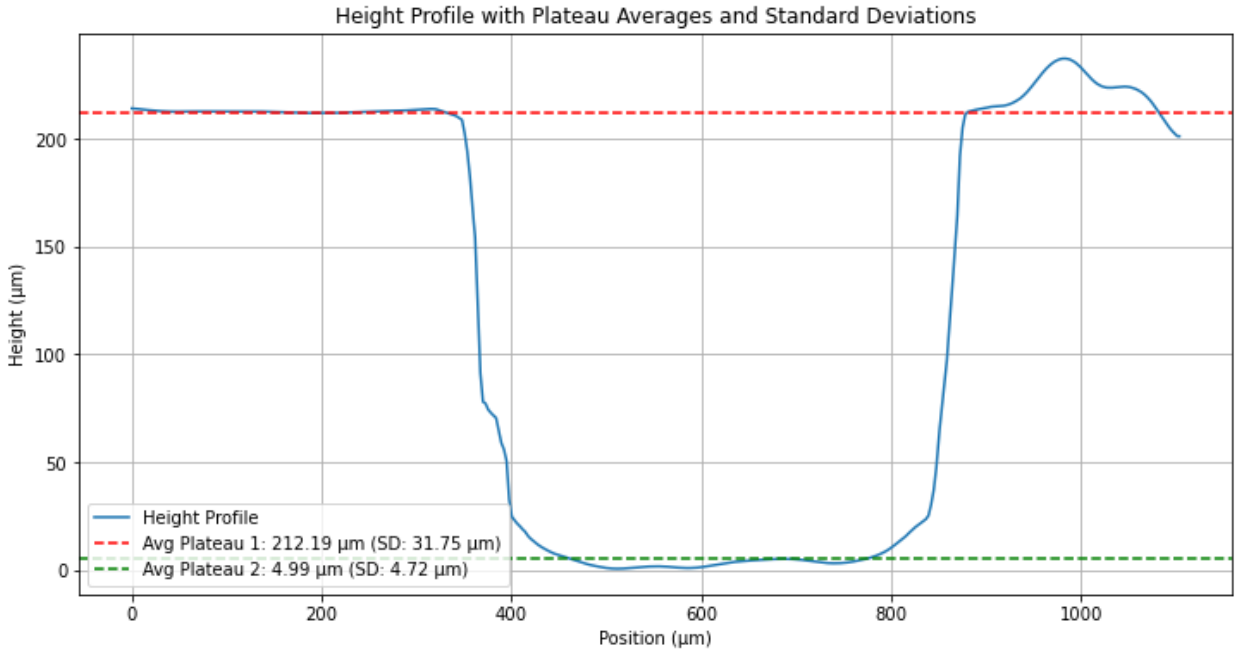

Figure 89: 500 reps

With the quantitative measured values depicted in table 8.

Repetitions	**Height difference** (μm)	**SD** (μm)	**Depth per rep** (μm)
50	37.18896	1.69007	0.74378
100	41.39314	1.32250	0.41393
150	63.22728	2.05872	0.42152
200	104.34736	2.54344	0.52174
250	137.22554	4.11447	0.54890
300	149.83201	3.58566	0.49944
350	172.80956	2.60476	0.49374
400	198.70524	1.59147	0.49676
450	218.88820	3.02764	0.48642
500	207.19930	4.71639	0.41440

Table 8: Height Difference, Standard Deviation, and Depth per Repetition at Various Repetitions

J.4 Depth to Speed

In this section the analysis is made on the effect the focal point velocity to the depth of the cut. Using 2000 repetitions and a power of 3%.

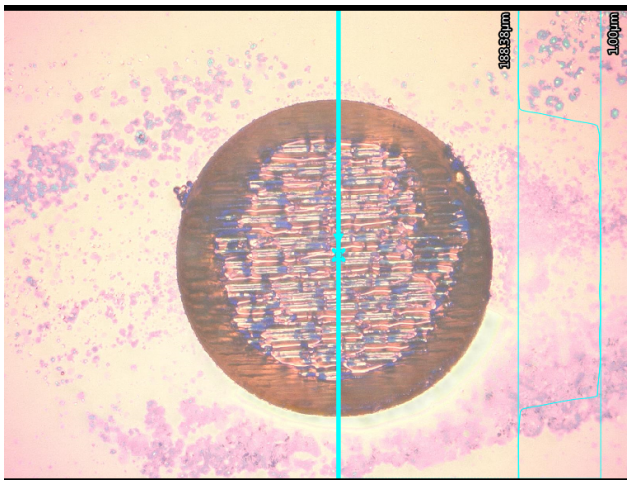

(a) 50 mm/sec

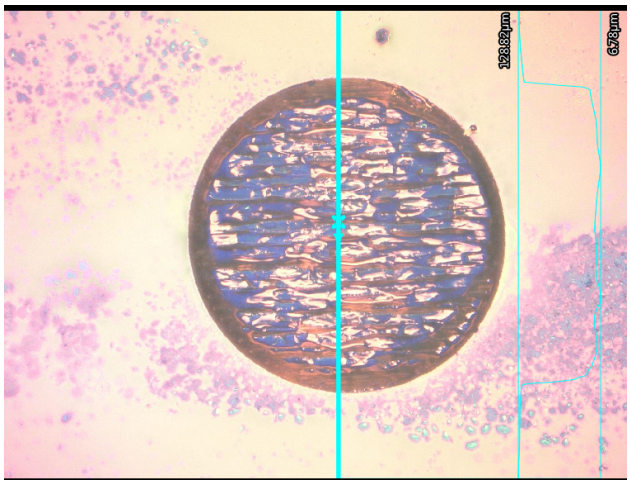

(b) 100 mm/sec

Figure 90

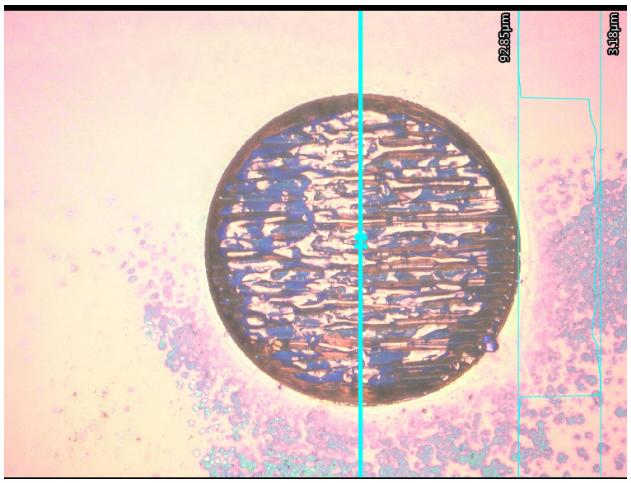

(a) 150 mm/sec

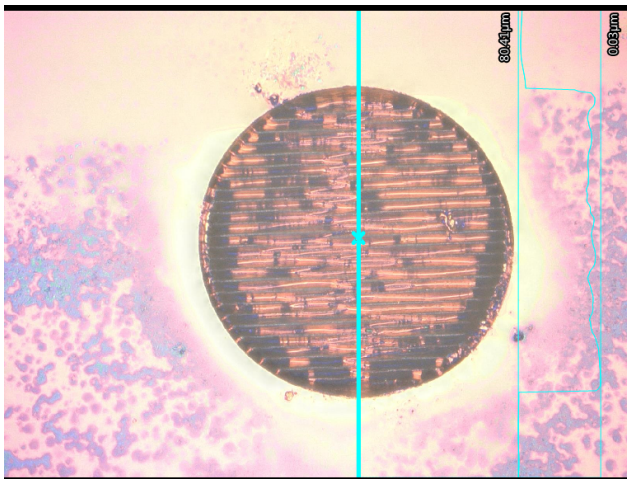

(b) 200 mm/sec

Figure 91

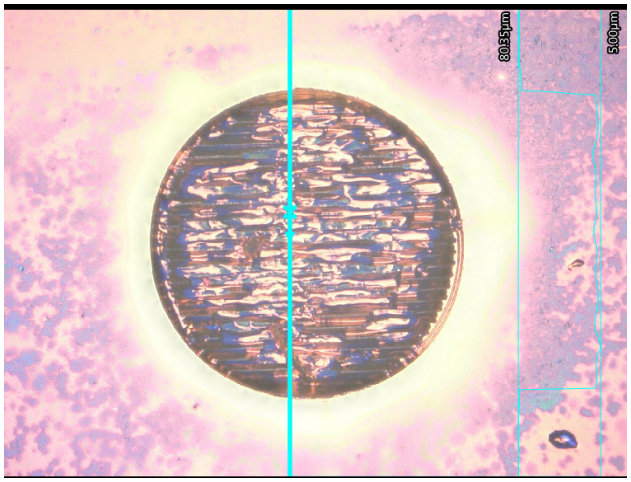

(a) 250 mm/sec

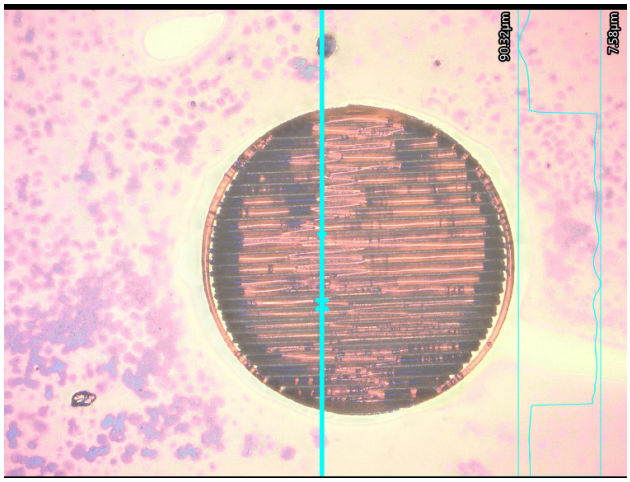

(b) 300 mm/sec

Figure 92

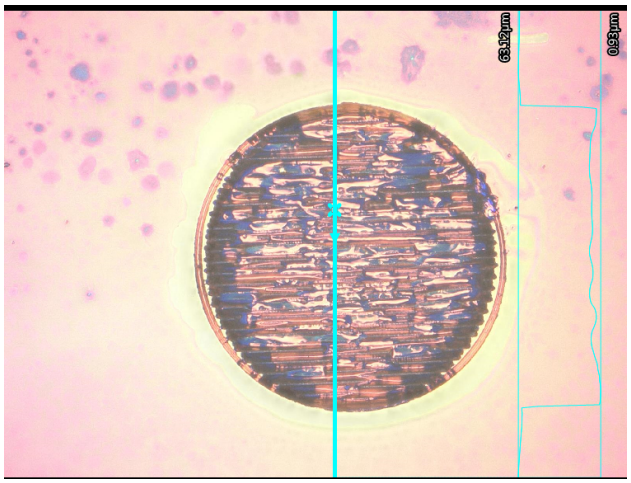

(a) 350 mm/sec

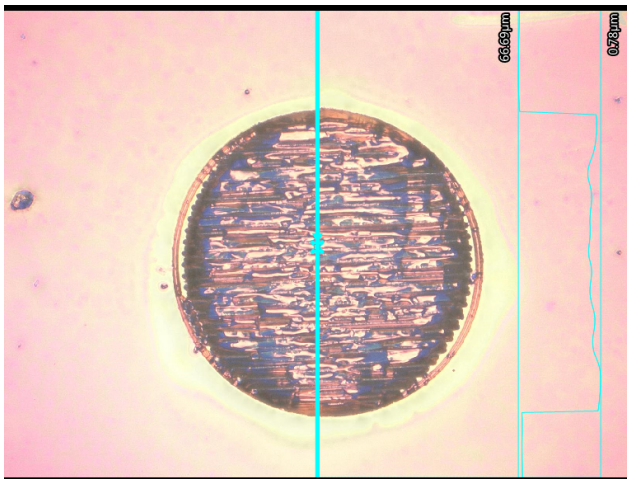

(b) 400 mm/sec

Figure 93

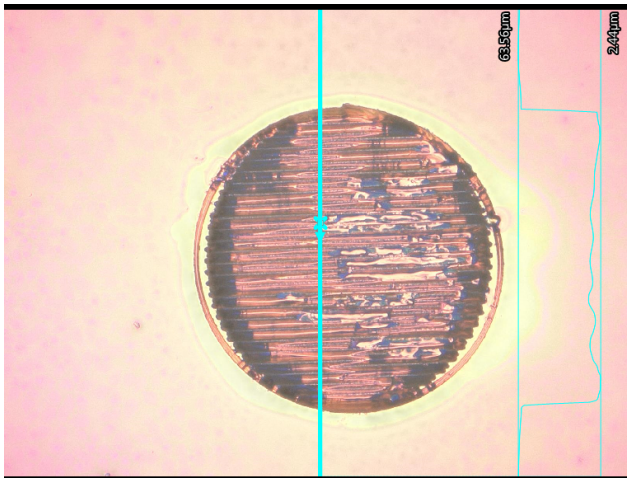

(a) 450 mm/sec

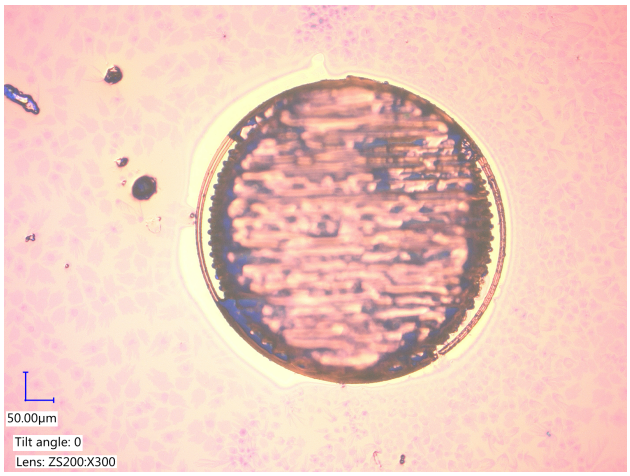

(b) 500 mm/sec

Figure 94

Here are the depth profiles illustrated in the following series of graphs:

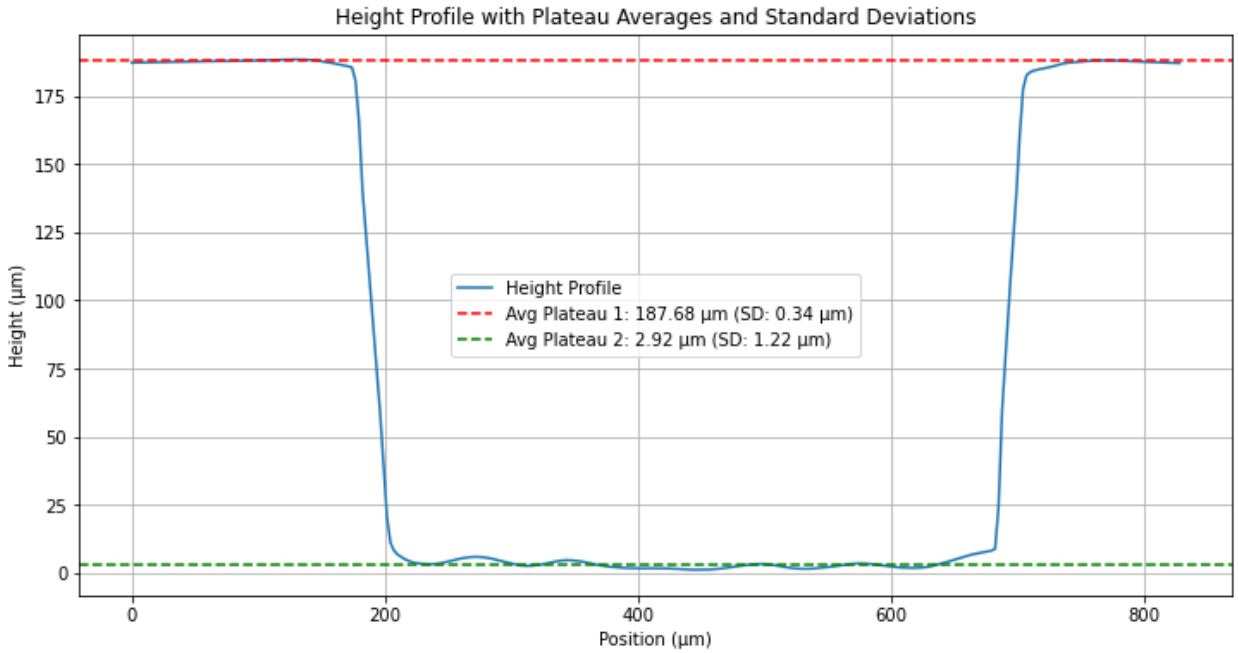

Figure 95: 50 mm/sec

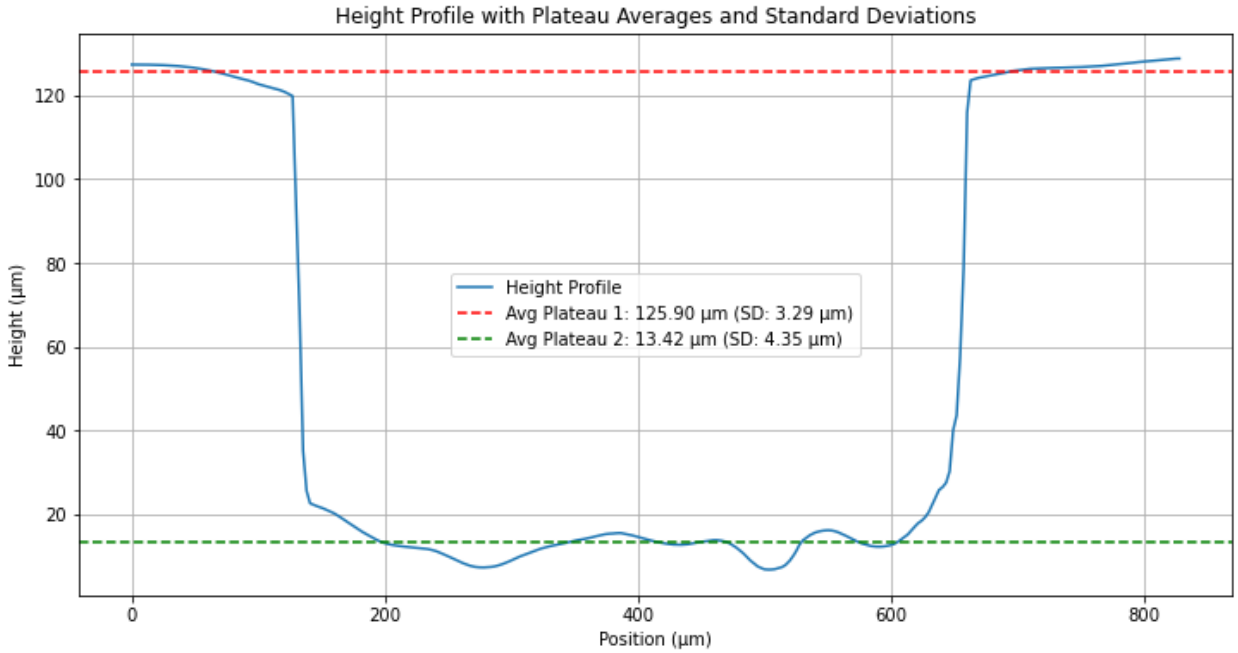

Figure 96: 100 mm/sec

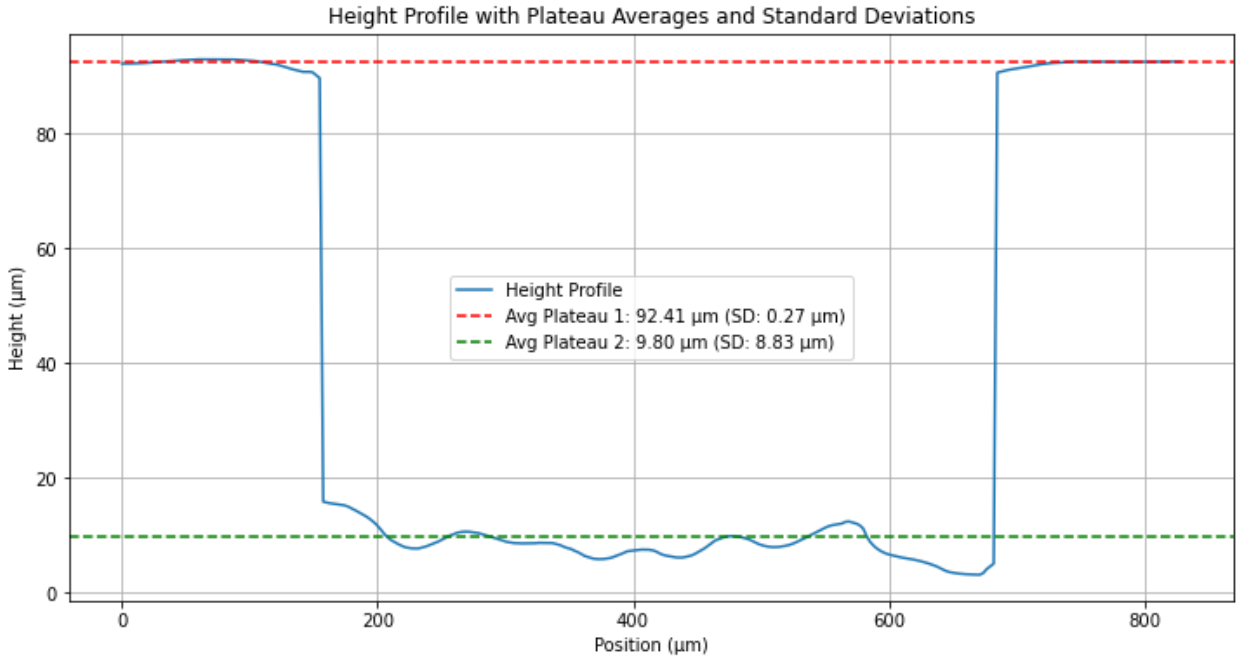

Figure 97: 150 mm/sec

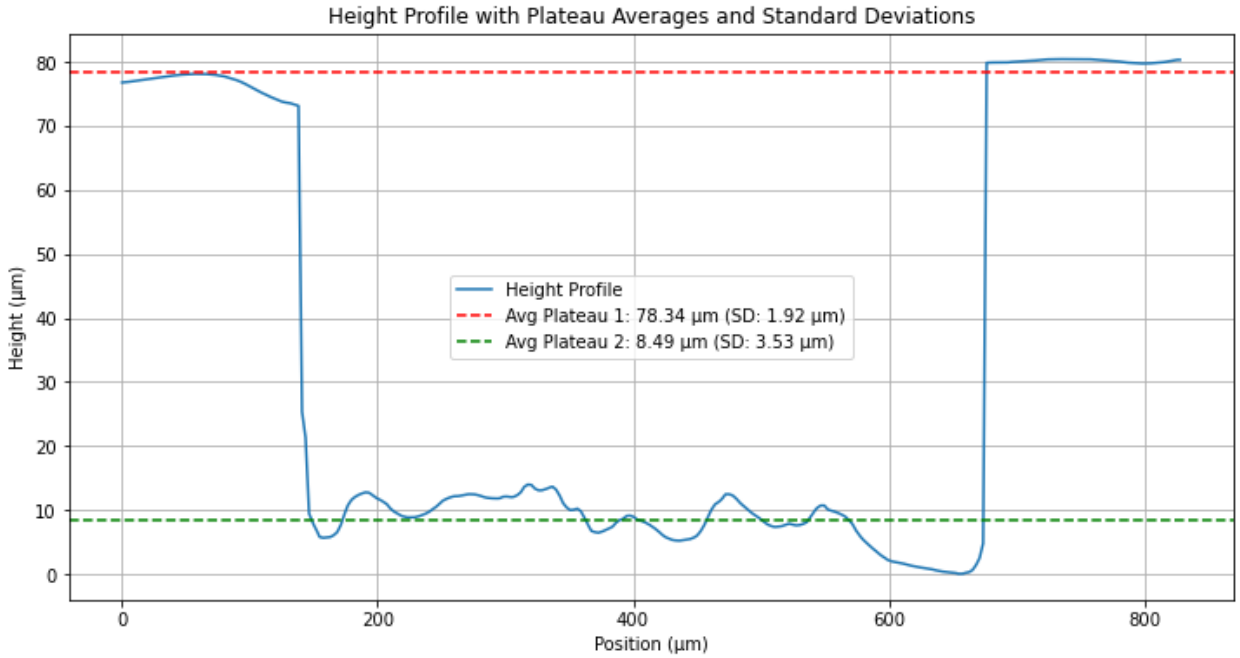

Figure 98: 200 mm/sec

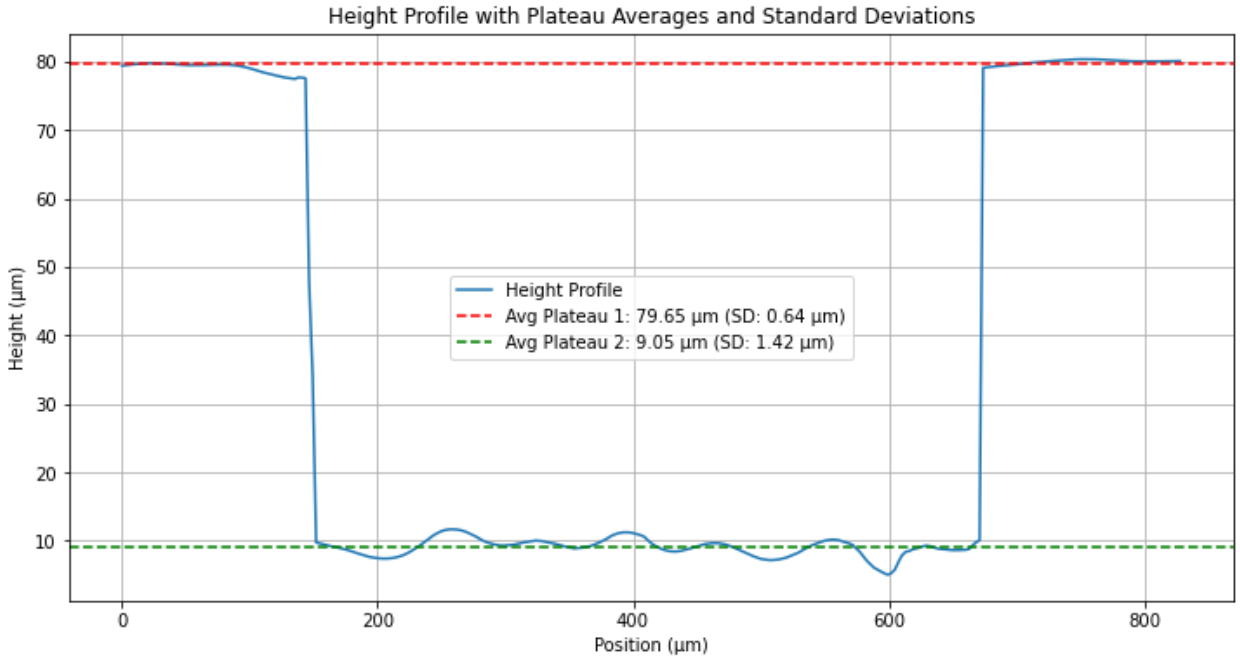

Figure 99: 250 mm/sec

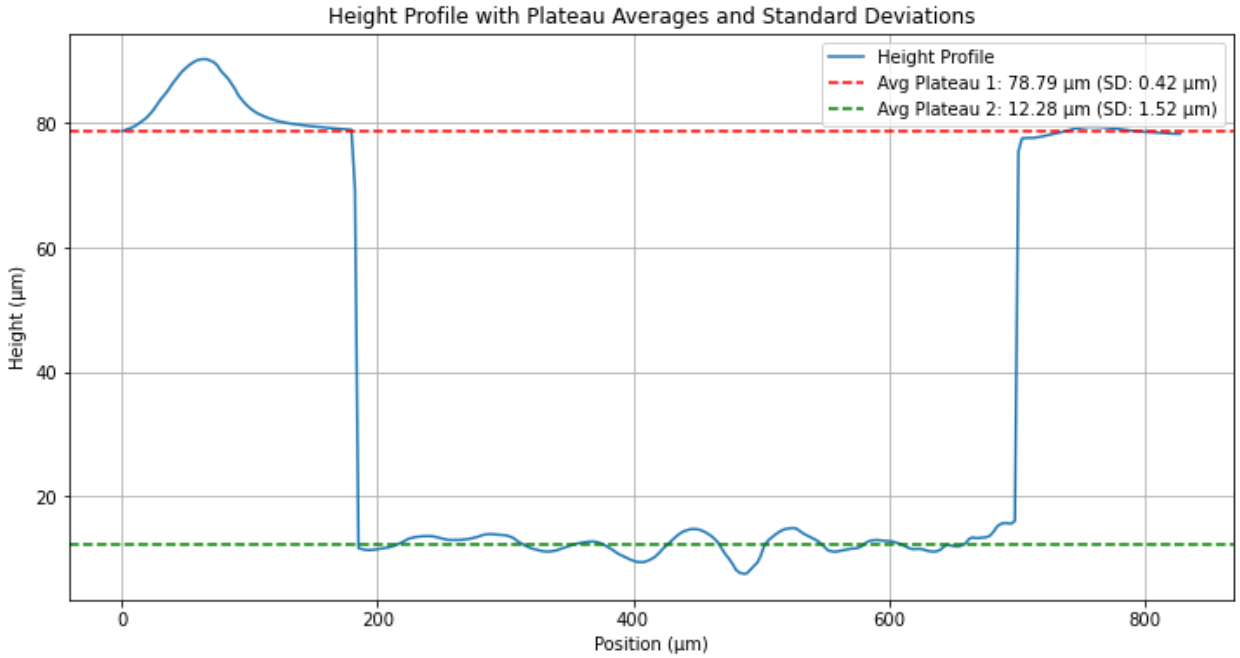

Figure 100: 300 mm/sec

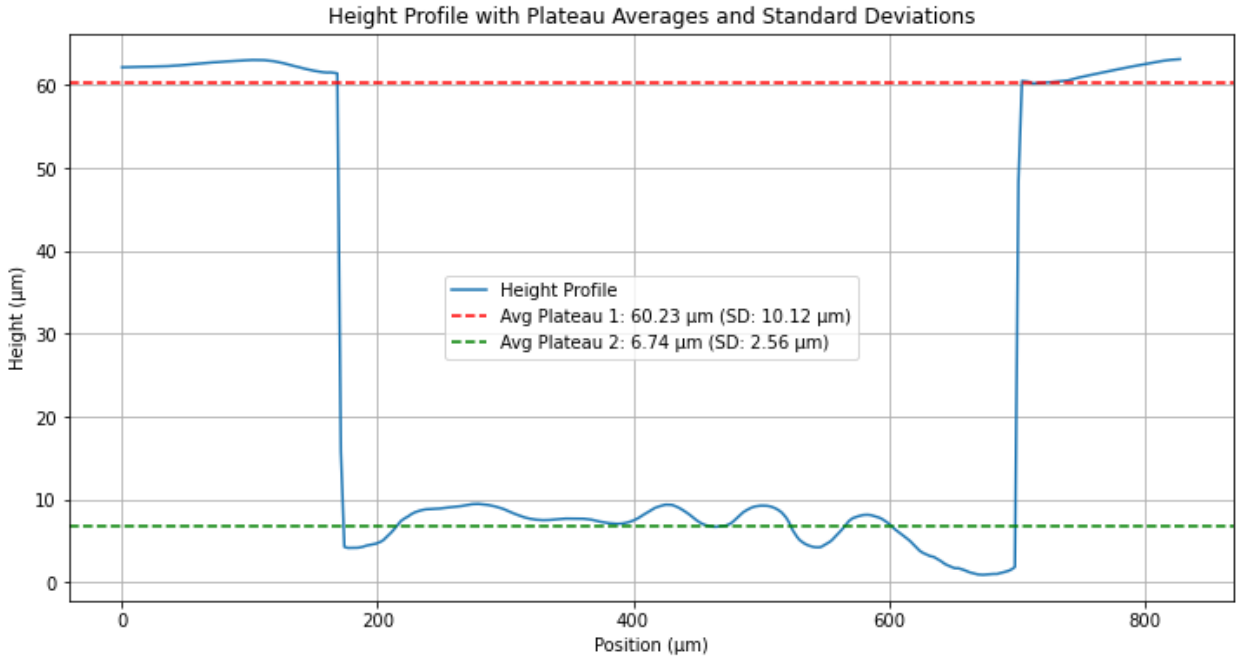

Figure 101: 350 mm/sec

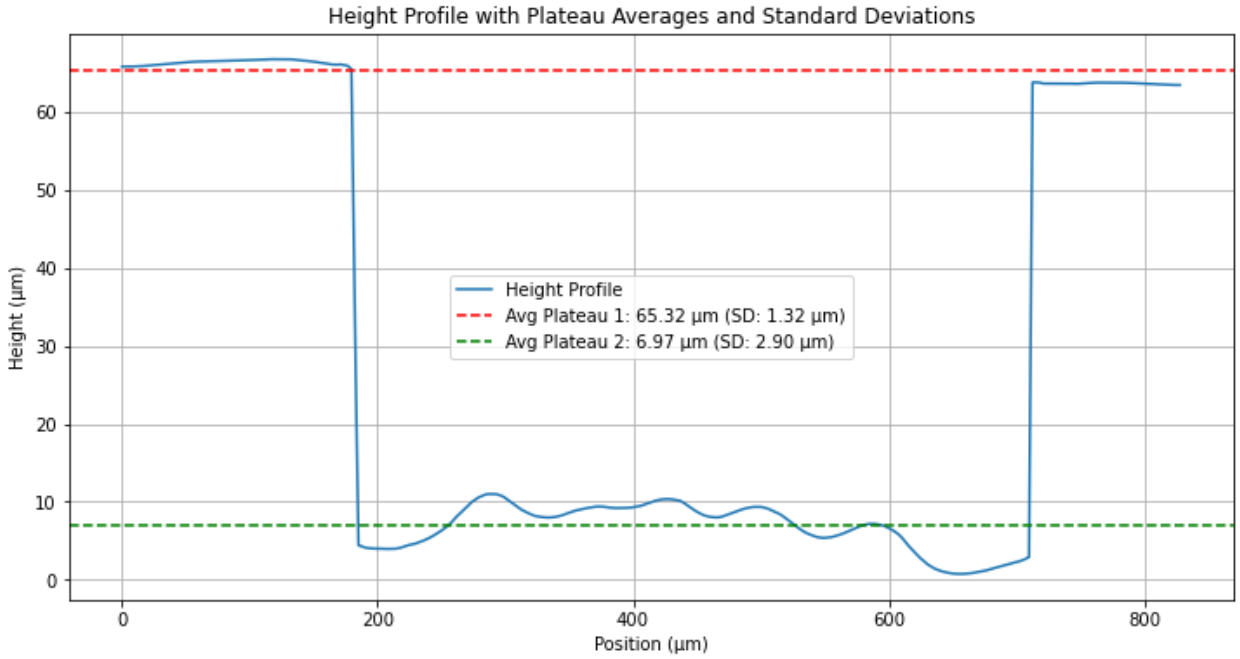

Figure 102: 400 mm/sec

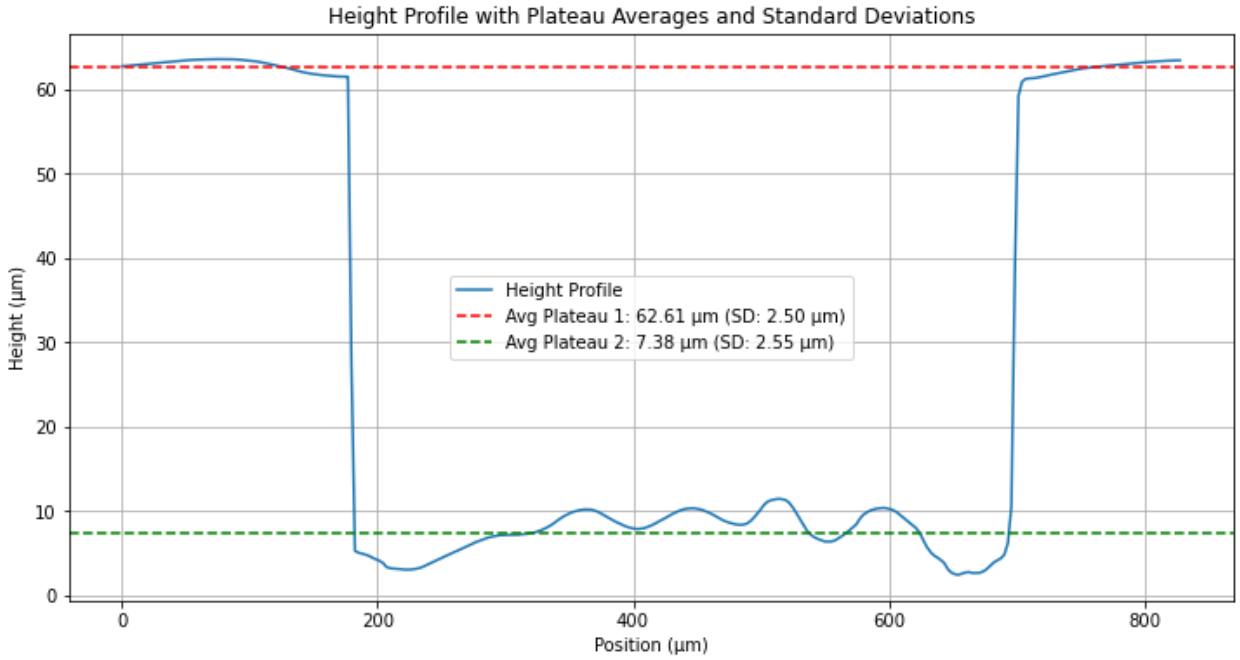

Figure 103: 450 mm/sec

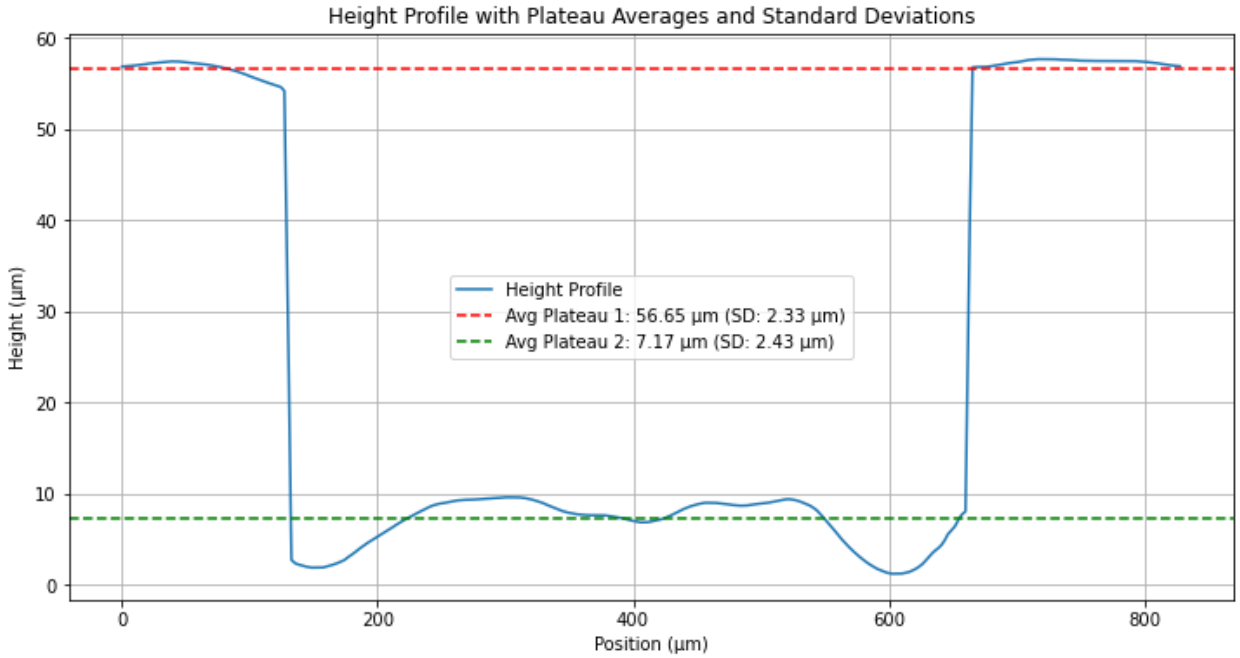

Figure 104: 500 mm/sec

With the quantitative measured values depicted in table 9.

Speed (mm/s)	**Height difference** (μm)	**Standard deviation** (μm)
50	184.7576208	1.223204205
100	112.4855324	4.347172102
150	82.61255032	8.828874964
200	69.84744775	3.52595958
250	70.60283009	1.424386469
300	66.51622297	1.523700269
350	53.48927126	2.556631587
400	58.34542547	2.903110351
450	55.23002789	2.553387977
500	49.47568612	2.432089024

Table 9: Height Differences and Standard Deviations at Various Speeds

J.5 Depth to Power

Analysis on the effect of power to the depth of the cut. Using 2000 repetitions and a focal point velocity of 50mm/sec.

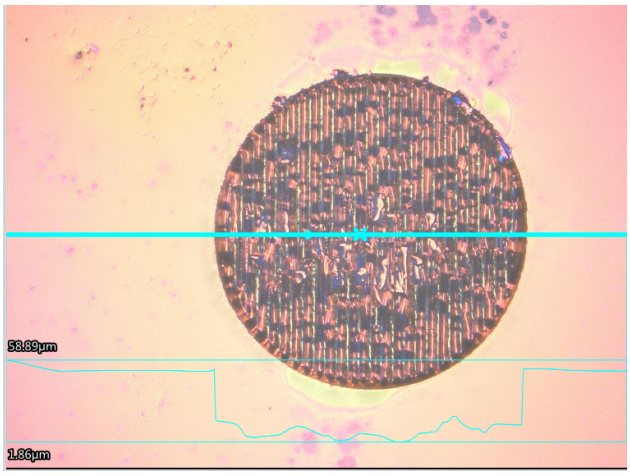

Figure 105: 100 mm/sec

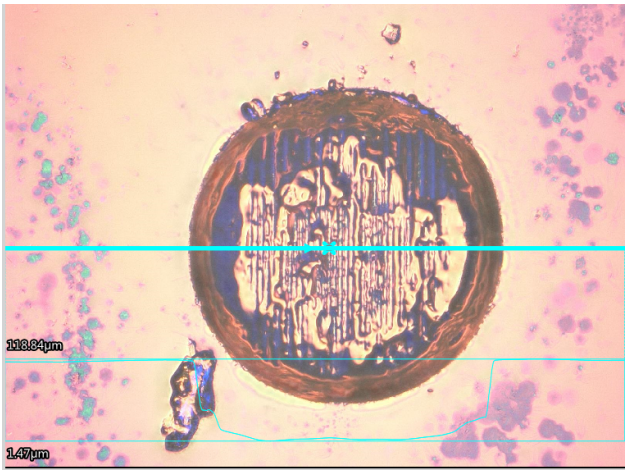

(a) 150 mm/sec

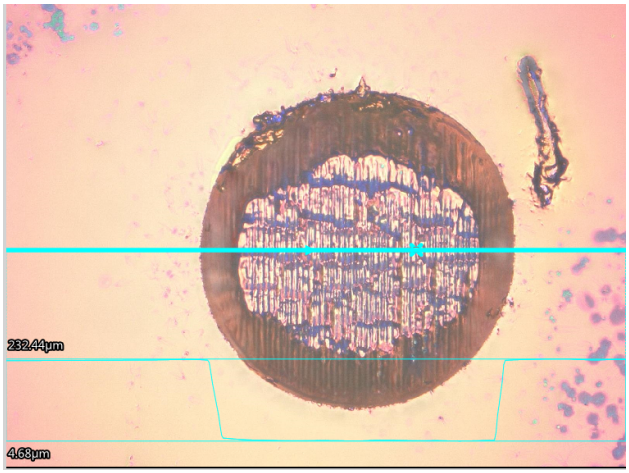

(b) 200 mm/sec

Figure 106

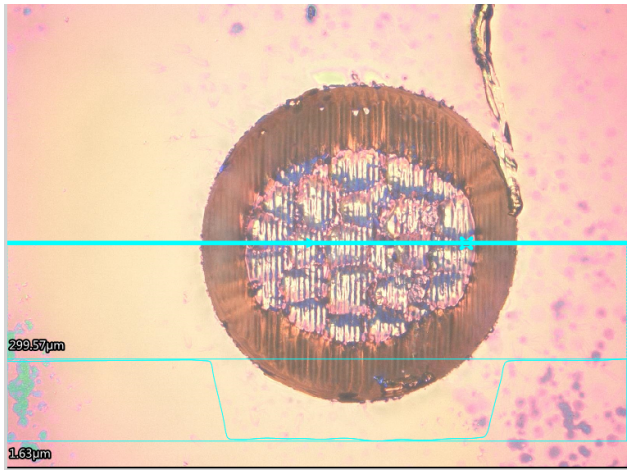

(a) 250 mm/sec

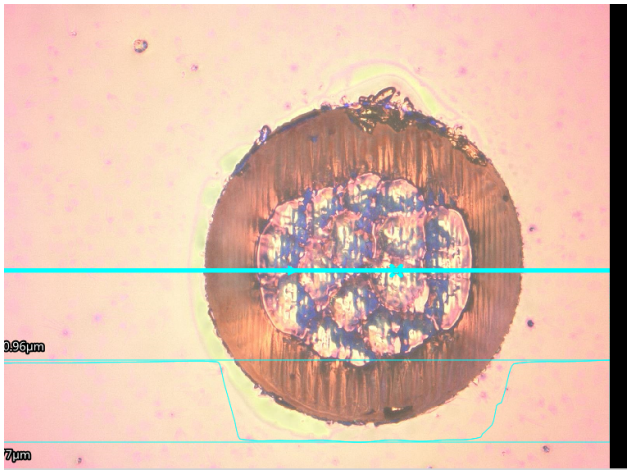

(b) 300 mm/sec

Figure 107

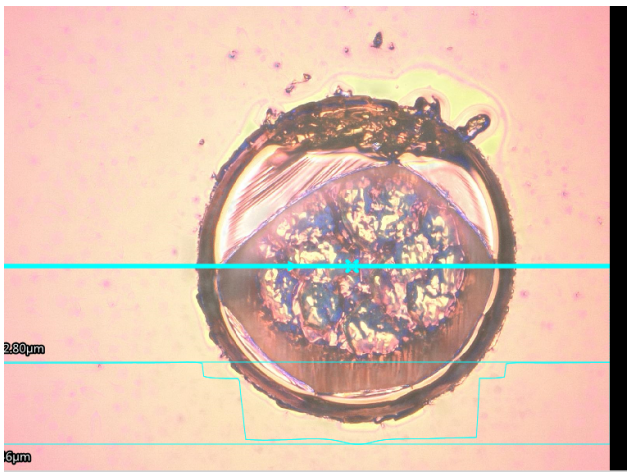

(a) 350 mm/sec

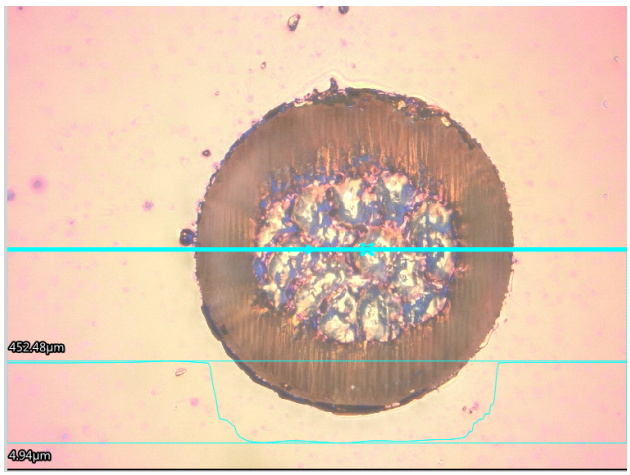

(b) 400 mm/sec

Figure 108

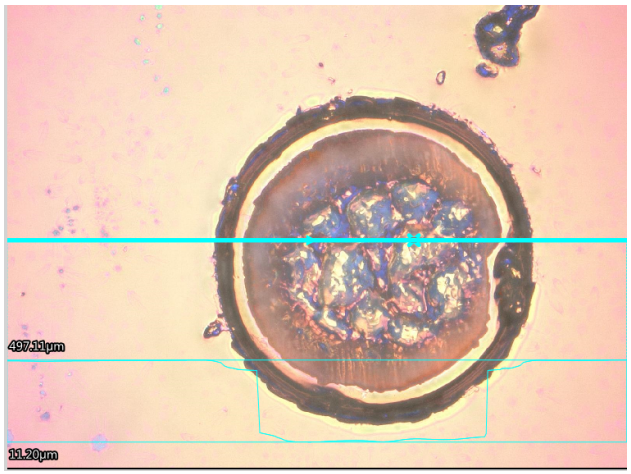

(a) 450 mm/sec

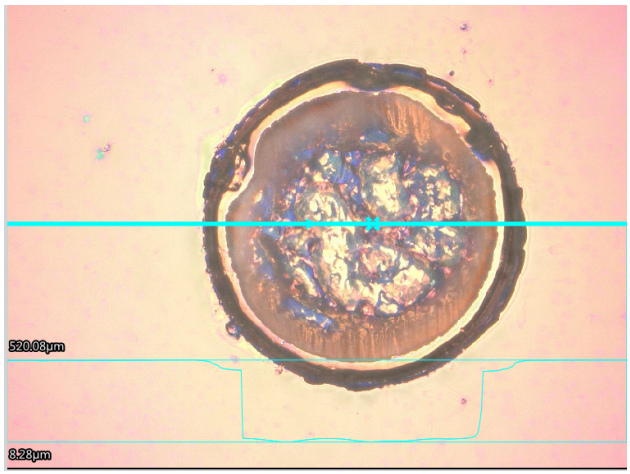

(b) 500 mm/sec

Figure 109

Here are the depth profiles illustrated in the following series of graphs:

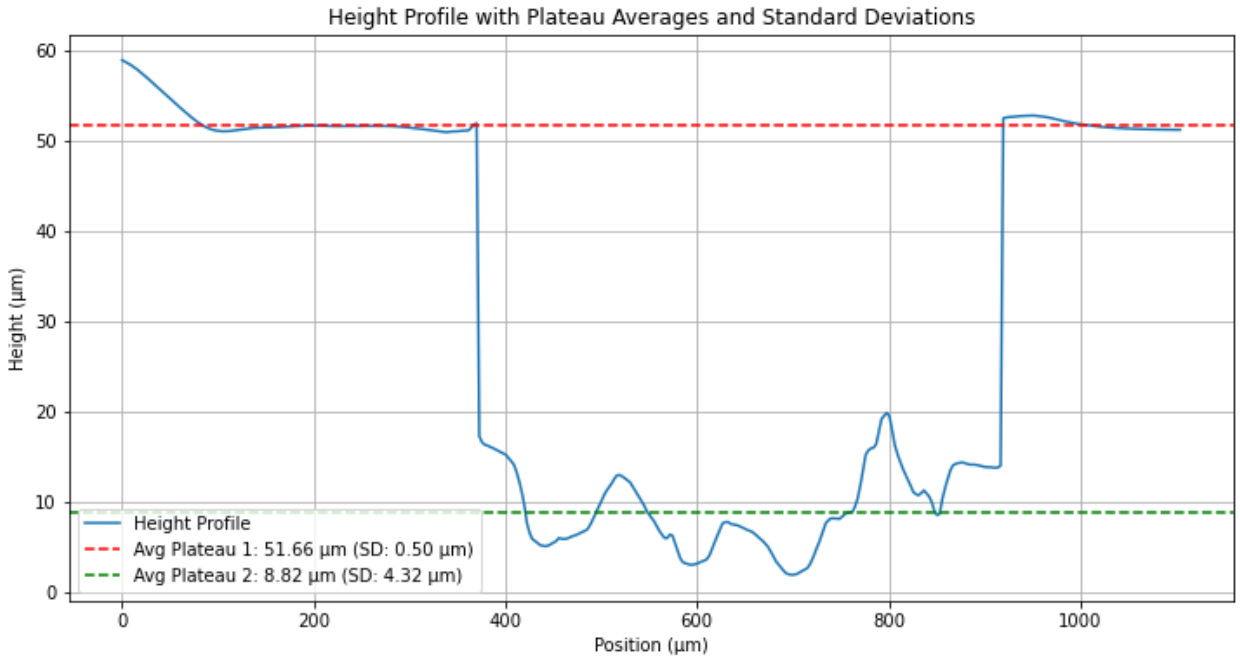

Figure 110: 2%

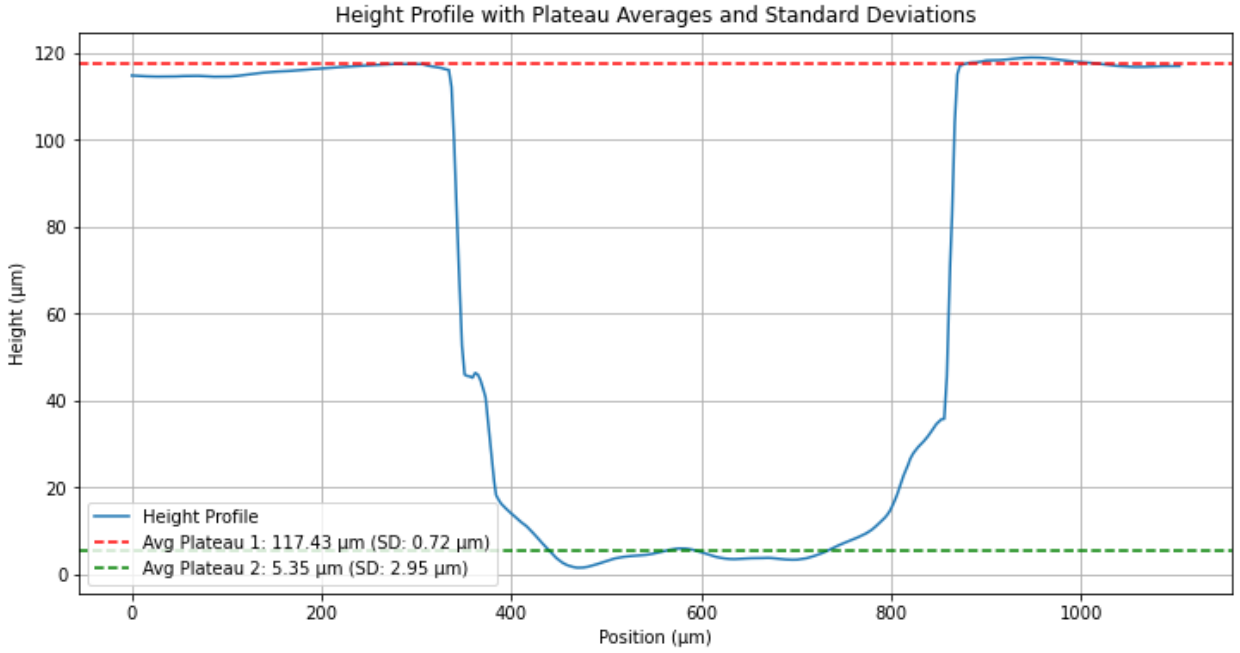

Figure 111: 3%

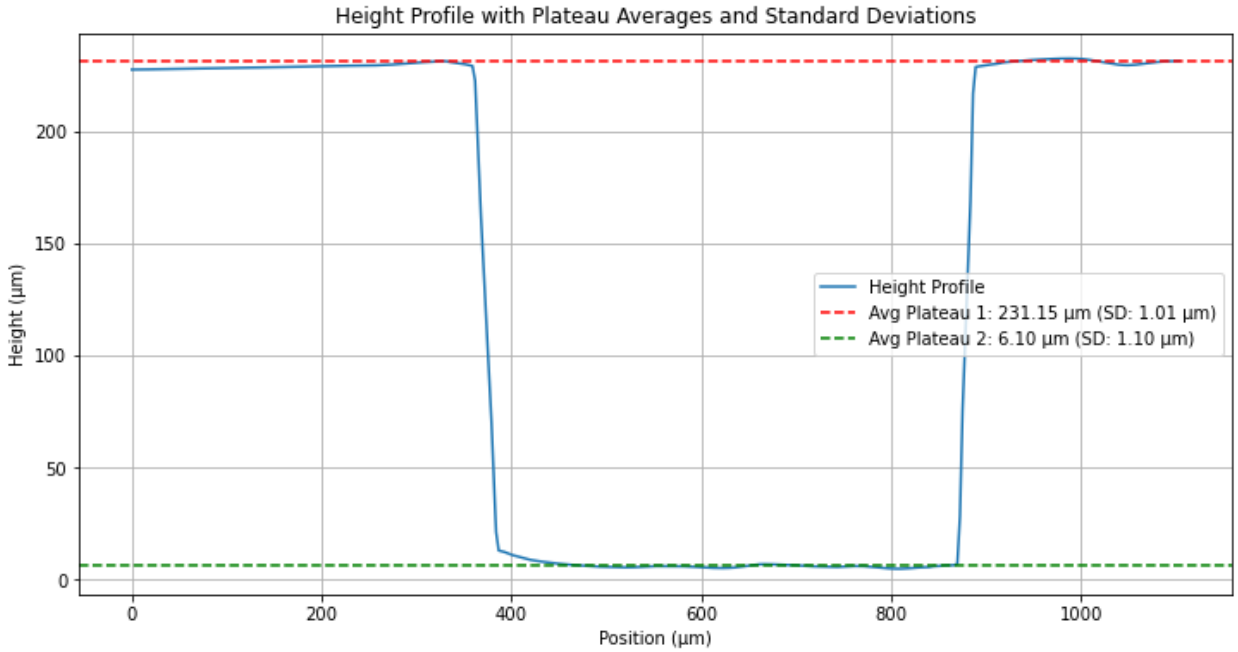

Figure 112: 4%

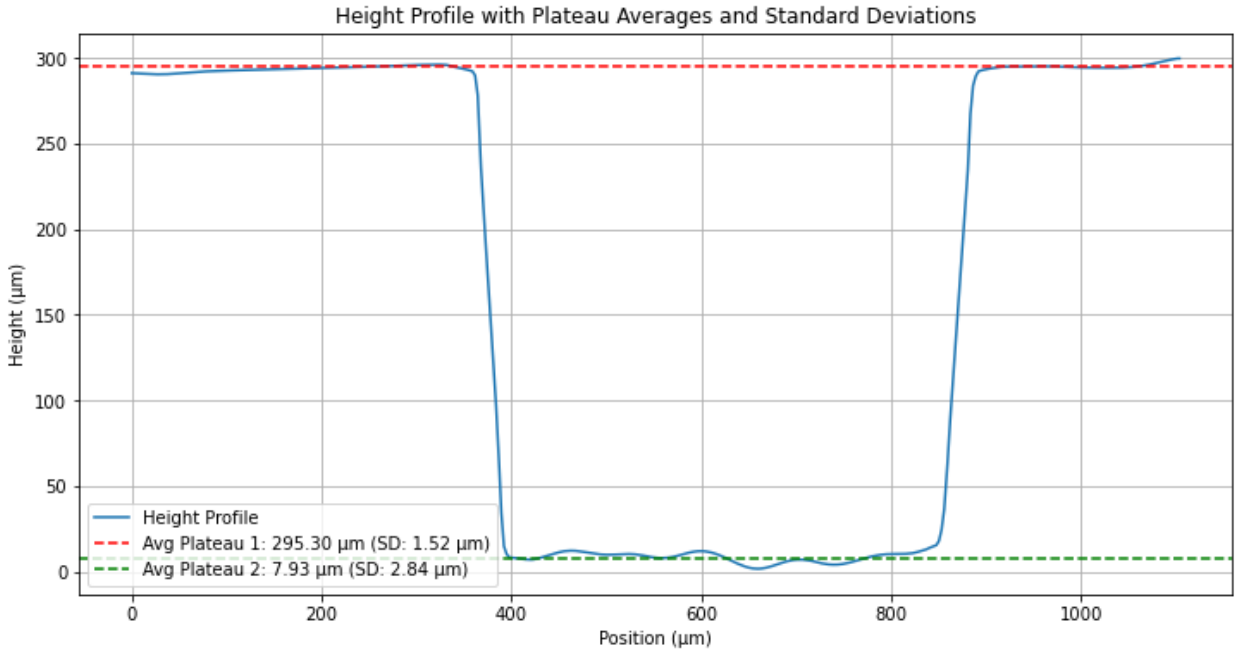

Figure 113: 5%

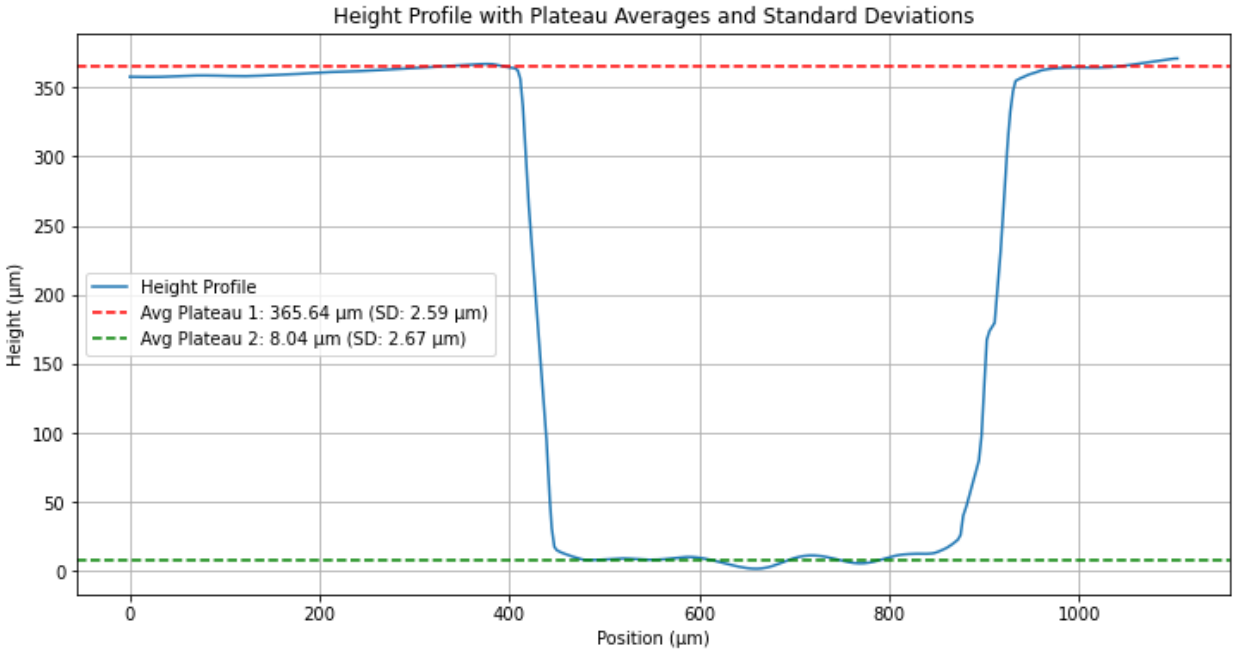

Figure 114: 6%

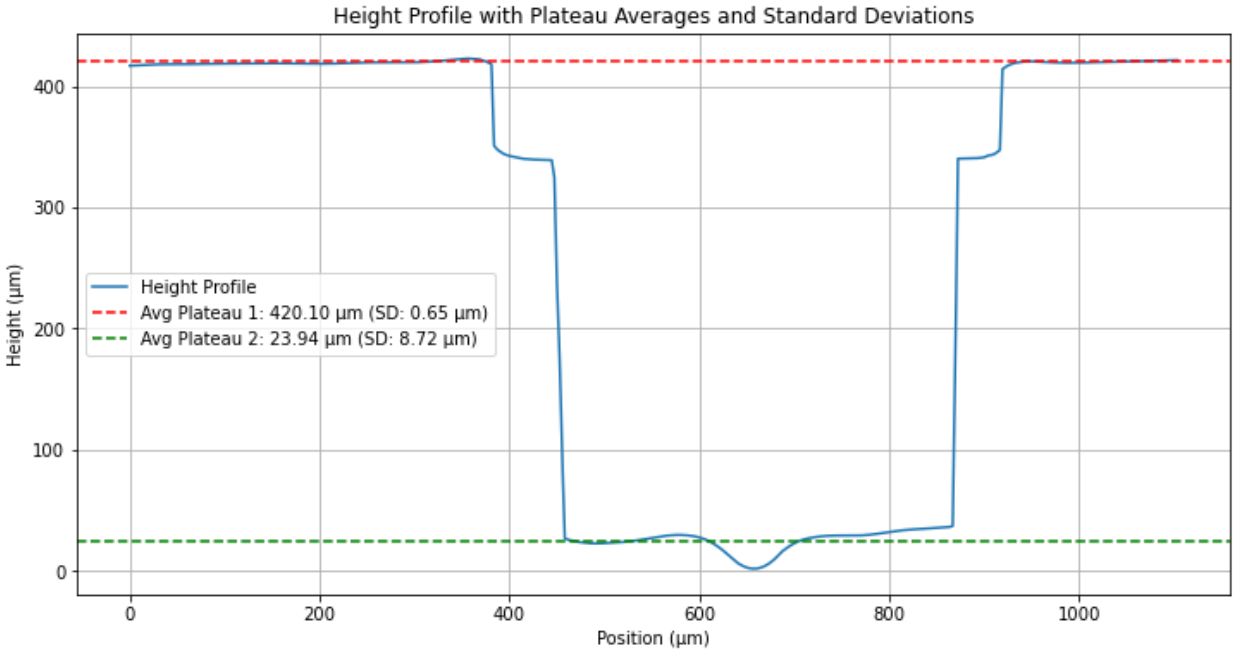

Figure 115: 7%

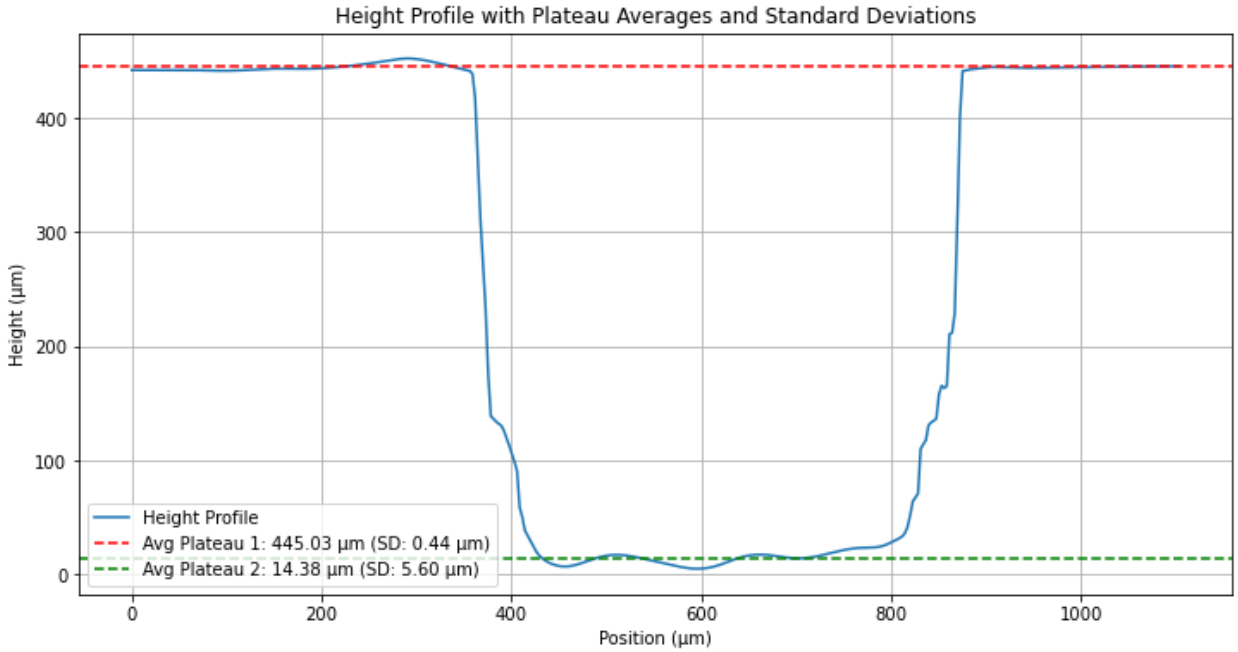

Figure 116: 8%

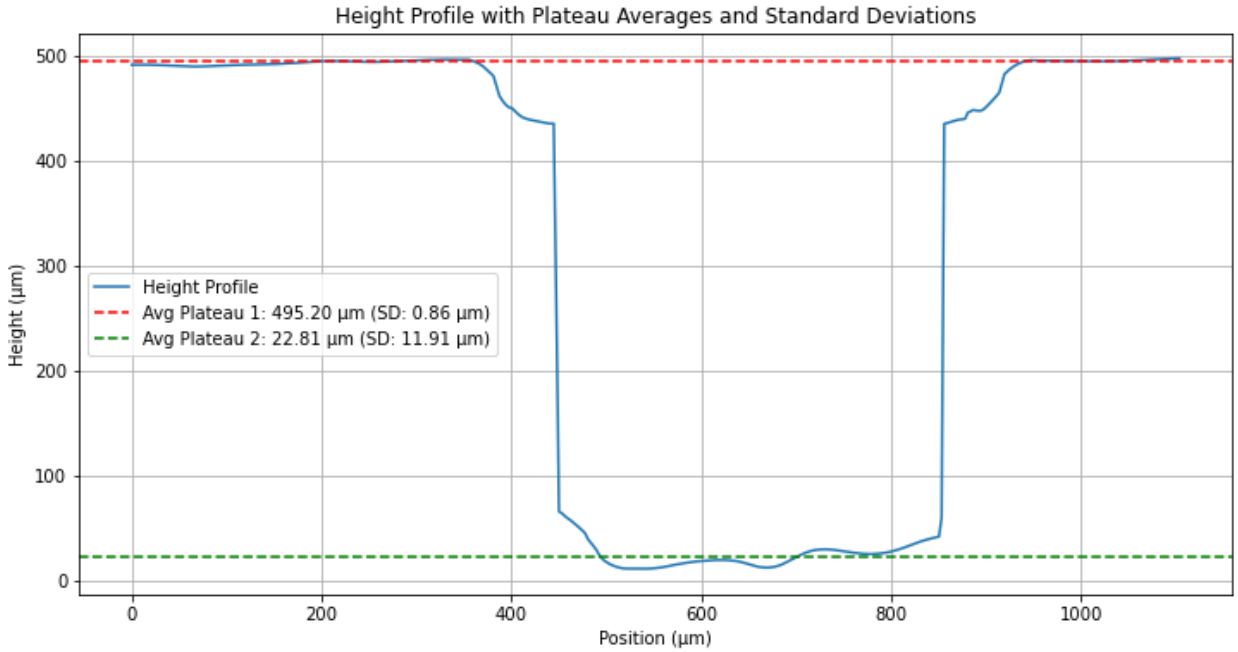

Figure 117: 9%

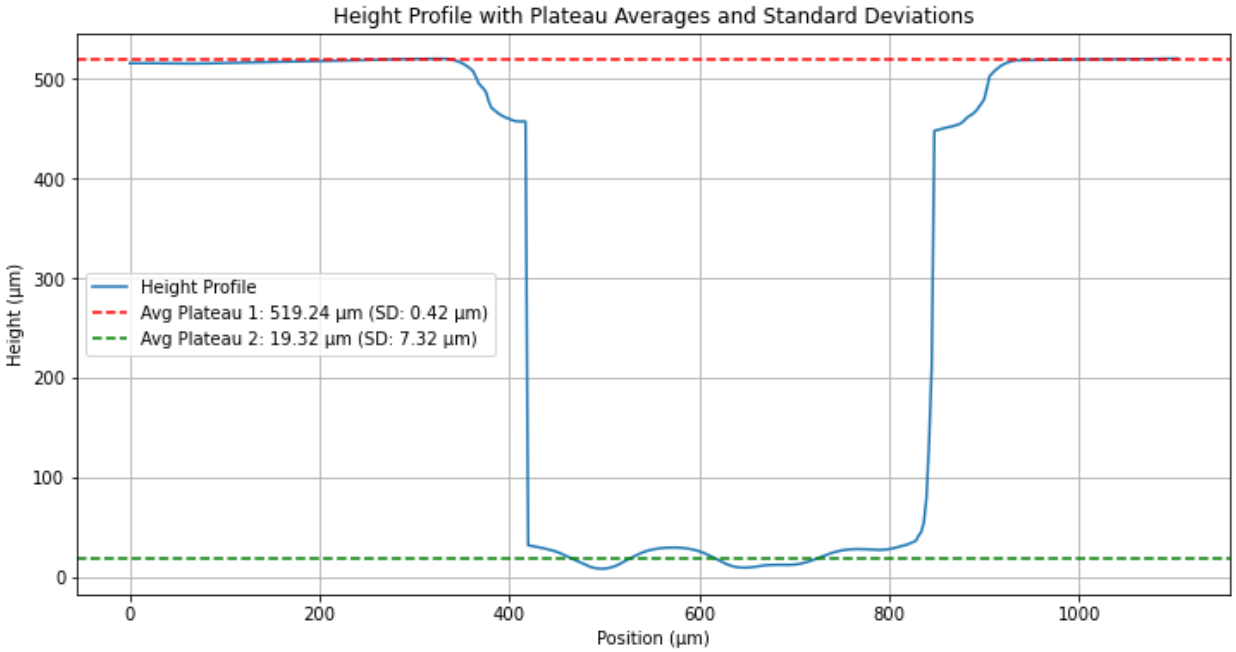

Figure 118: 10%

With the quantitative measured values depicted in table 10.

Power(%)	**Depth** (μm)	**SD** (μm)
2	42.8314	4.31699
3	112.0869	2.95093
4	225.0479	1.10155
5	287.3751	2.83821
6	357.6090	2.66943
7	396.1620	8.71534
8	430.6529	5.59992
9	472.3893	11.9064
10	499.9191	7.32233

Table 10: Depth and Standard Deviation at Various Power Levels

K White Light Interferometry

This appendix presents all the images of the white light interferometry results. These images give insight in the surface profile of the glass surrounding the through hole.

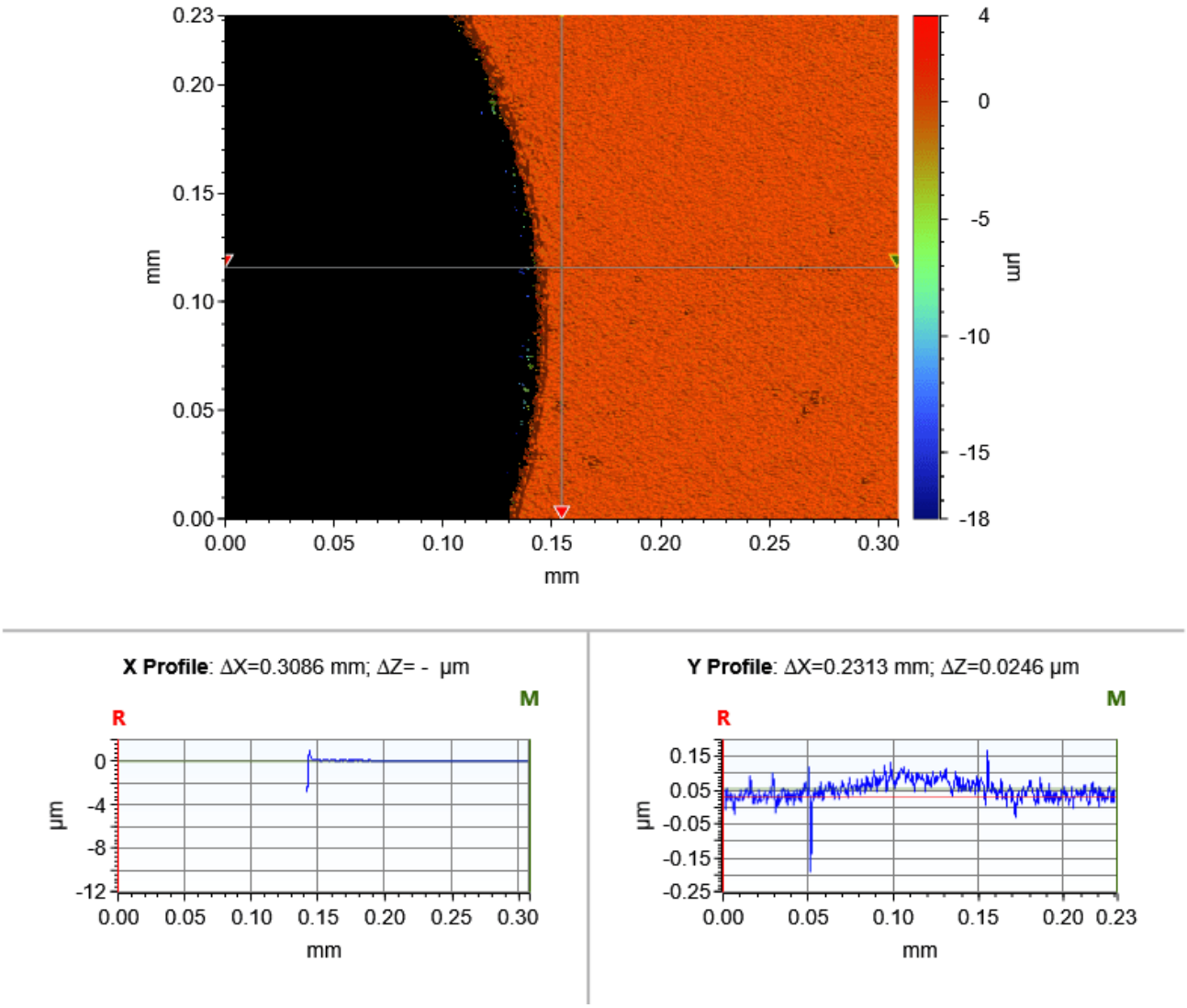

Figure 119: Results hole 1

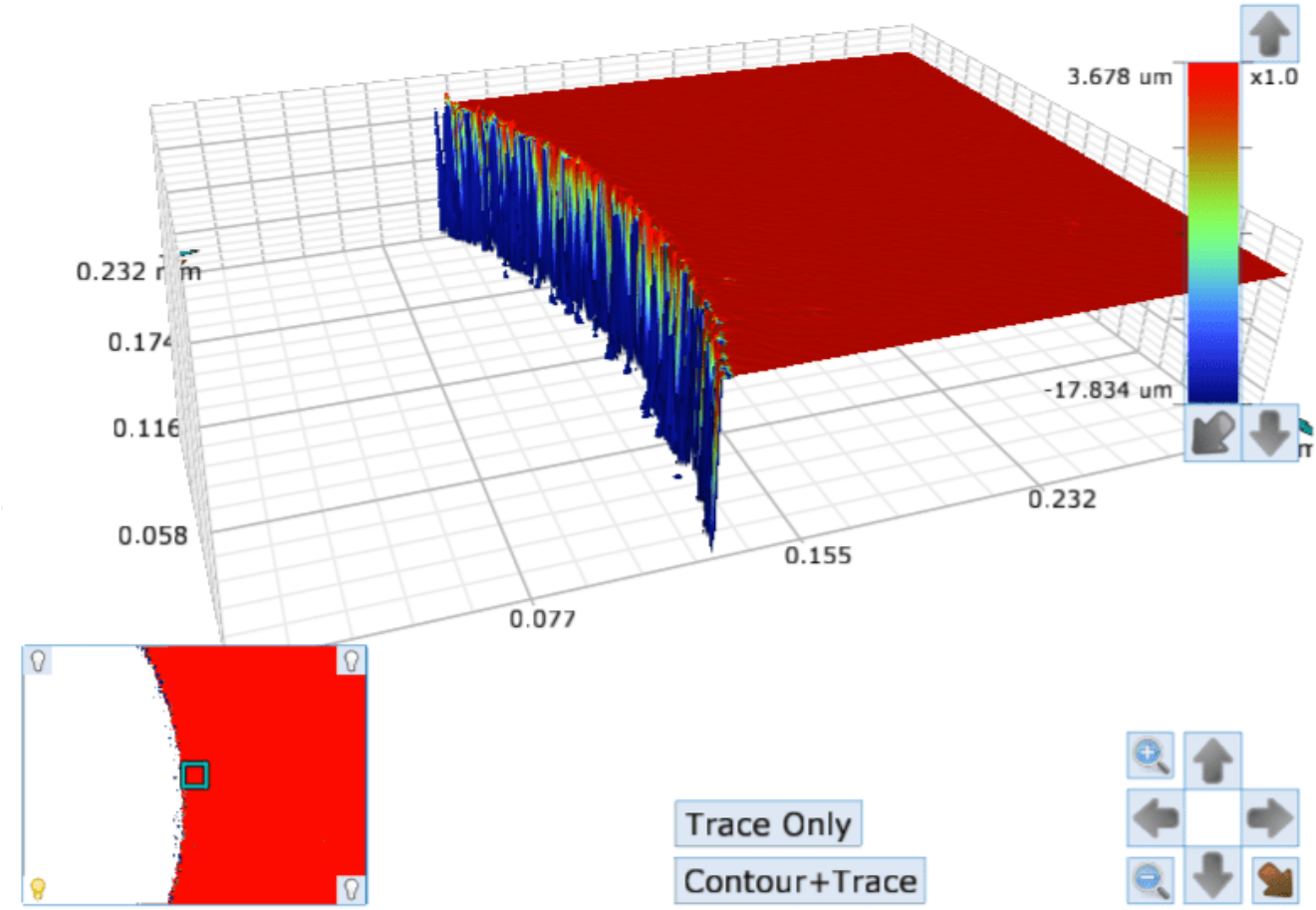

Figure 120: Results hole 1

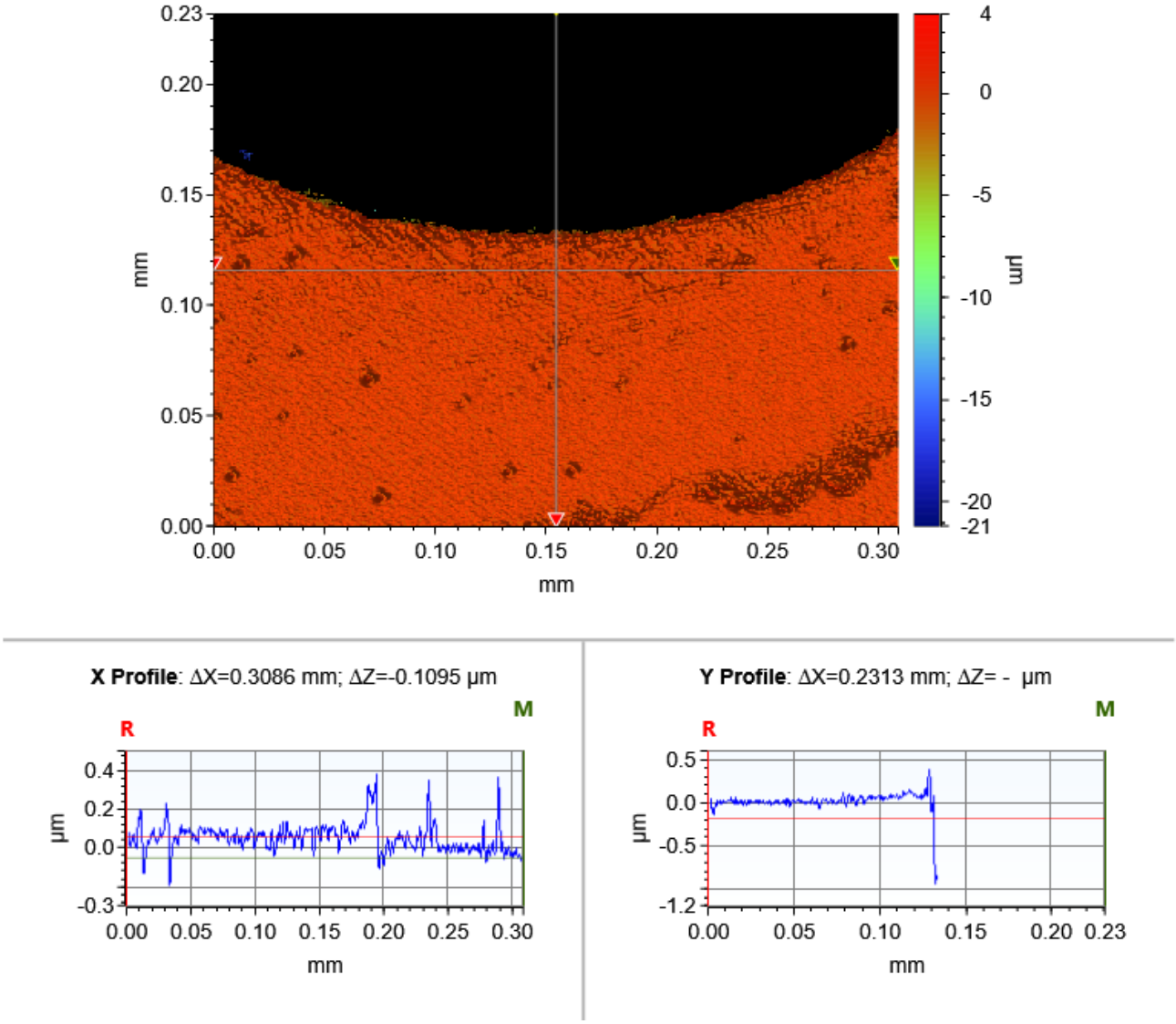

Figure 121: Results hole 3

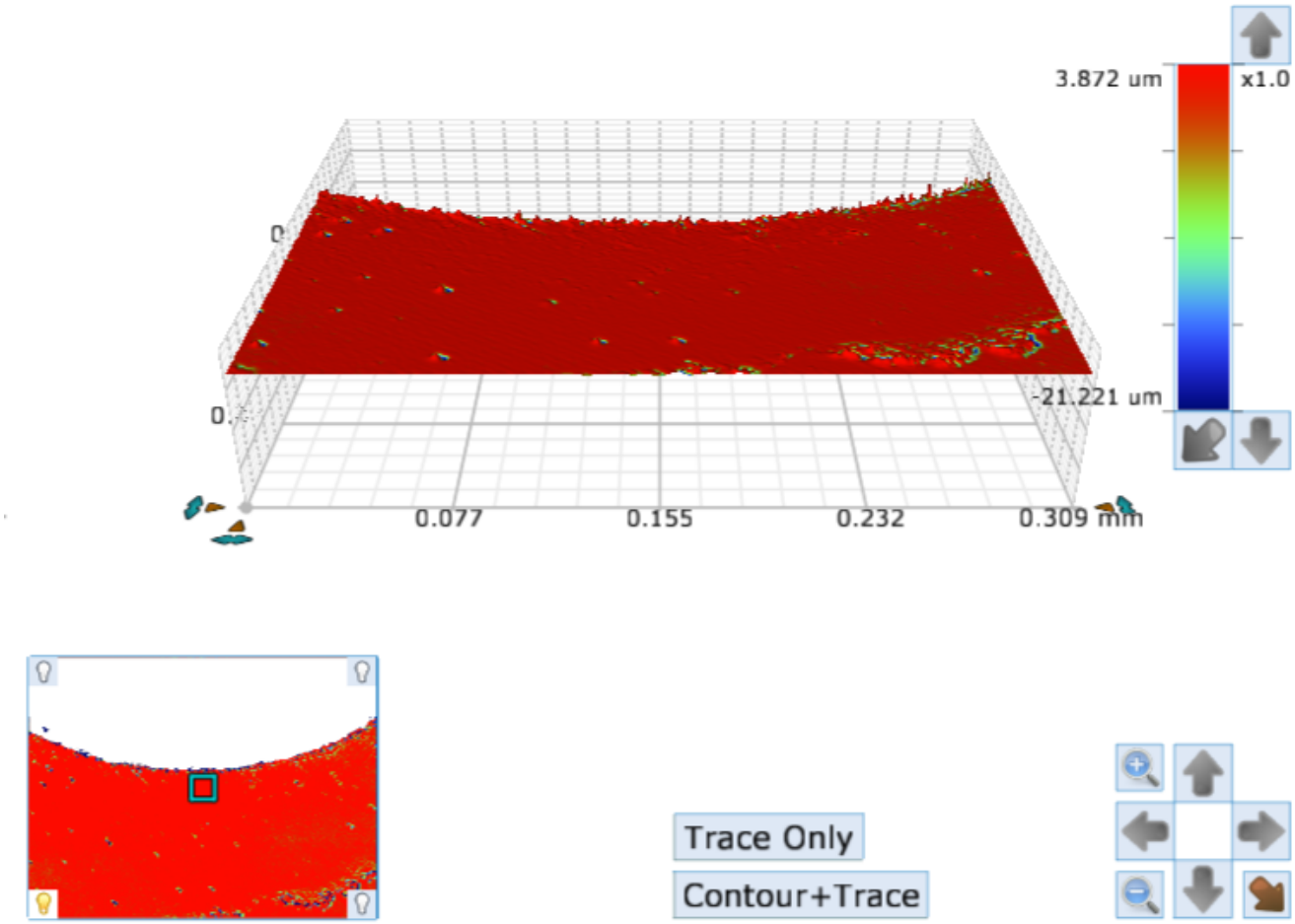

Figure 122: Results hole 3

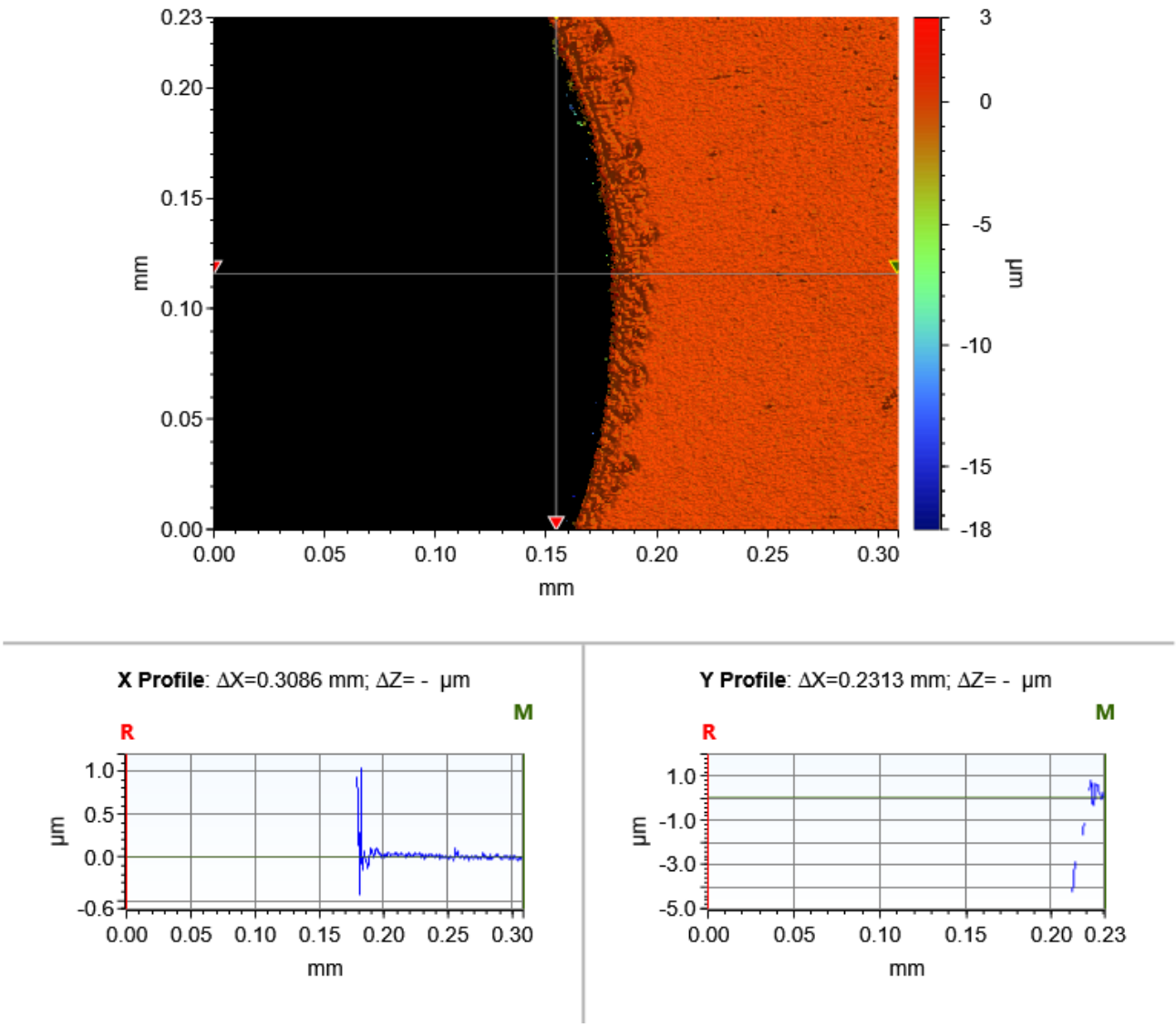

Figure 123: Results hole 4

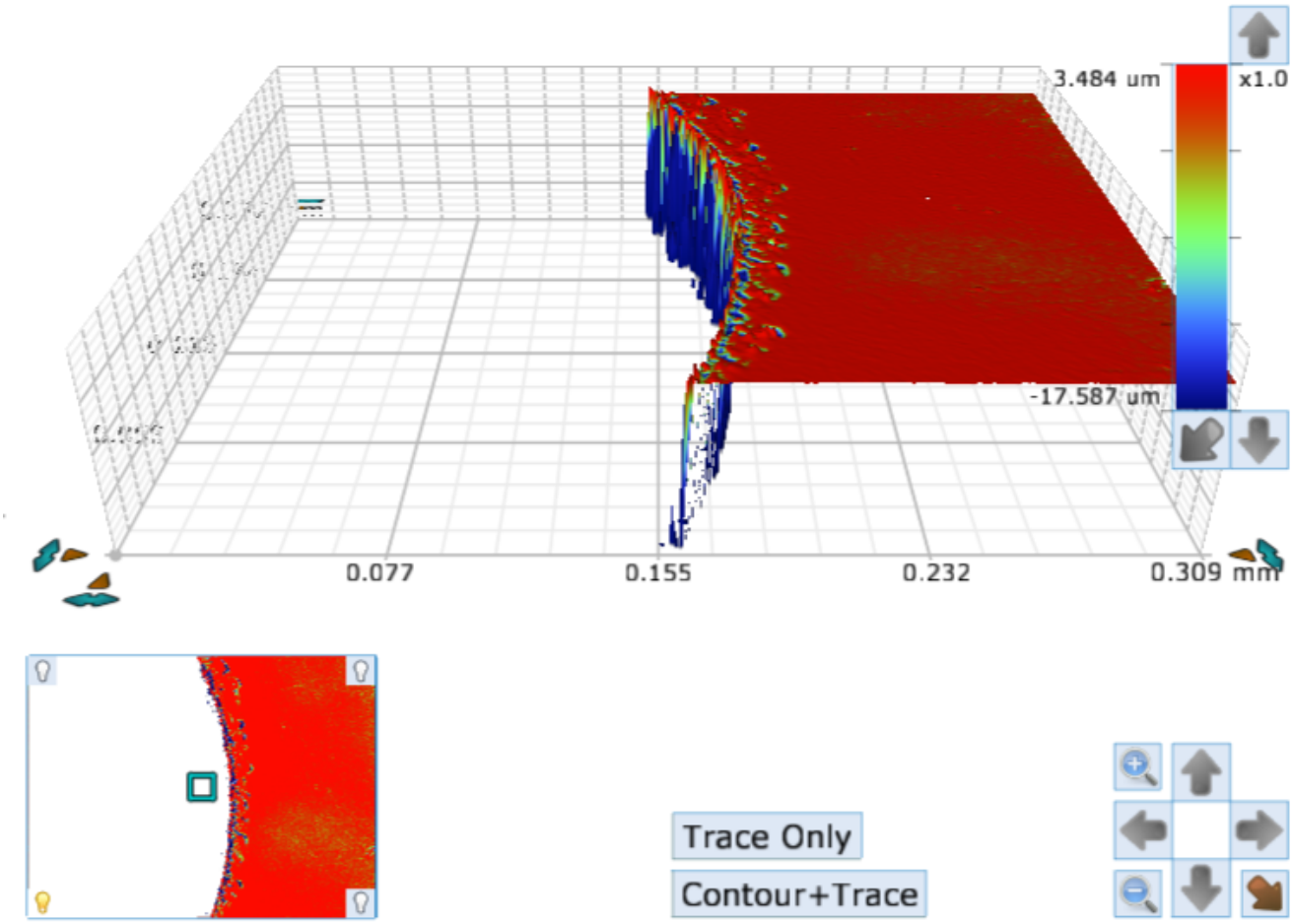

Figure 124: Results hole 4

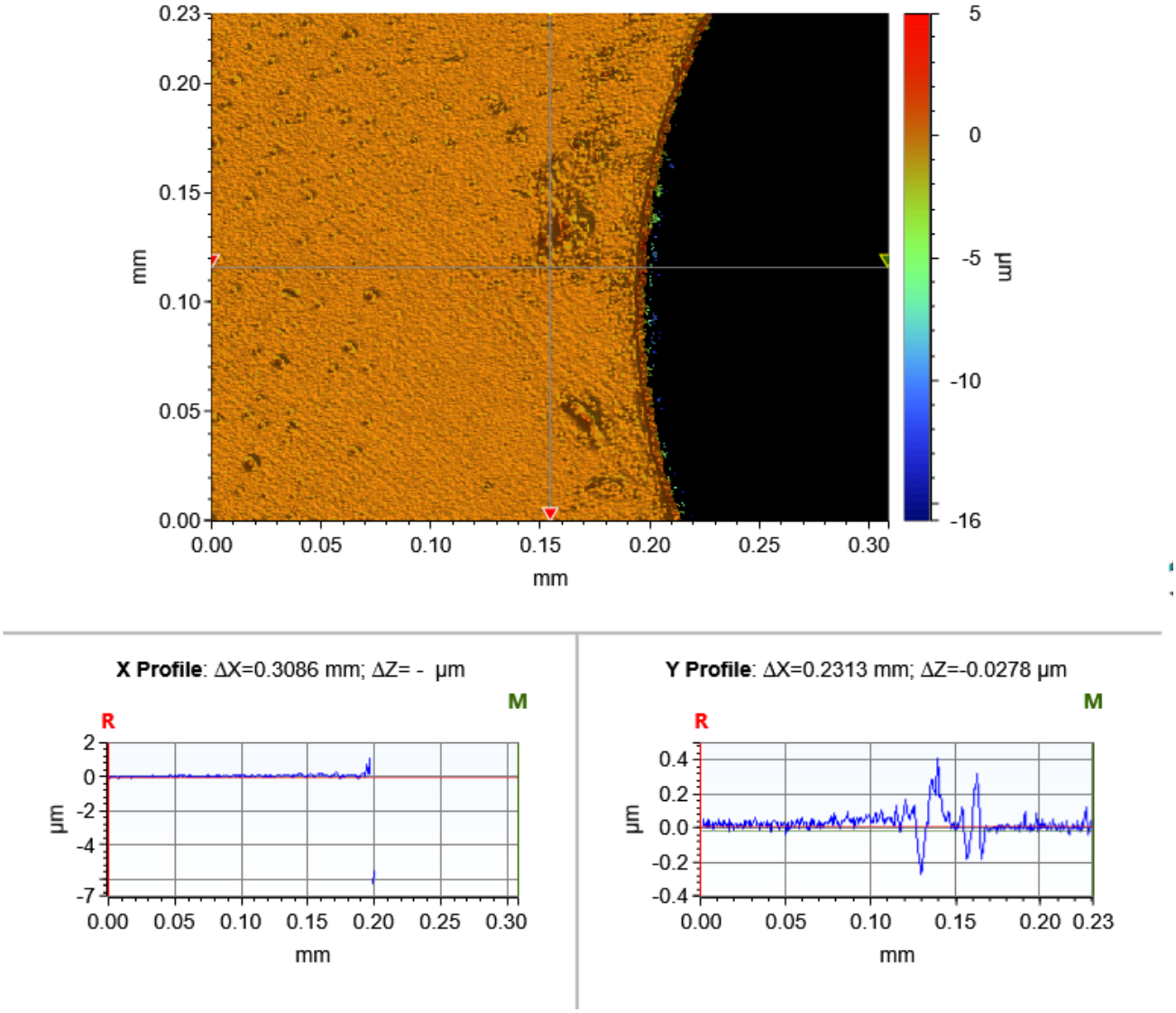

Figure 125: Results hole 5

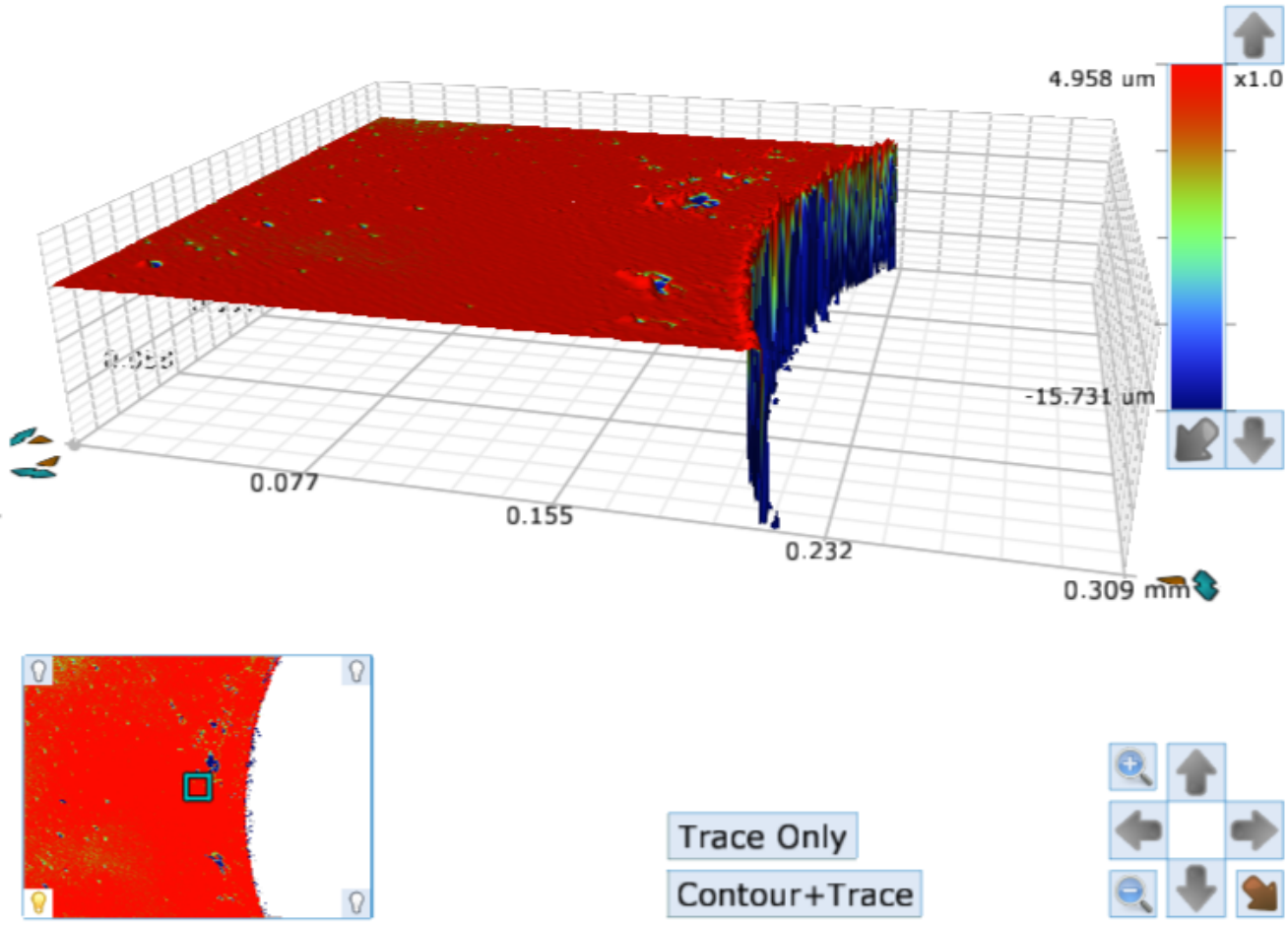

Figure 126: Results hole 5

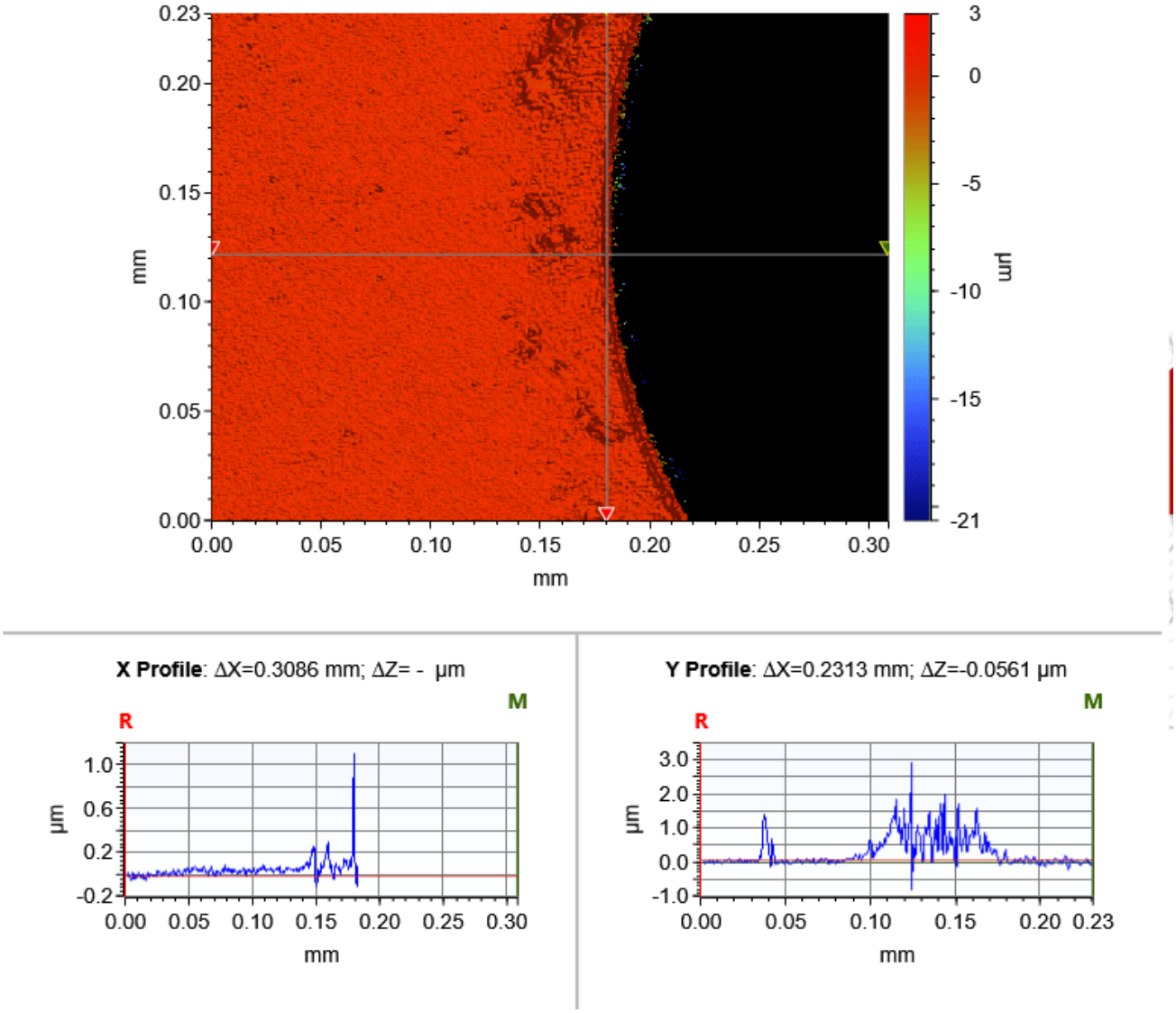

Figure 127: Results hole 6

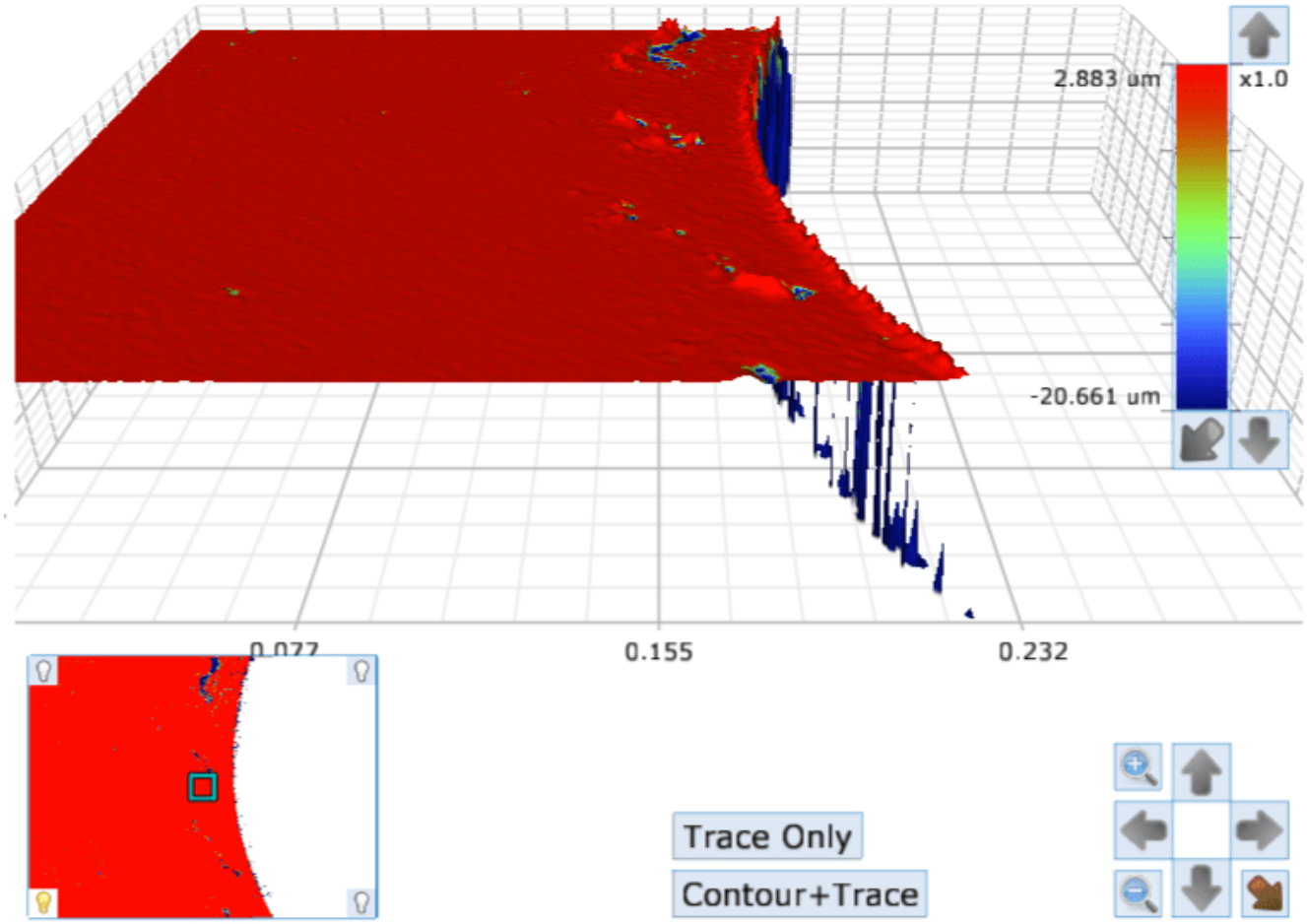

Figure 128: Results hole 6

L Fabricated Microfluidic Chips

This appendix displays images of all the different chips. Throughout the process of creating the nine chips, improvements were made with each iteration. Each chip follows one of the three previously mentioned configurations. The improvements made in fabrication time, by better setting up the Laser recipes. And more profound edge definition was applied, by for example rotating the specimen. Chip 4, shown in Figure 132, served as a valuable lesson, demonstrating that a single sticky note warning not to change the oven temperature for the risk of melting is insufficient in a student lab environment.

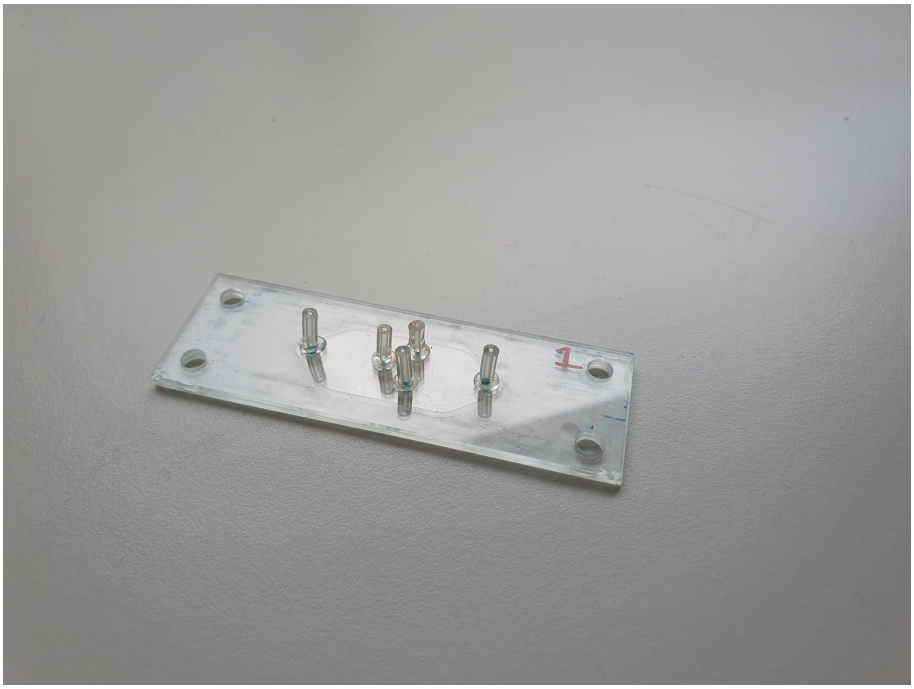

Figure 129: Chip 1, Configuration 1

Figure 130: Chip 2, Configuration 1

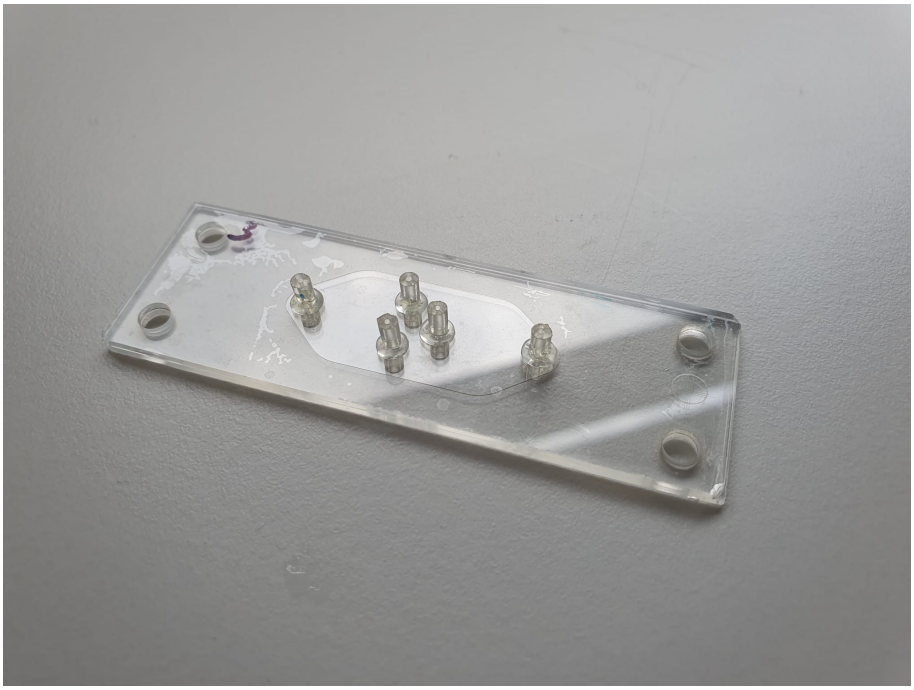

Figure 131: Chip 3, Configuration 1

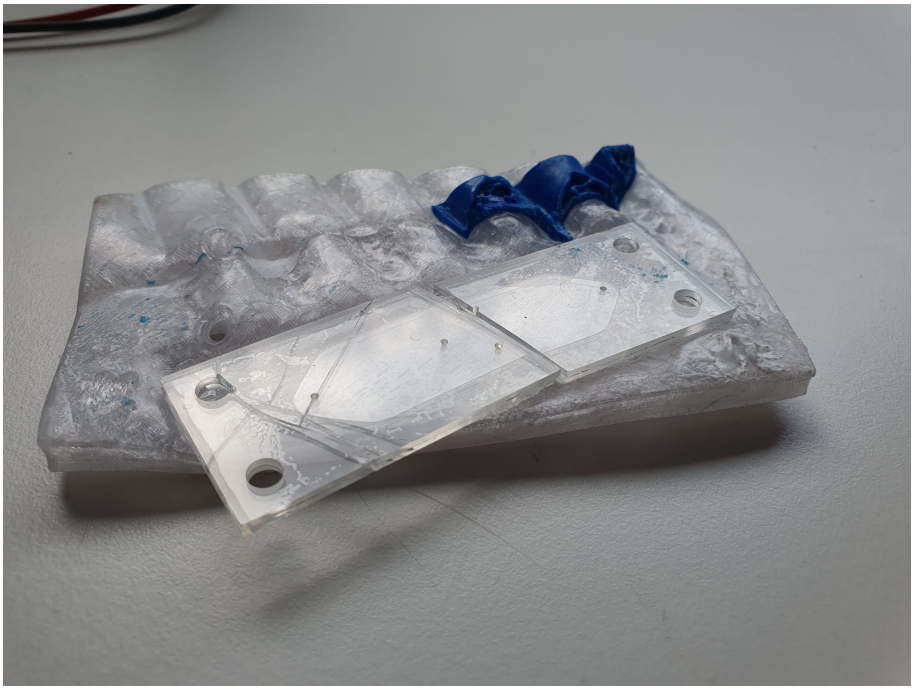

Figure 132: Chip 4, Configuration 2

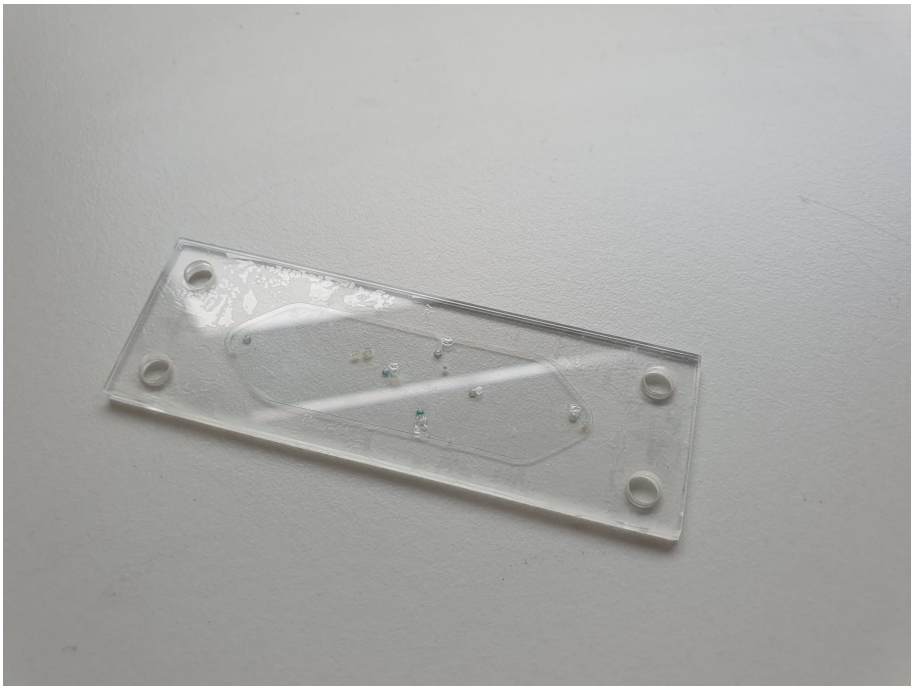

Figure 133: Chip 5, Configuration 3

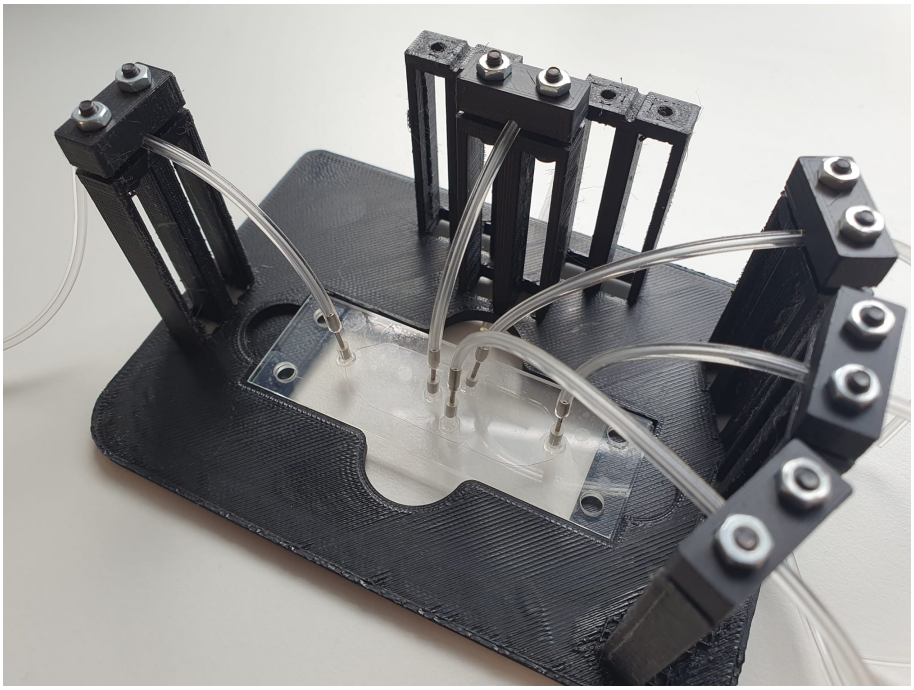

Figure 134: Chip 6, Configuration 2

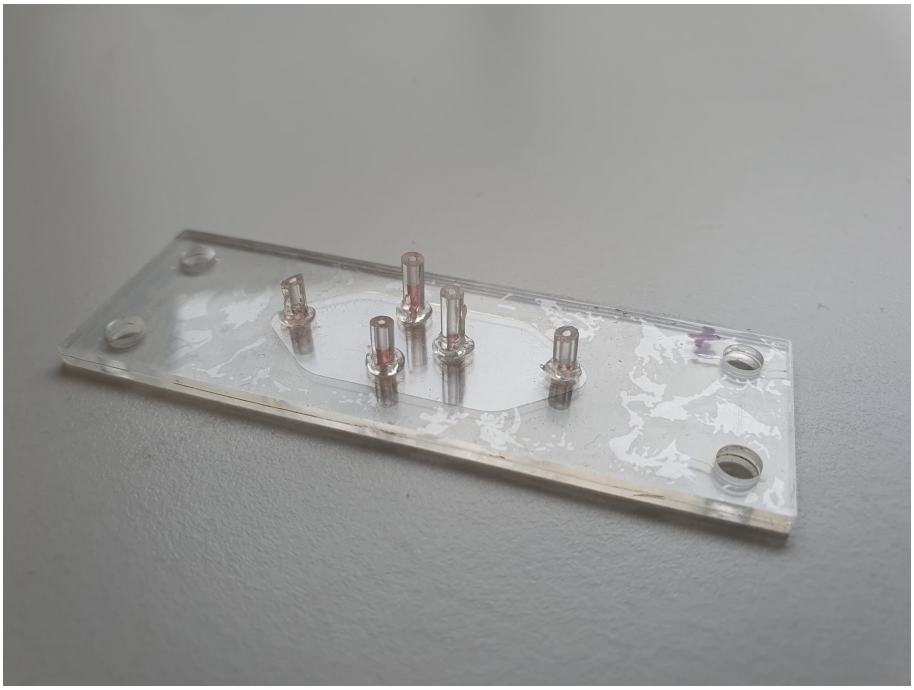

Figure 135: Chip 7, Configuration 2

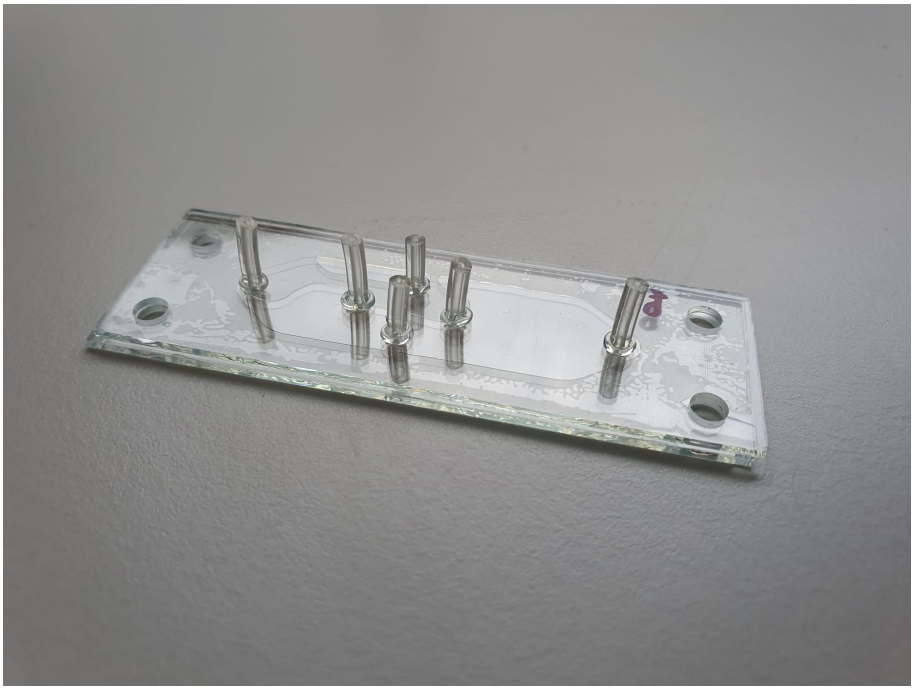

Figure 136: Chip 8, Configuration 3

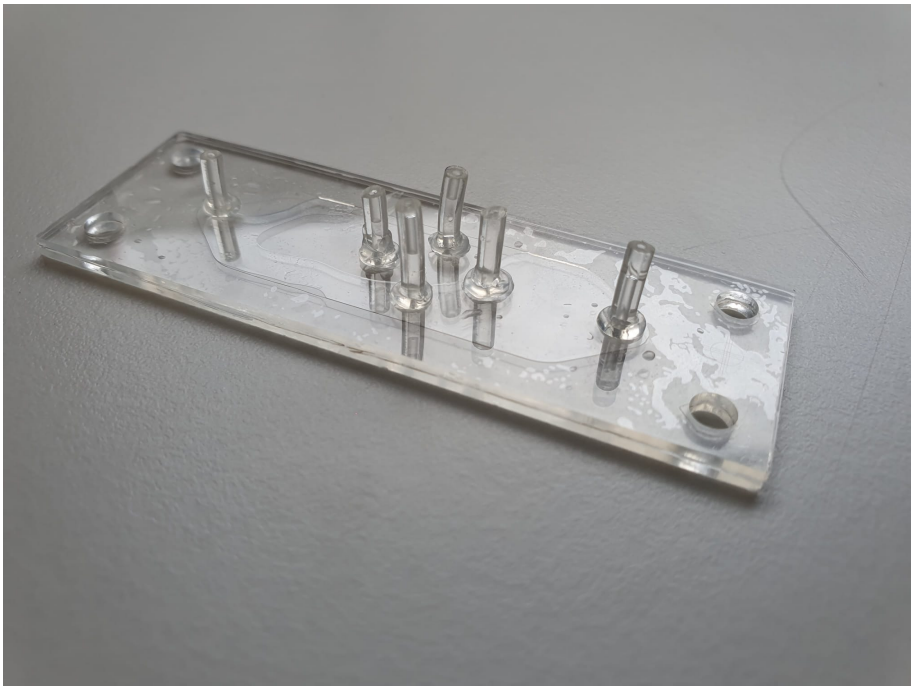

Figure 137: Chip 9, Configuration 3

M Scripts used for image processing

M.1 Diameter and Roundness analyser (Python)

```
import cv2
 import numpy as np
import matplotlib.pyplot as plt

def load_image(image_path):
    """Load an image from file."""
    image = cv2.imread(image_path)
    return image

def preprocess_image(image):
    """Convert image to grayscale and apply thresholding."""
    gray = cv2.cvtColor(image, cv2.COLOR_BGR2GRAY)
    _, thresh = cv2.threshold(gray, 0, 255, cv2.THRESH_BINARY_INV + cv2.THRESH_OTSU)
    return gray, thresh

def find_contours(thresh):
    """Find contours in the thresholded image."""
    contours, _ = cv2.findContours(thresh, cv2.RETR_EXTERNAL, cv2.CHAIN_APPROX_SIMPLE)
    return contours

def approximate_contours(contours, epsilon_scale=0.02):
    """Approximate the contours to simplify them."""
    approximated_contours = []
    for contour in contours:
        epsilon = epsilon_scale * cv2.arcLength(contour, True)
        approx = cv2.approxPolyDP(contour, epsilon, True)
        approximated_contours.append(approx)
    return approximated_contours

def overlay_contours(image, contours):
    """Overlay contours on the image."""
    cv2.drawContours(image, contours, -1, (0, 255, 0), 2)
    return image

def crop_image(image, xmin, xmax, ymin, ymax):
    """Crop the image based on given coordinates."""
    cropped_image = image[ymin:ymax, xmin:xmax]
    return cropped_image

def calculate_diameter(contour):
    """Calculate the diameter of the bounding circle for the contour."""
    _, radius = cv2.minEnclosingCircle(contour)
    diameter = 2 * radius
    return diameter

def calculate_perimeter_length(contour):
    """Calculate the perimeter length of the contour."""
    return cv2.arcLength(contour, True)

def calculate_roundness(contour):
    """Calculate the roundness of a contour."""
    area = cv2.contourArea(contour)
    perimeter = calculate_perimeter_length(contour)
    if perimeter == 0:
```

```
        return 0
    roundness = 4 * np.pi * area / (perimeter ** 2)
    return roundness

def find_longest_contour(contours):
    """Find the contour with the longest perimeter."""
    max_perimeter = 0
    longest_contour = None
    for contour in contours:
        perimeter = calculate_perimeter_length(contour)
        if perimeter > max_perimeter:
            max_perimeter = perimeter
            longest_contour = contour
    return longest_contour

def calculate_centroid(contour):
    """Calculate the centroid of the contour."""
    M = cv2.moments(contour)
    if M['m00'] == 0:
        return None
    cx = int(M['m10'] / M['m00'])
    cy = int(M['m01'] / M['m00'])
    return np.array([cx, cy])

def measure_diameters(contour, centroid, num_samples=100):
    """Measure several diameters within the perimeter of the contour
    passing through the centroid."""

    num_points = len(contour)
    diameters = []
    for i in range(num_samples):
        p1 = contour[np.random.randint(0, num_points)][0]
        direction = centroid - p1
        direction = direction / np.linalg.norm(direction)
        p2 = p1 + 2 * direction * np.linalg.norm(centroid - p1)
        diameter = np.linalg.norm(p1 - p2)
        diameters.append(diameter)
    return diameters

def calculate_standard_deviation(diameters):
    """Calculate the standard deviation of the diameters."""
    return np.std(diameters)

def analyze_image(image_path, xmin, xmax, ymin, ymax,
epsilon_scale=0.02, pixel_to_micrometer=1.0):

    """Analyze the roundness of the cuts in an image."""
    image = load_image(image_path)
    image = crop_image(image, xmin, xmax, ymin, ymax)
    gray, thresh = preprocess_image(image)
    contours = find_contours(thresh)

    # Approximate contours to reduce noise
    approximated_contours = approximate_contours(contours, epsilon_scale)

    # Find the longest contour
    longest_contour = find_longest_contour(approximated_contours)
    if longest_contour is not None:
```

```
        roundness = calculate_roundness(longest_contour)
        avg_diameter = calculate_diameter(longest_contour) * pixel_to_micrometer
        perimeter_length = calculate_perimeter_length(longest_contour) * pixel_to_micrometer
        centroid = calculate_centroid(longest_contour)
        diameters = measure_diameters(longest_contour, centroid, num_samples=100)
        diameters = [d * pixel_to_micrometer for d in diameters]
        diameter_std = calculate_standard_deviation(diameters)
    else:
        roundness = None
        avg_diameter = None
        perimeter_length = None
        diameters = None
        diameter_std = None
        print("No contours found.")

    # Overlay the longest contour on the original image
    if longest_contour is not None:
        image_with_contours = overlay_contours(image.copy(), [longest_contour])
    else:
        image_with_contours = image

    # Plotting the images
    fig, axes = plt.subplots(1, 3, figsize=(20, 10))
    axes[0].imshow(cv2.cvtColor(image_with_contours, cv2.COLOR_BGR2RGB))
    axes[0].set_title('Longest Contour')
    axes[0].axis('off')

    axes[1].imshow(gray, cmap='gray')
    axes[1].set_title('Grayscale Image')
    axes[1].axis('off')

    axes[2].imshow(thresh, cmap='gray')
    axes[2].set_title('Thresholded Image')
    axes[2].axis('off')

    plt.show()

    return roundness, avg_diameter, perimeter_length, diameters, diameter_std

# Example usage:
image_path = 'E:\\TU-Delft\\Thesis\\Microscopy results\\Speed 10\\2.tif'
xmin = 300  # Minimum x-coordinate
xmax = 1500  # Maximum x-coordinate
ymin = 0  # Minimum y-coordinate
ymax = 1200  # Maximum y-coordinate
epsilon_scale = 0.0005 # Scale factor for approximation accuracy
pixel_to_micrometer = 100 / 90  # Conversion factor from pixels to micrometers
roundness, avg_diameter, perimeter_length, diameters, diameter_std =
analyze_image(image_path, xmin, xmax, ymin, ymax, epsilon_scale, pixel_to_micrometer)

# Print results in cell format for easy copying to Excel
print(f"Epsilon_scale\t{epsilon_scale}")
print(f"Roundness\t{roundness}")
print(f"Average Diameter (micrometers)\t{avg_diameter}")
print(f"Perimeter Length (micrometers)\t{perimeter_length}")
print(f"Standard Deviation of Diameters (micrometers)\t{diameter_std}")

#E:\\TU-Delft\\Thesis\\Microscopy results\\Chip 9\\H5T1.tif
```

```
#E:\\TU-Delft\\Thesis\\Microscopy results\\Speed 11\\10.tif
#E:\\TU-Delft\\Thesis\\Microscopy results\\082024\\H1_2.tif
```

M.2 Cut Width and Roughness analyser (Python)

```
    import cv2
import numpy as np
from matplotlib import pyplot as plt

# Path to the image
image_path = 'E:\\TU-Delft\\Thesis\\Microscopy results\\Powerlow 1\\2_2.tif'

# Coordinates for the region of interest
xmin = 600
xmax = 1400
ymin = 100
ymax = 1000

# Conversion factor from pixels to micrometers
pixels_per_micrometer = 44 / 5

# Adjustable plot resolution (dpi)
plot_dpi = 600  # You can adjust this value for higher or lower resolution

# Load the image
image = cv2.imread(image_path)
if image is None:
    print("Error: Image not found.")
else:
    # Convert the image to grayscale
    gray = cv2.cvtColor(image, cv2.COLOR_BGR2GRAY)

    # Define the region of interest
    if ymax is None:
        ymax = gray.shape[0]
    if xmax is None:
        xmax = gray.shape[1]

    # Ensure the specified region is within the image boundaries
    ymin = max(0, ymin)
    ymax = min(gray.shape[0], ymax)
    xmin = max(0, xmin)
    xmax = min(gray.shape[1], xmax)

    # Crop the region of interest
    roi = gray[ymin:ymax, xmin:xmax]

    # Apply thresholding to isolate dark areas
    _, thresholded = cv2.threshold(roi, 50, 255, cv2.THRESH_BINARY_INV)

    # Find contours in the thresholded image
    contours, _ = cv2.findContours(thresholded, cv2.RETR_EXTERNAL, cv2.CHAIN_APPROX_SIMPLE)

    if len(contours) == 0:
        print("No contours found.")
    else:
        # Assuming the largest contour is the cut
        cut_contour = max(contours, key=cv2.contourArea)

        # Separate the contour points into left and right edges based on their x-coordinates
        left_edge_points = []
```

```
right_edge_points = []

for point in cut_contour:
    x, y = point[0]
    if x < np.mean(cut_contour[:, 0, 0]):
        left_edge_points.append([x, y])
    else:
        right_edge_points.append([x, y])

left_edge_points = np.array(left_edge_points)
right_edge_points = np.array(right_edge_points)

# Fit a line to the left edge points
[vx_left, vy_left, x_left, y_left] = cv2.fitLine(left_edge_points,
cv2.DIST_L2, 0, 0.01, 0.01)
left_slope = vy_left[0] / vx_left[0]
left_intercept = y_left[0] - (left_slope * x_left[0])

# Fit a line to the right edge points
[vx_right, vy_right, x_right, y_right] = cv2.fitLine(right_edge_points,
cv2.DIST_L2, 0, 0.01, 0.01)
right_slope = vy_right[0] / vx_right[0]
right_intercept = y_right[0] - (right_slope * x_right[0])

# Calculate the width of the cut at 100 equally spaced y coordinates
y_coords = np.linspace(0, thresholded.shape[0] - 1, 100)
widths = []

for y in y_coords:
    x_left = (y - left_intercept) / left_slope
    x_right = (y - right_intercept) / right_slope
    width = x_right - x_left
    widths.append(width)

# Calculate average width and standard deviation
average_width = np.mean(widths) / pixels_per_micrometer
std_deviation = np.std(widths) / pixels_per_micrometer

# Calculate roughness as the maximum deviation from the fitted line
def calculate_deviation(points, slope, intercept):
    deviations = []
    for point in points:
        x, y = point
        # Calculate the expected x position on the line for this y
        expected_x = (y - intercept) / slope
        deviation = x - expected_x
        deviations.append(deviation)
    return np.max(deviations), np.min(deviations), np.std(deviations)

left_max_dev, left_min_dev, left_std_dev = calculate_deviation(left_edge_points,
left_slope, left_intercept)

right_max_dev, right_min_dev, right_std_dev = calculate_deviation(right_edge_points,
right_slope, right_intercept)


# Convert deviations to micrometers
left_max_dev = left_max_dev / pixels_per_micrometer
```

```
left_min_dev = left_min_dev / pixels_per_micrometer
left_std_dev = left_std_dev / pixels_per_micrometer
right_max_dev = right_max_dev / pixels_per_micrometer
right_min_dev = right_min_dev / pixels_per_micrometer
right_std_dev = right_std_dev / pixels_per_micrometer

# Display the results with 5 decimal places
print(f"Average width of the cut\t {average_width:.5f} ") #micrometers
print(f"Standard deviation of the width\t {std_deviation:.5f} ") #micrometers
print(f"Left edge max deviation\t {left_max_dev:.5f}\t  min deviation\t
{left_min_dev:.5f}\t  std deviation\t {left_std_dev:.5f} ") #micrometers

print(f"Right edge max deviation\t {right_max_dev:.5f}\t  min deviation\t
{right_min_dev:.5f}\t  std deviation\t {right_std_dev:.5f} ") #micrometers


# Visualization of the lines and the region of interest
image_with_lines = image[ymin:ymax, xmin:xmax].copy()
thresholded_with_lines = cv2.cvtColor(thresholded.copy(), cv2.COLOR_GRAY2BGR)

def plot_line(image, slope, intercept, color=(0, 255, 0)):
    y1 = 0
    y2 = image.shape[0]
    x1 = int((y1 - intercept) / slope)
    x2 = int((y2 - intercept) / slope)
    cv2.line(image, (x1, y1), (x2, y2), color, 2)

plot_line(image_with_lines, left_slope, left_intercept, color=(0, 255, 0))
plot_line(image_with_lines, right_slope, right_intercept, color=(0, 0, 255))
plot_line(thresholded_with_lines, left_slope, left_intercept, color=(255, 0, 0))
plot_line(thresholded_with_lines, right_slope, right_intercept, color=(0, 255, 0))

plt.figure(figsize=(15, 5), dpi=plot_dpi)  # Adjusted resolution with dpi parameter

plt.subplot(1, 2, 1)
plt.title("Original Image with Fitted Lines")
plt.imshow(cv2.cvtColor(image_with_lines, cv2.COLOR_BGR2RGB))

plt.subplot(1, 2, 2)
plt.title("Thresholded Image with Fitted Lines")
plt.imshow(thresholded_with_lines)

plt.tight_layout()
plt.show()
```